

Development of multifunctional catalysts for the valorization of lignocellulosic and marine biomass into value added products

by

Samrin Salim Shaikh
10CC21J26034

A thesis submitted to the
Academy of Scientific & Innovative Research
for the award of the degree of
DOCTOR OF PHILOSOPHY
in
(SCIENCE)

Under the supervision of
Dr. Vijay. V. Bokade
Dr. Chandrashekhar. V. Rode



CSIR- National Chemical Laboratory, Pune



Academy of Scientific and Innovative Research
AcSIR Headquarters, CSIR-HRDC campus
Sector 19, Kamla Nehru Nagar,
Ghaziabad, U.P. – 201 002, India

September 2023

Certificate

This is to certify that the work incorporated in this Ph.D. thesis entitled, “Development of multifunctional catalysts for the valorization of lignocellulosic and marine biomass into value added products”, submitted by Samrin Salim Shaikh to the Academy of Scientific and Innovative Research AcSIR in fulfillment of the requirements for the award of the Degree of Doctor of Philosophy, embodies original research work carried-out by the student. We, further certify that this work has not been submitted to any other University or Institution in part or full for the award of any degree or diploma. Research material(s) obtained from other source(s) and used in this research work has/have been duly acknowledged in the thesis. Image(s), illustration(s), figure(s), table(s) etc., used in the thesis from other source(s), have also been duly cited and acknowledged.



(Signature of Student)

Name with date

Samrin Salim. Shaikh
11/08/2023



(Signature of Co-Supervisor)
if-any

Name with date

Dr. C. V. Rode
11/08/2023



(Signature of Supervisor)

Name with date

Dr. V. V. Bokade
11/08/2023

STATEMENTS OF ACADEMIC INTEGRITY

I Shaikh Samrin Salim, a Ph.D. student of the Academy of Scientific and Innovative Research (AcSIR) with Registration No. 10CC21J26034 hereby undertake that, the thesis entitled “Development of multifunctional catalysts for the valorization of lignocellulosic and marine biomass into value added products” has been prepared by me and that the document reports original work carried out by me and is free of any plagiarism in compliance with the UGC Regulations on *“Promotion of Academic Integrity and Prevention of Plagiarism in Higher Educational Institutions (2018)”* and the CSIR Guidelines for *“Ethics in Research and in Governance (2020)”*.



Signature of the Student

Date: 11/08/2023

Place: Pune

It is hereby certified that the work done by the student, under my/our supervision, is plagiarism-free in accordance with the UGC Regulations on *“Promotion of Academic Integrity and Prevention of Plagiarism in Higher Educational Institutions (2018)”* and the CSIR Guidelines for *“Ethics in Research and in Governance (2020)”*.



Signature of the Co-supervisor (if any)

Name: Dr. C. V. Rode

Date: 11/08/2023

Place: Pune



Signature of the Supervisor

Name: Dr. V. V. Bokade

Date: 11/08/2023

Place: Pune

**My thesis is dedicated to my beloved
family for their unconditional
support and
encouragement
throughout and mother nature.**



My PhD tenure has been one of the most wonderful scientific journey of my life. Wherein, I went on learning and each time I stepped forward towards a new achievement. Just as the footsteps on wet cement makes an impression on it, similarly my PhD journey has had several valuable experiences and unforgettable moments that has left an impression on my mind which can never be erased. I feel fortunate to have had been accompanied and supported by several people and I take the opportunity to thank them.

*I feel highly obliged and I express my deepest benediction and thanks to my research supervisor **Dr. C. V. Rode**, Emeritus scientist, Chemical engineering and Process Development Division, CSIR-National Chemical laboratory, India for giving me an opportunity to be a part of his esteemed group. His encouragement, constant support, excellent guidance, valuable suggestions and healthy discussions throughout my doctoral research has enabled me to complete my thesis successfully. His helpful comments and revisions during my thesis writing are greatly appreciated. I thank him for being an inspiration for me and for developing in me a passion towards my research. His innovative ideas, scientific temper and wealth of experience in this field have helped me to grow and excel in my PhD studies. I acknowledge the freedom granted to me for independent thinking, planning and execution of research work in the laboratory. I would also like to extend my thanks to my doctoral advisory committee members Dr. Kiran Kulkarni, Dr. S. P. Kamble, Dr. R. Kontham for their valuable suggestions and comments during the DAC meetings and thesis writing. I would also like to thank my supervisor Dr. V. V. Bokade for his constant support, suggestions, guidance and instructions that he provided me throughout my doctoral studies.*

I would like to thank the head of Chemical Engineering and Process Development Division Dr. C. Gadgil and the head of Inorganic Chemistry and catalysis Division Dr. S. Umbarkar for providing me with various divisional and technical facilities to carry out my research work. I would also like to thank the former Director Dr. A. K. Nangia and Dr. Ashish. K. Lele, Director CSIR-NCL, Pune for providing me various facilities, research amenities and infrastructure to carry out my research work. I am grateful to Council of Scientific and Industrial Research (CSIR-HRDG) for funding me and providing me Junior Research Fellowship through the project during the course of me PhD tenure. I would also like to thank Dr. E. Balaraman, Dr. S. B. Mhaske and Dr. C. V. Ramana to be a part of an industrial project at CSIR-NCL for their constant support, valuable suggestions and kind comments throughout the project tenure.

I also wish to thank my seniors and lab mates Dr. Sharda, Dr. Chetana, Dr. Bhanu Pratap, Dr. Dnyanesh, Dr. Gaytri, Dr. Roopa, Dr. Rajan and Ms. Komal. My special thanks to my friends Rinto, Medha, Angshuman for always being there for me emotionally and intellectually throughout my PhD tenure. I would like to extend my gratitude to and special thanks to the Sao Chairperson Dr. S. B. Mhaske, Dr. C. P. Vinod, Mrs. Vaishali, Mrs. Vijaya, Mrs. Komal for being so dedicated and supportive and for helping me in all possible manners. I also thank Dr. R. S. Gholap and his team Ms. Medha, Mrs. Shruti, Mr. Chetan, Mr. Tushar for providing excellent service during SEM and TEM analysis. I also thank Dr. Uday. K. Mareli and his team for their help in carrying out the NMR analysis. I also thank the non-scientific staff Mr. Raheja, Mr. Palash and Mr. Patane for their help and cooperation they provided to complete my thesis work successfully.

Last but not the least words cannot express my gratitude and love to my family without whom I could not have undertaken this journey. I thank my (Late) father for being an inspiration for me and for laying my foundation so strong. My mother for being my backbone and for her constant emotional and morale support throughout. My lovely brother Salman and my sister Almas for always encouraging me to move forward in life and for boosting me to do my best...

With many thanks,

Samrin Salim Shaikh

Table of contents

Contents

List of contents	i
List of Tables	x
List of Figures	xi
List of Schemes	xv
Abbreviations	xvii
Abstract	xviii

List of contents

Section No:	Title	Page No.
--------------------	--------------	-----------------

Chapter 1. Introduction

1.1 Biomass	1
1.2 Need for biomass valorization	2
1.3 Composition of lignocellulosic biomass	4
1.3.1 Cellulose	5
1.3.2 Hemicellulose	6
1.3.3 Lignin	7
1.4 Composition of marine biomass	7
1.5 The biorefinery concept	9

1.6 Platform molecules and their commercial potential	10
1.7 Catalytic reactions for the conversion of lignocellulosic and marine biomass derived platform molecules.	13
1.7.1 Isomerization	17
1.7.2 Dehydration	17
1.7.3 Hydration reaction	21
1.7.4 Hydrogenation reaction	21
1.7.5 Hydrogenolysis	22
1.7.6 Transesterification of Glycerol to glycidol	22
1.8 Catalysis	23
1.9 Characteristics of a good catalyst	23
1.9.1 solid acid catalysis	24
1.10 Various parameters affecting the activity of solid catalysts in biomass conversion	24
1.10.1 Substrate concentration	25
1.10.2 Reaction medium	25
1.10.3 Effect of temperature	25
1.10.4 Effect of time	26

1.10.5 Effect of pressure	26
1.11 Objectives of the thesis	27

Chapter-2 Experimental

2.1 Introduction	35
2.2 Materials used	35
2.3 Synthesis of catalysts: solid acid catalysis	36
2.3.1 Preparation of Ba-Zr mixed metal oxide by co-precipitation method	36
2.3.2 Preparation of SBA-15	37
2.3.3 Wet impregnation of Phosphotungstic acid supported on SBA-15	37
2.3.4 Direct synthesis of Phosphotungstic acid supported on SBA-15	37
2.3.5 Direct synthesis of Phosphomolybdic acid supported on SBA-15	37
2.3.6 Direct synthesis of Silicotungstic acid supported on SBA-15	37
2.3.7 Direct synthesis of Silicomolibdic acid supported on SBA-15	38
2.3.8 Preparation of Barium oxide	38
2.3.9 Preparation of Sr/Cu-Al by Co-precipitation method	39
2.4 Catalyst characterization techniques	40

2.4.1	X-ray diffraction	42
2.4.2	Physico-chemical measurements and N ₂ sorption studies	43
2.4.3	Temperature programmed desorption of ammonia (NH ₃ and CO ₂ TPD)	44
2.4.4	Fourier transform infrared spectroscopy (FTIR)	45
2.4.4.1	Pyridine FTIR technique	45
2.4.4.2	MeOH FTIR technique	46
2.4.5	Inductively coupled plasma atomic emission spectroscopy (ICP-AES)	47
2.4.6	X-ray photoelectron Spectroscopy	49
2.4.7	Raman Spectroscopy	51
2.4.8	Transmission Electron Microscopy	51
2.4.9	Field Emission-Scanning Electron Microscopy	52
2.4.10	Thermal analysis	52
2.5	Catalyst activity measurement	52
2.5.1	Round bottom flask reflux reaction set-up for glucose isomerization	53
2.5.2	Parr reactor set-up for NAG conversion	53
2.6	Analytical methods for quantitative analysis	54
2.6.1	Gas Chromatography	55
2.6.2	High Performance Liquid Chromatography	55

2.7 Catalyst activity performance	56
2.7.1 Turn over number (TON)	56
2.7.2 Turn over Frequency (TOF)	56
2.7.3 Formulae	56

Chapter-3

Cooperative acid-base sites of solid Ba-Zr mixed oxide catalyst for efficient isomerization of glucose to fructose in aqueous medium

3.1 Introduction	59
3.2 Experimental	60
3.3 Results and discussion	62
3.3.1 Catalyst characterization	63
3.3.1.1 XRD analysis	63
3.3.1.2 SEM analysis	63
3.3.1.3 TEM analysis	64
3.3.1.4 BET and surface area measurement	65
3.3.1.5 Raman analysis	66
3.3.1.6 FTIR analysis	68
3.3.1.7 XPS analysis	69
3.3.2 Activity studies	70
3.3.3 Catalyst screening and catalyst optimization	72

3.3.4	Effect of various molar ratio of Ba-Zr	74
3.3.5	Effect of substrate to catalyst ratio	76
3.3.6	Effect of temperature	78
3.3.7	Effect of solvent	78
3.3.8	Recycle run	80
3.4	Conclusion	81

Chapter-4

Direct Conversion of N-Acetyl-D-glucosamine to N-containing heterocyclic compounds 3-acetamidofuran and 3-acetamido-5-acety furan.

4.1	Introduction	89
4.2	Experimental	91
4.3	Results and discussion	92
4.3.1	Catalyst characterization	92
4.3.1.1	XRD analysis	92
4.3.1.2	SEM analysis	93
4.3.1.3	TEM analysis	94
4.3.1.4	A FTIR analysis	95
4.3.1.5	B MeOH FTIR analysis	96
4.3.1.6	BET, surface area measurement and TPD analysis	97
4.3.2	Catalyst screening and catalyst optimization on NAG conversion	99
4.3.3	Effect of substrate to catalyst ratio on NAG conversion	101

4.3.4	Effect of time on NAG conversion	101
4.3.5	Effect of temperature on NAG conversion	102
4.3.6	Effect of solvent on NAG conversion	103
4.3.7	Effect of addition of water on reaction pathway	104
4.3.8	Recycle run	105
4.4	Plausible reaction mechanism	107
4.4	Conclusion	116

Chapter-5

One pot glycidol synthesis and separation via glycerol transesterification with DMC over mixed metal oxide

5.1	Introduction	124
5.2	Experimental section	127
5.2.1	Chemicals and materials	127
5.2.2	Experimental procedure	127
5.3	Results and discussion	127
5.3.1	Catalyst characterization	127
5.3.1.1	BET, surface area measurement and TPD analysis	127
5.3.1.2	XRD analysis	129
5.3.1.3	FTIR analysis	130
5.3.1.4	XPS analysis	131
5.3.1.5	A FE-SEM and E-DAX analysis	132

5.3.1.4 B FE-SEM analysis of MMO in varying ratios	134
5.3.1.4 C Elemental mapping	135
5.3.1.5 HR-TEM analysis	135
5.4 Activity performance	136
5.4.1 support screening	137
5.4.2 Catalyst screening and catalyst optimization	138
5.4.3 Parameter optimization	140
5.4.3.1 Temperature	140
5.4.3.2 Time on stream	141
5.4.3.3 Catalyst loading	142
5.4.3.4 Metal loading	143
5.5 Product analysis by Gas Chromatography	145
5.6 Product separation by vacuum distillation	148
5.7 Conclusion	149

Chapter-6

Conclusions and future scope

Section A:

6.1 Conclusion remarks	154
6.2 Future scope	156

Section B:

1.	Abstract for indexing.	158
2.	List of Publications	159
3.	List of posters	159
4.	Copy of SCI Publications	160

List of Tables

Table No	Title	Page No.
<u>Chapter 3</u>		
Table 3.1 a.	The physico-chemical properties of the prepared catalysts.	67
Table 3.1 b	Crystallite sizes of all the three phases formed in all Ba:Zr MMO catalyst	68
Table 3.2	Isomerisation of glucose to fructose over different metal oxide catalysts	76

Table No	Title	Page No.
<u>Chapter 4</u>		
Table 4.1	Physico-chemical properties of the catalysts	100
Table 4.2	Catalyst screening for NAG conversion to 3AF and 3A5AF	100

Table No	Title	Page No.
<u>Chapter 5</u>		
Table 5.1.	Physico-chemical properties of prepared catalyst.	128
Table 5.2	Binding energy and peak area for the two-core level excitation in Sr-Cu-Al catalyst.	131
Table 5.3	Support screening for the glycidol synthesis.	137
Table 5.4	Catalyst screening for the glycidol synthesis.	139
Table 5.5	Effect of catalyst loading on Glycerol transesterification	143
Table 5.6	Effect of Sr-loading on Glycerol transesterification	144
Table 5.7.	GC oven temperature program.	146

List of Figures

Figure No	Title	Page No.
<u>Chapter 1</u>		
Fig. 1.1	Composition of lignocellulosic biomass	5
Fig. 1.2	Structure of cellulose	6
Fig. 1.3	Structure of hemicelluloses	6
Fig 1.4	Structure of lignin	7
Fig. 1.5	Chitin and chitosan biomass resource	8
Fig. 1.6.	Hierarchy of a biorefinery	9
Fig. 1.7.	Platform Chemicals	13
Fig. 1.8	Structure of lignin	14
Fig. 1.9	Structure of cellulose	14
Fig. 1.10	Structure of hemicellulose	14
Fig. 1.11	Structure of chitin	16
Fig. 1.12	Structure of chitosan	16

Chapter 2

Fig.2.1. a	Preparation of Ba-Zr by Co-precipitation method.	36
Fig.2.1. b	Preparation of Cu-Al by Co-precipitation method.	38
Fig. 2.2	Powder XRD instrument.	40
Fig. 2.3	Autosorb 1, Quantachrome instrument.	42
Fig. 2.4	Shimadzu FTIR-8201 PC spectrophotometer.	44
Fig. 2.5	VG Microtech Multilab ESCA 3000 XPS spectrometer.	47
Fig. 2.6	Horiba JY Lab Ram HR-800 micro-raman spectrometer.	49
Fig. 2.7	JEOL-1200 EX TEM apparatus.	50

Fig. 2.8 JEOL 1200 EX HR-TEM instrument.	50
Fig. 2.9 LEO–LEICA STEREOSCAN 440 FE-SEM instrument.	51
Fig. 2.10 Parr reactor set-up for NAG conversion.	53

Chapter 3

Fig. 3.1 Powder XRD pattern for calcined BaO, ZrO ₂ , and Ba-Zr mixed metal oxide catalysts.	64
Fig. 3.2 Scanning Electron Micrographs for a) BaO, b) Ba-Zr (0.5:1), c) Ba-Zr (1:1), d) Ba-Zr (2:1) and e) Ba-Zr (3:1) catalysts.	65
Fig. 3.3 (A-C) Transmission Electron Micrographs and D) SAED pattern for Ba-Zr (2:1) catalyst.	66
Fig. 3.4 Raman Spectra for Ba-Zr (0.5-3:1) catalysts.	69
Fig. 3.5 FT-IR spectra for calcined BaO, ZrO ₂ , and Ba-Zr mixed metal oxide catalyst.	70
Fig. 3.6 XPS analysis of different phases in the screened catalysts.	71
Fig. 3.7 Schematic presentation of Ba-Zr (2:1) catalyst.	72
Fig. 3.8 Effect of catalyst molar ratio on glucose isomerization.	77
Fig. 3.9 Effect of Substrate concentration on glucose isomerization.	78
Fig. 3.10 Effect of temperature on glucose isomerization.	79
Fig. 3.11 Effect of solvent on glucose isomerization.	81
Fig. 3.12 Catalyst recycle study.	82

Chapter 4

Fig. 4.1 PXRD plots for CaO, BaO, La ₂ O ₃ , Ce ₂ O ₃ , ZrO ₂ , Al ₂ O ₃ catalyst.	93
Fig. 4.2 Scanning Electron Micrographs for A) CaO B) BaO C) La ₂ O ₃ and D) Ce ₂ O ₃ .	94
Fig. 4.3 (A-B) Transmission Electron Micrographs La ₂ O ₃ catalyst and C) d-spacing for La ₂ O ₃ catalyst.	95

Fig. 4.4 A FT-IR spectra for all metal oxide catalyst.	96
Fig. 4.4 B FT-IR spectra for MeOH adsorbed on all metal oxide catalysts.	97
Fig. 4.5 Effect of substrate to catalyst ratios on 3AF production.	101
Fig. 4.6 Effect of time on 3AF production.	102
Fig. 4.7 Effect of temperature on 3AF production.	103
Fig. 4.8 Effect of solvent on 3AF production.	104
Fig. 4.9 Effect of water on 3AF production.	105
Fig. 4.10 Catalyst recycle study.	106
Fig. 4.11 Powder XRD pattern for fresh calcined La ₂ O ₃ and used La ₂ O ₃ metal oxide catalysts.	106
Fig. 4.12 FT-IR spectra for Fresh and used La ₂ O ₃ catalyst.	107
Fig. 4.13: ¹ H NMR spectrum of 3A5AF produced from N-acetyl-D-glucosamine.	109
Fig. 4.14: ¹ H NMR spectrum of 3AF produced from N-acetyl-D-glucosamine.	109
Fig. 4.15: ¹³ C NMR spectrum of 3A5AF produced from N-acetyl-D-glucosamine.	110
Fig. 4.16: ¹³ C NMR spectrum of 3AF produced from N-acetyl-D-glucosamine.	110
Fig. 4.17: HR-MS chromatogram of 3AF produced from N-acetyl-D-glucosamine.	111
Fig. 4.18: HR-MS chromatogram of 3A5AF produced from N-acetyl-D-glucosamine.	111
Fig. 4.19: FTIR plot for N-acetyl-D-glucosamine.	112
Fig. 4.20: FTIR plot for 3AF and 3A5AF.	112
Fig. 4.21: EDS for CaO catalyst.	113
Fig. 4.22: EDS for BaO catalyst.	113
Fig. 4.23: EDS for Ce ₂ O ₃ catalyst.	113
Fig. 4.24: EDS for La ₂ O ₃ catalyst.	114
Fig. 4.25: TGA for CaO, BaO, La ₂ O ₃ , Ce ₂ O ₃ , ZrO ₂ , Al ₂ O ₃ catalyst.	114
Fig. 4.26 BET Isotherm for various catalysts.	115
Fig. 4.27 TPD plots for various catalysts.	115
Fig 4.28: Calibration curve of N-acetyl glucosamine (NAG).	116

Chapter 5

Figure 5.1. N ₂ adsorption-desorption isotherm for prepared catalyst.	128
Figure 5.2. Wide angle XRD patterns of bare SrO and Mixed oxides of Cu-Al and Sr at various ratios.	129
Figure 5.3. FTIR spectra for the prepared catalyst.	130
Figure 5.4. a-c High-resolution spectra (core XPS spectra) of Sr 3d, O 1s, Cu 2p, respectively.	131-132
Figure 5.5. FESEM images and corresponding EDAX pattern (i, ii, iii) for a), SrO, b) Cu-Al (1:1) and c) Sr-Cu-Al (2-4-4).	133
Figure 5.6. FE-SEM images of Sr-Cu-Al catalyst.	133
Figure 5.7. Elemental mapping images of Sr-Cu-Al catalyst.	134
Figure 5.8. HRTEM images for Sr-Cu-Al (2-4-4) catalyst.	135
Figure 5.9. Activity performance of various alkali and alkaline earth metal for the one pot synthesis of glycidol.	140
Figure 5.10. Effect of temperature.	141
Figure 5.11. Time on stream.	142
Figure 5.12. Effect of catalyst loading.	143
Figure 5.13. Effect of Sr loading.	145
Figure 5.14. GC chromatogram for CO ₂ (44 g/mol).	146
Figure 5.15. GC chromatogram for MeOH (32 g/mol).	146
Figure 5.16. GC chromatogram for DMC.	146
Figure 5.17. GC chromatogram for Glycidol.	147
Figure 5.18. GC chromatogram for Glycidol carbonate.	147
Figure 5.19. GC chromatogram for Glycerol mono-carbonate.	147
Figure 5.20. GC chromatogram for Glycerol carbonate.	148
Figure 5.21. GC chromatogram for total analysis of reactants and products formed.	148
Figure 5.22. ¹³ C-NMR of glycidol.	149

List of Schemes

Schemes No	Title	Page No.
<u>Chapter 1</u>		
	Scheme I: Hydrolysis of lignocellulosic biomass.	2
	Scheme II A: Biomass to value addition.	3
	Scheme: III A Lignocellulosic biomass to lignin, cellulose and hemicellulose.	14
	Scheme: III B Marine biomass to chitin and chitosan.	15
	Scheme IV: Glucose to fructose isomerization.	17
	Scheme VA: Fructose to HMF.	17
	Scheme V B: Fructose transformation into value added products.	18
	Scheme VI A: Chitin to 3AF and 3A5AF.	19
	Scheme VI B: Transformation of 3A5AF to value added products.	19
	Scheme-VII HMF to levulinic acid.	21
	Scheme-VIII Levulinic Acid to γ -Valero Lactone.	21
	Scheme IX: Glycerol hydrogenolysis.	22
	Scheme IX: Trans-esterification of glycerol to glycidol.	22

Schemes No	Title	Page No.
<u>Chapter 3</u>		
	Scheme 3.2 a Glucose isomerization to fructose, mannose and other byproducts.	73
	Scheme 3.2 b Base catalysed Isomerisation of glucose to fructose.	74

Schemes No	Title	Page No.
<u>Chapter 4</u>		
	Scheme-I Plausible mechanism for base catalyzed dehydration and partial deoxygenation of N-Acetyl-D-glucosamine. (Route A: Formation of 3- acetamido furan, Route B: Formation of 3- acetamido- 5- acetyl furan).	108

Schemes No	Title	Page No.
-------------------	--------------	-----------------

Chapter 5

Scheme 5.1. One pot synthesis of glycidol *via* glycerol transesterification of glycerol. 124

Scheme 5.2 Glycerol transesterification with DMC to produce Glycidol. 136

Abbreviations

%	Percentage
°C	Degree Celsius
K	Kelvin
h	Hour
min	Minutes
psig	Pressure Square Inch per gauge
μ	Specific growth rate
μg	Microgram
μL	Microlitre
mg	Miligram
KJ	Kilo joule
mL	Mililitre
mm	Milimeter
Mt	Metric ton
B.E.	Binding Energy
eV	Electron Volt
K. E.	Kinetic Energy
LCB	Lignocellulosic Biomass
5-HMF	5-(Hydroxymethylmethyl) furfural
3A5AF	3-acetamido-5-acetylfuran
3AF	3-acetamidofuran
USDOE	United States Department of Energy
LBAE	Lobry-de-Bryun-Van-Ekenstein
HCl	Hydrochloric acid
HF	Hydrofluoric acid
HNO ₃	Nitric acid
H ₂ SO ₄	Sulphuric acid
FDCA	2, 5-furan-dicarboxylic acid
PET	polyethylene terephthalate
NAG	N-acetyl-D- glucosamine
HFCS	High fructose corn syrup

USD	United States dollar
LA	Levulinic acid
FA	Formic acid
GVL	4-hydroxy levulinic acid/ γ -Valero Lactone
DMC	Dimethyl carbonate
GC	Glycerol carbonate
GD	Glycidol
DMA	Dimethyl acetamide
DMSO	Dimethyl sulfoxide
DMF	Dimethyl formamide
MeOH	Methanol
EtOH	Ethanol
HPLC	High performance liquid chromatography
La ₂ O ₃	Lanthanum oxide
CaO	Calcium oxide
Ce ₂ O ₃	Cerium oxide
ZrO ₂	Zirconium oxide
Al ₂ O ₃	Aluminum oxide
BaOH ₂	Barium hydroxide
ACN	Acetonitrile
MIBK	Methyl Isobutyl Ketone
MMO	Mixed Metal Oxide
RB	Round bottom flask
RPM	Rotations per minute
DI	De-ionized
TEOS	Tetraethyl Ortho silicate
PWA	Phosphotungstic acid
XRD	X-ray diffraction
JCPDS	Joint committee for powder diffraction standards
BET	Brunauer, Emmett, and Teller
BJH	Barrett-Joyner-Halenda
TPD	Temperature programmed desorption
TCD	Thermal conductivity detector

FTIR	Fourier transform infrared spectroscopy
ICP-AES	Inductively coupled plasma atomic emission spectroscopy
XPS	X-ray photoelectron Spectroscopy
ESCA	electron spectroscopy for chemical analysis
TEM	Transmission Electron Microscopy
HR-TEM	High-resolution transmission electron microscopy
SEM	Scanning electron microscope
EDAX	Energy dispersive X-ray analysis
DTGA	Differential thermogravimetric analysis
STA	Simultaneous Thermal Analyzer
GC	Gas chromatography
GC-MS	Gas chromatography coupled with mass spectrometer
FFAP	Free fatty acid phase column
FID	Flame Ionization detector
TON	Turn over number
TOF	Turn over Frequency
GI	Glucose Isomerization
atm	Atmosphere
3A5HEF	3-Acetamido-5-(1-hydroxyethyl) furan
[BMIM]Cl	1-butyl-3-methyl imidazolium chloride
¹ H-NMR	Proton nuclear magnetic resonance
¹³ C-NMR	Carbon nuclear magnetic resonance
HRMS	High resolution mass spectroscopy
SE	Scattered electron
EDX	Electron Dispersive X-ray
TCD	Therma coupled detector
La	Lewis acidity
BA	Brønsted acidity
IPA	Iso propyl alcohol
EL	ethyl levulinate
FWHM	Full width half maxima

Chapter 1

Introduction

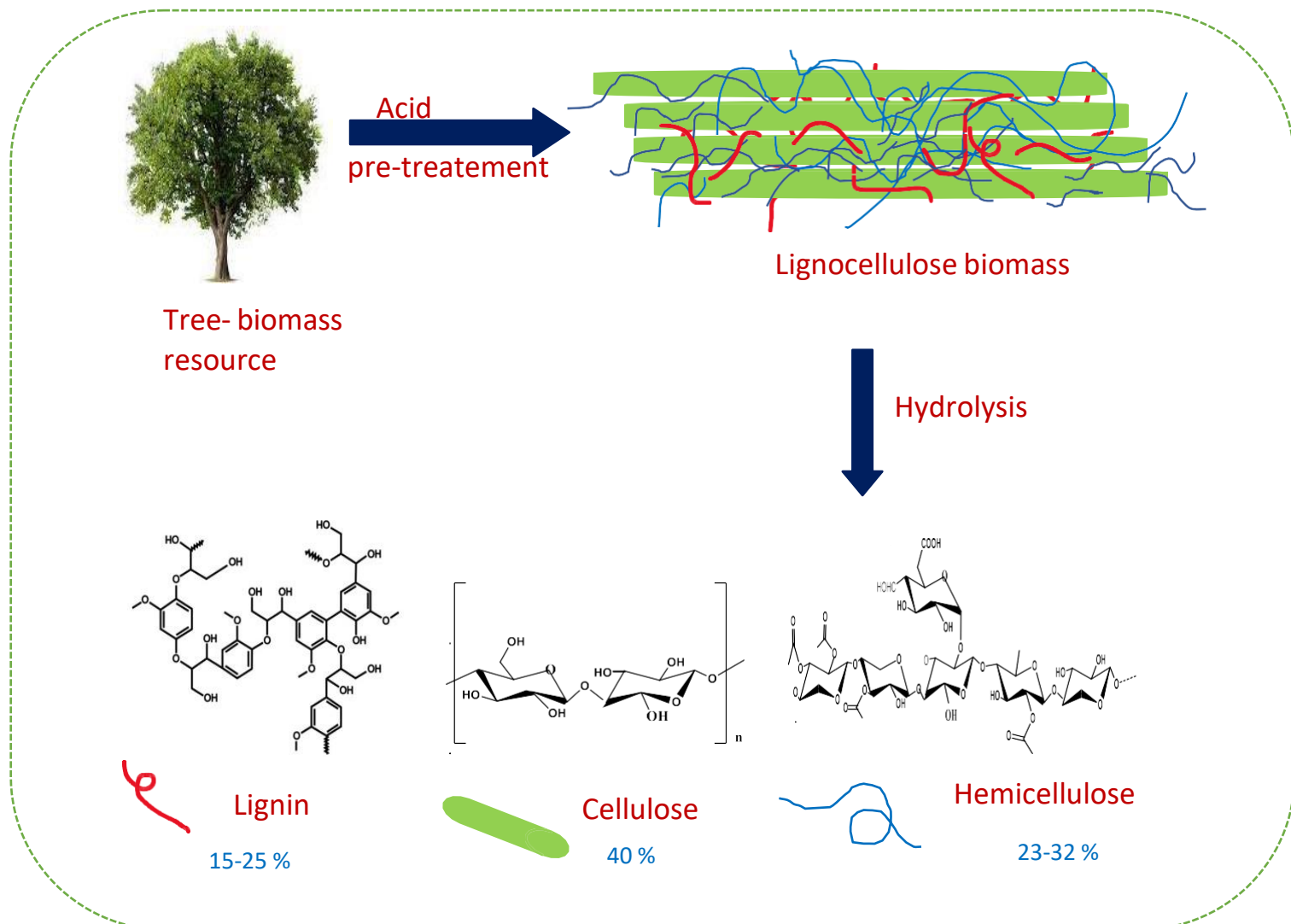
Introduction

1. Biomass

Biomass is an organic renewable material obtained from plants and animals. There are two major types of biomasses available on earth, viz. lignocellulosic biomass and marine biomass^(1,2). The lignocellulosic biomass is the most abundantly available biomass on earth with 181.5 billion metric tonnes produced annually. It is obtained from waste agro-materials, such as crop residues, wood wastes, urban bio-wastes, forest products such as wood, logging residues, trees, shrubs, energy crops (low cost crops grown for the production of fuel such as the bio-ethanol) like starch crops such as corn, wheat, barley; sugar crops; grasses; woody crops; vegetable oils; hydrocarbon plants, or aquatic biomass such as algae, water weed, water hyacinth.⁽³⁾ Plants use carbon dioxide and water in the presence of solar energy to produce carbohydrate and oxygen during the process of photosynthesis.^(4,5) Thus, biomass consists of 75 wt. % of sugar polymers in the form of cellulose and hemicellulose. Lignocellulosic biomass consists of polymers containing carbohydrates namely cellulose and hemicellulose and lignin polymer containing aromatic moiety.^(6, 7, 8) Whereas, after cellulosic biomass, chitin stands second most abundant biomass on earth with 100 billion tons produced annually. Chitin biomass is obtained from crustaceans like crabs, lobsters, shrimps, crayfish, arthropods as well as from cell wall of fungi and yeast.^(9, 10) Cellulosic biomass on valorization produces value added compounds containing mainly C, H, and O^(11, 12) whereas, marine biomass produces compounds containing not only C, H, and O but also the 7 wt. % of the renewable N atom in the skeleton which may be otherwise produced by the highly energy consuming ammonia synthesis.⁽¹³⁾

Both the lignocellulosic and marine biomass upon treatment with mineral acids depolymerise to produce corresponding monomers, lignin (10-15), cellulose (38–50 %), hemicellulose (23-32 %) **Scheme I** and chitin and chitosan, **Scheme III B**.^(14, 15) These on further catalytic transformation results in formation of several value-added products such as fructose, HMF (5-hydroxymethylfurfural), levulinic acid, 3-acetamidofuran (3AF), 3-acetamido-5-acetylfuran (3A5AF), glycidol (GD) etc. These compounds have wide range of applications in food, paint, chemical and pharmaceuticals industries.

Scheme I: Hydrolysis of lignocellulosic biomass



1.2 Need for biomass valorization

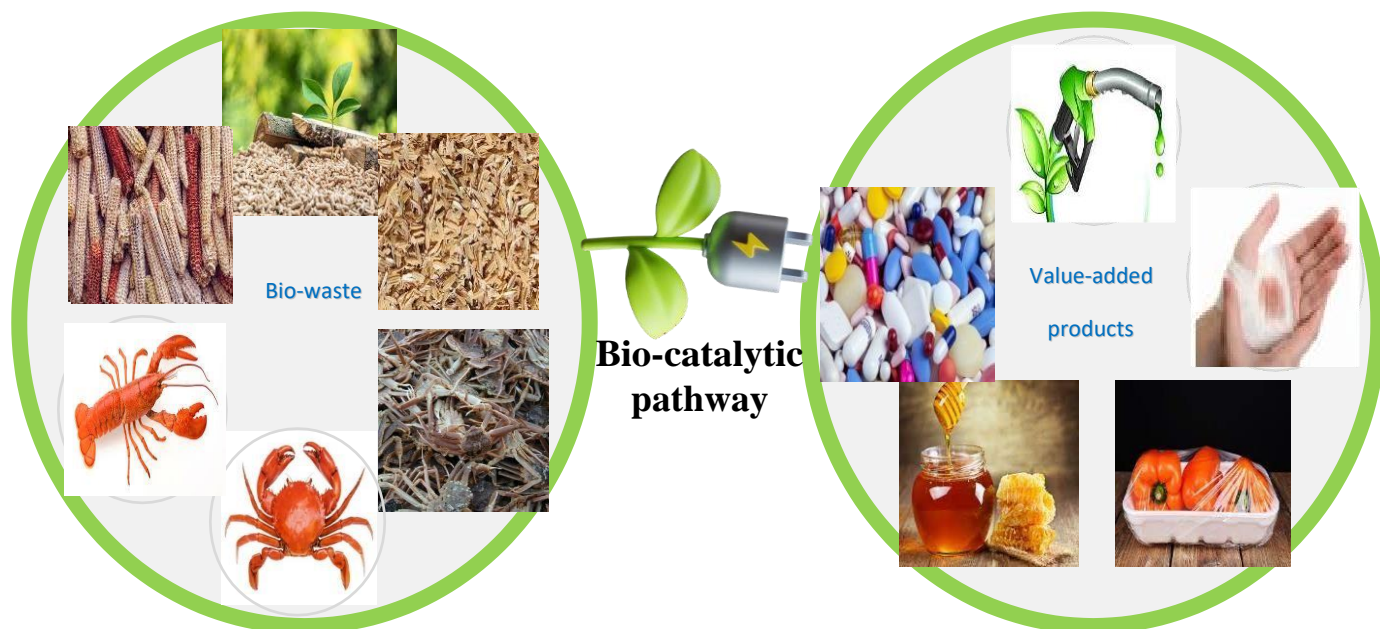
Around 87 % of the energy, world-wide comes from the non-renewable fossil fuels and its rapid depletion urges a need for the development of an alternative renewable and green energy resource.⁽¹⁶⁾ Due to rapid growth in the world population to around 8 billion in 2023, there has been increasing demands in the use of coal, gas and oil obtained from natural resources.⁽¹⁷⁾ This has led to several alarming situations such as global warming, green house effects, food and energy crisis.^(18, 19) Thus, it has become very important to develop a cost effective, simple and easy route for the valorization of biomass to value added compounds such as commodity chemicals, platform chemicals, fuel additives and pharmaceuticals

scheme II A.

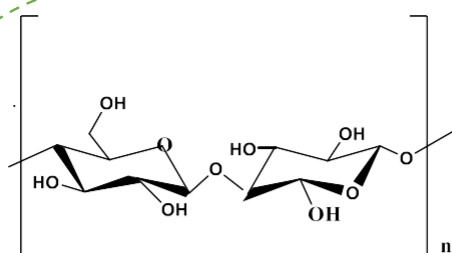
Chapter1

Both lignocellulosic and marine biomass face many challenges in terms of their depolymerization to its corresponding monomeric units.^(20, 21) The existence of many functional groups including heteroatoms (such as O and N) makes the procedure difficult and causes a number of side reactions that result in the production of undesired compounds.⁽²²⁾ This is followed by further mineralization, deproteinization, and purification. For the pre-treatment of lignocellulosic and marine biomass, destructive techniques like biological, chemical, and thermal methods are necessary.⁽²³⁾ In order to increase the digestibility of the biomass feedstock, various techniques like acid hydrolysis (HCl, HNO₃, HF, H₂SO₄, ionic liquid, supercritical water treatment, hot water treatment, and hydro thermolysis, explosive decompression technique, aqua and organo-solvolytic method, steam fractionation and enzymatic treatment methods have been used. Thus, cellulose, hemicellulose and lignin are the main components obtained from the lignocellulosic biomass whereas, chitin and chitosan are obtained from the marine biomass upon its hydrolysis as shown below in **scheme II B**.⁽²⁴⁻²⁷⁾

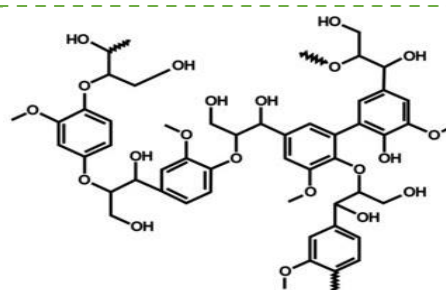
Scheme II A: Biomass to value addition



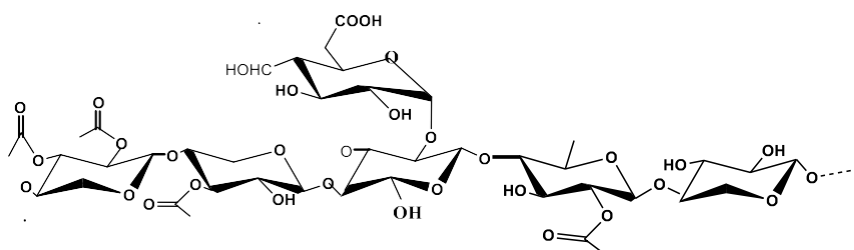
Scheme: II B



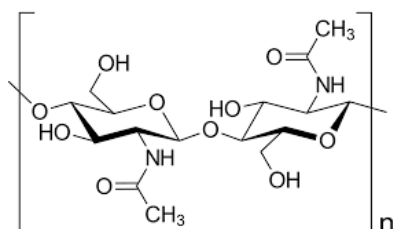
Cellulose



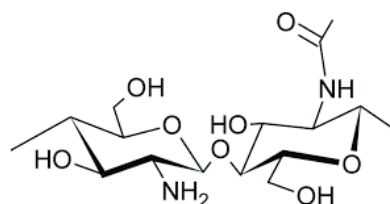
Lignin



Hemicellulose



Chitin



Chitosan

1.3 Composition of lignocellulosic biomass:

The main structural component of plant is the cell wall. It comprises of cellulose, hemicellulose, lignin, pectin and minerals collectively known as lignocellulosic biomass as shown in the **Fig.1.1.** ⁽¹⁴⁾ The other components present in biomass include oil, fat, lipids, proteins, triglycerides etc. These different components of lignocellulosic biomass have varied

Chapter1

unique properties which require chemical and enzymatic pre-treatment methods for their transformation into value added products.^(28, 29)

1.3.1 Cellulose:

Cellulose is the major component of lignocellulosic biomass and it accounts for 35-50 % of dry wood mass. Cellulose is a linear polysaccharide in which the D-glucopyranoside monomer units are linked to each other through β -1, 4 glycosidic linkages with characteristic folded chains.⁽³⁰⁾ It is a linear polymeric chain composed of complex polysaccharide units with basic structural unit as 4-o- β -D-glucopyranosyl-D-glucopyranose as shown in the **Fig 1.2**. The presence of H-bonding stabilizes the flat and linear structure of the cellulose polymer. Cellulose has highly stable and crystalline structure due to the presence of intermolecular H-bonding between the -OH group of the third carbon atom and the oxygen atom of the glycosidic ring of cellulose and this provides it resistance to hydrolysis.

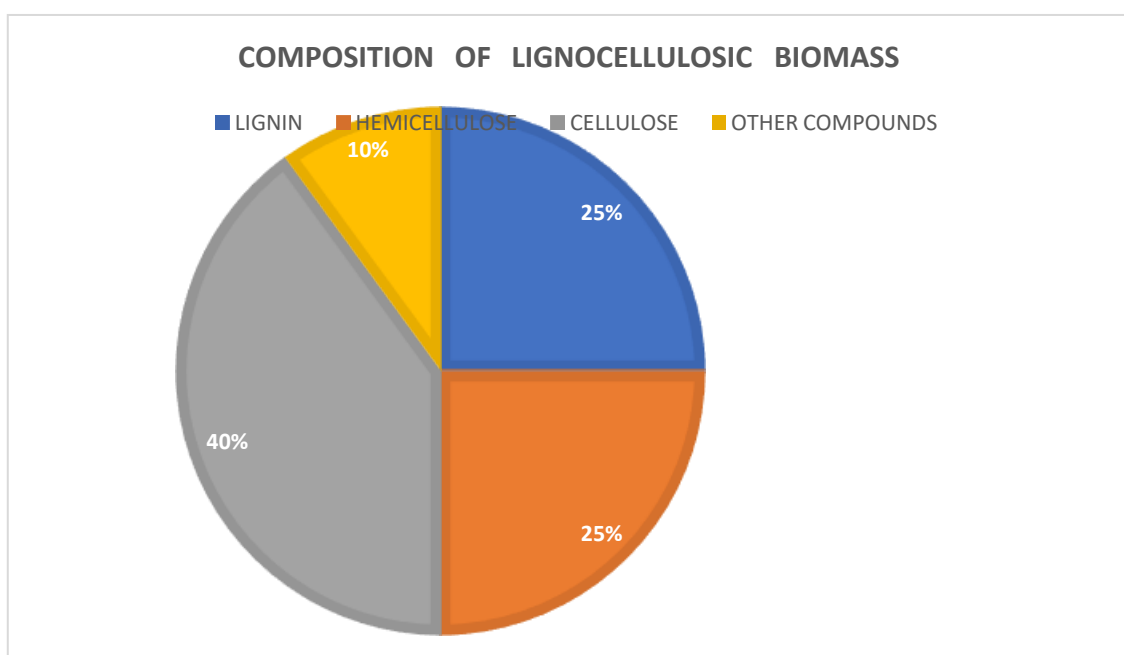


Fig. 1.1 Composition of lignocellulosic biomass

It is hydrolysed into cellobiose (dimer), cellotriose (trimer) and cellotetrose (tetramer) upon partial acid hydrolysis. Whereas, on complete hydrolysis it yields glucose monomers. The density of crystalline cellulose is slightly lower than that of amorphous cellulose (difference of 0.088 g/cm^3). Amorphous cellulose upon hydrolysis yields glucose monomers.⁽³¹⁾

Chapter1

Cellulose has become one of the most important components of plant cell wall with wide range of applications in food, chemical, paper, pulp, textile and pharmaceutical industries and one of the major feedstocks for synthesis of renewable biofuels.⁽³²⁾

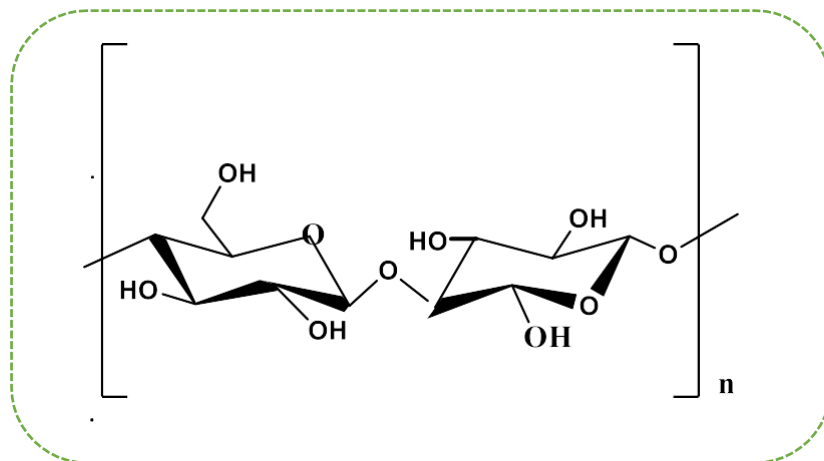


Fig. 1.2 Structure of cellulose

1.3.2 Hemicellulose:

It is an amorphous, two-dimensional sugar co-polymer that is found in plant cell walls. As shown in the **Fig. 1.3** it is a branched polysaccharide and due to its amorphous nature, it can be hydrolysed easily. It makes up 23–32 % of the dry wood mass. It is a complex polysaccharide made up of five distinct sugars, including hexoses (glucose, mannose, and galactose) and pentoses (Xylose and arabinose). Hemicellulose, one of these five sugars, primarily consists of xylose.⁽³³⁾ Hemicellulose is simpler to hydrolyse than cellulose because it is more branched and amorphous. It has structural irregularities and is soluble in water.⁽³⁴⁾

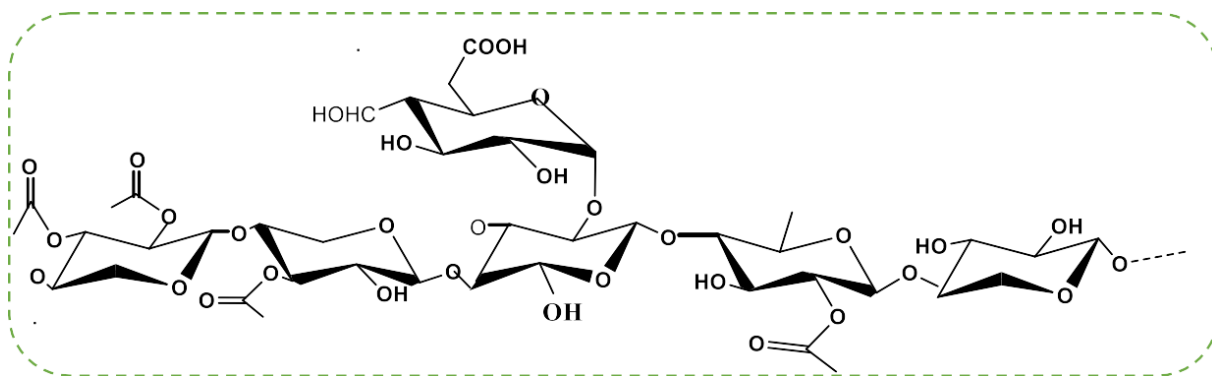


Fig. 1.3 Structure of hemicelluloses

1.3.3 Lignin:

Lignin is composed of 3-D network of phenylpropane monomer units linked to each other thereby forming an aromatic polymer, amorphous in nature as shown in **Fig. 1.4**. By joining cellulose and hemicellulose, lignin gives strength to the plant cell wall. 15–25 % of the dry wood mass is made up of lignin, a complex, branching, aromatic polymer with three dimensions. The majority of lignin is present in woody biomass, resulting in soft wood lignin that includes coniferyl alcohol and hard wood lignin that contains both types of alcohols. ⁽³⁵⁻³⁶⁾ Contrarily, the lignin found in grass wood is a combination of coumaryl, coniferyl, and sinapyl alcohols. A polymer called lignin is created by the enzymatic process of free radical polymerization and is made up of an uneven network of phenylpropane units connected by C-O and C-C connections.

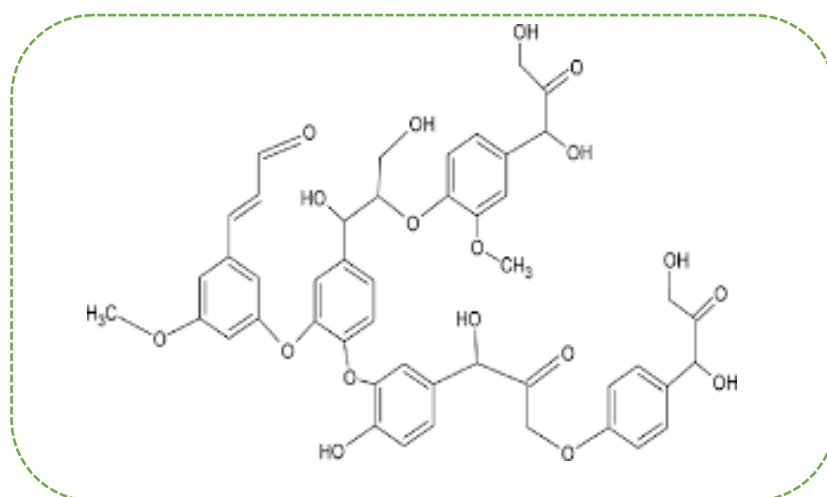


Fig 1.4 Structure of lignin

1.4 Composition of Marine biomass:

Marine biomass comprises of chitin, chitosan, minerals and proteins. Marine biomass is found in the waste of the crustaceans such as crabs, lobsters, shrimp shells, cell wall of fungi etc as shown in **Fig. 1.5**. The marine biomass waste on treatment with acid followed by depolymerization and demineralization leads to the formation of the corresponding polymers

Chapter1

chitin and chitosan. Chitosan is obtained by deacetylation of chitin.⁽³⁷⁾ Chitin and chitosan are amino biopolymers containing rigid structure which provides strength to the exoskeleton of the marine flora and fauna.

Chitin is a polymer containing N-acetyl-d-glucosamine as a repeating unit linked to each other by 1, 4-glycosidic linkage thus forming long polymeric chains. Chitin is present in three different allomorphic forms which are crystalline in nature namely α , β , γ form of chitin chain. α -chitin is composed of N, N-diacetylchitobiose unit linked together thus forming intramolecular H-bonding thus forming polymeric chains.⁽³⁸⁾ These chains further form sheets due to the presence of N-H bonds thus providing rigidity and crystallinity to the structure. The β -chitin has N, N-diacetylchitobiose as the repeating monomeric unit which sheet like structure due to the presence of only intermolecular H-bonding. Whereas, γ -chitin contains both parallel as well as anti-parallel orientations of the dimeric chain. The presence of acetyl-amino group imparts unique physico-chemical properties to chitin and chitosan.⁽³⁹⁾ These unique properties impart chitin and chitosan with various applications in catalysis, waste water treatment, biomedical applications, food processing industries, paint and textile industries etc.⁽⁴⁰⁾

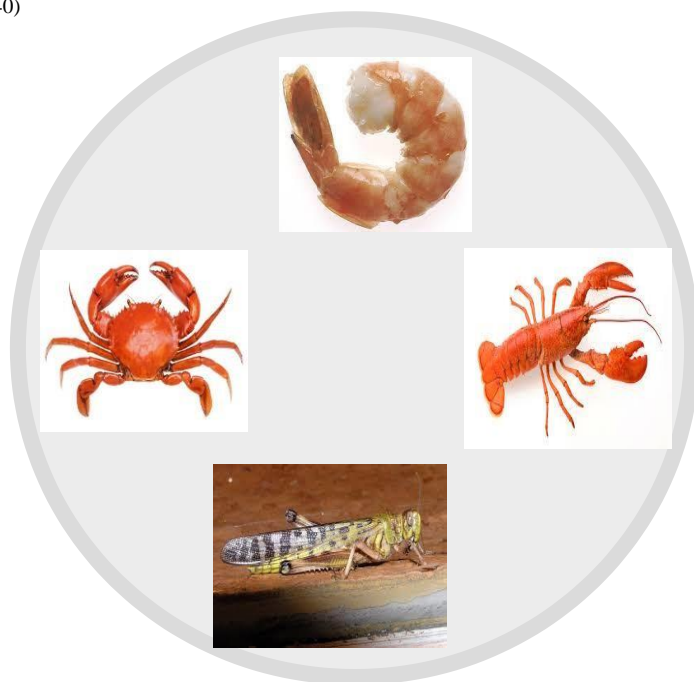
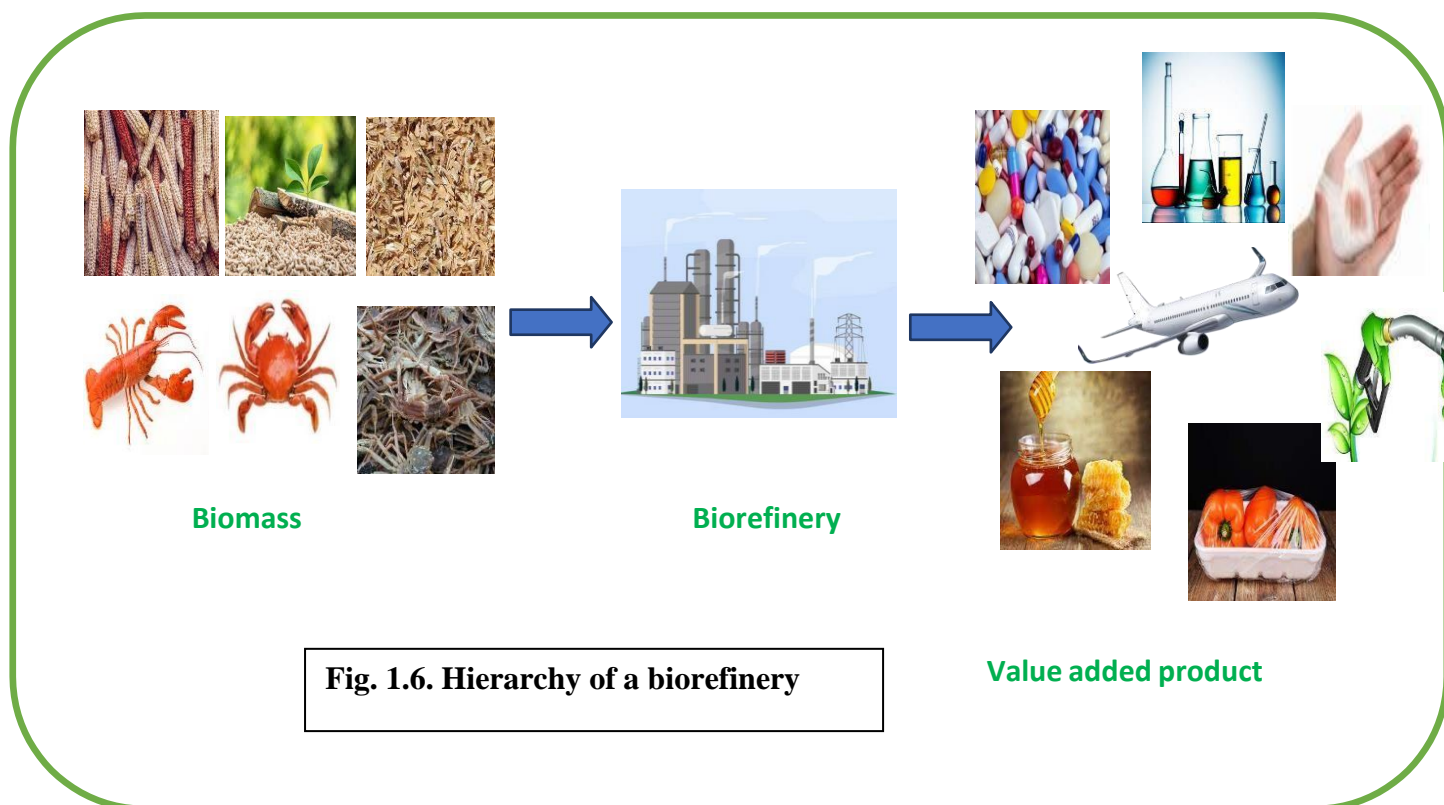


Fig. 1.5 Chitin and chitosan biomass resource

1.5 The biorefinery concept:

A facility that integrates a biomass conversion process and equipment to create power, value-added chemicals, commodity chemicals, and biofuel is referred to as a biorefinery. Biorefinery seeks to utilise ecologically friendly and economically advantageous technology for the manufacturing of platform chemicals and value-added compounds for biofuel and petrochemical applications, thus aims to reduce the carbon and water footprints.⁽⁴¹⁾ The idea of a bio-refinery was the beginning of many technological and industrial advancements. The fundamental idea behind bio-refineries is to increase the value of biomass waste while producing the minimum amount of waste possibly during the process.⁽⁴²⁾ Thus, sustainable production of value-added chemicals, biofuels, and commodity chemicals can be achieved by incorporating the idea of green chemistry into bio-refineries and using sophisticated technology with little environmental impact. The bio-refinery can be divided into seven categories based on the sorts of sources it uses: agricultural, forestry, oilseed, cereal, lignocellulosic, green, and industrial waste. In contrast, certain biorefineries are divided into groups based on the source of their feedstock, including first-generation biorefineries (food crops, animal fat, and energy crops), second-generation biorefineries (lignocellulosic biomass), third-generation biorefineries (microbes and algae), and fourth-generation biorefineries (algae).^(43, 44) Thus, the concept of integrated bio-refinery has been proposed in order to enhance the efficiency of bio-refinery towards the eco-friendly production of value-added products from biomass waste through conversion processes such as thermochemical, biochemical and chemo-catalytic pathways.^(45, 46) This involves the integration of various advanced technologies for biomass conversion in a cost effective and environmentally benign way as depicted in the **Fig 1.6**. Thus, integrated bio-refinery makes use of multiple biomass feedstock to generate value added products. But the designing of the bio-refinery and integrated bio-refinery is very challenging as the properties and the characteristics of several feedstocks are different from others and it also involves process designing and development of various analytical tools and technologies.^(47, 48) The efficiency of the bio-refinery depends upon the conversion process utilized for biomass transformation that includes namely, biochemical, thermochemical and chemo- catalytic process. Thus, by involving the concept of process integration the economical and environmental performance of the bio-refinery can be enhanced.



1.6 Green chemistry, platform molecules and their commercial potential:

Green chemistry is the branch of sustainable chemistry that involves the amalgamation of the chemical research as well as engineering skills for the designing and developing of chemical products and chemical processes that invigorate the minimum use and minimum generation of hazardous waste during the transformation and process intensification. The twelve principles of green chemistry that aid in the sustainable development of environmentally benign products and chemical processes are as follows:

1. Prevention of waste generation
2. Renewable feedstock
3. Exclude unnecessary derivatization
4. Designing degradable products
5. Atom economy
6. Use and generation of less hazardous substances

7. Development of less toxic and environmentally benign products

8. Minimal use of solvents and use of additives must be avoided

9. Ambient temperature and pressure

10. Selective use of catalysts

11. In process monitoring of pollution prevention

12. Safety management

The development of bio-refineries as an alternative to petrochemicals has improved the production of bio-based value-added chemicals. The development of sustainable technologies for the manufacture of chemicals, biofuel, and plastics has advanced as a result of the depletion of fossil fuels, the energy crisis, the food crisis, and rising health concerns. Platform chemicals were described as "bio-derived chemicals whose constituting elements totally originated from biomass and could be used as building blocks for the production of commodity and refined chemicals" by the US Department of Energy (US DOE).⁽⁴⁹⁾

These include the production of commodity chemicals, fuel additives and chemical intermediates by employing bio-chemical pathway. Twelve of the most important building block chemicals have been selected by the US DOE as platform chemicals with potential industrial uses. These 12 platform chemicals, which can be created from sugars by biochemical pathways, include ethanol, lactic acid, furfural, glycerol, hydroxy-propanoic acid, 5-hydroxymethyl furfural (HMF), levulinic acid, succinic acid, sorbitol, xylitol, 2, 5-furan-dicarboxylic acid (FDCA), and isoprene unit as shown in the **Fig. 1.7**.⁽⁵⁰⁾ The dehydration of glucose and fructose yields 5-HMF, a renewable platform chemical with numerous uses in the manufacture of plastic, chemicals, medicines, fine chemicals, and solvents.

5-HMF undergoes several transformations such as esterification, reduction, oxidation etc. due to the presence of formyl and hydroxyl functional group as well as reactive furan ring in the molecule. Due to the presence of this multifunctionality and versatility in reactivity it is termed as sleeping Giant available from biomass.⁽⁵¹⁾ The oxidation of 5-HMF produces one of the promising platform chemical **2, 5-furandicarboxylic acid** which acts as a building block for the formation of polymers. Thus, it can be used as an alternative to the polyethylene terephthalate (PET) and terephthalic acid in polyester.⁽⁵²⁾ **Levulinic acid** also called as 4-

Chapter1

oxopentanoic acid is a 5-carbon organic keto acid and contains two functional groups carbonyl of keto and carboxylic acid. It finds wide range of applications in the production of cosmetics, pesticides, pharmaceuticals, plastics, fuel additives and food industries. The compound 5-amino levulinic acid a derivative of levulinic acid acts as a very important drug in the treatment of skin cancer.⁽⁵³⁻⁵⁵⁾

Furfural is a very important platform chemical and can be transformed into several value-added chemicals such as furfural alcohol, tetrahydrofuran, levulinic acid and bio-fuel etc. Furfural is the dehydration product of pentose sugar xylose derived from lignocellulosic biomass.^(56, 57) **Glycerol** is one of the most important platform chemicals obtained as a by-product of biorefinery. Abundant availability of glycerol through biodiesel synthesis made enforcement for the use of glycerol as a feedstock for the synthesis of various attractive chemicals like, diols, carbonates (both linear and cyclic), esters, lactic acid *etc.* Glycerol is considered one of the top most 12 bio-derived platform molecules. The most interesting aspect of glycerol is its versatile reactivity to produce broad spectrum of compounds like acrolein, acrylic acid, lactic acid, 1,2-propanediol, 1,3-propanediol, allyl alcohol, dihydroxyacetone, hydroxy acetone, glycerol carbonate, and glycidol.⁽⁵⁸⁻⁶⁰⁾

Ethanol is a primary alcohol and a renewable fuel with two carbon atoms obtained from corn, starch, sugarcane, wood chips etc. It is colourless, transparent and flammable liquid with high octane number than gasoline. Around 10 % of ethanol is blended with gasoline to attain the desired octane number in order to prevent the engine knocking. It has various applications in beverages, medicines, solvent, cosmetics, perfumes, tonics.^(61, 62) **Lactic acid** is a 3-carbon organic acid readily soluble in water. It is produced by the fermentation of carbohydrates in the presence of enzymes or by chemical pathways. It has applications food industry as food additive, flavouring agent and is used in the synthesis of biopolymer polylactic acid.^(63, 64)

Succinic acid is a 4-carbon organic acid and is produced by the fermentation process. It is used in the production of several valuable chemicals such as pharmaceuticals, food additives, perfumes, paints, plasticizers, bio-polymers, polyurethanes etc. succinic acid and its esters find application in the synthesis of petrochemical products such as 1,4-butanediol, tetrahydrofuran and pyrrolidinone derivatives.^(65, 66)

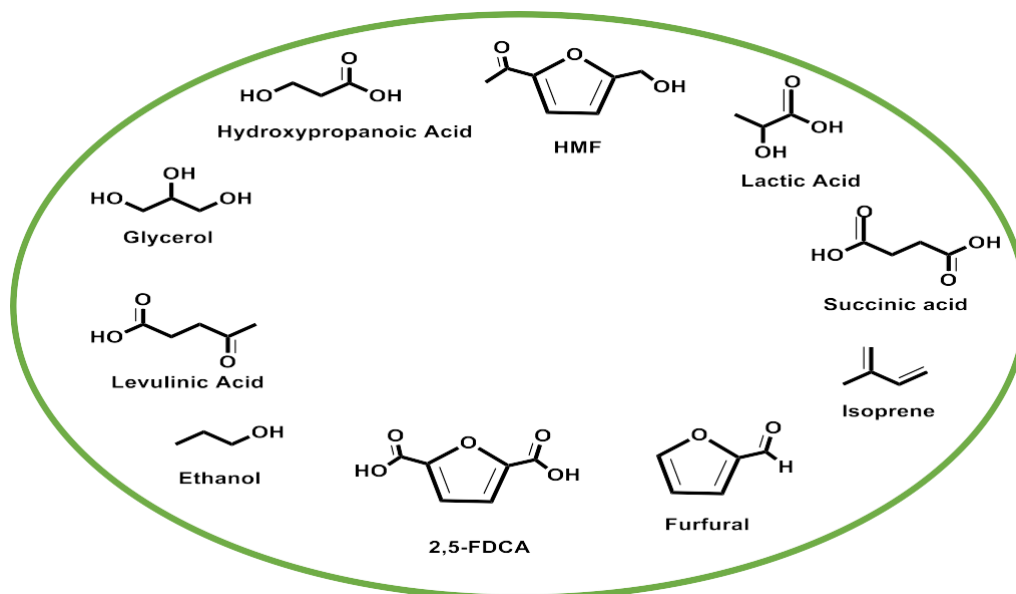


Fig. 1.7. Platform Chemicals

1.7 Catalytic reactions for the conversion of lignocellulosic and marine biomass derived platform molecules

Acidic conditions are necessary for the conversion of lignocellulosic and marine biomass into value added compounds. Lignocellulosic biomass in the presence of acidic condition results in the formation of lignin, cellulose, hemicellulose, pectin and minerals. Cellulose and hemicellulose can be further depolymerised by acid catalysed hydrolysis to produce corresponding monomers such as glucose, fructose and xylose respectively. The acidic condition is required for the cleavage of the glycosidic bond between the sugar units in the polymers to produce corresponding monomers.^(67, 68)

Scheme: III A Lignocellulosic biomass to lignin, cellulose and hemicellulose

The lignocellulosic biomass comprises of the lignin, cellulose and hemicellulose as the three major components as shown in **scheme III A (Fig. 1.8-1.10)**. The lignocellulosic biomass upon hydrolysis in the presence of mineral acids leads to the formation of the corresponding polymers lignin, cellulose and hemicellulose which on further depolymerization results in the formation of the corresponding monomers which can be further functionalized into several derivatives having wide range of commercial applications.

The concentrated HCl is the most widely used industrial pathway for the production of C-5 and C-6 sugars from cellulose and hemicellulose but it suffers from several drawbacks such

Chapter 1

as poor recovery of the acid, difficulty in separation of the products from the reaction mixture. The different sources/feedstock for the lignocellulosic biomass has varied composition of the cellulose, hemicellulose and lignin.

Thus, the depolymerization and deoxygenation (transportation chemicals and fuels) step remain the main basis for the transformation of the lignocellulosic biomass into value added products. Several Bio-catalytic as well as chemo-catalytic pathways have been employed for the transformation of the lignocellulosic biomass to form value added chemicals such as commodity chemicals, platform chemicals and pharmaceuticals.

Scheme: III A Lignocellulosic biomass to lignin, cellulose and hemicellulose

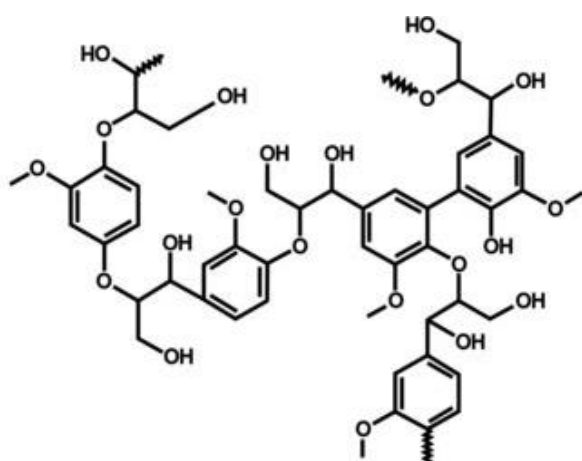


Fig. 1.8 Structure of lignin

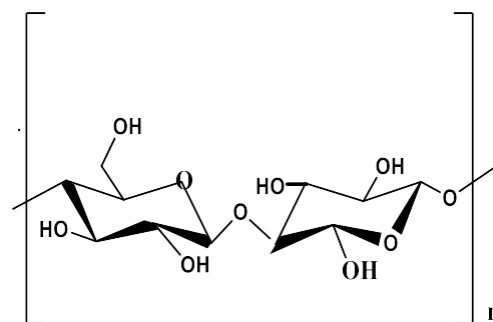


Fig. 1.9 Structure of cellulose

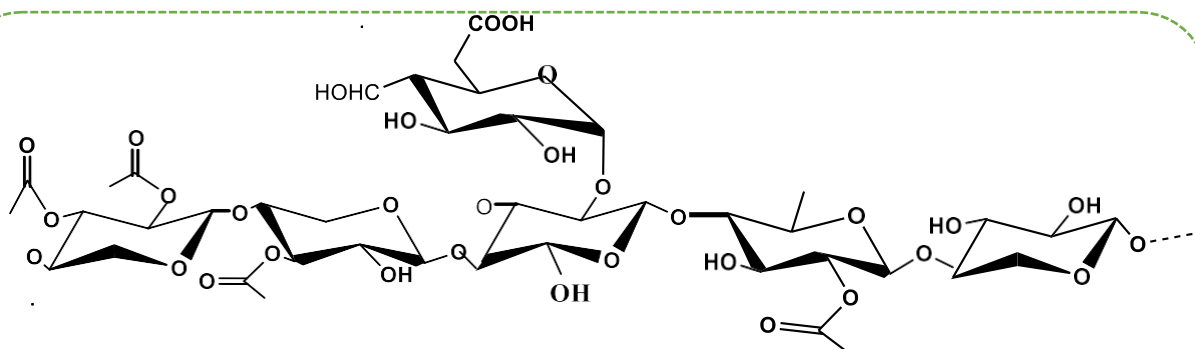
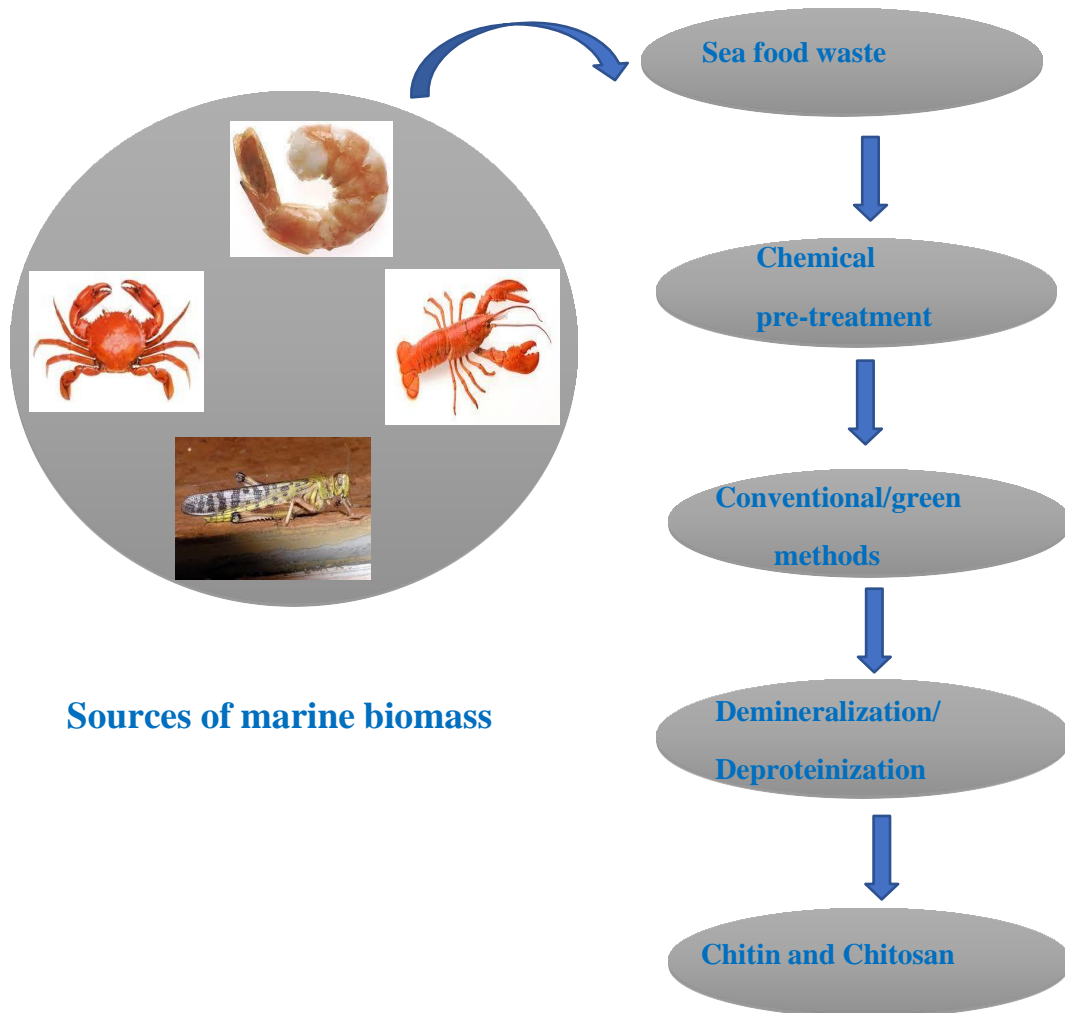
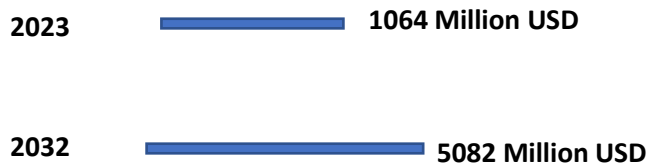


Fig. 1.10 Structure of hemicellulose

Scheme: III B Marine biomass to chitin and chitosan



Global Chitin market



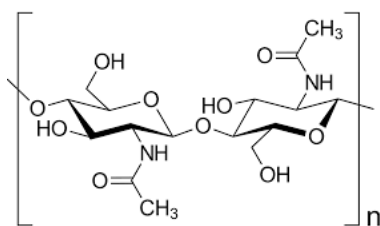


Fig. 1.11 Structure of chitin

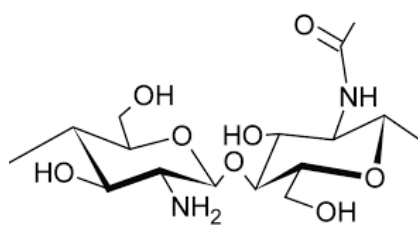
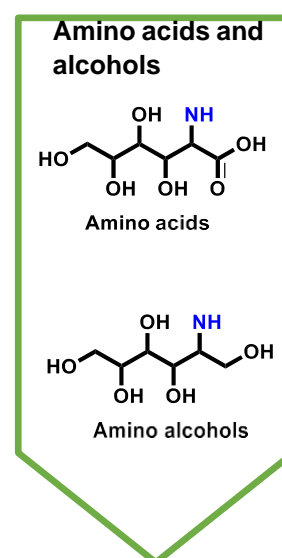
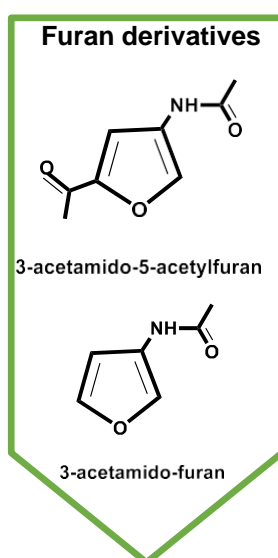
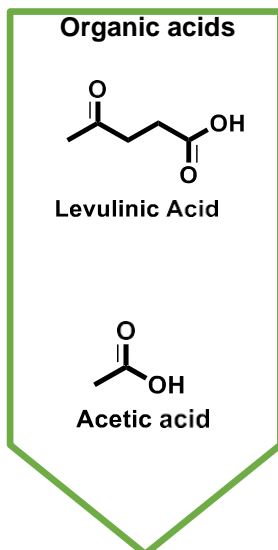


Fig. 1.12 Structure of chitosan



The marine biomass is second most abundantly available renewable on earth and therefore can be explored for the production of several value-added compounds. The marine biomass obtained from the sea waste particularly from the crustaceans such as the crabs, lobsters, shrimp shells and the cell wall of fungi on treatment with the mineral acids or green solvents such as ionic liquids followed by deproteinization and demineralization can be further hydrolysed to the corresponding polymers chitin and chitosan as shown in the **Fig. 1.11** and **Fig. 1.12** respectively. These polymers can be further depolymerised into its corresponding monomers N-acetyl-D-glucosamine (NAG) and chitin on deacetylation results in the formation of chitosan which can be further depolymerised to form glucosamine. These

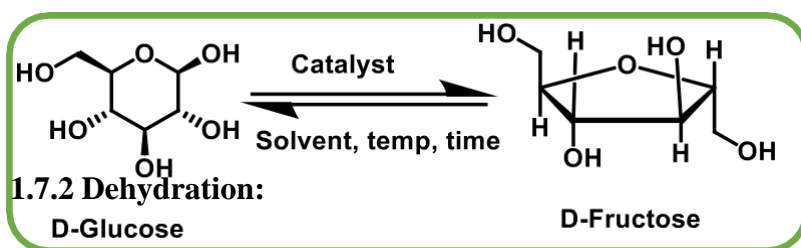
Chapter1

monomers on further treatment in the presence of chemo-catalytic pathways can be transformed into industrial applicable value-added products as shown in the **scheme III B**.

1.7.1 Isomerization:

As shown in the **Scheme IV** in the presence of both acidic and basic conditions at mild temperatures, glucose can isomerize into fructose. Since fructose is employed as a platform chemical in the synthesis of numerous value-added chemicals, including HMF, levulinic acid, alkyl fructoside, etc., glucose to fructose isomerization has greatly expanded in commercial utilisation. Additionally, the optimisation of several reaction parameters throughout the glucose to fructose isomerization process contributes to a greater selectivity to HMF.⁽⁶⁹⁾

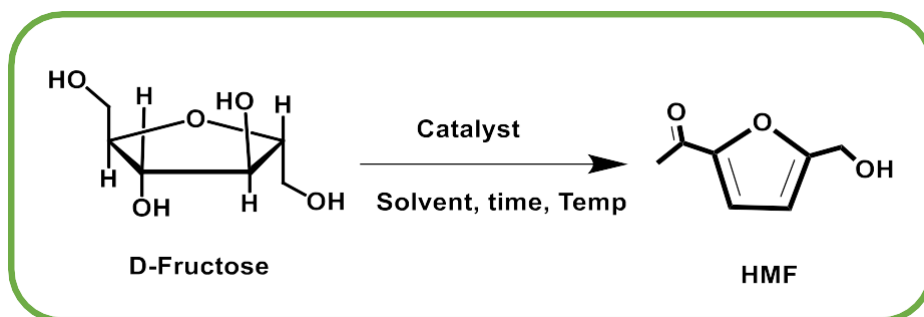
Scheme IV: Glucose to fructose isomerization



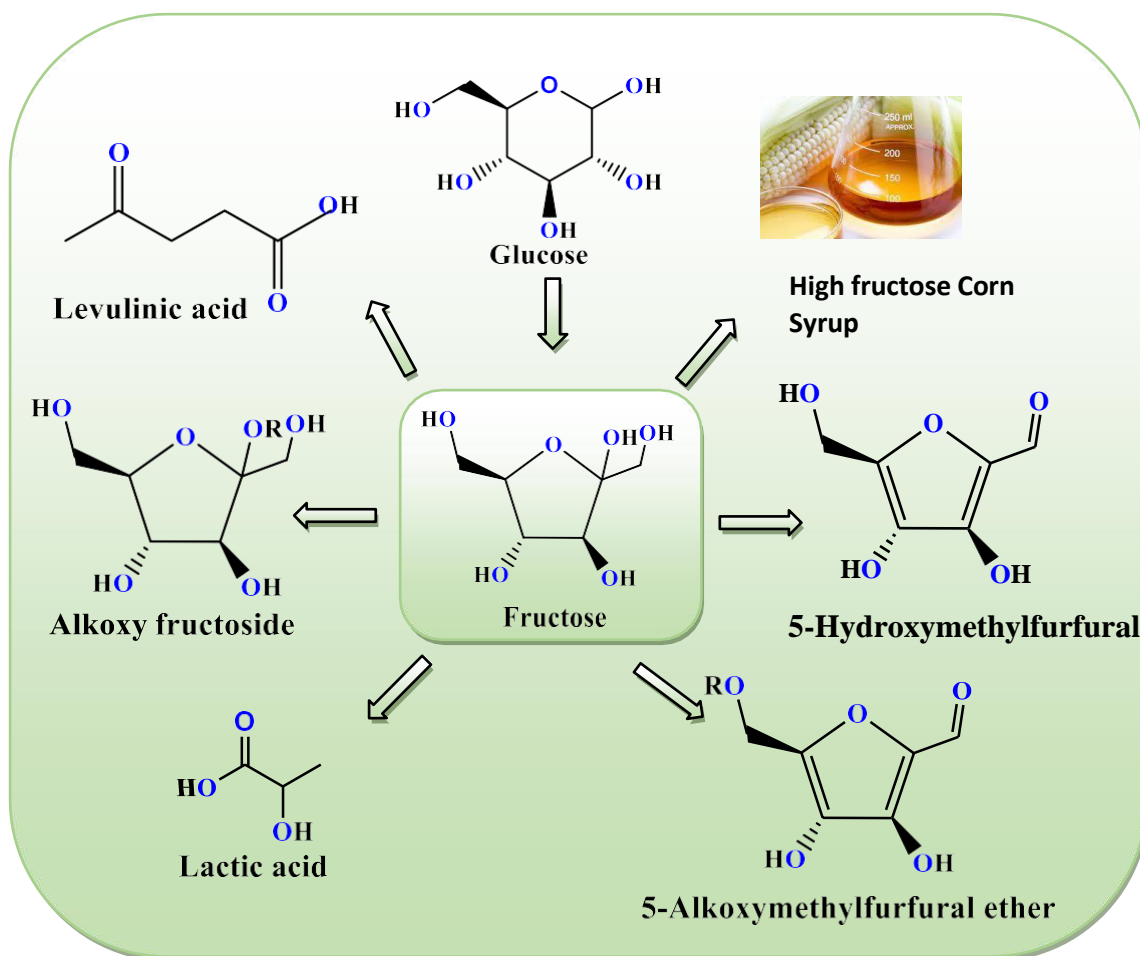
1.7.3 dehydration reactions:

It is a chemical reaction in which the water molecule from the substrate is removed. **Scheme V** below represents the dehydration of fructose in the acidic medium to produce HMF as the major dehydration product. For the creation of numerous value-added products including HMF, 3A5AF, and 3AF, among others, the dehydration of carbohydrates as well as chitin and chitosan biomass has been extensively investigated as shown in the **Scheme VI**. In cases where chitin serves as the substrate, the dehydration reactions have been observed in water, ionic liquids, organic solvents, supercritical water systems, and biphasic systems at relatively higher temperatures. For this transformation to yield 5-HMF and 3A3AF and 3AF, a variety of solid acid catalysts, including mixed metal oxides, ion exchange resins, and zeolites, have been described.^(70, 71) The stability of the generated products is significantly influenced by pH of the reaction medium.

Scheme V A: Fructose to HMF



Scheme V B: Fructose transformation into value added products:

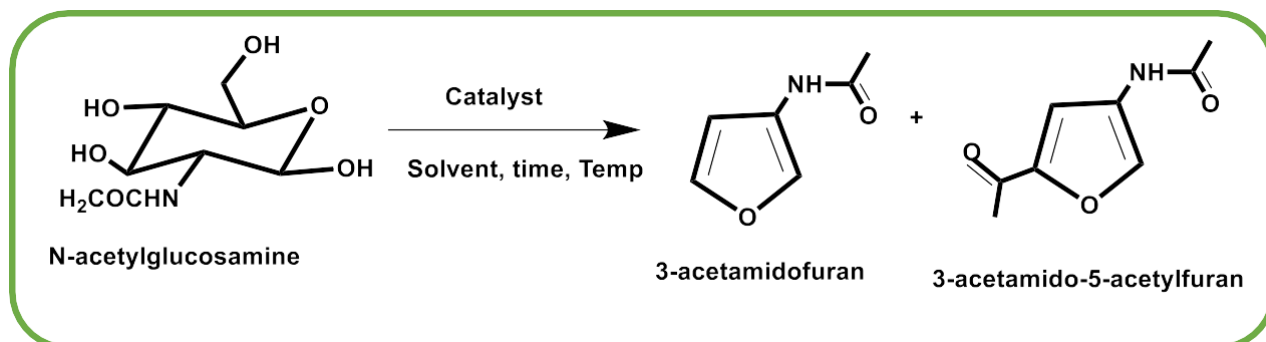


As shown above in the **Scheme VB**, fructose shows tremendous applications as a platform chemical and is used for several transformations to give value added products. Fructose is used as a sweetener commercially for the production of HFCS and was reported to have a global fructose market of 8791 million USD which is expected to grow to about 15, 556 million USD in 2033. Fructose acidic as well as basic condition in the presence of alcoholic solvent results in the formation of alkoxy fructoside, whereas fructose requires strong Brønsted acidic sites for its transformation into HMF with the elimination of 3 water molecules, the use of mineral acids and solid acid catalysts has been reported for the dehydration of fructose followed by its rehydration (4 times) and dehydration (2 times) in the presence of polar solvent to produce levulinic acid (LA) and formic acid (FA) as the products. In this conversion the isomerization of glucose to fructose is the rate determining step that

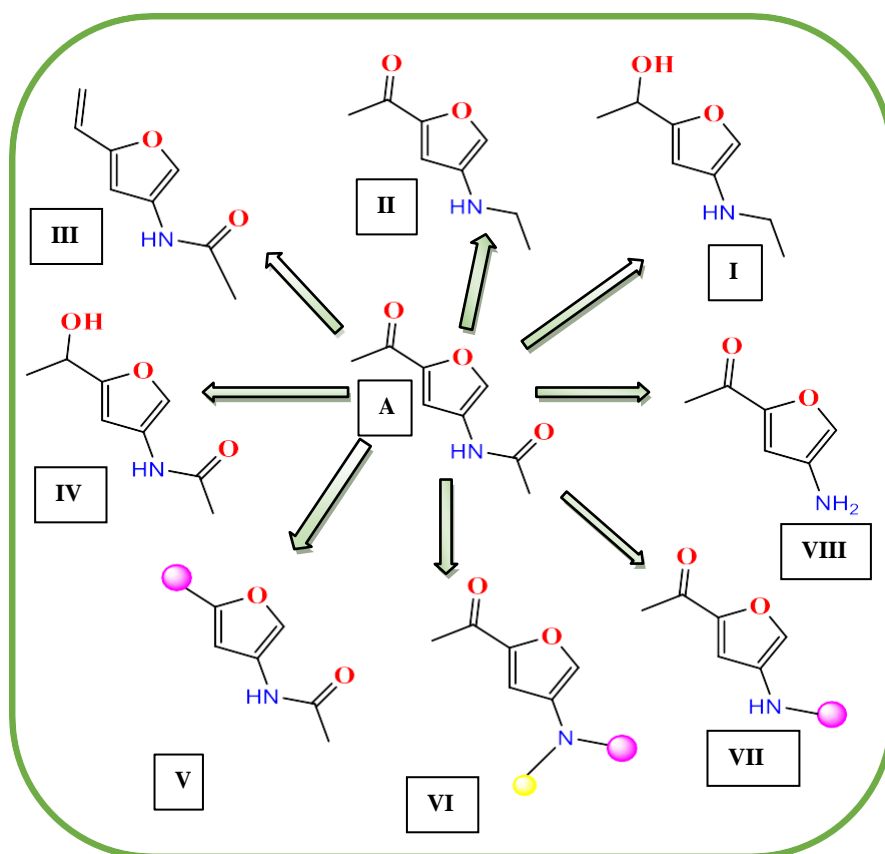
Chapter1

operates at higher temperature as compared to the second step which involves the conversion of fructose to LA and FA.

Scheme VI A: Chitin to 3AF and 3A5AF



Scheme VI B: Transformation of 3A5AF to value added products



As shown above the **Scheme VI B** represents the transformation of the renewable amine 3A5AF into various valuable products. Brønsted acid catalysts such as H_2SO_4 , HCl have been widely used for the chitin (chitosan, NAG) conversion into HMF because of its merits such as easy and cost-effective production at industrial scale. The addition of HCl has

Chapter1

been found to show promotional effect in the hydrolysis of the chitin biomass by the disruption of the hydrogen bonding present in the substrate thereby resulting in enhanced reaction rates. The co-operative effect of the Brønsted and Lewis acidic sites in sulphamic acid has been reported to catalyze the conversion of glucosamine/chitosan biomass into HMF and levulinic acid via chitosan hydrolysis followed by the dehydration of glucosamine. Several Lewis acid catalysts such as the metal salts $\text{SnCl}_4 \cdot 5\text{H}_2\text{O}$, FeCl_2 , ZnCl_2 , CuCl_2 , MnCl_2 , containing metal cation and anion have been found to show a profound effect on chitin/chitosan conversion to form HMF, Levulinic acid and 3A5AF (N-containing furan derivative).

The presence of the anion has been reported to facilitate the substrate ionization by forming a chelate complex with the substrate thereby enhance the dehydration of the substrate. In the production of the renewable amine 3A5AF the Lewis acids not only enhance the dehydration step but also drive the enol isomerization that improves the product yield but it has also been found to show a negative effect as it facilitates the substrate carbonization thereby resulting in the formation of by-product as humins. Therefore, in several reports a combination of both Lewis and Brønsted acid catalyst has been used for this transformation.

Several reports on the use of ionic liquids as catalysts have been reported for the chitin conversion into furan derivative 3A5AF. This is due to the ability of the ionic liquid to accelerate the substrate dissolution and degradation. The ionic liquid has the property to cleave the hydrogen bonding present in the chitin polymer and form hydrogen bonding between the substrate and the anions resulting in the improved solubility of the substrate. The catalytic transformation of the chitin/chitosan biomass in the presence of water facilitates the formation of value-added compounds such as HMF and Levulinic acid with the expense of removal of the renewable N-atom from the substrate in the form of NH_3 that may further result in the deactivation of the catalyst.

Thus, the production of the renewable amine/amide containing furan derivative is an attractive strategy for the chitin biomass transformation as it results in the retention of the (biologically fixed) N-atom in the product that can be otherwise produced by the energy expensive Haber process. Also, it has been reported that the products 3A5AF and 3AF can be used as a promising synthetic precursor for the synthesis of the antitumor drug molecule proximicin a and b. But the challenge in the transformation is the retention of the amide functionality that can be easily hydrolysed in the presence solvent and catalytic systems that

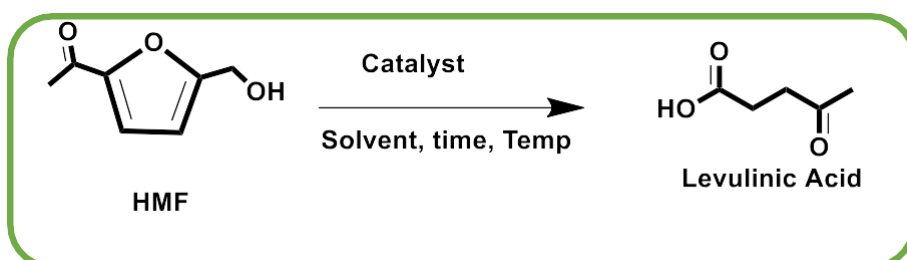
Chapter1

facilitates the hydrolysis. Therefore, the choice of the catalyst, tuning of the Lewis and Brønsted sites at the catalytic surface, catalyst surface area, solvent system and various parameter optimization plays a vital role in this transformation.

1.7.3 Hydration reactions:

The acid catalysed hydration of 5-HMF followed by opening of the furan ring produces a mixture of levulinic acid and formic acid. Heterogeneous catalytic systems Zeolites, amberlyst resin, dowex etc. have been employed for this transformation as shown in the **Scheme VII** ^(72,73)

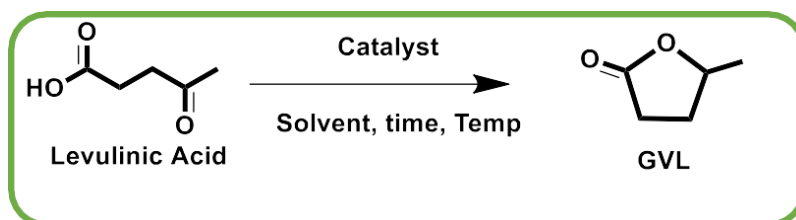
Scheme-VII HMF to levulinic acid



1.7.4 Hydrogenation reactions:

In order to deoxygenate the biomass derived molecules hydrogenation reactions can be carried out on both lignocellulosic and marine biomass in the presence of Pt, Pd, Ru, Ni, Co, and Cu based catalysts at moderate hydrogen pressures (10-25 bar) and temperatures in the range (90-145 °C). The solvent type, partial hydrogen pressure, and the existence of active sites at the catalytic surface significantly contribute to the product distribution in these reactions. ⁽⁷⁴⁾ Levulinic acid undergoes hydrogenation to make 4-hydroxy levulinic acid (GVL) as shown in **Scheme VIII**, whereas, 3A5AF produced from chitin/N-acetyl-d-glucosamine dehydration undergoes hydrogenation to form an amino acid precursor. ^(75,76)

Scheme-VIII Levulinic Acid to γ -Valero Lactone

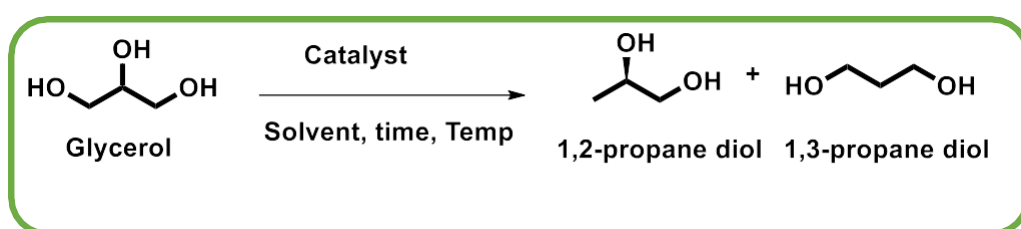


Chapter1

1.7.5 Hydrogenolysis:

With the aid of metal catalysts like Pt, Ru, Pd, Ni, and Cu supported on a suitable support, the hydrogenolysis of the polyols is carried out in the presence of acidic as well as basic conditions at hydrogen pressure (15-300 bar) and temperatures between 140 °C and 220 °C. In the hydrogenolysis reaction, the C-O bond are selectively broken, resulting in the production of diols, triols, and polyols such 1,2-propane diol and 1,3-propane diol, among others as shown in the **Scheme IX**. These compounds have applications in the synthesis of polymer and pharmaceuticals. ^(77,78)

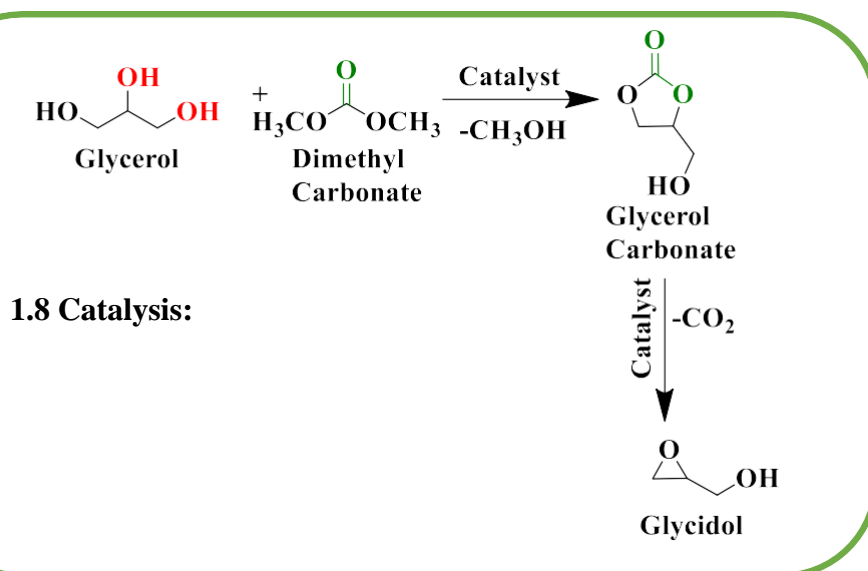
Scheme IX: Glycerol hydrogenolysis



1.7.6 A Trans-esterification of glycerol to glycidol:

Glycidol is prepared by first trans-esterifying glycerol to glycidol carbonate, which is then converted into glycidol by way of decarboxylation as shown in the **Scheme X**. Traditionally, the transesterification of glycerol is carried out by treating allylic alcohol with oxidising agent H₂O₂ and vanadium oxide and tungsten oxide-based catalyst. One pot glycidol synthesis has been reported which makes use of urea or dimethyl carbonate (DMC) as a carbonylating agent to form glycerol carbonate followed by decarboxylation to form Glycidol. For this transformation numerous homogeneous and heterogeneous metal-based catalysts for this transition have been described in the literature. ⁽⁷⁹⁻⁸¹⁾

Scheme X: Trans-esterification of glycerol to glycidol



1.8 Catalysis:

Chapter1

Today catalysis has become one of the most important aspects and deciding factor to enhance the world's economy, by converting the biomass raw materials into value added products, fuels and commodity chemicals in a cost effective and environmentally benign manner.⁽⁸²⁾ Heterogeneous catalysis has innumerable applications in industrial processes in chemical, food, pharmaceuticals, fuel cell, automobile, nanotechnology, biorefining and petrochemical industries.^(83, 84) Thus, it has been reported that 90 % of the chemical processes use heterogeneous catalysis. Therefore, catalysis plays a very important role in industries for the development of advanced processes. The industrial catalysts are complex materials with highly optimized structures, shape and size controlled, morphologies, surface area and physico-chemical properties.

A catalyst may be defined as a material that transforms reactants into desired products in which the catalyst participates in increasing the rate of reaction by lowering the energy of activation and is regenerated to its original form at the end of each cycle. There are several advantages of using a heterogeneous catalyst being a solid catalyst it can be easily separated and recycled for a particular transformation. The heterogeneous catalyst contains the presence of large surface area with active sites present at the catalytic surface which play a very important role in the transformation of reactants into products. Hence, it is required to increase the number of active sites per reactor volume to enhance the selectivity and yield of the desired products.⁽⁸⁵⁻⁸⁷⁾

1.9 Characteristics of a good Catalyst:

1. The catalyst should be selective towards the formation of desired products with minimum production of unwanted and un desired products.
2. The catalyst must be stable for a longer period of time at given reaction conditions.
3. The catalyst should possess large surface area with distribution of active sites at its surface in-order to achieve high yields of the products.

1.9.1 Solid Acid catalysis:

Mineral acids like HCl, H₂SO₄, HF, HNO₃, and Lewis and Bronsted acids like AlCl₃, BF₃, and B(OH)₃ are needed for a number of organic and biomass transformations such alkylation, acylation, esterification, etherification, isomerization, dehydration, and hydration. These chemicals produce a lot of organic waste that is discharged into the environment, are dangerous, and are difficult to handle. Therefore, it has become crucial to create solid acidic

Chapter1

and basic catalysts that are highly selective, shape and size-controlled, cost-effective, and environmentally benign in order to achieve the desired conversions. During the biomass transformations, these transformations must be concentrated with improved selectivity and fewer waste or by-product formation.

Solid acid catalysts are a special class of materials that possess characteristic physico-chemical properties such as Bronsted or Lewis acidity, specific surface area, pore size and pore volume at the catalytic surface. Heterogeneous catalysis has several advantages over homogeneous catalysis and conventional acidic reagents such as

- a) Easy recovery and separation from the reaction mixture
- b) Easily recyclable
- c) Lower toxicity
- d) Higher selectivity and lower formation of inorganic waste

1.10 Various parameters affecting the activity of solid catalysts in biomass conversion:

The rate at which reactants change into products is referred to as a reaction rate. Various chemical reactions take place at varying rates, which in turn is influenced by a number of variables, including the nature and type of the reaction, the media used in the reaction, the ratio of catalyst to substrate, and the effects of time, temperature, and pressure.⁽⁸⁸⁾ These variables significantly affect the conversion and selectivity towards a desired transformation during the course of a chemical reaction. Therefore, it is now crucial to provide ecologically friendly and cost-effective technologies for the required conversion of biomass into value-added products including commodity chemicals, fuel additives, and platform chemicals.

1.10.1 Substrate Concentration:

William Lewis and Max Trautz first presented the Collision Theory in 1910, and Max Trautz followed suit in 1916. According to the collision hypothesis, the frequency, energy, and orientation of molecular collisions as well as the rate of a specific reaction are all influenced by one another. When reactant molecules collide with one another in a specific orientation during a chemical reaction, successful collisions occur, supplying the activation energy necessary for the synthesis of the desired products.⁽⁸⁹⁾

Chapter1

1.10.2 Reaction medium:

Both lignocellulosic as well as marine biomass provide renewable feedstock for the production of bio-fuels, commodity chemicals and pharmaceuticals. Solvents are essential for a number of phenomena, including heat transport, reaction media provision, reactant solubility, product separation, and purification. The biorefinery concept has, however, faced significant difficulties in producing the needed chemicals with high yields and selectivity. The selectivity and conversion rates of biomass into platform chemicals have been found to benefit from the use of organic solvents. Finding a suitable solvent is therefore one of the most crucial steps in the conversion of biomass into fuel additives, furanic chemicals, and sugars. For the biomass transformations, a number of solvent systems, including water and organic solvents such DMA, DMSO, MIBK, MeOH, EtOH, and DMF, as well as the solvent effect of combining organic solvents with water, have been studied.⁽⁹⁰⁻⁹²⁾ The polar protic solvent water has been found to enhance the Fructose, HMF and levulinic acid formation whereas the solvents such as the DMA, DMSO, DMF has been found to enhance the dehydration of the chitin and cellulosic biomass. Minimizing humin production during biomass transformation is one of the main issues in solvent optimization. The addition of water is found to be deleterious in the case of marine biomass for the conversion of NAG to 3A5AF and 3AF, resulting in a drop in product yield with an increase in humin production.

1.10.3 Effect of temperature:

The increase in temperature induces heat transfer, which increases particle collisions and raises the collision frequency. This increase in the number of fruitful collisions with specific orientation increases the yield of product up to a certain extent. As a result, the activation energy is reduced and the reaction rates are enhanced thereby resulting in the formation of the products. Usually, the biomass conversions are carried out in the temperature range (90 °C to 220 °C). It has been discovered that raising the temperature above 180 °C accelerates up the formation of humins in the majority of biomass conversion processes.^(90, 93)

1.10.4 Effect of time:

When a chemical reaction is occurring, time is crucial. The rate of reaction is typically found to slow with passage of time. This is due to the fact that as time passes, the reactants continue to be transformed into products, lowering their concentration. Therefore, in order to construct a process that is more industrially feasible, it is crucial to design a reaction that has a

Chapter1

maximum yield and selectivity towards the intended transformation within a shorter time frame.

1.10.5 Effect of pressure:

High pressure reactors for biomass conversion may offer a number of benefits, including greater reaction rates, larger yields of valuable products, higher throughput, and cheaper compression costs for product gases.

However, comprehensive information on the impact of operating pressure on product yields and thermal effects during biomass conversion must be gathered prior to designing high pressure gasification and pyrolysis operations.

On the impact of pressure on the pyrolysis process' heat effects, there is a paucity of experimental evidence. According to reported literature increasing the operating pressure during the pyrolysis of cellulose lowers the necessary heat of reaction, increases the production of char and CO₂, and decreases the yields of CO and all other hydrocarbons produced during the process.⁽⁹⁴⁾

1.11 Objective of the thesis:

The aim of present research work is to design a multifunctional catalytic system for the transformation of both lignocellulosic as well as marine biomass into value added products with high selectivity, shape and size controlled, easily separable with excellent recyclability.

1. The work is focused on the synthesis of various mixed metal oxide catalysts containing micro-mesoporous channels that have interconnected micropores and mesopores and tuning its acidity and basicity to obtain desired biomass transformation.
2. The catalyst preparation methods include a) Co-precipitation method b) Wet impregnation method and c) Sol-gel method.
3. One of the objectives of this study is to develop the qualitative and quantitative approach based on the physico-chemical characterization that correlates the catalytic performance with micro-mesoporous properties of the mixed metal oxide catalysts.
4. Finally, three catalytic systems were studied mainly to evaluate the structure-activity correlations in valorization of lignocellulosic and marine biomass

Chapter1

- a) Bifunctional mixed metal oxide catalyst promoted isomerization of glucose to fructose
 - b) Brønsted basic dehydration of N-acetyl-d-glucosamine to 3A5AF and 3AF.
 - c) Transesterification of glycerol to glycidol in the presence of Sr doped on Cu-Al as a support.
5. Detailed physico-chemical characterization of the prepared catalysts.
 6. Development of various quantitative and qualitative analytical methods for the separation, purification and identification of the products formed.
 7. Optimization of various reaction parameters such as substrate and catalyst molar ratio, time, temperature, pressure, solvent system etc. in-order to achieve maximum substrate conversion and product selectivity.

References:

1. Marriott PE, Gómez LD, McQueen-Mason SJ. Unlocking the potential of lignocellulosic biomass through plant science. *New phytologist*. 2016 Mar;209(4):1366-81.
2. Sawant SS, Salunke BK, Tran TK, Kim BS. Lignocellulosic and marine biomass as resource for production of polyhydroxyalkanoates. *Korean Journal of Chemical Engineering*. 2016 May; 33:1505-13.
3. Bonechi C, Consumi M, Donati A, Leone G, Magnani A, Tamasi G, Rossi C. Biomass: an overview. *Bioenergy systems for the future*. 2017 Jan 1:3-42.
4. Beadle CL, Long SP. Photosynthesis is it limiting to biomass production?. *Biomass*. 1985 Jan 1;8(2):119-68.
5. Zhu XG, Long SP, Ort DR. What is the maximum efficiency with which photosynthesis can convert solar energy into biomass?. *Current opinion in biotechnology*. 2008 Apr 1;19(2):153-9.
6. Stefanidis SD, Kalogiannis KG, Iliopoulou EF, Michail of CM, Pilavachi PA, Lappas AA. A study of lignocellulosic biomass pyrolysis via the pyrolysis of cellulose, hemicellulose and lignin. *Journal of analytical and applied pyrolysis*. 2014 Jan 1; 105:143-50.
7. Hamawand I, Seneweera S, Kumarasinghe P, Bundschuh J. Nanoparticle technology for separation of cellulose, hemicellulose and lignin nanoparticles from lignocellulose biomass: a short review. *Nano-Structures & Nano-Objects*. 2020 Oct 1;24: 100601.

Chapter1

8. Wu Z, Yang W, Chen L, Meng H, Zhao J, Wang S. Morphology and microstructure of co-pyrolysis char from bituminous coal blended with lignocellulosic biomass: Effects of cellulose, hemicellulose and lignin. *Applied Thermal Engineering*. 2017 Apr 1; 116:24-32.
9. Chirapart A, Praiboon J, Ruangchuay R, Notoya M. Sources of marine biomass. *Marine bioenergy: trends and developments*. 2015 May 21:15-44.
10. Kurita K. Chitin and chitosan: functional biopolymers from marine crustaceans. *Marine biotechnology*. 2006 Jun; 8:203-26.
11. Huang YF, Lo SL. Predicting heating value of lignocellulosic biomass based on elemental analysis. *Energy*. 2020 Jan 15; 191:116501.
12. Mohamed AR, Mohammadi M, Darzi GN. Preparation of carbon molecular sieve from lignocellulosic biomass: A review. *Renewable and Sustainable Energy Reviews*. 2010 Aug 1;14(6):1591-9.
13. Sebestyén Z, Jakab E, Domán A, Bokrossy P, Bertóti I, Madarász J, László K. Thermal degradation of crab shell biomass, a nitrogen-containing carbon precursor. *Journal of Thermal Analysis and Calorimetry*. 2020 Oct; 142:301-8.
14. Sorek N, Yeats TH, Szemenyei H, Youngs H, Somerville CR. The implications of lignocellulosic biomass chemical composition for the production of advanced biofuels. *Bioscience*. 2014 Mar 1;64(3):192-201.
15. Berni R, Cai G, Hausman JF, Guerriero G. Plant fibers and phenolics: A review on their synthesis, analysis and combined use for biomaterials with new properties. *Fibers*. 2019 Aug 31;7(9):80.
16. Rahman MM, Mostafiz SB, Paatero JV, Lahdelma R. Extension of energy crops on surplus agricultural lands: A potentially viable option in developing countries while fossil fuel reserves are diminishing. *Renewable and Sustainable Energy Reviews*. 2014 Jan 1; 29:108-19.
17. Lutz W, Butz WP, Samir KE, editors. *World population & human capital in the twenty-first century: An overview*.
18. Hoel M, Kverndokk S. Depletion of fossil fuels and the impacts of global warming. *Resource and energy economics*. 1996 Jun 1;18(2):115-36.
19. Shepardson DP, Niyogi D, Choi S, Charusombat U. Students' conceptions about the greenhouse effect, global warming, and climate change. *Climatic Change*. 2011 Feb;104(3-4):481-507.

Chapter1

20. Singhvi MS, Gokhale DV. Lignocellulosic biomass: hurdles and challenges in its valorization. *Applied microbiology and biotechnology*. 2019 Dec; 103:9305-20.
21. Bhatia SK, Jagtap SS, Bedekar AA, Bhatia RK, Patel AK, Pant D, Banu JR, Rao CV, Kim YG, Yang YH. Recent developments in pretreatment technologies on lignocellulosic biomass: effect of key parameters, technological improvements, and challenges. *Bioresource technology*. 2020 Mar 1; 300:122724.
22. Nørskov JK, Bligaard T, Rossmeisl J, Christensen CH. Towards the computational design of solid catalysts. *Nature chemistry*. 2009 Apr;1(1):37-46.
23. Sidana A, Yadav SK. Recent developments in lignocellulosic biomass pretreatment with a focus on eco-friendly, non-conventional methods. *Journal of Cleaner Production*. 2022 Feb 10;335: 130286.
24. Brownell HH, Saddler JN. Steam pretreatment of lignocellulosic material for enhanced enzymatic hydrolysis. *Biotechnology and bioengineering*. 1987 Feb 5;29(2):228-35.
25. Schell DJ, Torget R, Power A, Walter PJ, Grohmann K, Hinman ND. A technical and economic analysis of acid-catalyzed steam explosion and dilute sulfuric acid pretreatments using wheat straw or aspen wood chips. *Applied biochemistry and biotechnology*. 1991 Mar; 28:87-97.
26. Zhao X, Cheng K, Liu D. Organosolv pretreatment of lignocellulosic biomass for enzymatic hydrolysis. *Applied microbiology and biotechnology*. 2009 Apr; 82:815-27.
27. Brandt A, Ray MJ, To TQ, Leak DJ, Murphy RJ, Welton T. Ionic liquid pretreatment of lignocellulosic biomass with ionic liquid–water mixtures. *Green Chemistry*. 2011;13(9):2489-99.
28. Uthandi S, Kaliyaperumal A, Srinivasan N, Thangavelu K, Muniraj IK, Zhan X, Gathergood N, Gupta VK. Microbial biodiesel production from lignocellulosic biomass: new insights and future challenges. *Critical Reviews in Environmental Science and Technology*. 2022 Jun 18;52(12):2197-225.
29. Chen W, Chen Y, Yang H, Xia M, Li K, Chen X, Chen H. Co-pyrolysis of lignocellulosic biomass and microalgae: Products characteristics and interaction effect. *Bioresource technology*. 2017 Dec 1; 245:860-8.
30. Guerriero G, Fugelstad J, Bulone V. What do we really know about cellulose biosynthesis in higher plants? *Journal of integrative plant biology*. 2010 Feb;52(2):161-75.
31. Nevell TP, Zeronian SH. Cellulose chemistry and its applications.

32. Sharma A, Thakur M, Bhattacharya M, Mandal T, Goswami S. Commercial application of cellulose nano-composites—A review. *Biotechnology Reports*. 2019 Mar 1;21: e00316.
33. Yu J, Paterson N, Blamey J, Millan M. Cellulose, xylan and lignin interactions during pyrolysis of lignocellulosic biomass. *Fuel*. 2017 Mar 1; 191:140-9.
34. Sella Kapu N, Trajano HL. Review of hemicellulose hydrolysis in softwoods and bamboo. *Biofuels, Bioproducts and Biorefining*. 2014 Nov;8(6):857-70.
35. Bhalla A, Cai CM, Xu F, Singh SK, Bansal N, Phongpreecha T, Dutta T, Foster CE, Kumar R, Simmons BA, Singh S. Performance of three delignifying pretreatments on hardwoods: hydrolysis yields, comprehensive mass balances, and lignin properties. *Biotechnology for biofuels*. 2019 Dec; 12:1-5.
36. Feldman D. Lignin and its polyblends-a review. *Chemical modification, properties, and usage of lignin*. 2002:81-99.
37. Chakravarty J, Edwards TA. Innovation from waste with biomass-derived chitin and chitosan as green and sustainable polymer: A Review. *Energy Nexus*. 2022 Sep 29:100149.
38. Peter S, Lyczko N, Gopakumar D, Maria HJ, Nzihou A, Thomas S. Chitin and chitosan-based composites for energy and environmental applications: a review. *Waste and Biomass Valorization*. 2021 Sep; 12:4777-804.
39. Zhou D, Shen D, Lu W, Song T, Wang M, Feng H, Shentu J, Long Y. Production of 5-hydroxymethylfurfural from chitin biomass: A review. *Molecules*. 2020 Jan 27;25(3):541.
40. Ali G, Sharma M, Salama ES, Ling Z, Li X. Applications of chitin and chitosan as natural biopolymer: potential sources, pre-treatments, and degradation pathways. *Biomass Conversion and Biorefinery*. 2022 Apr 23:1-5.
41. Bernardi A, Giarola S, Bezzo F. Spatially explicit multi-objective optimization for the strategic design of first and second generation biorefineries including carbon and water footprints. *Industrial & Engineering Chemistry Research*. 2013 Jun 5;52(22):7170-80.
42. Clark J, Deswarte F. The biorefinery concept: an integrated approach. *Introduction to chemicals from biomass*. 2015 Feb 13:1-29.
43. Rodionova MV, Bozieva AM, Zharmukhamedov SK, Leong YK, Lan JC, Veziroglu A, Veziroglu TN, Tomo T, Chang JS, Allakhverdiev SI. A comprehensive review on lignocellulosic biomass biorefinery for sustainable biofuel production. *International Journal of Hydrogen Energy*. 2022 Jan 8;47(3):1481-98.0

44. Kumar B, Bhardwaj N, Agrawal K, Chaturvedi V, Verma P. Current perspective on pretreatment technologies using lignocellulosic biomass: An emerging biorefinery concept. *Fuel Processing Technology*. 2020 Mar 1; 199:106244.
45. Ruiz HA, Rodríguez-Jasso RM, Fernandes BD, Vicente AA, Teixeira JA. Hydrothermal processing, as an alternative for upgrading agriculture residues and marine biomass according to the biorefinery concept: a review. *Renewable and Sustainable Energy Reviews*. 2013 May 1; 21:35-51.
46. Seo MW, Lee SH, Nam H, Lee D, Tokmurzin D, Wang S, Park YK. Recent advances of thermochemical conversion processes for biorefinery. *Bioresource Technology*. 2022 Jan 1; 343:126109.
47. Tomishige K, Yabushita M, Cao J, Nakagawa Y. Hydrodeoxygenation of potential platform chemicals derived from biomass to fuels and chemicals. *Green Chemistry*. 2022;24(15):5652-90.
48. Jäger G, Büchs J. Biocatalytic conversion of lignocellulose to platform chemicals. *Biotechnology journal*. 2012 Sep;7(9):1122-36.
49. Maitra S, Singh V. A consolidated bioprocess design to produce multiple high-value platform chemicals from lignocellulosic biomass and its techno-economic feasibility. *Journal of Cleaner Production*. 2022 Dec 1; 377:134383.
50. Choi S, Song CW, Shin JH, Lee SY. Biorefineries for the production of top building block chemicals and their derivatives. *Metabolic engineering*. 2015 Mar 1; 28:223-39.
51. Sailer-Kronlachner W, Rosenfeld C, Konnerth J, van Herwijnen H. 5-Hydroxymethylfurfural-Based Adhesives: Challenges and Opportunities. *Biobased Adhesives: Sources, Characteristics and Applications*. 2023 May 15:477-97.
52. Sajid M, Zhao X, Liu D. Production of 2, 5-furandicarboxylic acid (FDCA) from 5-hydroxymethylfurfural (HMF): recent progress focusing on the chemical-catalytic routes. *Green chemistry*. 2018;20(24):5427-53.
53. Rackemann DW, Doherty WO. The conversion of lignocellulosics to levulinic acid. *Biofuels, Bioproducts and Biorefining*. 2011 Mar;5(2):198-214.
54. Bozell JJ, Moens L, Elliott DC, Wang Y, Neuenschwander GG, Fitzpatrick SW, Bilski RJ, Jarnefeld JL. Production of levulinic acid and use as a platform chemical for derived products. *Resources, conservation and recycling*. 2000 Feb 1;28(3-4):227-39.

55. Zhang M, Wang N, Liu J, Wang C, Xu Y, Ma L. A review on biomass-derived levulinic acid for application in drug synthesis. *Critical Reviews in Biotechnology*. 2022 Feb 17;42(2):220-53.
56. Yan K, Wu G, Lafleur T, Jarvis C. Production, properties and catalytic hydrogenation of furfural to fuel additives and value-added chemicals. *Renewable and sustainable energy reviews*. 2014 Oct 1; 38:663-76.
57. Machado G, Leon S, Santos F, Lourega R, Dullius J, Mollmann ME, Eichler P. Literature review on furfural production from lignocellulosic biomass. *Natural Resources*. 2016 Mar 11;7(3):115-29.
58. García JI, García-Marín H, Pires E. Glycerol based solvents: synthesis, properties and applications. *Green Chemistry*. 2014;16(3):1007-33.
59. Tan HW, Aziz AA, Aroua MK. Glycerol production and its applications as a raw material: A review. *Renewable and sustainable energy reviews*. 2013 Nov 1; 27:118-27.
60. McNutt J, Yang J. Utilization of the residual glycerol from biodiesel production for renewable energy generation. *Renewable and Sustainable Energy Reviews*. 2017 May 1; 71:63-76.
61. Dalena F, Senatore A, Iulianelli A, Di Paola L, Basile M, Basile A. Ethanol from biomass: future and perspectives. In *Ethanol 2019* Jan 1 (pp. 25-59). Elsevier.
62. Lynd LR, Cushman JH, Nichols RJ, Wyman CE. Fuel ethanol from cellulosic biomass. *Science*. 1991 Mar 15;251(4999):1318-23.
63. Li Y, Bhagwat SS, Cortés-Peña YR, Ki D, Rao CV, Jin YS, Guest JS. Sustainable lactic acid production from lignocellulosic biomass. *ACS Sustainable Chemistry & Engineering*. 2021 Jan 12;9(3):1341-51.
64. Martinez FA, Balciunas EM, Salgado JM, González JM, Converti A, de Souza Oliveira RP. Lactic acid properties, applications and production: A review. *Trends in food science & technology*. 2013 Mar 1;30(1):70-83.
65. Verma M, Mandyal P, Singh D, Gupta N. Recent developments in heterogeneous catalytic routes for the sustainable production of succinic acid from biomass resources. *ChemSusChem*. 2020 Aug 21;13(16):4026-34.
66. Pinazo JM, Domine ME, Parvulescu V, Petru F. Sustainability metrics for succinic acid production: A comparison between biomass-based and petrochemical routes. *Catalysis Today*. 2015 Jan 1; 239:17-24.

67. Lenihan P, Orozco A, O'Neill E, Ahmad MN, Rooney DW, Mangwandi C, Walker GM. Kinetic modelling of dilute acid hydrolysis of lignocellulosic biomass. *Biofuel production-recent developments and prospects*. Intech, Croatia. 2011 Sep 15:293-308.
68. Lee JW, Jeffries TW. Efficiencies of acid catalysts in the hydrolysis of lignocellulosic biomass over a range of combined severity factors. *Bioresource technology*. 2011 May 1;102(10):5884-90.
69. Delidovich I, Palkovits R. Catalytic isomerization of biomass-derived aldoses: A review. *ChemSusChem*. 2016 Mar 21;9(6):547-61.
70. Akien GR, Qi L, Horváth IT. Molecular mapping of the acid catalysed dehydration of fructose. *Chemical Communications*. 2012;48(47):5850-2.
71. Omari KW, Dodot L, Kerton FM. A simple one-pot dehydration process to convert N-acetyl-D-glucosamine into a nitrogen-containing compound, 3-acetamido-5-acetylfuran. *ChemSusChem*. 2012 Sep;5(9):1767-72.
72. Kang S, Fu J, Zhang G. From lignocellulosic biomass to levulinic acid: A review on acid-catalyzed hydrolysis. *Renewable and Sustainable Energy Reviews*. 2018 Oct 1; 94:340-62.
73. Mukherjee A, Dumont MJ, Raghavan V. Sustainable production of hydroxymethylfurfural and levulinic acid: Challenges and opportunities. *Biomass and Bioenergy*. 2015 Jan 1; 72:143-83.
74. Adu-Mensah D, Mei D, Zuo L, Zhang Q, Wang J. A review on partial hydrogenation of biodiesel and its influence on fuel properties. *Fuel*. 2019 Sep 1; 251:660-8.
75. Dutta S, Iris KM, Tsang DC, Ng YH, Ok YS, Sherwood J, Clark JH. Green synthesis of gamma-valerolactone (GVL) through hydrogenation of biomass-derived levulinic acid using non-noble metal catalysts: A critical review. *Chemical Engineering Journal*. 2019 Sep 15; 372:992-1006.
76. Liu Y, Stähler C, Murphy JN, Furlong BJ, Kerton FM. Formation of a Renewable Amine and an Alcohol via Transformations of 3-Acetamido-5-acetylfuran. *ACS Sustainable Chemistry & Engineering*. 2017 Jun 5;5(6):4916-22.
77. Martin A, Armbruster U, Gandarias I, Arias PL. Glycerol hydrogenolysis into propanediols using in situ generated hydrogen—A critical review. *European journal of lipid science and technology*. 2013 Jan;115(1):9-27.

Chapter1

78. Gómez-Jiménez-Aberasturi O, Ochoa-Gómez JR. New approaches to producing polyols from biomass. *Journal of Chemical Technology & Biotechnology*. 2017 Apr;92(4):705-11.
79. Prete P, Cespi D, Passarini F, Capacchione C, Proto A, Cucciniello R. Glycidol syntheses and valorizations: Boosting the glycerol biorefinery. *Current Opinion in Green and Sustainable Chemistry*. 2022 Apr 4:100624.
80. Rozulan N, Halim SA, Razali N, Lam SS. A review on direct carboxylation of glycerol waste to glycerol carbonate and its applications. *Biomass Conversion and Biorefinery*. 2022 Oct;12(10):4665-82.
81. Behr A, Eilting J, Irawadi K, Leschinski J, Lindner F. Improved utilisation of renewable resources: New important derivatives of glycerol. *Green Chemistry*. 2008;10(1):13-30.
82. De S, Dutta S, Saha B. Critical design of heterogeneous catalysts for biomass valorization: current thrust and emerging prospects. *Catalysis Science & Technology*. 2016;6(20):7364-85.
83. Sudarsanam P, Zhong R, Van den Bosch S, Coman SM, Parvulescu VI, Sels BF. Functionalised heterogeneous catalysts for sustainable biomass valorisation. *Chemical Society Reviews*. 2018;47(22):8349-402.
84. Ross JR. *Heterogeneous catalysis: fundamentals and applications*. Elsevier; 2011 Aug 17.
85. Satterfield CN. *Heterogeneous catalysis in industrial practice*.
86. Borek G. *Heterogeneous catalysis*. Nova Publishers; 2003.
87. Védrine JC. *Metal oxides in heterogeneous catalysis*. Elsevier; 2018 Jan
88. De S, Dutta S, Saha B. Critical design of heterogeneous catalysts for biomass valorization: current thrust and emerging prospects. *Catalysis Science & Technology*. 2016;6(20):7364-85.
89. Widom B. Collision theory of chemical reaction rates. *Advances in Chemical Physics*, Volume 5. 2009 Sep 8; 5:353.
90. Shuai L, Luterbacher J. Organic solvent effects in biomass conversion reactions. *ChemSusChem*. 2016 Jan;9(2):133-55.
91. Kruse A, Dahmen N. Water—A magic solvent for biomass conversion. *The Journal of Supercritical Fluids*. 2015 Jan 1; 96:36-45.
92. Mellmer MA, Sener C, Gallo JM, Luterbacher JS, Alonso DM, Dumesic JA. Solvent effects in acid-catalyzed biomass conversion reactions. *Angewandte chemie international edition*. 2014 Oct 27;53(44):11872-5.

Chapter1

93. Szabolcs Á, Molnár M, Dibó G, Mika LT. Microwave-assisted conversion of carbohydrates to levulinic acid: an essential step in biomass conversion. *Green Chemistry*. 2013;15(2):439-45.
94. Razaq WA, Golonka M, Scholz M, Białowiec A. Opportunities and challenges of high-pressure fast pyrolysis of biomass: A review. *Energies*. 2021 Aug 31;14(17):5426.

Experimental

2.1. Introduction:

A catalyst is a material that speeds up the reaction. Heterogeneous catalysis is a sorption phenomenon in which the catalyst does not undergo any chemical change during the course of the reaction. The reaction proceeds by the sorption of the reactants at the surface of the catalyst (electrostatic interaction, physisorption, chemisorption). This results in lowering of the activation energy required to initiate the chemical reaction. The activation energy is the difference between the reactants and the transition state formed during the course of a reaction. Thus, the catalyst is found to stabilize the transition state formed thereby reducing/lowering the energy required to form the product.

Main types namely, homogeneous, heterogeneous, and bio-, exist to speed up the process. Almost 80 % of the reactions carried out at industries commercially involve the use of heterogeneous catalysts because of various advantages associated with their use which includes robustness, ease of separation, easy handling, recyclability and low operating costs thus making the process economically beneficial.

In a particular course of reaction, catalysts are crucial because they speed up the reaction and reduce the activation energy. In heterogeneous catalysis, the design, synthesis, and adjustment of the acidic and basic characteristics at the catalytic surface are crucial. The distribution of acidic and basic sites on the catalytic surface, the acid-base density, and the morphology, shape, and size of the catalyst are all studied through the detailed characterization of the catalyst, which is a highly important aspect.

The current chapter outlines the entire process for creating catalysts using a variety of approaches, activity testing for the catalyst, characterization of the catalyst, and the analytical methods applied to the process. This section provides a detailed discussion of the techniques utilized for both the quantitative and qualitative analysis of the catalyst and the products formed.

2.2. Materials

Barium nitrate, zirconyl oxy nitrate, barium oxide, zirconium oxide, tin oxide, molybdenum nitrate, zinc nitrate, tungsten nitrate and potassium carbonate were purchased from Thomas Baker chemicals, India. The chemicals were used as received without further purification.

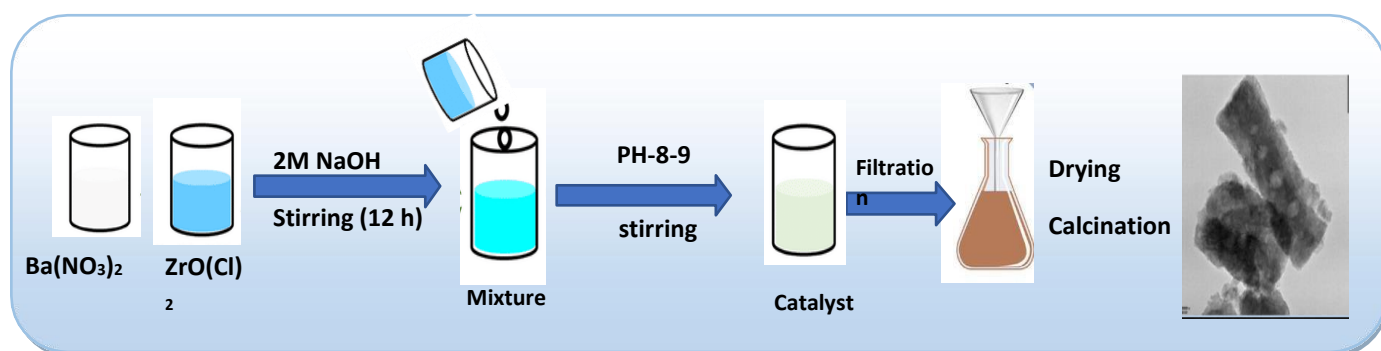
Chapter 2

The solvents such as MeOH, DMF and DMSO and other chemicals used as standards for the calibration of HPLC analysis were also purchased from Thomas Baker chemicals, India. N-acetyl glucosamine, lanthanum oxide (La_2O_3), calcium oxide (CaO), cerium oxide (Ce_2O_3), zirconium oxide (ZrO_2), glycerol, dimethyl carbonate, methanol, ethanol, acetonitrile, isopropanol, dimethyl formamide, aluminum oxide (Al_2O_3) and barium hydroxide (BaOH_2) were purchased from Thomas Baker Chemicals, India. The chemicals were used as received without further purification. The solvents such as MeOH, DMF, DMSO, ACN, n-Hexane, EtOAc, DMA, MIBK, dioxane and other chemicals were also purchased from HIMEDIA chemicals, India. DMSO-d6 was purchased from Sigma Aldrich, India and was used as NMR solvent.

2.3. Catalyst preparation: Solid acid catalysts

2.3.1 Preparation of Ba-Zr mixed metal oxide by co-precipitation method

Typical co-precipitation method was used to synthesize nano-size Ba-Zr mixed metal oxide (MMO) catalyst under alkaline conditions as shown in the **Fig. 2.1**. Accordingly, 0.4 mol of $\text{Ba}(\text{NO}_3)_2$ (5.22 g) and 0.2 mol of $\text{ZrO}(\text{NO}_3)_2 \cdot 6\text{H}_2\text{O}$ (2.31 g), each in 50 mL of DI water was dissolved separately (for 2:1 Ba-Zr composition), to make a homogenous solution. These solutions were then taken in a 250 mL, 3-neck round bottom flask to which, 0.8 M K_2CO_3 was added drop wise with the help of an addition funnel, until the pH reached to 8-9 under constant stirring (1000 rpm) at room temperature. The precipitate thus obtained was aged for 3 h at room temperature. The resulting product was then recovered by filtration and washed repetitively with DI water until neutralization. It was dried at 110 °C for 24 h and then calcined at 550 °C for 3 h. Several other samples of Ba-Zr MMO were also prepared by varying Ba-Zr ratio as 0.5:1, 1:1, 2:1, 3:1 which were named as Ba-Zr (0.5:1), Ba-Zr (1:1), Ba-Zr (2:1), and Ba-Zr (3:1), respectively.



Chapter 2

Fig.2.1. a Preparation of Ba-Zr by Co-precipitation method

2.3.2 Preparation of SBA-15

SBA-15 solid support was prepared as given in literature ⁽¹⁾. In a teflon beaker 4.05 g of Pluronic p-123 was dissolved in 146.8 g de-ionized water and 2.2 g of conc. HCl (37 %), was stirred overnight at 35 °C. A milky suspension is produced which is aged at 100 °C for 24 h in a Teflon lined steel autoclave. To this solution 16 g of TEOS (Tetraethyl ortho silicate) was added and stirred for 24 h at 35 °C. The solid product thus obtained was filtered, washed with water to excess of TEOS, dried and calcined at 550 °C for 5 h.

2.3.3 Wet impregnation of Phosphotungstic acid supported on SBA-15

Phosphotungstic acid supported on SBA-15 composites were synthesized by a wetness impregnation as described in the literature. Various concentrations ranging from 5 % to 30 % solution of phosphotungstic acid loading were prepared in water. These solutions of phosphotungstic acid were added to 3 g of SBA-15 synthesis as shown in the Fig. 2.1. These samples were charged to an RB (round bottom flask) flask and the mixture were stirred at 80 °C for 6 h. Then the catalyst mixture is evaporated on Rota-vapour and dried. The solid product thus obtained was dried overnight and calcined at 300 °C for 3 h. The resulting sample was labelled as 20 % PWA/SBA-15 imp (imp refers to wet impregnation method) ⁽²⁾

2.3.4 Direct synthesis of Phosphotungstic acid supported on SBA-15

Phosphotungstic acid supported on SBA-15 composites were synthesized by a direct synthesis method of various concentrations ranging from 5 % to 30 % loading. Accordingly, 5 %, 10 %, 20 %, 30 % solution of phosphotungstic acid were prepared in water which were added to the final samples during SBA-15 synthesis. These samples were loaded in Teflon lined autoclave, stirred and heated at 35 °C for 24 h. The solid product thus obtained was filtered, washed with water to excess of TEOS, dried and calcined at 550 °C for 5 h.

2.3.5 Direct synthesis of Silicotungstic acid supported on SBA-15

Silicotungstic acid supported on SBA-15 composites were synthesized by a direct synthesis method of concentrations of 20 % loading. 20 % solution of silicotungstic acid were prepared in water. This solution of silicotungstic acid were added to the final samples during SBA-15 synthesis. These samples were loaded in Teflon lined autoclave, stirred and heated at 35 °C

Chapter 2

for 24 h. The solid product thus obtained was filtered, washed with water to excess of TEOS, dried and calcined at 550 °C for 5 h.

2.3.6 Preparation of Barium oxide

Barium hydroxide was calcined at 550 °C for 6 h to produce barium oxide.

2.3.7 Preparation of Sr/Cu-Al by Co-precipitation method:

Mixed metal oxide of Sr with Cu and Al was prepared by varying ratios viz. 1:4.5:4.5, 2: 4:4, 3:3.5:3.5, 4:3:3 using typical co precipitation method. The nano structured mixed oxide catalyst was prepared by simultaneously co-precipitation, digestion method in which aqueous solution of required concentration of $\text{Cu}(\text{NO}_3)_2 \cdot 3\text{H}_2\text{O}$, $\text{Al}(\text{NO}_3)_3 \cdot 9\text{H}_2\text{O}$ and $\text{Sr}(\text{NO}_3)_2$ were added along with 0.2M K_2CO_3 as precipitating agent in a round bottom flask. After complete addition the precipitate was digested for 4 h and then filtered, washed with deionized water in order to remove the traces for potassium. The obtained precipitate was then dried in oven at 110 °C for 8h. Further calcined at 550 °C and nominated as Sr:Cu:Al (1:4.5:4.5), (2:4:4), (3:3.5:3.5), (4:3:3). Using same co-precipitation method all the alkali and alkaline earth metals like, Na, Mg, Ca, Rb, Sr, Cs, Ba were mixed with Cu-Al to prepare mixed oxide catalyst.

2.4 Catalyst Characterization Techniques

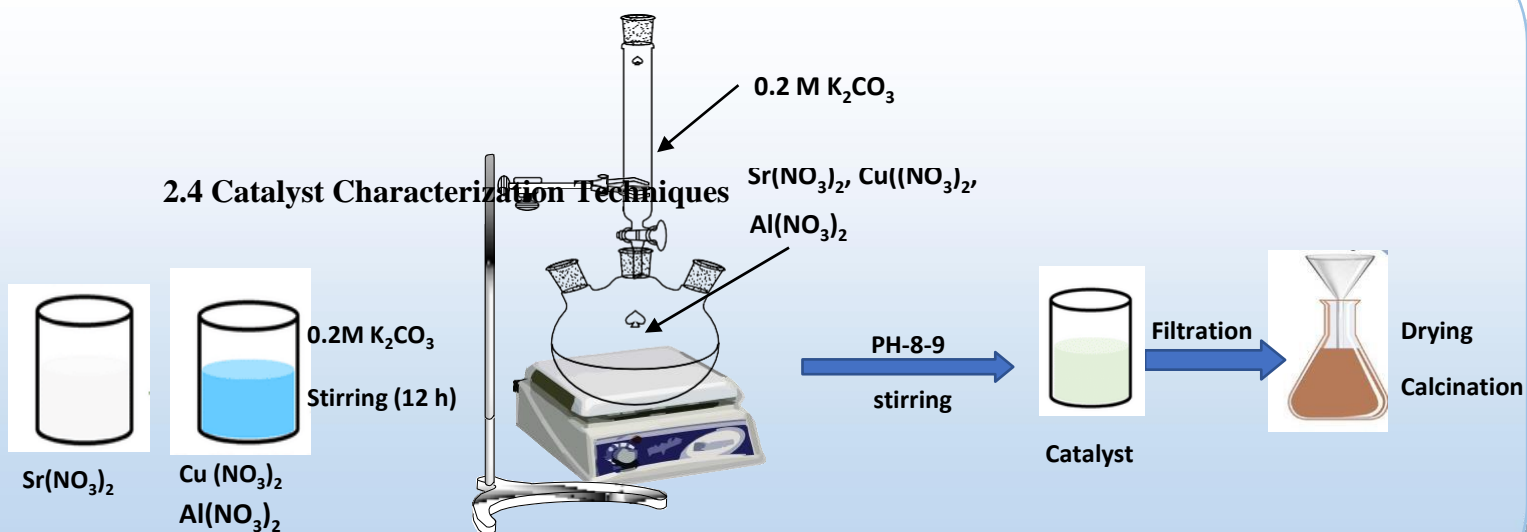


Fig.2.1. b Preparation of Cu-Al by Co-precipitation method

Chapter 2

2.4.1 X-ray diffraction

A non-destructive method for qualitative and quantitative investigation of solid or powdered crystalline materials is X-ray diffraction (XRD). It aids in figuring out whether a catalyst is crystalline or amorphous, determining the size of crystallites, clarifying crystal structure, and determining phase purity. The atoms present in the lattice structure interact with the incident monochromatic X-rays (Cu K/ Mo K) in this process as shown in the (Fig. 2.2).

According to the Braggs law, which states that $n \lambda = 2d \sin\theta$, where n is an integer known as the order of reflection, d is the distance between the two lattice planes, and θ is the angle between the two lattice planes, the X-rays scattered by the atoms in an octahedral lattice interact constructively. ⁽³⁾ The mixed metal oxide catalysts were characterized by using various techniques. The X-ray diffraction (XRD) analysis was carried out on a P Analytical PXRD system (Model X-Pert PRO-1712), using Ni filtered Cu K α radiation ($\lambda = 0.154$ nm) as an X-ray source (current intensity, 30 mA; voltage, 40 kV) and an X-accelerator detector. XRD measurements were carried out in a 2θ range of 5° – 85° with a scanning rate of $5^\circ/\text{min}$. The Scherrer equation, $L = K/\cos$, was used to calculate the crystallite size of the materials, where θ and λ are the Braggs angle and wavelength of the incident X-ray radiation, respectively.

The line width on the 2θ scale in radians is represented by the constant K , which is typically taken to be 0.9. On the basis of a comparison between the line positions and the intensity distribution of a group of reflections from a catalyst sample and a data base (JCPDS), qualitative phase analysis of the catalysts was carried out. To calculate crystallite size, peak widths are fitted to the Debye-Scherrer equation. The Vegards rule, which asserts that there is a linear relationship between the concentration of a substitutional dopant and the change in the lattice parameter, is frequently used to interpret shifts caused by substitutional doping. It is also unclear if the observed shift in lattice parameters is the result of doping or the small size of the crystallite because the lattice parameters of small nanocrystals rely on the crystallite size.⁽⁴⁾

Chapter 2



Fig. 2.2 Powder XRD instrument

2.4.2 Physico-chemical measurements and N₂ sorption studies

The most typical kind of adsorption is physisorption. Physisorbed molecules can move across the sample's surface fairly freely. The adsorbed molecules have a tendency to layer over the entire adsorbent surface as more gas molecules are added to the system. One can estimate the number of molecules, N_m , using the well-known Brunauer, Emmett, and Teller (BET) hypothesis. The sample area is obtained by multiplying N_m by the cross-sectional area of an adsorbate molecule. The BET formula is given below

$$P/V (P_0 - P) = 1/V_m C + [(C-1)/V_m C] (P/P_0) \dots\dots\dots (2a)$$

Where P_0 denotes the adsorbate's saturation vapour pressure at the experimental temperature (T_a),

P indicates the adsorption equilibrium pressure (Pa),

V is the volume of the gas adsorbed at the pressure P (Cm^3),

C is the constant related to the heat of adsorption and liquification.

Plotting $P/V (P - P_0)$ against (P/P_0) results in a straight line that is often within the range of 0.05 (P/P_0) 0.35. The monolayer volume V_m can be calculated as $1/(S+1)$, where S is the slope and equals $(C-1)/V_m C$, and I is the intercept and equal to $I/V_m C$. The equation relates the catalyst's surface area (S_{BET}) to V_m .⁽⁵⁾

$$(V_m/22414) = S_{BET} N_a \sigma \dots\dots\dots (2b)$$

Chapter 2

where N_a is the Avogadro number, and is the typical cross-sectional area that one adsorbate molecule covers. The N_2 (nitrogen gas) has a standard value of 0.1622 nm^2 . The surface area and porosity are important properties in the field of heterogeneous catalysis. The surface area and porosity are important properties in the field of heterogeneous catalysis. Total surface area is an important criterion for solid catalysts since it determines the accessibility of the active sites and is frequently associated to the catalytic activity. Total surface area defines the accessibility of the active sites and is frequently tied to the catalytic activity. A heterogeneous catalyst's pore structure determines selectivity in the catalysed processes and regulates transport phenomena. Pore size and volume are thus crucial characteristics, especially in the case of shape selectivity catalysis.

The adsorption isotherm is the first significant finding from the physisorption investigation regarding the surface and porosity. It can identify the precise dimensions and types of porosity that are present in the given catalytic sample. According to **Fig. 2.3**, there are a total of 6 different types of adsorption isotherms. The existence of micropores, where molecules are adsorbed by the micropore filling, is represented by the type I isotherm. The presence of nonporous and microporous surfaces, which only very weakly interact with the molecules being adsorbed, is suggested by the type II isotherm, which is suggestive of the multilayer adsorption process. Through its hysteresis loop, or non-overlapping of the adsorption and the desorption peaks, the type IV isotherm provides useful information on the presence of the mesoporous material. Despite having relatively weak adsorbent-adsorbate interactions, the type V isotherm shares several characteristics with the type IV isotherm. The type VI isotherm is a stepped adsorption isotherm that results from the adsorbed molecular layer's phase transition or from adsorption on the various faces of crystalline solids. With the aid of the physisorption isotherm, a variety of computational techniques are available to clarify the pore size distribution and pore volume of the catalytic sample. The (BJH) Barrett-Joyner-Halenda approach, which enables the determination of the catalyst's pore size from equilibrium gas pressure, is one of the most often used methods. As a result, we may create experimental isotherms that relate the volume of the adsorbed gas with the respective saturation pressures at equilibrium and transform these to various different pore size distribution.

Adsorbate fills all of the pores as the equilibrium adsorbate pressures get close to saturation. Total pore volume of the sample can be estimated if the density of the adsorbate is known.

Chapter 2

The adsorption and desorption isotherms hardly ever cross each other because the adsorption and desorption mechanisms are different. The subsequent hysteresis loop gives rise to the isotherm shape, which is one of the distinguishing characteristics of the specific pore shape. The typical approach for determining the surface area, pore size, and pore volume of the catalytic sample is to analyse nitrogen adsorption using the BET equation at low pressures 10-14 Torr and liquefaction temperature of N_2 (77 K). The Autosorb 1, Quantachrome equipment was used for all of these measurements (**Fig. 2.4**).

The surface areas of all the basic catalysts using BET equation were measured on Quantachrome v 2.0 instrument. The basic sites present on the catalyst surface were quantitatively analysed by CO_2 -TPD carried out on Micromeritics-2720 (ChemisoftTPx) volumetric instrument. The samples were pre-treated from room temperature to 200 °C under a helium flow rate of 25 mL min^{-1} followed by CO_2 adsorption at 40 °C and finally CO_2 desorption with heating rate of 10 °C min^{-1} starting from adsorption temperature to 700 °C.⁽⁶⁾



Fig. 2.3 Autosorb 1, Quantachrome instrument

2.4.3 Temperature programmed desorption of ammonia (NH_3 and CO_2 TPD)

As opposed to physisorption, the chemisorption process entails the establishment of potent chemical bonds between the molecules that are being adsorbate and particular regions referred to as the active sites located on the surfaces of the catalytic sample. Thus, the main purpose of chemisorption is to quantify the presence of active sites at the catalytic surfaces that are in charge of the catalytic activity. One of the chemisorption techniques is the NH_3 -

Chapter 2

TPD measurement, which is employed to assess the acidity, presence of acidic sites at the catalytic surface, acidic strength, and interaction between the solid catalyst and its gaseous environment as the temperature is linearly increased over time. The instrument used for measuring the amount of desorbed NH_3 gas in the carrier gas includes a sample container charged with the catalyst in a furnace that may have its temperature modified. It also includes a thermal conductivity detector (TCD). On a Micromeritics 2720 by 1, all the catalysts' NH_3 TPDs were measured by removing impurities that have adhered to the sample's surface by

1. pre-treating the catalytic sample with helium gas flow at 473 K.
2. Ammonia gas adsorption at a temperature of 50 °C
3. Heating at a rate of 10 K/min from 50 °C to 700 °C for the desorption of the adsorbed ammonia. Utilising the Origin software programme, the area of the desorption peak in low and high temperature areas is measured in order to quantitatively examine the active acidic sites that are present at the catalytic surface. Similarly in order to analyze the presence of basic sites at the catalytic surface the entire procedure is repeated by using the CO_2 gas is used instead of NH_3 gas. The analysis was carried out on Autosorb 1, Quantachrome equipment as shown in **Fig. 2.3**

2.4.4 Fourier transform infrared spectroscopy (FTIR):

In 1937, Buswell and colleagues reported using IR spectroscopy to study surface chemistry and catalysis. Infrared radiation is located between the visible and microwave regions of the electromagnetic spectrum. The frequency of infrared radiation is higher than that of microwave radiation and lower than that of visual radiation. The IR principle states that molecule vibrations occur after IR radiation has been absorbed when the applied IR frequency coincides with the natural IR vibration frequency. The elucidation of the functional group in the substance and chemical analysis are two common applications of the IR spectroscopy technology. It provides details on the dipole-moment bearing polyatomic species' vibrational structure. The vibrational modes connected to changes in the molecule dipole moment are therefore discovered to be IR active by IR spectroscopy.

At room temperature, metal oxides are one of the most significant and useful materials that are covered in oxide layers and show catalytic activity for a variety of transformations. Here, the characteristics of the oxide layers that naturally grow on metal implants when oxygen is present increase the biocompatibility of those devices. One of the most crucial parts of

Chapter 2

heterogeneous catalysis is the study of how molecules of the substrate and solvent interact with the catalyst surface. Thus, a thorough understanding of chemical processes, binding power, and the adsorption phenomena has become crucial.

Every bond or functional group absorbs light at a particular frequency; hence every molecule has a distinctive peak. A specific molecule's existence of different functional groups, the identification of unidentified compounds, and the amount of constituents present in a given sample can all be determined using FTIR spectroscopy. FTIR can be used in catalysis to identify different species adsorbed at the catalytic surfaces, the existence of an adsorbed water molecule at the catalytic surface, and the identification of a metal interacting with a hetero atom.⁽⁷⁾ The majority of metal oxides only absorb light with low energy (below 1000 cm^{-1}) in the IR spectrum. Utilizing FTIR spectroscopy, the metal oxide's production was identified. The analysis was done on a Shimadzu FTIR-8201 PC spectrophotometer as shown in **Fig.2.4**, the spectra were captured in the $400\text{--}4000\text{ cm}^{-1}$ wavenumber range. In DRIFT mode, the materials were transformed into KBr pellets (1 weight percent) or as such. Generally speaking, neat KBr was utilized as a reference.



Fig. 2.4 Shimadzu FTIR-8201 PC spectrophotometer

2.4.4.1 Pyridine FTIR technique:

The most popular method for identifying the type of acidic sites on the catalytic surface is pyridine FT-IR. These locations could be Lewis, Bronsted, or both. The region of the spectrum between $1400\text{--}1700\text{ cm}^{-1}$ is examined for the pyridine FTIR study. The pyridine that is co-ordinately bound to the surface has a distinct spectrum than the pyridinium ion. This enables the acidic type to be distinguished on the surface of the acidic solids. Although

Chapter 2

pyridine is a relatively strong base, it is substantially weaker than ammonia and does not react with some of the weaker acidic sites that would react with ammonia because NH_3 is a strong base ($\text{p}K_b = 5$), which allows it to react with extremely weak acid sites.

Pyridine is thus employed to identify acidic regions on the catalytic surface. A band at 1540 cm^{-1} is produced by the pyridinium ion but is not present in pyridine or co-ordinated pyridine ($\text{Py} \rightarrow \text{BH}_3$). The co-ordinately and hydrogen-bonded pyridine exhibit a distinctive band in the range of 1440 and 1465 cm^{-1} . Thus, the Lewis acidic peak is found at 1450 cm^{-1} , while the Brønsted acidic peak exhibits a distinctive band at 1540 cm^{-1} . Using the ex-situ Pyridine adsorption FTIR method, different mixed metal oxide catalysts with both Brønsted and Lewis acidic sites were examined. The catalytic samples were stored overnight in a desiccator containing pyridine after being dried at $100\text{ }^\circ\text{C}$ for 2 hours. Pyridine was permitted to adsorb on the catalyst's surface.

2.4.4.2 MeOH FTIR technique:

The MeOH FTIR spectroscopy approach is a crucial tool for identifying the fundamental sites that are present at the catalytic surface. The catalytic surfaces may contain Lewis, Brønsted, or both Lewis and Brønsted basic sites. The in-situ FT-IR spectra that were created by subtraction of pristine metal oxide and adsorbed MeOH on metal oxide spectra. By using in-situ methanol adsorption-IR spectroscopy, Brønsted basicity was investigated. In the past, Verneker et al. used MeOH adsorption IR spectroscopy to investigate different interactions of $\text{FeO}(\text{OH})$ at the surface. According to their findings, MeOH interacts with the catalytic surface's basic sites to produce monodentate and bidentate methoxy species as well as molecularly adsorbed species, with bands seen at 1115 cm^{-1} , 1092 cm^{-1} , and 1064 cm^{-1} .

The surface of the basic metal oxide catalysts was investigated in order to form H-bonded molecularly adsorbed MeOH, which showed the presence of a band at 1064 cm^{-1} . As opposed to this, the bands at 1115 cm^{-1} and 1092 cm^{-1} showed the emergence of monodentate and bidentate methoxy species as well as metal complexed methoxy species. The fundamental metal oxide catalysts used to study NAG dehydration showed all of these bands.

2.4.5. Inductively coupled plasma atomic emission spectroscopy (ICP-AES)

The analytical method known as inductively coupled plasma atomic emission spectroscopy (ICP-AES) is used to find trace metals. It is a sort of emission spectroscopy that creates

Chapter 2

excited atoms and ions using an inductively coupled plasma that emits electromagnetic radiation at wavelengths specific to a given element. The concentration of the element in the sample can be determined by the intensity of this emission.

2.4.6 X-ray photoelectron Spectroscopy

XPS, often referred to as electron spectroscopy for chemical analysis (ESCA), is based on the observation of the photoelectric effect. X-rays are used to bombard the sample surface, and the resulting photoemitted electrons are then measured. The emitting atoms' and their bonding states' distinctive kinetic energies are present in the photo-emitted electrons. These changes in the core level energies provide in-depth details about the elemental composition of the surface, the oxidation states of the elements, empirical formula, electronic states, and chemical analysis of the samples that are present at the catalytic surface in concentrations greater than 1 atomic percent to be studied. The elemental stoichiometry of the near surface region can be determined using this quantitative spectroscopic method, which is which is often different from the bulk composition. ^(8,9)

Because the catalytic activity in heterogeneous catalysis depends on the surface composition and electronic characteristics, XPS is one of the most well-liked and often used analytical tools. XPS calculates the photoelectron's intensity as a function of kinetic energy. The input photon flux, its photoionization cross-section, the sample concentration, the mean free path of the emitted photoelectron, and experimental parameters like photoelectron collection and detection efficiency all play a significant role in determining the strength of the XPS peak.

The energy of the X-ray radiation, $h\nu$, determines the kinetic energy of these photoelectron, and the electron binding energy is dictated by,

$$E_K = h\nu - E_b \dots\dots\dots (2c.)$$

Whereas, the experimentally measured energy is given by

$$E_K = h\nu - E_b - \psi \dots\dots\dots (2d.)$$

Where, E_K is the kinetic energy of the photoelectron

h is the Plank's constant and ν is the frequency of the excited electron

E_b is the binding energy of the photoelectron with respect to the Fermi level

Ψ is the work function of the spectrometer

Chapter 2

As a function of their kinetic energy, XPS calculates the photoelectrons' intensity. The chemical state of the emitting electron can change the binding energy and the peak's form. As a result, XPS offers details on chemical bonding, identifying constituents both inside the material and on its surface, electronic structure, and the density of the electronic state inside the material. The oxidation state of the active catalyst, the interaction of the metal with the support, variations in the oxidation state of the catalyst during the course of the reaction, and the presence of surface contaminants can all be determined using XPS.⁽¹⁰⁾ The XPS data of various catalysts were collected on a VG Microtech Multilab ESCA 3000 spectrometer using a non-monochromatized MgK α (1253.6 eV) X-ray source at a pressure of 1×10^{-9} Torr (50 eV of pass energy and 55° was the take-off angle) with resolution of 0.7 eV determined from the full width at half maxima of the 4f 7/2 core level of the gold surface as shown in **Fig. 2.5**. The binding energy values had an inaccuracy of less than 0.1 eV. The carbon C1s signal at 284.6 eV was used to accomplish the binding energy correction.



Fig. 2.5 VG Microtech Multilab ESCA 3000 XPS spectrometer

2.4.7 Raman Spectroscopy

Dr. C. V. Ramana made the discovery of Raman spectroscopy in 1928. It is a spectroscopic method for observing a substance's vibrational, rotational, and translational frequency. The species in the catalytic sample scatter a portion of the radiation when it travels through a clear medium in all directions. The alteration in the vibration linked to the IR spectrum causes

Chapter 2

Raman scattering. The scattering of the radiation is the fundamental idea at the heart of Raman spectroscopy. The majority of radiation is elastically scattered after irradiation, a process known as Rayleigh scattering. A minor percentage, however, exhibits inelastically scattered Raman scattering, which contains Stokes and anti-Stokes lines. The scattering that takes place reveals details of the molecular structure. The bands in the Raman spectra that are more prominent are those that result from bonds that are highly polarizable because pi-electrons are present. ⁽¹¹⁻¹²⁾

Raman spectroscopy is based on the inelastic scattering of the photons, which loses energy by the exciting vibrations in the sample, Raman spectroscopy is used for the characterization of the catalytic material to find out the crystallographic orientations of the sample and the chemical structure of the molecule. One of the most important properties required for a molecule to be Raman active is the polarizability of the electron density.

It is used for the detailed analysis of the surface metal oxides species on a typical oxide material as a support as in case of the mixed metal oxide catalysts. It permits evaluation of the molecular vibrations below 1100 cm^{-1} . ⁽¹³⁻¹⁴⁾ The radial breathing mode is commonly used technique for the analysis and determination of the diameter of the sample and to analyze the structure of the material. The Raman samples were recorded on the Horiba JY LabRam HR-800 micro-Raman spectrometer with 17 mW 632.8 nm laser excitation as shown below in **Fig. 2.6**.

The Raman spectroscopic technique was used to analyze the catalytic samples containing bi-functional character i.e. both Lewis and Brønsted acidic as well as basic sites at the catalytic surface. The detailed Raman analysis of the mixed metal oxide catalyst revealed the effect of doping of the metal on another metal on the structural properties of the MMO. It also gave information about the formation of a particular phase which was further confirmed by the XRD analysis.

Chapter 2



Fig. 2.6 Horiba JY Lab Ram HR-800 micro-Raman spectrometer

2.4.8 Transmission Electron Microscopy

Microscopy is the study of small objects with the use of a microscope that are beyond the resolution range of a normal eye. Microscopy can be divided into three categories: optical microscopy, electron microscopy, and scanning probe microscopy. It was discovered in 1940 that interaction between electrons and atoms may alter an electron wave's phase and enable the use of phase contrast to observe a single atom. High-resolution transmission electron microscopy (HR-TEM) has this as its theoretical foundation. For morphological and compositional investigation, thin films of solid samples are imaged in high resolution using TEM analysis. The electron source/gun and a collection of electromagnetic lenses are the two most crucial parts of an electron microscope. ⁽¹⁸⁻¹⁹⁾

It is predicated on the idea that an electron beam scatters when it travels through a thin film of test material. Depending on the mode of operation, these scattered electrons are focused into an image or a diffraction pattern by the electromagnetic lenses. The TEM instruments operate under circumstances that include 100–200 KeV electrons, 10–6 mbar vacuum, 0.5 nm resolution, and 105 times magnification. For structural characterization and phase identification of the various phases present in the catalytic material, the morphological information obtained by the TEM in the area of the atomic resolution can be used. The samples were subjected to TEM examination using a JEOL-1200 EX apparatus as shown in **Fig. 2.7** running at 100 KV. The JEOL 1200 EX model was used for the HR-TEM analysis **Fig. 2.8**, represents the TEM instrument, which revealed details on the morphology, particle

Chapter 2

size, d-spacing, and fringe width. The powdered samples were dissolved in iso-propanol and sonicated for 15 minutes before to analysis. Drops of the suspension were then applied to a dried, room-temperature copper grid that had been coated with carbon. The samples are characterised in detail, and images at various magnifications are provided in the respective chapters.



Fig. 2.7 JEOL-1200 EX TEM apparatus



Fig. 2.8 JEOL 1200 EX HR-TEM instrument

Chapter 2

2.4.9 Field Emission-Scanning Electron Microscopy

The scanning electron microscope is a type of microscope that scans the sample with a focused electron beam to obtain images of the material. These electrons interact with the sample's atoms to produce a variety of signals that provide details about the sample's surface topography and chemical makeup. The tungsten filament or a field emission gun generates the electron beam, according to the fundamental theory. High voltage accelerates this electron beam, creating a thin beam of electrons. The specimen surface is scanned by this electron beam. As a result, the sample's surface emits electrons, which the detector then collects after scanning. This method can be applied to the characterization of catalytic samples and various organic and inorganic materials. It can be used to ascertain the given sample's topography, morphology, surface composition, particle size, d-spacing, and elemental composition. ⁽¹⁵⁻¹⁷⁾

As shown in the **Fig. 2.9**, the SEM-EDAX analysis was carried out in order to study the morphology and elemental composition of the catalysts on a LEO–LEICA STEREOSCAN 440 instrument. Prior to the analysis the powdered samples were dispersed in iso-propanol and sonicated for 15 minutes. Then drops of the suspension were deposited on a carbon-coated copper grid and dried, at room temperature before analysis.



Fig. 2.9 LEO–LEICA STEREOSCAN 440 FE-SEM instrument.

2.4.10 Thermal analysis:

A collection of procedures known as thermal analysis examines how the properties of a sample change when it is subjected to a controlled temperature change. The most often

Chapter 2

employed thermal procedures include differential thermogravimetric analysis (DTGA), thermogravimetric analysis (DTA), and thermogravimetric analysis (TGA), among others. These methods investigate the thermal behavior of a catalyst while it is heated continuously. In the TGA and DTGA methods, the sample is heated at a constant rate while the variation of the sample mass time (dm or dm/dt) is measured as a function of temperature. The Simultaneous Thermal Analyzer SDT-650 equipment was used to perform the TGA analysis of the catalyst. The analysis was performed at a 40 mLmin^{-1} air flow rate at a heating rate of $10 \text{ }^\circ\text{C min}^{-1}$ from room temperature to $800 \text{ }^\circ\text{C}$.⁽²⁶⁾

2.5 Catalyst activity measurement

2.5.1 Round bottom flask reflux reaction set-up for glucose isomerization

In a 50 mL round bottom flask equipped with a condenser, 1 mmol of glucose (180 mg) in 6 mL DI water and catalyst (100 mg) was refluxed under constant stirring for 6 h. The reaction mixture was allowed to cool at room temperature and the catalyst was separated by filtration. The filtrate was collected and the initial (0 h), intermediate (3 h) and final (6 h) samples were prepared to carry out the analysis on HPLC.

2.5.2 Parr reactor set-up for NAG conversion

The reaction was carried out in a parr reactor equipped with a heating arrangement, stirrer, thermos well, gas inlet and outlet, liquid sampling valve, safety rupture disc, pressure gauge, transducer for digital pressure display and controller to control the temperature and RPM and high temperature cut-off module as shown below in the Fig. 2.11. In a 50 mL Parr reactor, N-Acetyl-glucosamine (1 gm), dioxane (25 mL) and catalyst (200 mg) were heated at $180 \text{ }^\circ\text{C}$ under constant stirring for 4 h. After the reaction was complete, the reaction mixture was filtered and the filtrate was concentrated on Buchi Rotavap at 140 mbar and $60 \text{ }^\circ\text{C}$.

Yellowish-red viscous liquid was obtained from which product was separated by solvent extraction using ethyl acetate and water. The humins were separated in water layer whereas the product was extracted in the ethyl acetate layer. The crude product thus obtained was then purified by silica gel column chromatography.

Chapter 2

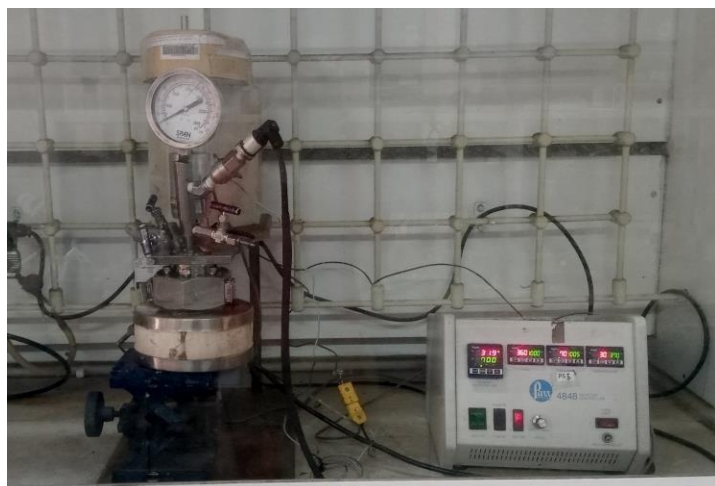


Fig. 2.10 Parr reactor set-up for NAG conversion

2.5.2 Parr reactor set-up for glycerol transesterification

The reaction was carried out in a parr reactor equipped with a heating arrangement, stirrer, thermos well, gas inlet and outlet, liquid sampling valve, safety rupture disc, pressure gauge, transducer for digital pressure display and controller to control the temperature and RPM and high temperature cut-off module. In a 50 mL parr autoclave assembly glycerol and dimethyl carbonate in 1:3 molar ratio charged along with 20 mL of methanol. Catalyst of 100 mg was also added and reaction was carried out at 140 °C for 90 min with 1000 rpm stirring. Product mixture was filtered to separate catalyst and sample from mother liquor was injected to GC for analysis.

2.6 Analytical methods for quantitative analysis

In chromatography, the components of the sample mixture are separated as a result of their differing distributions between the stationary phase and the mobile phase, two immiscible phases. A column containing a distributed stationary phase is transported alongside the sample component introduced in a mobile phase. The species in the sample interact repeatedly with both the mobile and stationary phases. Compared to those that are distributed selectively in the mobile phase, components that bind tightly to the stationary phase are kept in the system for a longer period of time. The sample component is split in the form of bands as the mobile phase is passed through the stationary phase, which can be accomplished by choosing both the phases.

The sample component is split in the form of bands as the mobile phase is passed through the stationary phase, which can be accomplished by choosing both the phases and the phases

Chapter 2

themselves. The number of theoretical plates, which is dependent on the column height, the polarity of the solvent system used as the mobile phase, and the mesh size of the silica/alumina used as the stationary phase are some of the elements that affect separation. Because of this, solutes are extracted from the mixture in the mobile phase in the order of increasing distribution coefficients relative to the stationary phase. The weakly bound component is eluted first, followed by the highly bound component. Depending upon the mobile phase the chromatography technique is divided into two types

1. Liquid Chromatography
2. Gas Chromatography

2.6.1 Gas Chromatography

The first liquid-gas chromatography was created in 1950 by John Porter Martin, a Nobel Prize recipient and the inventor of modern gas chromatography. In gas chromatography, an inert gas such as helium, hydrogen, or nitrogen is utilized as the mobile phase. The samples that will be tested must be volatile and thermally stable, which is one of the most crucial requirements. The table below outlines the stationary phase's specifics as well as the required operating conditions. ⁽²⁰⁻²²⁾

Below is a detailed explanation of the analysis's methodology.

1. GC: Shimadzu 2025
2. Column: HP FFAP (Free fatty acid phase column)
3. Column details: 30m length × 0.53 mm ID × 1µm film thickness
4. Column stationary phase: Polyethylene glycol
5. Carrier gas: He
6. Detector: FID
7. Injector temperature: 300 °C
8. Detector temperature: 300 °C
9. Total run time: 15 min
10. Injection volume: 1 µL

Chapter 2

11. Oven temperature programme: Temp: 60, 220 °C, Ramp: 20 °C/min, hold time 1, 5 min

2.6.2 High Performance Liquid Chromatography

The liquid product was separated by syringe filtration and the resulting product was analyzed by HPLC (Agilent 1260) equipped with Hipler-Ca column (300 mm length) connected to Refractive Index detector. The quantification was carried out on the basis of external standard solution of sugars (glucose, fructose and mannose).

The glucose conversion was analyzed by HPLC (Agilent 1260) equipped with Phenominex-Ca⁺² column (300 mm length) equipped with refractive index detector. Deionized water was used as a mobile phase, which was filtered and then subjected degassing. The HPLC analysis was carried out by keeping 0.6 mL/min flow rate of prepared mobile phase keeping column temperature at 80 °C and total analysis time of 18 minutes.

The NAG conversion was analyzed by HPLC (Agilent 1260) equipped with Hipler-Pb column (300 mm length) equipped with refractive index detector. Deionized water (DI) was used as a mobile phase, which was filtered and used. The NAG conversion was quantitatively determined by HPLC analysis by keeping 0.5 mL/min flow rate of the prepared mobile phase maintaining column temperature at 80 °C and total analysis time of 20 minutes. ⁽²³⁻²⁵⁾

2.7 Catalyst activity performance:

A catalyst is a substance that can fasten the rate of reaction without getting consumed in the reaction and thereby lowering the energy of activation to form the desired products. Almost, 80 % of the products are produced commercially by employing the use of heterogeneous catalysts. It neither changes the spontaneity nor changes the chemical equilibrium of the chemical reaction. Catalysts work by changing the path of the reaction and accelerating the rate of the reaction to yield the desired products selectively. Catalysis is a surface phenomenon in which the reactants get sorbed at the catalytic surface (Physisorption/ Chemisorption). Industrially catalysts play a very important role in increasing the actual yield of the desired product thereby driving the chemical reaction towards the selective formation of the desired product. The effectiveness, stability and the efficiency of the catalyst can be determined by the calculating the Turn over number and turn over frequency as given below.

Chapter 2

2.7.1 Turn over number (TON):

Turn over frequency can be used to determine the catalyst's effectiveness and efficiency. It is the ratio of reactant to catalyst moles per unit time.

2.7.2 Turn over Frequency (TOF):

The turn over frequency can be used to determine the stability of the catalyst. It is the ratio of the moles of reactant reacted per moles of the catalyst.

2.7.3 Formulae

$$1. R_f = \frac{\text{concentration in moles}}{\text{area under the peak}}$$

$$2. \% \text{ Conversion} = \frac{\text{initial moles of substrate} - \text{final moles of substrate}}{\text{initial moles of substrate}} \times 100$$

$$3. \% \text{ Selectivity} = \frac{\text{moles of product formed}}{\text{moles of substrate consumed}} \times 100$$

$$4. \text{ Turn over number (TON)} = \frac{\text{moles of substrate consumed}}{\text{catalytic active sites of catalyst in moles}}$$

$$5. \text{ Turn over frequency (TOF)} = \frac{\text{moles of substrate consumed}}{\text{catalytic active sites of catalyst in moles} \times \text{reaction time (h)}}$$

Chapter 2

References:

1. Zhao D, Feng J, Huo Q, Melosh N, Fredrickson GH, Chmelka BF, Stucky GD. Triblock copolymer syntheses of mesoporous silica with periodic 50 to 300 angstrom pores. *science*. 1998 Jan 23;279(5350):548-52.
2. Wang J, Zhu HO. Alkylation of 1-dodecene with benzene over H₃PW₁₂O₄₀ supported on mesoporous silica SBA-15. *Catalysis letters*. 2004 Mar; 93:209-12.
3. Chauhan A, Chauhan P. Powder XRD technique and its applications in science and technology. *J Anal Bio anal Tech*. 2014 Sep 1;5(5):1-5.
4. Epp J. X-ray diffraction (XRD) techniques for materials characterization. In *Materials characterization using non-destructive evaluation (NDE) methods* 2016 Jan 1 (pp. 81-124). Woodhead Publishing.
5. Brunauer S, Emmett PH, Teller E. Adsorption of gases in multimolecular layers. *Journal of the American chemical society*. 1938 Feb;60(2):309-19.
6. Sing KS. Adsorption methods for the characterization of porous materials. *Advances in colloid and interface science*. 1998 Jul 1; 76:3-11.
7. Zaera F. New advances in the use of infrared absorption spectroscopy for the characterization of heterogeneous catalytic reactions. *Chemical Society Reviews*. 2014;43(22):7624-63.
8. Freund HJ. PK Ghosh: *Introduction to Photoelectron Spectroscopy*, Vol. 67 aus: *Chemical Analysis: A Series of Monographs on Analytical Chemistry and its Applications*, John Wiley Sons Ltd., New York, Chichester, Brisbane, Toronto, Singapore 1983. 377 Seiten, Preis: £ 52.25.
9. Siegbahn KM. A discussion on photoelectron spectroscopy-electron spectroscopy for chemical analysis (ESCA). *Philosophical Transactions of the Royal Society of London. Series A, Mathematical and Physical Sciences*. 1970 Nov 5;268(1184):33-57.
10. Watts JF. X-ray photoelectron spectroscopy. *Surface science techniques*. 1994;45(5).
11. Ferraro JR. *Introductory raman spectroscopy*. Elsevier; 2003 Jan 13.
12. Laserna JJ, editor. *Modern techniques in Raman spectroscopy*. New York: Wiley; 1996 Sep 10.
13. Stavitski E, Weckhuysen BM. Infrared and Raman imaging of heterogeneous catalysts. *Chemical Society Reviews*. 2010;39(12):4615-25.

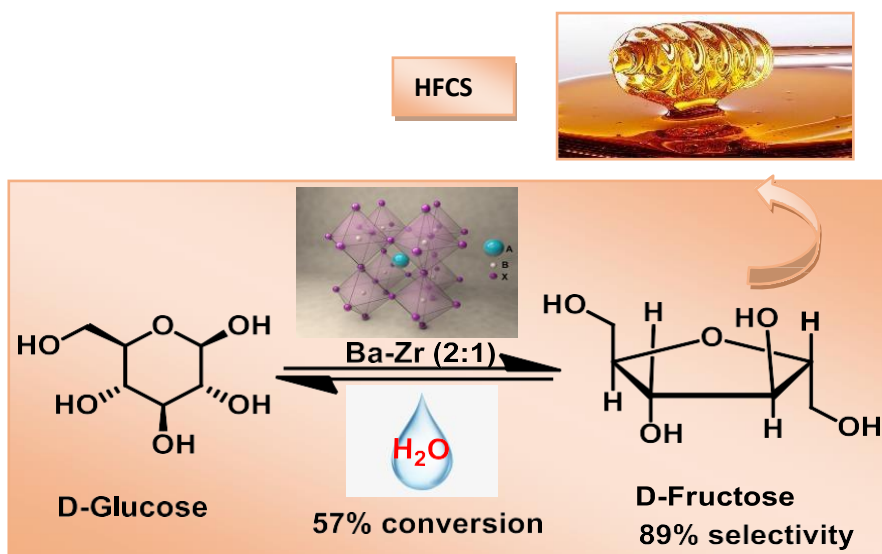
Chapter 2

14. Hess C. New advances in using Raman spectroscopy for the characterization of catalysts and catalytic reactions. *Chemical Society Reviews*. 2021;50(5):3519-64.
15. Uyeda N, Kobayashi T, Suito E, Harada Y, Watanabe M. Molecular image resolution in electron microscopy. *Journal of Applied Physics*. 1972 Dec;43(12):5181-9.
16. Lawes, Grahame. "Scanning electron microscopy and X-ray microanalysis." (1987).
17. Bell DC, Garratt-Reed AJ. Energy dispersive X-ray analysis in the electron microscope. Garland Science; 2003 Jul 10.
18. Fryer JR. The chemical applications of transmission electron microscopy. University of Glasgow (United Kingdom); 1983.
19. Imeson D. Studies of supported metal catalysts using high resolution secondary electron imaging in a STEM. *Journal of Microscopy*. 1987 Jul;147(1):65-74.
20. Scott RP. Introduction to analytical gas chromatography, revised and expanded. CRC press; 1997 Nov 24.
21. Scott RP. Techniques and practice of chromatography. CRC Press; 1995 Apr 18.
22. Niessen WM, editor. Current practice of gas chromatography-mass spectrometry. CRC Press; 2001 Apr 4.
23. Horváth C, editor. High-performance liquid chromatography: advances and perspectives.
24. Hamilton RJ, Sewell PA. Introduction to high performance liquid chromatography. Springer Netherlands; 1982.
25. Meyer VR. Practical high-performance liquid chromatography. John Wiley & Sons; 2013 Mar 25.
26. Prime RB, Bair HE, Vyazovkin S, Gallagher PK, Riga A. Thermogravimetric analysis (TGA). *Thermal analysis of polymers: Fundamentals and applications*. 2009 Apr 1:241-317.

Cooperative acid-base sites of solid Ba-Zr mixed oxide catalyst for efficient isomerization of glucose to fructose in aqueous medium

Abstract

Efficient and highly selective isomerization of glucose to fructose was achieved by using the inexpensive Ba-Zr mixed metal oxide catalyst. Catalyst was prepared by varying Ba-Zr ratios using co-precipitation method. Various phases formed, planes exposed, morphology, elemental composition and particle size, basic site density and strength, oxidation state of elements were well studied by using various characterization techniques. XRD analysis clearly indicates the presence of Ba^{+2} and Zr^{+4} in the form of BaO , ZrO_2 and BaZrO_3 phases. SEM and HR-TEM images indicate that, Ba-Zr (2:1) catalyst prepared showed uniform morphology with spherical and rod-shaped particles with sizes ranging from 300 to 600 nm. Under the optimized reaction conditions, Ba-Zr (2:1) catalyst exhibited excellent results in terms of 57 % of glucose conversion with 89 % selective formation of fructose. The presence of both acidic as well as basic sites play vital roles in activating the substrate molecules to yield fructose selectively. Ba-Zr (2:1) catalyst showed excellent recyclability performance up to four recycles.



Publication: Shaikh S. S, Patil C. R, Kondawar S. E, Rode C. V. Cooperative Acid-Base Sites of Solid Ba-Zr Mixed Oxide Catalyst for Efficient Isomerization of Glucose to Fructose in Aqueous Medium. *ChemistrySelect*. 2020 Oct 29; 5(40): 12505-13.

3.1 Introduction

Today the world has become completely dependent on the fossil fuels for energy consumption in several ways and its rapid depletion has led to alarming situations such as global warming, energy and food crises. ⁽¹⁾ Thus, this problem could be solved by developing an alternative renewable cost-effective biomass conversion route for the production of various value-added products such as commodity chemicals, fuel additives, pharmaceuticals etc.

In recent years, glucose to fructose isomerization has gained tremendous importance in food and beverage industry, as fructose is sweeter than glucose. Fructose is not only used for the production of High Fructose Corn Syrup (HFCS), where it is used as a sweetener but also in the production of various platform molecules, fuel additives and value-added chemicals like 5-hydroxymethylfurfural, 2, 5-furandicarboxylic acid,⁽²⁻⁵⁾ levulinic acid and its esters, lactic acid, alkoxy fructoside, 5-alkoxymethylfructoside.⁽⁶⁻¹²⁾ Lobry-de-Bryun-Van-Ekenstein (LBAE), first reported aldose to ketose isomerization in both acidic as well as basic medium, where formation of ene-diol as an intermediate i.e. proton transfer mechanism yields a mixture of glucose, fructose and mannose, which is a well-accepted mechanism.⁽¹³⁾ This pioneering discovery enhanced the large scale glucose to fructose isomerization at industrial level. The glucose isomerization is carried out commercially by bio-catalytic pathway, which employs glucose isomerase/ xylose isomerase enzyme (GI).⁽⁹⁾ But thermal and chemical deactivation of the enzyme, narrow pH range, low operating temperature and presence of Ca^{+2} hinders the activity of GI thus making the process less economical.⁽¹⁴⁾ Industrial chemical isomerization of glucose involves the homogenous process using mineral acid or alkali, which suffers from several drawbacks such as low fructose yield, slow rate of reaction, formation of large amount of

byproducts due to side reactions such as aldolization/ retro aldolization, β -elimination and benzilic rearrangement reactions that take place simultaneously along with isomerization and post synthesis neutralization step.^(15, 16) Various bases such as sodium hydroxide, sodium carbonate, calcium hydroxide, magnesium hydroxide, trisodium phosphate, and sodium sulphite, basic ion- exchange resins and derivatives of ammonia have been reported for the conversion of glucose to fructose but with low fructose yields (20-30 %), due to side reactions that lead to the formation of colored substances, organic acids, saccharinic acid and other undesired products.^(17, 18) Liu *et al.* reported glucose to fructose isomerization by using organic amines such as triethyl amine in water at 100 °C, to give 57 % glucose conversion with 54 % and 31 % fructose selectivity and yield, respectively. The mixture of glucose, fructose and triethyl amine was further separated by chromatography.⁽¹⁹⁾ Rendleman *et al.* reported maximum yield of fructose (72 %) by using aluminate resin containing hydroxide group⁽²⁰⁾ with 68 % glucose conversion and 72 % fructose selectivity.⁽²¹⁾ Among solid catalysts, magnesium-Aluminum hydrotalcites have been also reported to catalyze the glucose isomerization to fructose with 30 % fructose yield, whereas Yabushita *et al.* reported 56 % fructose yield with 80 % fructose selectivity in ethanol as a solvent. The gradual decrease in the catalytic activity could be restored by calcination and rehydration of the hydrotalcites.^(22, 23) The use of MgO as a catalyst has been reported by Marianou *et al.* to afford 44 % fructose yield with 75 % fructose selectivity, which has been attributed to the basicity of the catalyst.⁽²⁴⁾ Glucose to fructose isomerization has been also carried out in the presence of Lewis acids such as AlCl_3 , FeCl_3 but the major drawback is the deactivation of the catalyst in aqueous media, which requires maintenance of anhydrous conditions.⁽²⁵⁾ Lewis acids such as CrCl_3 has been also reported for glucose isomerization in which $[\text{Cr}(\text{H}_2\text{O})_5\text{OH}]^{+2}$ complex acts as active species for catalyzing the isomerization *via* de-

protonation, hydride shift and proton donation to sugar.⁽²⁶⁾ The heterogeneous catalyst Sn- β zeolite, in which tin metal acts as Lewis acid has been reported to show 31 % fructose yield.⁽²⁷⁾ Thus isomerization of glucose to fructose has been reported to be carried out in the presence of either acidic or basic catalytic system. In the present work for the first time, we report mixed metal oxides of Ba and Zr as an acid-base heterogeneous catalyst for selective glucose isomerization to fructose. There are various methods reported for the synthesis of nano structured BaZrO₃ which involve sol-gel,^(29, 30) co-precipitation,⁽³¹⁾ thermal decomposition⁽³²⁾ and hydrothermal techniques.⁽³³⁾ Urea-induced precipitation followed by a low-temperature thermal treatment was also reported for the synthesis of nano scale BaZrO₃.⁽³⁴⁾ The present research is focused on co-precipitation method for the size and shape controlled synthesis of BaZrO₃ particles which catalyzed the glucose isomerization. Our Ba-Zr catalyst exhibited both Lewis acidic as well as basic sites which play an important role in glucose to fructose isomerization to give the highest selectivity of 89 % towards fructose. Detail studies on the catalyst characterization by XRD, TEM, SEM, NH₃ and CO₂-TPD and FT-IR, along with effect of reaction parameters on glucose conversion and selectivity for fructose have been also carried out.

3.2 Experimental

Typical co-precipitation method was used to synthesize nano-size Ba-Zr mixed metal oxide (MMO) catalyst under alkaline conditions and their detail experimental procedure is discussed in Chapter 2 (Section 2.3.1). The prepared catalysts were characterized by XRD, BET-surface area, NH₃-TPD, HR-TEM, SEM-EDX, FT-IR, Py-IR, Raman and XPS techniques as mentioned in Chapter 2 (sections 2.4.1 -2.4.4, 2.4.6, 2.4.10 and 2.4.13, respectively). The Catalyst activity testing was done in a 50 mL round bottom flask equipped with a condenser as mentioned in the chapter 2 (section 2.5.1). The liquid product was separated by syringe filtration and the resulting product was analyzed by HPLC (chapter 2, section 2.6.2) in order to monitor the progress of the

reaction. At the end of reaction, the catalyst was recovered by filtration and washed three times with 10 mL DI water, then dried at 120 °C overnight in a vacuum oven followed by calcination at 550 °C for 3 h and reused.

3.3 Results and discussion

3.3.1 Catalyst characterization

3.3.1.1 XRD analysis

Fig. 3.1 shows the powder XRD patterns for both single components (Ba and Zr) and mixed metal oxides prepared by varying Ba-Zr ratio. The wide angle XRD patterns for ZrO₂ samples showed the reflections at $2\theta = 23.7^\circ, 55.8^\circ$ ascribed to ZrO₂ phase [JCPDS # 86-1451] whereas, reflections at $2\theta = 19.6^\circ, 23.7^\circ, 45.1^\circ$ confirmed the presence of BaO phase [JCPDS # 47-1488]. However, in case of MMO samples, intensities of ZrO₂ peaks were found to be weakened with the doping of Ba in the zirconium lattice, which clearly suggests there might be deformation of the crystal structure of ZrO₂. This was further supported by appearance of new reflections other than BaO, ZrO₂ phases at $2\theta = 23.7^\circ, 27.7^\circ, 34.1^\circ, 39.5^\circ, 41.9^\circ$ corresponding to (211), (220), (222), (330) and (400) planes, respectively, which indicated the presence of perovskite type cubic phase of BaZrO₃ [JCPDS # 01-0890].⁽³⁵⁾ It is well reported that during calcination process, the barium present at the surface reacted with zirconia to form BaZrO₃ phase. All the peaks can be indexed to the cubic phase of BaZrO₃ (**Fig. 3.1**). The crystallite size of BaZrO₃ phase calculated for Ba-Zr (2:1) catalyst by Scherrer equation was found to be 29.35 nm. Moreover, in case Ba-Zr (2:1) catalyst, it was observed that all the phases including BaO (49.5 nm), ZrO₂ (44.2 nm) and BaZrO₃ found to be having lowest crystallite size as compared to all the other catalysts studied in this work. This might be the reason for its better performance (**Table 3.1 b**). The morphologies of various Ba-Zr MMO samples were studied by SEM analysis.

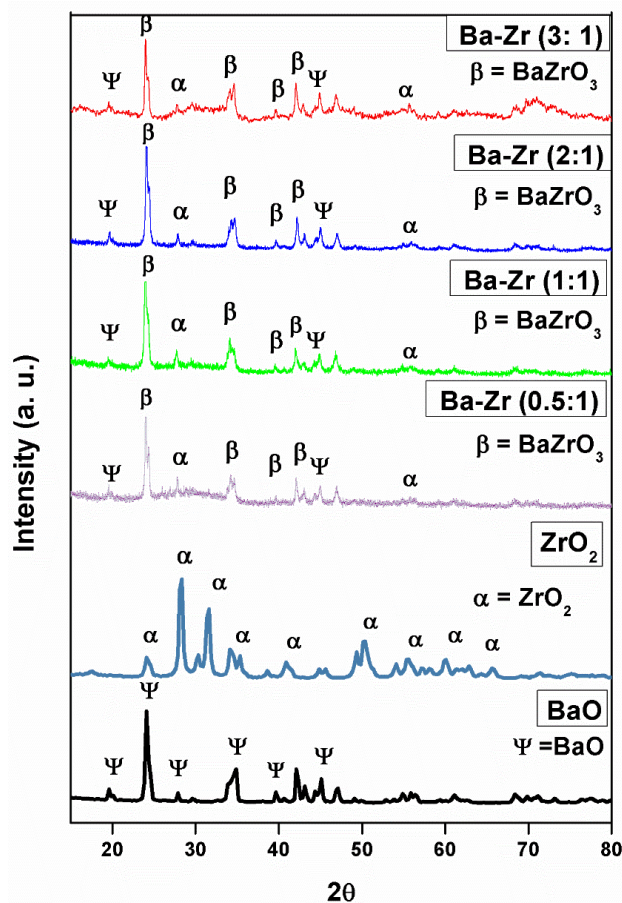


Fig. 3.1 Powder XRD pattern for calcined BaO, ZrO₂, and Ba-Zr mixed metal oxide catalysts

3.3.1.2 SEM and EDX analysis

Fig. 3.2 displays the SEM images for BaO and Ba-Zr MMO catalysts. In case of bare BaO, mixed morphology of rod and sphere was observed with predominant presence of rod-shaped particles as encircled in **Fig 3.2 a**. The introduction of Zr in MMO clearly showed that there was a growth of small particles on the surface which might be due to the formation of BaZrO₃ perovskite type cubic phase or ZrO₂ phase, presence of which has already been revealed by XRD. The Ba-Zr MMO samples showed the presence of mixed morphology with spherical deposits on rod shape particles (**Fig.s 3.2 b-e**). Interestingly, as Ba concentration was increased in Ba-Zr MMO (for ratios of 0.5:1 and 1:1), rod shape morphology started appearing. The size of the rod shape particles was found to be in the range 250-300 nm for Ba-Zr (1:1) (**Fig. 3.1 b**),

which increased to about 250-550 nm in case of Ba-Zr (2:1) (**Fig. 3.1 c**), which was the best catalyst. The size of the spherical particles was found to be in the range 220-450 nm while, the length of the rod was found to be in the range 1-2.8 μm . The EDX measurement of the optimized Ba-Zr (2:1) catalyst confirmed the presence of Ba, Zr and O having the composition as 54 %, 24 %, and 21 % by weight; respectively.

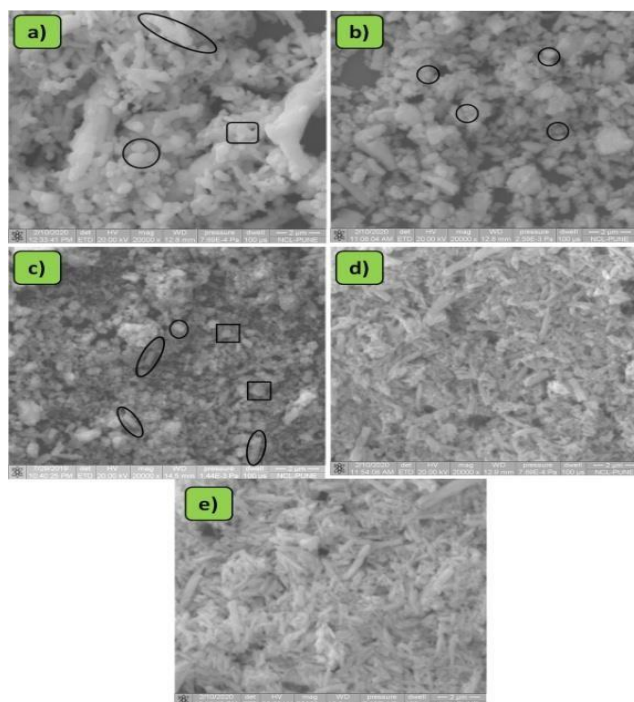


Fig. 3.2 Scanning Electron Micrographs for a) BaO, b) Ba-Zr (0.5:1), c) Ba-Zr (1:1), d) Ba-Zr (2:1) and e) Ba-Zr (3:1) catalysts.

3.3.1.3 TEM analysis

Fig. 3.3 (A-C) shows TEM images of Ba-Zr (2:1) catalyst which clearly exhibited cubic morphology of a typical individual particle. The d-spacing of the observed lattice fringes was 0.27 nm, which can be associated with the [110] plane of the cubic phase of BaZrO_3 . The spacings of the observed lattice fringes are 0.27 and 0.36 nm, respectively, and have been correspondingly indexed to the [110] and [100] planes of the cubic phase of BaZrO_3 . The SAED

pattern for Ba-Zr (2:1) catalyst in **Fig. 3 (D)** with spacing of lattice fringes of 0.30 nm shows the cubic phase of BaZrO₃ which could be indexed to the [110] planes, and was in good agreement with the XRD (confirm this) result. ⁽³⁶⁾

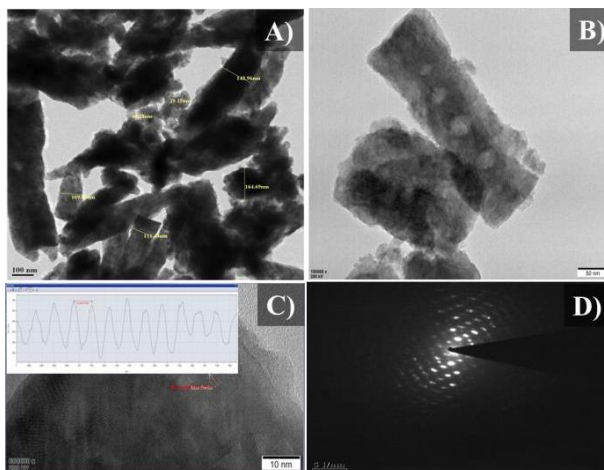


Fig. 3.3 (A-C) Transmission Electron Micrographs and **D)** SAED pattern for Ba-Zr (2:1) catalyst

3.3.1.4 BET and surface area analysis

Table 3.1 reveals the physico-chemical properties of the prepared catalysts. The specific surface areas of Ba-Zr catalysts were found in the range of 11-24 m²g⁻¹. Ba-Zr (2:1) catalyst showed 11.50 m²g⁻¹ surface area which was the lowest among all the studied catalysts. The basic property of the Ba-Zr mixed metal oxide catalysts was evaluated by CO₂-TPD measurement since it is known that the catalysts with the strong basic sites promote the glucose isomerization.

Table 3.1 shows the total and temperature range wise CO₂ desorbed in terms of mmolg⁻¹ for all the samples under study. The first peak in the region of 100-200 °C was due to the weak basicity corresponding to desorption of physisorbed CO₂. Catalyst showed a broad peak in the region of 200-400 °C revealing the presence of medium strength basic sites. A broad peak in the region of 450-650 °C indicated the presence of strong basic sites. The trend of basicity was found to be Ba-Zr (0.5:1) < Ba-Zr (1:1) < Ba-Zr (2:1) < Ba-Zr (3:1). The acidic strength and acidic site density

were estimated in terms of total NH_3 desorbed (mmol g^{-1}) by NH_3 -TPD analysis. From **Table 3.1**, NH_3 -TPD trend was opposite to that of CO_2 -TPD as Ba-Zr (3:1) < Ba-Zr (2:1) < Ba-Zr (1:1) < Ba-Zr (0.5:1). The activity results of all the prepared Ba-Zr MMO and bare oxides of Ba and Zr catalysts were correlated with their total basic site density calculated from CO_2 TPD and discussed later. Furthermore, ratio of basic site density/acidic site density was also calculated and it was observed that BaO possessed the highest basicity and as Ba concentration was increased in zirconium lattice, the ratio also increased, the later was the lowest for single component of Zr (**Table 3.1**). Out of all the catalyst studied, Ba-Zr (2:1) catalyst exhibited basicity/acidity ratio of 2.0 which was the most balanced ratio required for the selective glucose isomerization to fructose observed in this work.

Table 3.1 a. The physico-chemical properties of the prepared catalysts.

Sr. No.	Catalyst	BET SA ^a m^2/g	Total Basicity ^b total CO_2 desorbed mmol g^{-1}	Total Acidity ^c total NH_3 desorbed mmol g^{-1}	Basicity/Acidity ratio
1	Ba-Zr (0.5:1)	12.76	0.1860	0.8781	0.2118
2	Ba-Zr (1:1)	14.10	0.3074	0.4782	0.6428
3	Ba-Zr (2:1)	11.50	0.5392	0.2695	2.0007
4	Ba-Zr (3:1)	23.72	0.7652	0.2023	3.7825

^a Determined by N_2 physisorption measurement, ^b Determined by CO_2 TPD, ^c Determined by NH_3 TPD

Table 3.1 b Crystallite sizes of all the three phases formed in all Ba:Zr MMO catalyst

Catalyst	Crystallite size (nm)		
	BaZrO ₃ phase	BaO phase	ZrO ₂ phase
Ba-Zr (0.5:1)	45.93	143.03	86.51
Ba-Zr (1:1)	36.90	80.25	56.80
Ba-Zr (2:1)	29.35	49.50	44.28
BaO	66.31	66.31	-
ZrO₂	56.11	-	56.11

3.3.1.5 Raman analysis

Fig. 3.4 shows the Raman spectra of all Ba-Zr samples which consist of a band at two photon lines around 87 and 135 cm⁻¹ which could be ascribed to TO1, TO2 first-order modes. The second order modes were ascribed to the band at 223 cm⁻¹. The band at 153 cm⁻¹ indicates that the crystal structure of zirconium oxide remaining intact after increasing the Ba concentration. Incorporation of barium in zirconium matrix did not completely distort the octahedral structure of zirconium but it induced oxygen vacancies in the zirconium oxide material. ^(37, 38)

In other words, it supports the doping of Ba in zirconium lattice, which form perovskite phase and provides strong basic sites required for glucose isomerization.

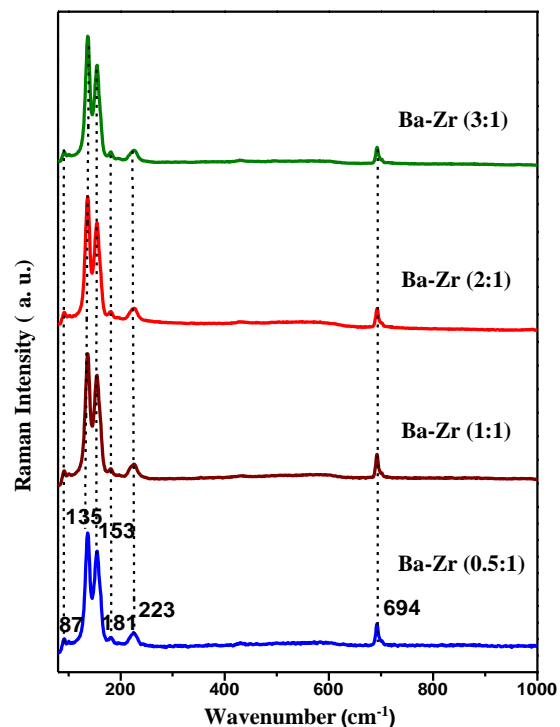


Fig. 3.4 Raman Spectra for Ba-Zr (0.5-3:1) catalysts.

3.3.1.6 FTIR analysis

Fig. 3.5 represents FT-IR spectra of calcined BaO, ZrO₂, and Ba-Zr mixed metal oxide catalysts. The FTIR spectrum of Ba-Zr samples with various ratios of Ba-Zr showed a prominent band at 3400-3500 cm⁻¹ which was assigned to the -OH stretching vibration due to the adsorbed water molecule on the catalytic surface. The absorption peaks in the range 400-780 cm⁻¹, 780-1145 cm⁻¹, 1145-1500 cm⁻¹, 450-560 cm⁻¹ were also observed. The absorption peak at 450-560 cm⁻¹ corresponds to Zr-O stretching mode of vibration in BaZrO₃, which clearly indicates the presence of ZrO₂ phase⁽³⁸⁾ which in accordance with XRD [JCPDS # 86-1451] studies as discussed above. The peak at 1416 cm⁻¹ is due to the oxalate vibrational frequency in BaZrO₃. The peak at 560 cm⁻¹ corresponds to the Zr present in the octahedral site in the perovskite

structure.⁽³⁹⁾ Hence, FTIR study also confirms the presence of three phase's viz. BaO, ZrO₂ and BaZrO₃ which was already characterized by other techniques.

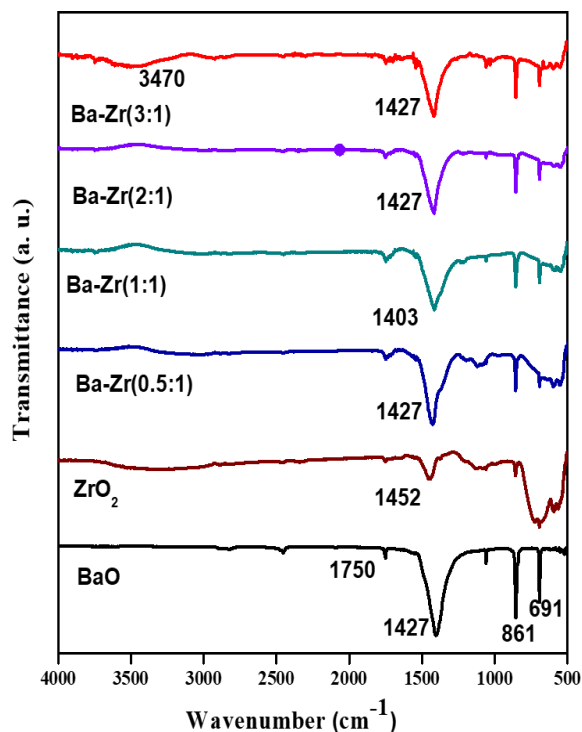


Fig. 3.5 FT-IR spectra for calcined BaO, ZrO₂, and Ba-Zr mixed metal oxide catalyst.

3.3.1.7 XPS analysis

Fig. 3.6 represents X-ray photoelectron spectra of Ba-Zr (1:1) catalyst. In which **Fig. 3.6 (a)** clearly showed a doublet of Zr 3d for Zr 3d_{3/2} and Zr 3d_{5/2} at B.E. of 183.2 and 185.5 eV, respectively.⁽⁴⁰⁾ XPS spectra of O 1s (**Fig. 3.6 c**), after deconvolution showed three peaks at B.E. of 533, 532.3 and 530.8 eV out of which peaks at B.E. of 533, 532.3 eV corresponded to Zr-O-Zr, Ba-O-Zr bridging oxygen atoms in the silica framework while, the peak at B.E. of 530.8 eV was assigned to non-bridging oxygen atoms as O-Zr. Ba 3d_{5/2} XPS shows a peak at 780.5 eV.⁽⁴¹⁾ XPS spectra of reused catalyst showed retention of all the peaks at same binding energy for Ba 3d_{5/2}, which clearly suggest there was not any considerable change in oxidation state of metals after use of the catalyst (**Fig. 3.6 a, d**). It was inferred that BaO phase mostly possessed rod

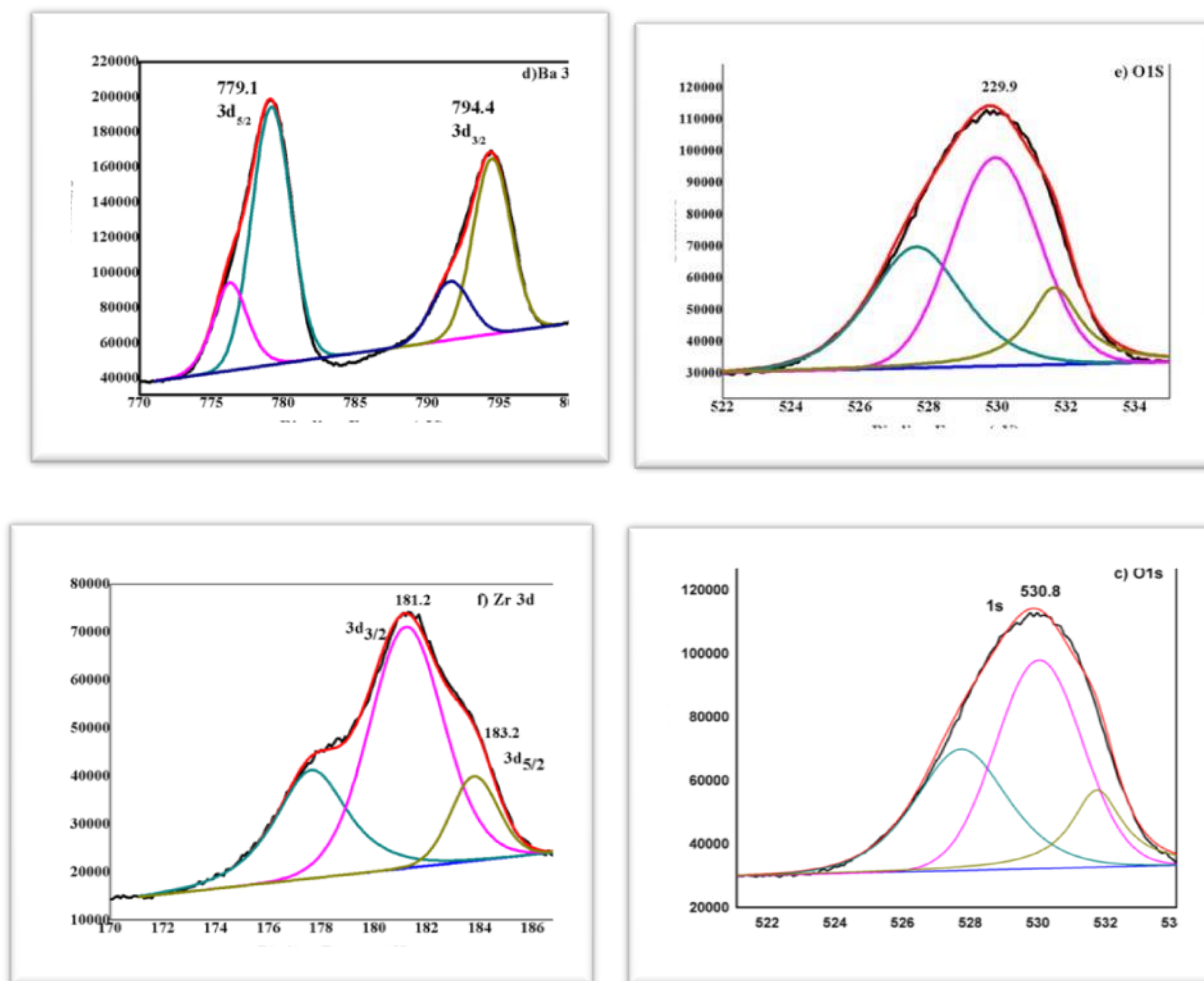


Fig. 3.6 XPS analysis of different phases in the screened catalysts: (a) Ba in used Ba-Zr (2:1), (b) Zr in used Ba-Zr (2:1), (c) and O in used Ba-Zr (2:1) (d) Ba in fresh Ba-Zr (2:1), (e) O in fresh Ba-Zr (2:1), (f) Zr in fresh Ba-Zr (2:1).

shape morphology covered with some spherical particles of zirconium oxide and cubic shape particles of BaZrO_3 . A schematic presentation of the catalyst structure is shown in **Fig. 3.7**.

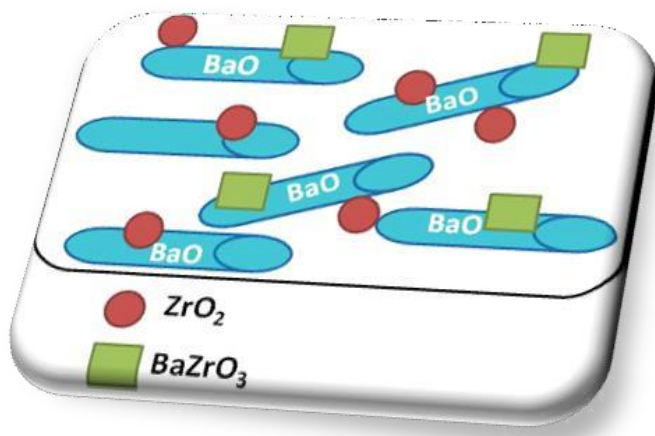
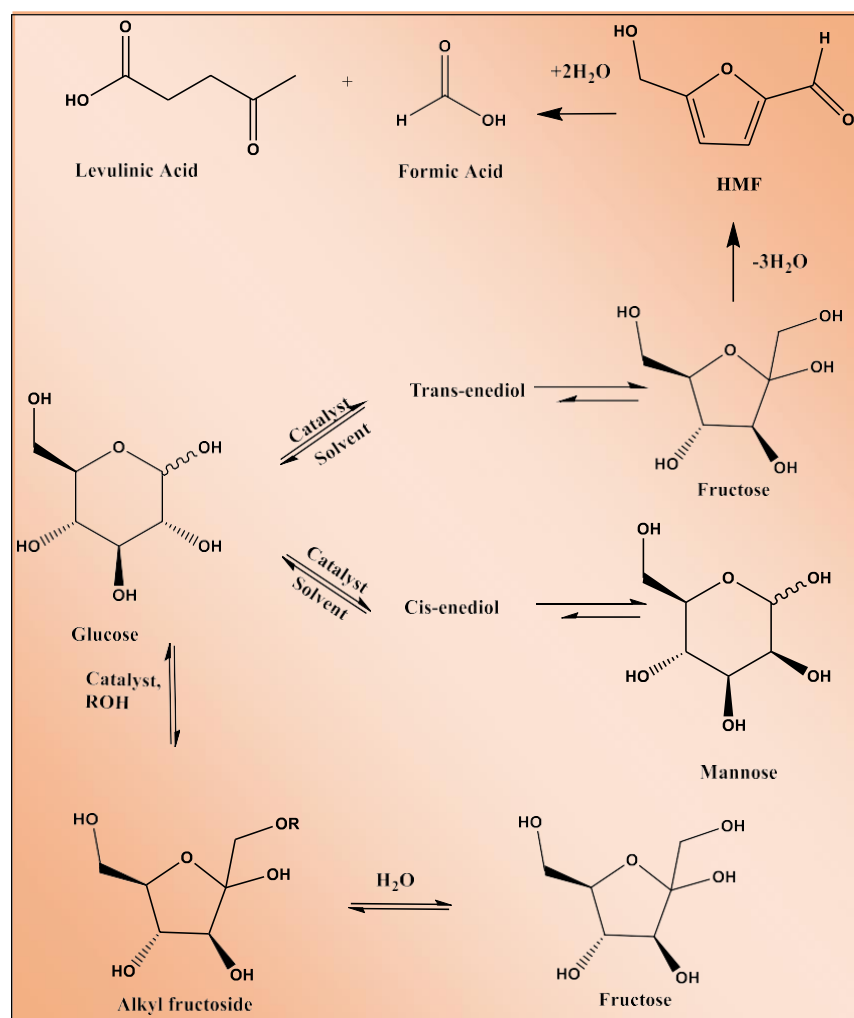


Fig. 3.7 Schematic presentation of Ba-Zr (2:1) catalyst.

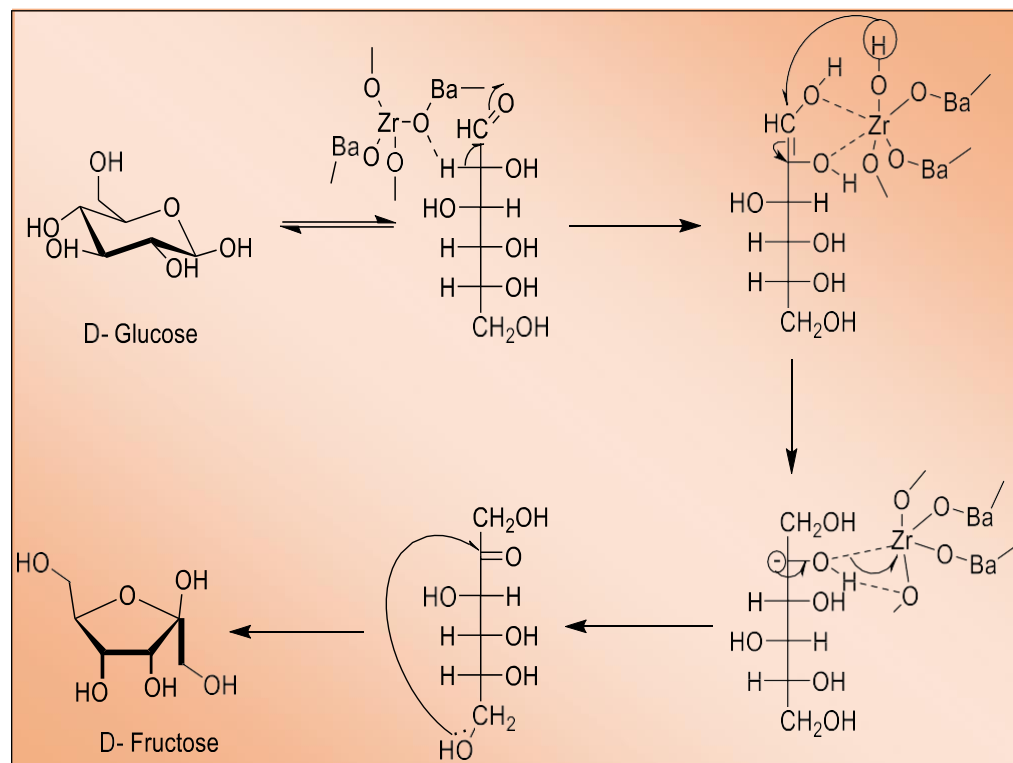
3.3.2 Activity studies

The base catalyzed glucose isomerization is reported to proceed through the ene-diol mechanism.⁽¹³⁾ According to this mechanism, C-2 proton on acyclic form of glucose is abstracted by the basic catalyst resulting in the formation of an ene-diol intermediate and followed by hydrogen transfer from O-2 to O-1 and protonation of C-1. This results in the formation of fructose as the major product and mannose as a minor product. The ene-diol mechanism involves the formation of trans-ene-diol to give D-fructose whereas; cis-enediol produces D-mannose as shown in the **Scheme 3.2 a**.^(42, 43) Whereas the Lewis acid catalyzed glucose to fructose isomerization involves opening of the glucose ring to open chain form followed by H-shift from C₂ to C₁ position and ring closure to form fructose. The acidic sites on catalytic surface play an important role in H-shift during isomerization reaction.⁽⁴⁴⁾ The mixed metal oxide catalyst prepared in this work, from alkaline earth metal Ba being basic and early transition metal Zr more acidic renders the Ba-Zr (2:1) catalyst to exhibit tunable base/acid bifunctional character efficiently catalyzed the glucose isomerization as shown in **Scheme 3.2 b**. Initially the glucose

molecule gets adsorbed at the catalytic surface where the basic sites actively participate in deprotonation at C₂ to form the ene-diol intermediate. The acidic sites are responsible for the stabilization of ene-diol intermediate formed and drive the deprotonation of the O-2 proton. The final step involves cyclization to give fructofuranose as the major product. Our study revealed that the Ba-Zr (2:1) MMO provides the accessibility to both the base/acid sites present on the catalytic surface that play an important role in the selective (89 %) isomerization of glucose to fructose in presence of water at 100 °C, 1 atm pressure within 6 h with 57 % conversion.



Scheme 3.2 a Glucose isomerization to fructose, mannose and other byproducts.



Scheme 3.2 b Base catalysed isomerization of glucose to fructose.

3.3.3 Catalyst screening:

Keeping in view that isomerization of glucose to fructose is catalyzed either by Lewis acid sites or basic sites we have screened various metal oxide and mixed metal oxide catalysts for this reaction and the results are as shown in **Table 3.2**. Zirconia (ZrO_2) has been used extensively as a catalyst and solid support as it possesses both acidic as well as basic properties and high thermal stability. Whereas, the basic sites generated from hydration of SnO_2 promote glucose isomerization. The experimental results showed that bare SnO_2 and ZrO_2 showed 12 % and 27 % conversion for glucose, respectively (**Table 3.2**, entries 1 and 2, respectively). Al_2O_3 gave very low conversion (04 %) (**Table 3.2**, entry 3). The basic metal oxides BaO and CaO also catalysed

isomerization of glucose and gave conversions of 20 % and 34 %, respectively (**Table 3.2**, entries 4 and 5 respectively). As metal oxides gave lower conversion, these were supported on SBA-15 as it provides high thermal stability, variable framework composition and high surface to volume ratio to promote the catalytic activity. Glucose isomerization did not proceed in absence of the catalyst as well as in presence of bare SBA-15 (**Table 3.2**, entry 6). Interestingly, SBA-15 supported metal oxides as Sn- SBA-15 and Zr-SBA-15 increased conversion of glucose to 36 and 32 %, respectively (**Table 3.2**, entries 7 and 8 respectively). To explore and to study the role of acidity on the catalytic activity and glucose isomerization, 20 % PWA-SBA-15 catalyst was used, which showed only 12 % conversion of glucose (**Table 3.2**, entry 9). Although acidic catalyst like 20 % PWA-SBA-15 showed poor performance, the mixed metal oxides of barium with acidic zirconium in Ba-Zr (1:1) showed excellent results with 50 % glucose conversion and 82 % fructose selectivity (**Table 3.2**, entry 10). Our study revealed that the Ba-Zr (1:1) MMO provides high surface to volume ratio and accessibility, to both the base/ acid sites present on the catalytic surface that plays an important role in the selective isomerization of glucose to fructose. The base/ acid sites present on the catalytic surface are found to accelerate the isomerization rate by participating in the reaction pathway. In order to study the effect of increased acidity, 20 % PWA was introduced to Ba-Zr (1:1) catalyst which showed no any improvement with 53 % glucose conversion and 65 % fructose selectivity (**Table 3.2**, entry 11). As Ba-Zr (1:1) MMO catalysed glucose isomerization effectively, further glucose isomerization studies were carried out using Ba-Zr mixed metal oxides prepared in various ratios. The objective being to tailor the basic character of the bifunctional catalyst by increasing the Ba concentration in varying ratios to enhance the glucose isomerization. The effects of the varying Ba-Zr ratios on glucose conversion and fructose selectivity are discussed below. CO₂-

TPD and NH₃-TPD study revealed that although bare BaO exhibits highest basicity but it showed very low conversion of glucose (20 %). On the other hand, ZrO₂ had negligible basicity in other words has highest acidity and showed slightly higher conversion (27 %). Whereas, all the MMO exhibited increasing order of basic site density with increasing Ba concentration, which effectively showed a linear rise in activity.

Table 3.2 Isomerisation of glucose to fructose over different metal oxide catalysts

Sr. No	Catalyst	Conv. (%)	Selectivity (%)	
			Fructose	Mannose
1	SnO ₂	12	37	04
2	ZrO ₂	27	78	10
3	Al ₂ O ₃	04	52	08
4	BaO	20	64	12
5	CaO	39	60	14
6	SBA-15	---	---	---
7	Sn-SBA-15	36	72	08
8	Zr-SBA-15	32	69	06
9	20%PWA-SBA-15	12	42	08
10	Ba-Zr (1:1)	50	82	18
11	20 % PWA-Ba-Zr (1:1)	53	65	10

Reaction Conditions: Glucose (180 mg, 1 mmol), Water (6 mL), Time (6 h), Temp (100 °C), Catalyst (100 mg).

3.3.4 Effect of various molar ratios of Ba-Zr:

Effect of various molar ratios of Ba-Zr on glucose isomerization was studied and the results are presented in **Fig. 3.8** which helps to explore role of base/ acid sites on the catalytic surface responsible for conversion. Ba-Zr (0.5:1) catalyst gave 44 % conversion of glucose with 80 % selectivity for fructose. Ba-Zr (1:1) showed higher conversion of 50 % glucose conversion and 82 % fructose selectivity towards fructose. Ba-Zr (2:1) gave the highest selectivity of 89 % to fructose with 57 % conversion of glucose. Further increase in barium molar ratio that is Ba-Zr

(3:1), did not show much improvement in the glucose conversion (57-59 %.). While, all Ba-Zr MMOs show very less selectivity towards mannose between 11-20 % as shown in Table 3.2. From previous reports, glucose isomerization mainly depends on base/acid mole ratio of metal oxides as base/ acid ratio greater than 1.0 would increase the fructose selectivity.⁽⁴⁵⁾ Since Ba-Zr (2:1) catalyst possessed the balanced ratio of basicity/ acidity it was found to be the most efficient catalyst for glucose isomerization (Table 3.1) and further studied for optimization of reaction parameters.

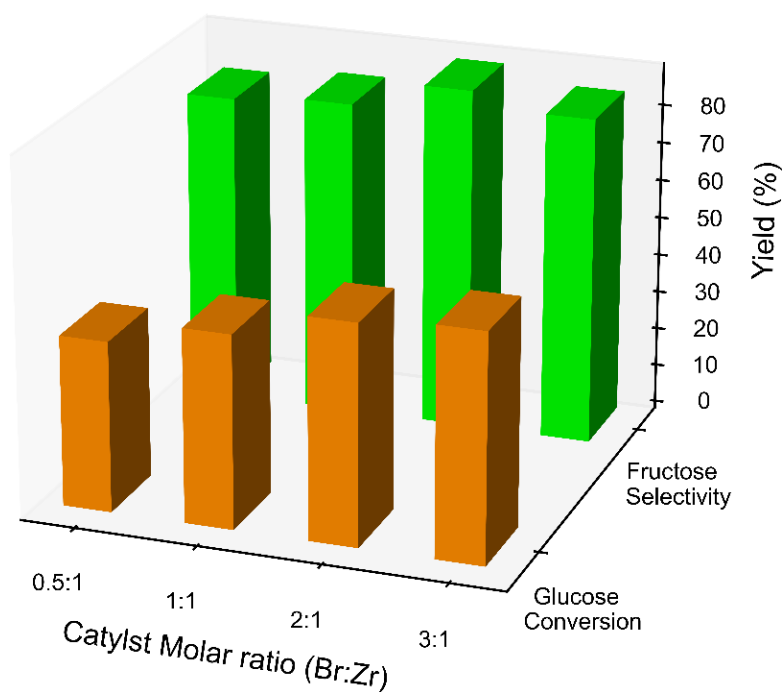


Fig. 3.8 Effect of catalyst molar ratio on glucose isomerization.

Reaction Conditions: Glucose (180 mg, 1 mmol), Water (6 mL), Time (6 h), Temp (100 °C), Catalyst (100 mg).

3.3.5 Effect of substrate to catalyst ratio:

Fig. 3.9 presents the effect of substrate to catalyst ratios on glucose isomerization. A range of substrate loading with respect to catalyst (constant at 100 mg) was studied to determine the optimal condition for glucose isomerization. The glucose to the Ba-Zr (2:1) catalyst ratio was varied from 1.8 to 18. The increase in substrate loading (moles of glucose) resulted in a decrease in the glucose conversion from 57 to 42 %, which could be attributed to low availability of active sites. As expected, fructose selectivity was found to be highest at glucose to catalyst ratio of 1.8 due to availability of increased number of active sites on catalytic surface. Thus, the catalyst is highly selective towards glucose isomerization to fructose.

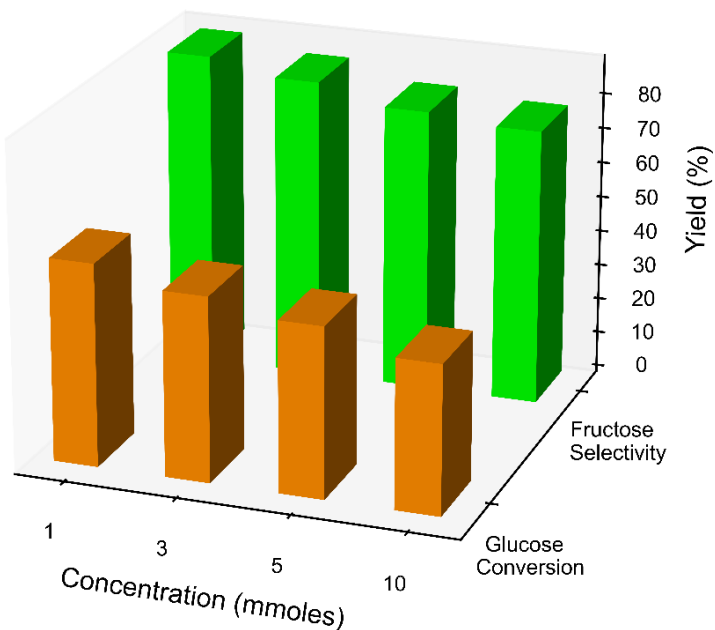


Fig. 3.9 Effect of Substrate concentration on glucose isomerization.

Reaction Conditions: Water (6 mL), Time (6 h), Temp (100 °C), Catalyst (100 mg).

3.3.6 Effect of temperature:

Fig. 3.10 shows the effect of temperature on glucose isomerization. The study of the influence of temperature on glucose isomerization was conducted in the temperature range 80-110 °C to accelerate the isomerization reaction. As glucose to fructose isomerization requires high activation energy, it is carried out at higher temperature ($T > 100$ °C). However higher temperature leads to low fructose selectivity as glucose and fructose being unstable decompose at higher temperatures. **Fig. 3.10** illustrates that with increase in temperature there was a linear increase in the glucose conversion from 36-59 % and fructose selectivity 89 % with fructose yield of about 29 %. The increase in temperature increased the reaction rates by increasing the number of collisions and lowering the energy of activation thereby resulting in glucose isomerization. The increasing temperature accelerated the isomerization and shortened the equilibration time for isomerization reaction. Thus, maximum fructose yield was observed at 100 °C in 6 h.

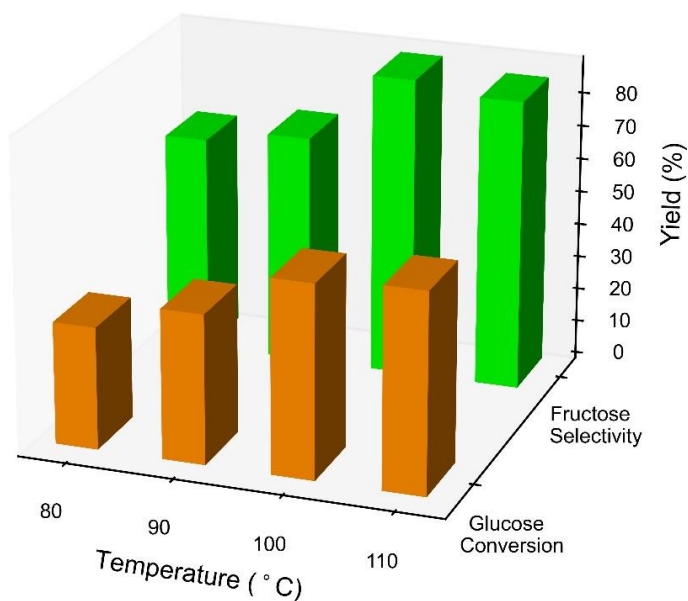


Fig. 3.10 Effect of temperature on glucose isomerization.

Reaction Conditions: Glucose (180 mg, 1 mmol), Water (6 mL), Time (6 h), Catalyst (100 mg).

3.3.7 Solvent screening:

Fig. 3.11 reveals the effect of solvent on glucose isomerization. In order to understand the influence of solvent system on glucose isomerization various mixtures of solvents such as (MeOH + H₂O), (DMSO + H₂O), (DMF + H₂O) and H₂O were screened. From the **Fig. 3.11** it is clear that the addition of organic phase to aqueous phase causes significant decrease in glucose conversion as well as fructose selectivity. Glucose being highly soluble in polar protic solvent i.e., water seems to have strong positive effect on glucose conversion. But the mixtures of polar aprotic i.e., organic solvents with water showed decrease in reaction rate, low glucose conversion with drastic decrease in the fructose selectivity.

This could be attributed to the formation of by-products such as mannose, organic acids, methyl glucoside *etc.* in presence of organic solvents as shown in **scheme 3.2 a**. Thus, water was used as a solvent for optimizing the other reaction parameters as it favours the proton exchange required for glucose to fructose isomerization.

Water as a solvent gave 57 % glucose conversion and 89 % fructose selectivity. Whereas the other mixture of solvents gave low conversion, (DMSO + H₂O) gave 46 %, (MeOH + H₂O) gave 44 % and (DMF + H₂O) gave 10 % glucose conversion. Thus, water was chosen to be the best solvent for glucose isomerization.

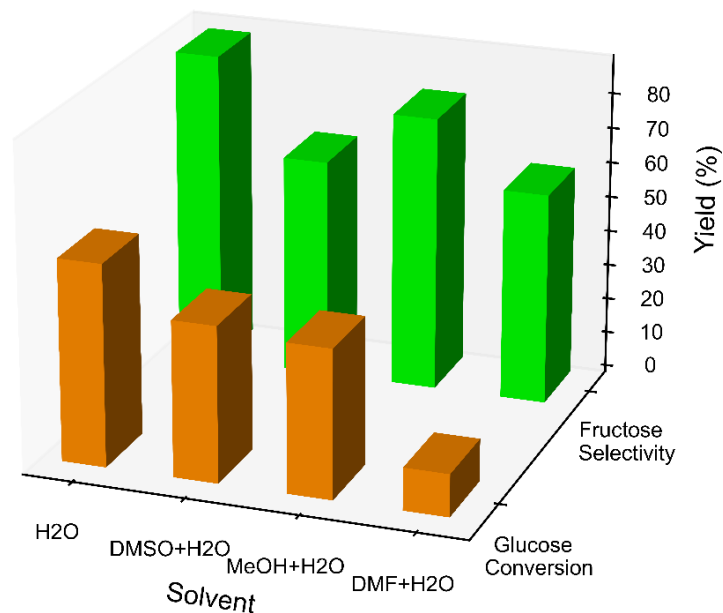


Fig. 3.11 Effect of solvent on glucose isomerization.

Reaction Conditions: Glucose (180 mg, 1 mmol), Time (6 h), Temp (100 °C), Catalyst (100 mg).

3.3.8 Catalyst Recycle Study:

One of the most important advantages of heterogeneous catalyst over homogeneous catalyst is its easy separation and reuse. In order to study the stability of the heterogeneous mixed metal oxide catalyst, the recycle study was carried out and results are as shown in **Fig. 3.12**. Hence, the optimized Ba-Zr (2:1) catalyst after the first run was filtered and washed with deionized water till the pale-yellow coloured catalyst became white; the catalyst was dried at 110 °C and then calcined at 550 °C for 3 hours and reused. The procedure was followed for four subsequent runs. The glucose conversion was found to decrease marginally from 57 % to 55 % due to handling losses, whereas the selectivity was found to be constant at 89 % to fructose and 11 % to mannose. Thus, the catalyst prepared by Co-precipitation method showed excellent recyclability performance up to 4 cycles.

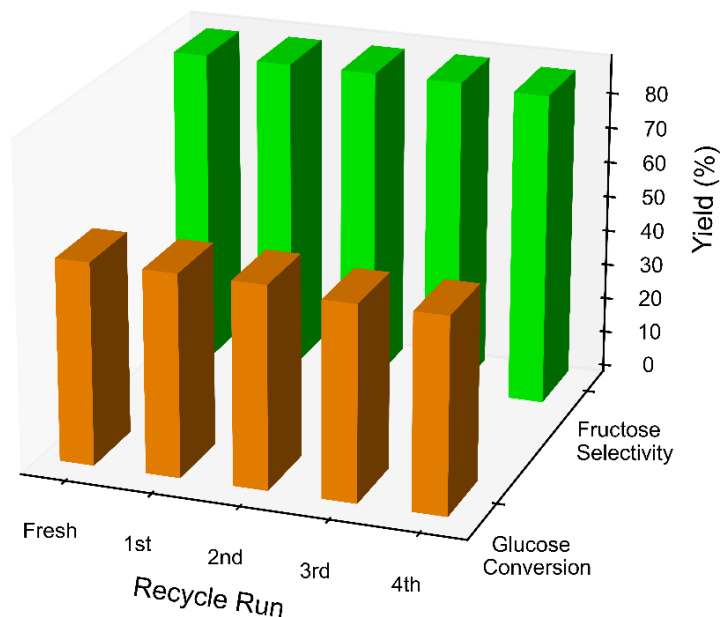


Fig. 3.12 Catalyst recycle study

Reaction Conditions: Glucose (180 mg, 1 mmol), Water (6 mL), Time (6 h), Temp (100 °C), Catalyst (100 mg).

4. Conclusion

Ba-Zr (2:1) MMO was found to be highly selective towards glucose to fructose isomerization (89 %) and this could be attributed to the structural and physico-chemical properties of the catalyst confirmed by XRD, SEM, CO₂ TPD and XPS analysis. XRD pattern for mixed metal oxides of Ba-Zr (2:1) clearly indicated the presence of BaO, ZrO₂ phases along with perovskite type cubic phase of BaZrO₃ with reflections at corresponding to (211), (220), (222), (330) and (400) planes, respectively. Various molar ratios of Ba-Zr were screened out of which Ba-Zr (2:1) was found to be efficient catalyst whereas on further increasing the concentration of Ba there was not much increase in glucose conversion. This could be attributed to the base/acid mole ratio of metal oxide. Various parameters such as solvent, temperature and substrate to catalyst ratio were studied in order to determine appropriate condition for efficient catalytic activity. Various

experiments carried out with organic solvents and their mixtures with water revealed that neat water acts as the best solvent for glucose isomerization thereby enhancing the glucose conversion. Thus, the bifunctional Ba-Zr (2:1) MMO plays an important role by providing base/acid active sites on the catalytic surface for selective (89 %) isomerization of glucose to fructose by participating in the reaction pathway in presence of water at 100 °C, 1 atm pressure within 6 h with 57 % conversion. The reaction pathway involved adsorption of glucose molecule at the catalytic surface where the basic sites actively participate in deprotonation at C₂ to form the enediol intermediate which is stabilized by the acidic sites present on the catalytic surface. The deprotonation of the O-2 proton followed by cyclization gives fructofuranose as the major product. Finally, the experimental results proved that the catalyst was easily separable and reused up to 4 cycles without any loss in activity.

References:

- 1) Jurgen O. Metzger. Aloys Huttermann, *Naturwissenschaften*, 2009, 96, 279–288
- 2) Xuewang Han, Liang Geng, Yong Guo, Rong Jia, Xiaohui Liu, Yongguang Zhang Yanqin Wang *Green Chem.*, 2016, 18, 1597-1604
- 3) Zehui Zhang and Kejian Deng, *ACS Catal.* 2015, 5, 6529–6544
- 4) Eranda Nikolla, Yuriy Roman-Leshkov, Manuel Moliner, Mark E. Davis, *ACS Catal.* 2011, 1, 408–410
- 5) Chetana R. Patil, Chandrashekhar V. Rode, *Fuel* 2018, 217, 38–44
- 6) Robert-Jan van Putten, Jan C. van der Waal, Ed de Jong, Carolus B. Rasrendra, Hero J. Heeres, and Johannes G. de Vries, *Chem. Rev.* 2013, 113, 1499–1597
- 7) Siew Ping Teong, Guangshun Yi and Yugen Zhang, *Green Chem.*, 2014, 16, 2015–2026
- 8) Basudeb Saha and Mahdi M. Abu-Omar, *Green Chem.*, 2014, 16, 24–38
- 9) Hu Li, Song Yang, Shunmugavel Saravanamurugan, Anders Riisager, *ACS Catal.* 2017, 7, 3010–3029
- 10) Avelino Corma, Sara Iborra, Alexandra Velty, *Chem. Rev.* 2007, 107, 2411–2502
- 11) Andreia A. Rosatella, Svilen P. Simeonov, Raquel F. M. Fradea Carlos A. M. Afonso, *Green Chem.*, 2011, 13, 754–793
- 12) Paivi Maki-Arvela, Irina L Simakova, Tapio Salmi, Dmitry Yu Murzin, *Chem. Rev.* 2014, 114, 3, 1909-1971
- 13) Lobry de Bruyn, C. A.; Alberda van Ekenstein, W. *Action Des Alcalis Sur Les Sucres*, II. Transformation Réciproque Des Uns Dans Les Autres Des Sucres Glucose, Fructose Et Mannose. *Recl. Trav. Chim. Pays-Bas* 1895, 14, 203–216.
- 14) Illanes, A.; Altamirano, C.; Zuniga, M. E. *Biotechnol. Bioeng.* 1996, 50, 609–616.

- 15) Shunmugavel Saravanamurugan, Marta Paniagua, Juan A. Melero, Anders Riisager, J. Am. Chem. Soc. 2013, 135, 5246–5249
- 16) Kooyman C., Vellenga K., and De Wilt H. G. J., Carbohydrate Research, 1977, 54, 33-44.
- 17) Gottfried, J. B.; Benjamin, D. G. Ind. Eng. Chem. 1952, 44, 141–145
- 18) Shigeo Suzuki, Nobuzo Tsumura, J. Org. Chem. 1972, 37, 245-248
- 19) Chi Liu, Jack M. Carraher, Jordan L. Swedberg, Caitlyn R. Herndon, Chelsea N. Fleitman, and Jean-Philippe Tessonnier, ACS Catal. 2014, 4, 4295–4298
- 20) Jacob A. Rendleman, JR., and John E. Hodge, Carbohydrate Research, 1979, 75, 83-99
- 21) S. Despax, B. Estrine, N. Hoffmann, J. Le Bras, S. Marinkovic, J. Muzart, Catal. Commun. 2013, 39, 35–38
- 22) I. Delidovich and R. Palkovits, Catal. Sci. Technol., 2014, 4, 4322-4329
- 23) Sandeep Kumar, Shelja Sharma, Sushil Kumar Kansal, Sasikumar Elumalai, ACS Catal. 2019, 9, 2101–2109
- 24) Asimina A. Marianou, Chrysoula M. Michailof, Dimitrios K. Ipsakis, Stamatia A. Karakoulia, Konstantinos G. Kalogiannis, Haris Yiannoulakis, Konstantinos S. Triantafyllidis, Angelos A. Lappas, Sustain. Chem. Eng. 2018, 6, 16459–16470
- 25) Jinqiang Tang, Xiawei Guo, Liangfang Zhu, Changwei Hu, ACS Catal. 2015, 5, 5097–5103
- 26) Samir H. Mushrif, Jithin J. Varghese and Dionisios G. Vlachos, Phys. Chem. Chem. Phys., 2014, 16, 19564-19572
- 27) Manuel Moliner, Yuriy Román-Leshkov, Mark E. Davis, PNAS 2010, 107, 6164–6168

- 28) Ling, H.; Li, A.; Wu, D.; Tang, Y.; Liu, Z.; Ming, N. *Mater. Chem. Phys.* 2002, 75, 170-173.
- 29) Sin, A.; Montaser, B. E.; Odier, P.; Weiss, F. J. *Am. Ceram. Soc.* 2002, 85, 1928-1932.
- 30) Brzezinska-Miecznik, J., Haberko, K., Bucko, M. M. *Mater. Lett.* 2002, 56, 273-278.
- 31) Kirby, N. M.; Van Riessen, A.; Buckley, C. E.; Wittorff, V. W. J. *Mater. Sci.* 2005, 40, 97-106.
- 32) Millot, N.; Xin, B.; Pighini, C.; Aymes, D. J. *Eur. Ceram. Soc.* 2005, 25, 2013-2016.
- 33) Boschini, F.; Robertz, B.; Rulmont, A.; Cloots, R. J. *Eur. Ceram. Soc.* 2003, 23, 3035-3042.
- 34) Henrike Kleineberg, Matthias Eisenacher, Horst Lange, Heinz Strutz, Regina Palkovits, *CatalSci Technol.* 2016, 6, 6057-6065.
- 35) Hongjun Zhou, Yuanbing Mao, Stanislaus S. Wong, *Chem. Mater.*, 2007, Vol. 19, No. 22, 5238-5249.
- 36) Aguiar C., Simoes A. Z., Paskocimas C. A., Cilense M., Longo E., Varela J. A., *J Mater Sci: Matter Electron* 2015, 26, 1993-2001
- 37) Zhouguang Lu, Yougen Tang, Limiao Chen, Yadong Li *Journal of Crystal Growth* 2004, Volume 266, Issue 4, 539-544.
- 38) Lavand Y. S. Malghe, *J Therm Anal Calorim* 2014, 118, 1613–1618
- 39) Chetana R. Patil and Chandrashekhar V. Rode, *Chemistry Select* 2018, 3, 12504–12511
- 40) Nachimuthu P., Kim Y. J., Y. J. Kuchibhatla Y. J., Z. Q. Yu, Jiang W., Engelhard M. H., Shutthanandan V., Ja'nos Szanyi, Thevuthasan S., *J. Phys. Chem. C* 2009, 113, 14324–14328

- 41) Haruyuki Kitajima, Yoshimasa Higashino, Shiho Matsuda, Heng Zhong, Masaru Watanabe, Taku M. Aida, Richard Lee Smith Jr., *Catalysis Today* 2016, 274, 67–72
- 42) Ref: Jack M. Carraher, Chelsea N. Fleitman, Jean-Philippe Tessonier, *ACS Catal.* 2015, 5, 3162–3173.
- 43) Vinit Choudhary, Ana B. Pinar, Raul F. Lobo, Dionisios G. Vlachos, Stanley I. Sandler, *Chem Sus Chem* 2013, 6, 2369 – 2376.
- 44) Guanna Li, Evgeny A. Pidko, and Emiel J. M. Hensen, *ACS Catal.* 2016, 6, 4162–4169
- 45) QiangGuo, LiminRen, Saeed M. Alhassan, Michael Tsapatsis, *Chem. Commun.*, 2019, 55, 14942-14945.

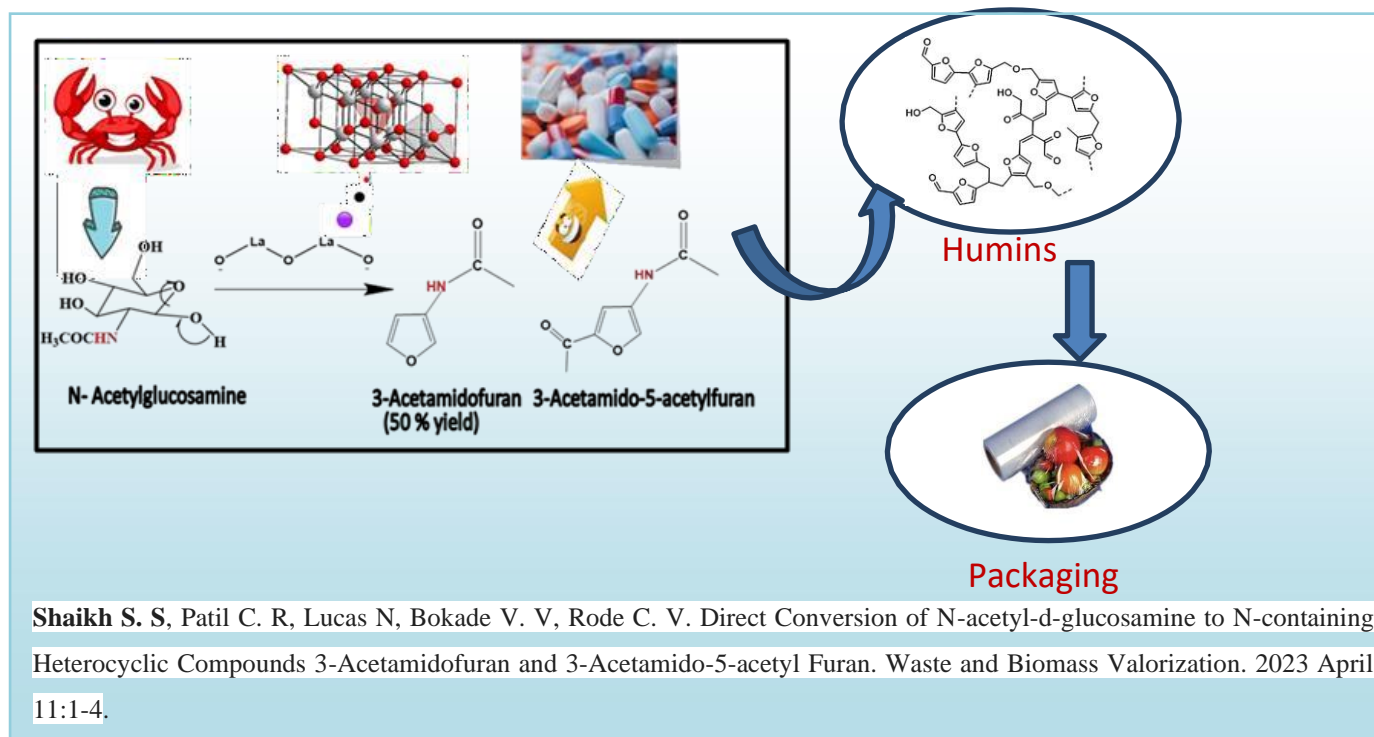
Direct Conversion of N-Acetyl-D-glucosamine to N-containing heterocyclic compounds 3-acetamidofuran and 3-acetamido-5-acety furan.

Abstract:

Effectual waste utilization from plant as well as marine biomass has gained tremendous importance with reference to sustainability. The valorization of marine biomass produces value added compounds containing not only C, H, O but also renewable N atom in the skeleton which widens the scope for its exploration which may prove to be economically beneficial to the society. Heterogeneous catalytic transformation of marine biomass i.e., N-acetyl glucosamine (NAG) to N-substituted aromatic heterocyclic is reported for the very first time. Cost effective and stable metal oxide catalysts were deployed for the transformation. Catalyst screening study showed that La_2O_3 was found to be an excellent catalyst for N-acetyl glucosamine (NAG) dehydration which mainly produced 3-acetamidofuran (3AF). The physicochemical properties of the metal oxide catalyst were investigated by various techniques such as XRD, FTIR, MeOH-FTIR, TPD, SEM, N_2 sorption studies and HR-TEM analysis for structure activity relationship. The effect of various reaction parameters such as catalyst concentration, reaction temperature, reaction time and solvent effect on dehydration of N-acetyl glucosamine has been studied in detail for higher yields. The results revealed that the presence of weak basic sites which are Brønsted in nature and nano pores present on the surface were responsible for improved dehydration of the chitin biomass to selectively yield 3-acetamidofuran (3AF). La_2O_3 catalyst showed optimum 50 % 3AF yield from N-Acetyl glucosamine at 180 °C in 3h. Efficacious exploitation of marine biomass to value added chemicals using heterogeneous catalyst through simple route and easy separation of N-substituted heterocyclic aromatics is the most innovative aspect of the current study. Thus, utilization of heterogeneous catalyst and renewable biomass as a raw material indicates a transition towards more sustainable and greener approach.

The rapid depletion of non-renewable fossil fuels has urged a need for biomass waste valorization in order to mitigate these alarming issues. Due to its abundance marine biomass on valorization widens its scope for production of value-added products and platform chemicals. As far as sustainability and green synthesis is concerned, we report for the first-time dehydration of NAG to

renewable N-containing furan derivatives by heterogeneous catalyst without use of any additives, ionic liquids or boron compounds. The catalyst showed high stability, easy separation and excellent recyclability upto 5 cycles. The co-operative effect of Brønsted basicity and nanopores on the catalyst play vital role in (100 %) NAG conversion to yield 50 % 3AF and 20 % 3A5AF.



4.1 Introduction

Efficient waste valorization has been in limelight as it could aid the society to mitigate the alarming environmental issues arising due to the depletion of fossil fuels such as energy crises, green house effects etc. ⁽¹⁻³⁾ Among the biomass variants, marine biomass is readily available as oceans occupy around 71 % of earth's surface. But for decades, the advancement and valorization of marine biomass has remained unexplored, which could emerge as a strong feedstock to bring sustainability and economic benefit to the society. After cellulosic biomass, chitin stands second most abundant biomass on earth with 100 billion tons produced annually. ⁽⁴⁾ Chitin biomass is obtained from shells of several marine animals like crabs, lobsters, shrimps, crayfish, arthropods as well as from cell wall of fungi and yeast. ⁽⁵⁻⁷⁾ Cellulosic biomass on valorization produces value added compounds containing mainly C, H, and O. Whereas, the marine biomass on valorization widens the scope for production of N-containing platform chemicals having various applications as adsorbents, waste water treatment, agricultural

chemicals, polymers, food industries, biomedical applications, formation of films, fibers, composites and cosmetics.⁽⁸⁻¹⁰⁾ Chitin biomass comprises of N-Acetyl glucosamine units linked through β -1, 4 glycosidic linkages to form polymeric chains in three different allomorphic forms α , β , γ . Therefore, the chitin biomass exhibits distinct physicochemical properties due to the presence of N-functionality in its skeleton and serves as most important natural source of nitrogen.^(8,11-13) Cellulosic biomass and chitin biomass have structural similarities with the exception that cellulosic biomass on valorization produces value added compounds and platform chemicals containing C, H and O whereas, chitin biomass produces chemicals containing C, H, O and N. Owing to the presence of 7 wt. % renewable N atom in chitin it has put the marine biomass on fame and has attracted the attention of researchers as it has tremendous scope for its valorization with wide range of applications.⁽¹⁴⁻¹⁵⁾ The chitin hydrolysis is carried out by biological, physical and chemical pretreatment methods which produces NAG, which requires number of steps and harsh conditions like use of mineral acids, high temperature and, thus suffers from major drawbacks making process non feasible. Also, the biological methods fail to eliminate the minerals and proteins from the crustacean shells and high cost of enzymes makes the process less cost effective.⁽¹⁶⁻¹⁷⁾ Prior to chitin hydrolysis, microwave irradiation and sonication were used to increase the chitin solubility in HCl thereby enhancing the chitin hydrolysis to produce NAG.⁽¹⁸⁻¹⁹⁾ Franich et al. reported for the first time that the pyrolysis of tar produced several degradation products with 5 % 3-acetamidofuran (3AF), 2 % 3-acetamido-5-acetyl furan (3A5AF) and 3 % 3-acetamidoacetaldehyde yield.⁽²⁰⁾ Chen et al. studied the NAG pyrolysis at 200 °C for 30 min to produce 3A5AF as the major product with 3AF and several furanic and pyrazine derivatives as minor products. The pyrolysis pathway results in the formation of number of products thus making the process less economical due to lower selectivity towards product formation.⁽¹⁶⁾ The platform chemical 3A5AF, is a precursor for the synthesis of an anticancer drug proximycin A.⁽²¹⁻²²⁾ Both the products 3AF and 3A5AF have N-containing amide functionality in the form of furanic aromatic platform chemicals which can further be explored for their transformations to value added products. But the challenge is retention of amide group as it easily gets fragmented from the main chain.⁽²³⁾ 3AF and 3A5AF may find a role as synthetic precursors for the synthesis of naturally occurring antibiotic and antitumor drug proximycin A, B and C and amino sugars, amino acids and dihydrodifuro pyridine derivatives, aminated bicyclic ethers, pyridine derivatives, bicyclic pyrrolidines via various multi step organic transformations due to its structural similarity and presence of N atom in its skeleton.⁽²⁴⁻²⁸⁾ 3A5AF on asymmetric reduction, produced (3-acetamido-5-(1-hydroxyethyl)furan, a precursor for the synthesis of amino sugar L-

rednose which is a precursor forming the structural unit of biologically active natural products such as Anthracycline⁽²⁹⁾, Saquamycin⁽³⁰⁾ and Rudolphomycin.⁽³¹⁾ Ha *et al.* reported chemoenzymatic dehydration of NAG and its further enantioselective asymmetric reduction to 3-Acetamido-5-(1-hydroxyethyl)furan(3A5HEF) with good yield.⁽³²⁾ Omari *et al.* reported the conversion of NAG to 3A5AF in the presence of B(OH)₃ and NaCl under high temperature microwave irradiation (220 °C for 15 min) to give 58 % 3A5AF yield. His group highlighted the importance of the presence of chloride and boron atoms in the hydrolysis of chitin and dehydration of NAG to 3A5AF, respectively.⁽²¹⁾ Drover *et al.* studied the transformation of NAG into 3A5AF with 60 % yield under microwave heating with ionic liquid, [BMIM]Cl in which imidazolium ring was found to play an important role in the conversion of NAG to 3A5AF.⁽³³⁾ Chen *et al.* introduced the acidic proton at C-2 position and reported the importance of Cl anion in the solubility and dissolution of chitin thereby accelerating its hydrolysis to yield value added products. They reported the direct conversion of chitin to 3A5AF with 7 % yield in ionic liquid using boric acid and HCl as an additive.⁽³⁴⁾ Hence, ionic liquids can be used as ideal solvents as they can bare high temperature range, non-volatile and are non-inflammable. But certain disadvantages like toxicity, handling difficulty and higher cost make ionic liquids less economical for use.⁽³⁵⁾ Surprisingly, the synthesis of furanic compounds remains unexplored using heterogeneous catalysts which excel others in cost, recyclability, ease of separation, catalyst tunability and process improvisation. Visualizing the importance of the marine waste valorization and advantages of the heterogeneously catalyzed conversion, the current study gives first hand report on dehydration and partial deoxygenation of NAG to N-containing renewable platform molecules using various metal oxide catalysts. Choice of catalyst originated from some striking features like stability, cost effectiveness and ease of preparation. A comparative study of acid and basic catalysts has been attempted to furnish insights into type of sites required for selective formation of furans. The best catalyst was characterized by XRD, FTIR, MeOH-FTIR and SEM along with effect of reaction parameters on NAG dehydration to produce 3AF has been carried out.

4.2. Experimental

Barium hydroxide was calcined at 550 °C for 6 h to produce barium oxide. The comparative study for all the catalysts were done by several characterization techniques. The catalysts were characterized by XRD, BET, CO₂ TPD, SEM-EDX, HR-TEM, FT-IR, MeOH FT-IR, TGA technique as mentioned in Chapter 2. (Sections 2.4.1 to 2.4.13). The activity testing for the prepared catalysts were done in a parr

reactor at 180°C temperature for 3h as mentioned in the Chapter 2 (section 2.5.2). The quantitative analysis of the product was done by HPLC analysis using a Pb-Phenomenex column (chapter 2, section 2.6)

4.3 Results and discussion

4.3.1 Catalyst characterization

4.3.1.1 X-ray diffraction

Fig. 4.1 shows the powder XRD pattern for the metal oxide catalysts. The wide angle XRD patterns of the sample of La_2O_3 showed reflections at $2\theta = 15.70^\circ, 27.18^\circ, 28.09^\circ, 39.41^\circ, 48.2^\circ$ ascribed to La_2O_3 phase [JCPDS # 05-0602] corresponding to (100), (002), (101), (102), (211) planes, respectively, with lattice constants as $a = 3.397 \text{ nm}$ and $b = 6.129 \text{ nm}$ which indicated the presence of hexagonal phase of La_2O_3 [JCPDS # 05-0602].⁽³⁶⁾ The diffraction peaks at $2\theta = 15.70^\circ$ and 48.80° can be indexed to the hexagonal phase of $\text{La}(\text{OH})_3$ corresponding to (100) and (211) planes with lattice constants as $a = 0.652 \text{ nm}$ and $b = 0.858 \text{ nm}$.⁽³⁷⁾ The appearance of sharp peaks for the hexagonal phases of La_2O_3 and $\text{La}(\text{OH})_3$ denote high crystallinity of La_2O_3 . La_2O_3 didn't show typical peak for carbonated form of lanthanum which can be observed at $2\theta = 10.2^\circ$, it confirmed the presence of La_2O_3 phase and small amount of $\text{La}(\text{OH})_3$ phase in the examined sample.⁽³⁸⁾ All the other catalysts used for comparison also showed well defined phase. The wide angle XRD pattern for tetragonal phase of BaO showed the reflections at $2\theta = 19.6^\circ, 23.7^\circ, 45.1^\circ$, [JCPDS#47-1488]. Whereas, reflections at $2\theta = 23.7^\circ, 29.1^\circ$ and 55.8° were ascribed to monoclinic ZrO_2 phase [JCPDS#86-1451].⁽³⁹⁾ The XRD pattern for CaO showed peaks at $18.14^\circ, 28.73^\circ, 34.16^\circ, 47.11^\circ, 50.86^\circ, 54.36^\circ, 62.76^\circ, 64.41^\circ, 72.05^\circ$, and 84.87° which confirmed the presence of CaO phase.⁽⁴⁰⁾ The cubic phase of CeO_2 as confirmed by the presence of the characteristic peaks observed at $2\theta = 28.83^\circ, 33.2^\circ, 47.9^\circ, 56.7^\circ$ and 59.4° corresponding to (111), (200), (220), (311), (222) planes, respectively.⁽⁴¹⁾ The XRD pattern for Al_2O_3 showed weak diffraction peaks, observed at $2\theta = 19.2^\circ, 31.0^\circ, 36.6^\circ, 39.3^\circ, 46^\circ, 61.5^\circ$, and 67° , which can be indexed to the reflections at (111), (220), (311), (222), (400), (511), (440) corresponding to the presence of γ -alumina phase according to JCPDS card: 100425.⁽⁴²⁾ The detailed morphology, surface topography of the catalysts was studied FE-SEM.

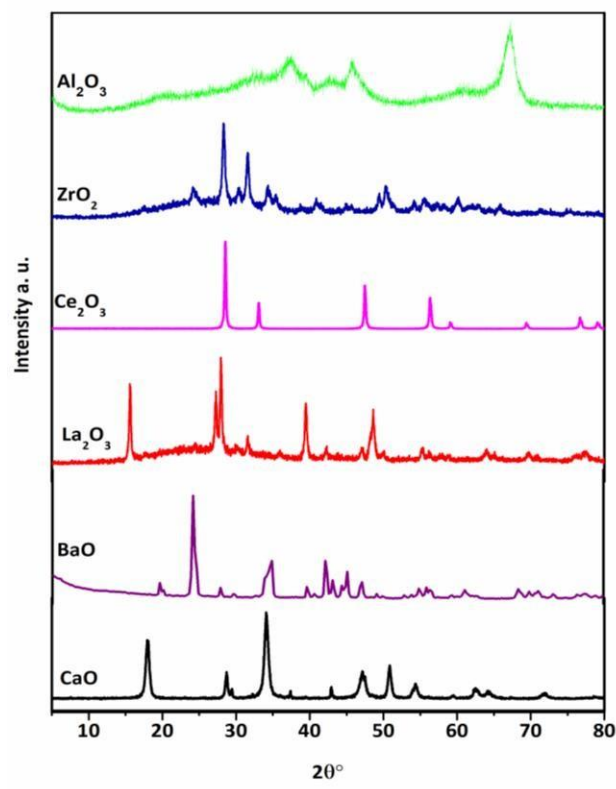


Fig. 4.1 PXR D plots for CaO, BaO, La₂O₃, Ce₂O₃, ZrO₂, Al₂O₃ catalyst.

4.3.1.2 Field emission scanning electron microscopy (FE-SEM) analysis

Fig. 4.2 displays the SEM images for various catalysts, in different magnifications *viz.* (a) CaO, (b) BaO, (c) La₂O₃, (d) Ce₂O₃. In case of calcined La₂O₃, irregular and uneven shaped particles were predominantly present as shown in Fig 2c. The SEM images clearly indicated the presence of pores of varied sizes in the range 90-450 nm on the surface. The presence of these nano pores aid in providing high surface area for adsorption. The SEM analysis of cerium oxide is shown in Fig.2d. The morphological investigation revealed the presence of pores with spherical shaped particles distributed on the surface with size 90-420 nm. BaO showed the presence of mixed morphology with spherical and rod-shaped particles. Rod shaped particles were present predominantly with length in the range of 1-2.8 μm and the size of the spherical particles in the range 220-450 nm as shown in Fig. 4.2 b.⁽³⁹⁾ In case of CaO as shown in Fig.2a, the morphology revealed to contain clusters of flaky particles with particle size, *viz.* 150-750 nm. The percentage elemental composition was acquired by EDS analysis for all four metal oxide catalysts screened (Supporting information Figs 4.21, 4.22, 4.23, 4.24). It confirmed the presence of La₂O₃ phase having composition in mass percentage of the elements as 39.69 % O and

60.31 % La by weight. The peak indexing of the elements for lanthanum was 4.63 KeV and for oxygen was 0.51 KeV.

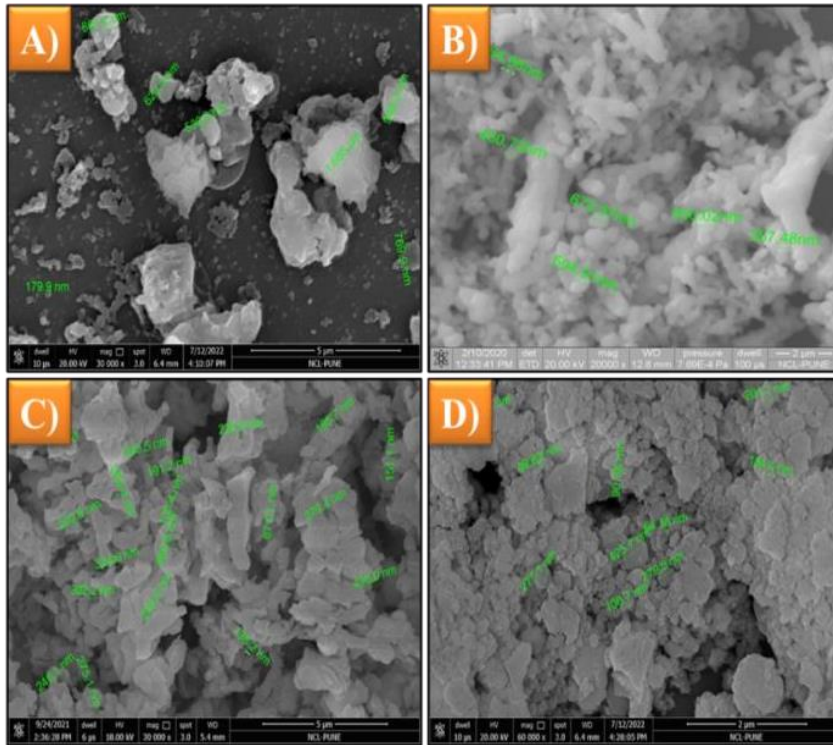


Fig. 4.2 Scanning Electron Micrographs for A) CaO B) BaO C) La₂O₃ and D) Ce₂O₃.

4.3.1.3 Transmission emission Microscopy analysis

Fig. 4.3 Irregular, unordered distributions of the particles were observed at the surface. The agglomeration of the nano particles due to aggregation of the particles by weak forces was observed with average pore size in the range 90-500 nm.⁽⁴³⁾ Thus, from the HR-TEM characterization we conclude that the agglomerated catalyst possess good porosity due to the presence of pores in the nano range.⁽⁴⁴⁾

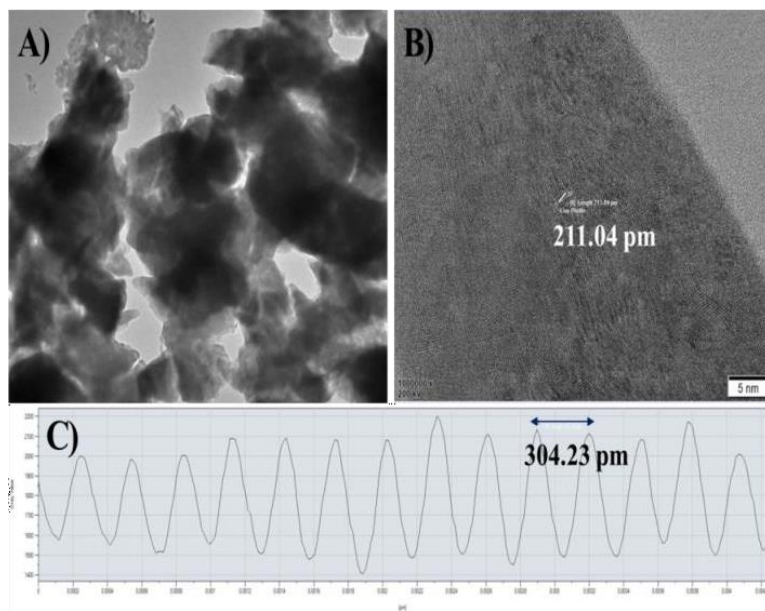


Fig. 4.3 (A-B) Transmission Electron Micrographs La₂O₃ catalyst and **C)** d-spacing for La₂O₃ catalyst.

4.3.1.4 A Fourier Transform Infrared spectroscopy

Fig. 4.4 A presents FT-IR spectra of calcined (La₂O₃) in the range 400 – 4000 cm⁻¹ which showed detailed information about the metal and oxygen bond present in the metal oxide catalysts. The FTIR spectrum of La₂O₃ sample showed a prominent band at 637 cm⁻¹ which was assigned to the stretching vibration of La-O. The intense and sharp absorption band at 3619 cm⁻¹ was ascribed to the -OH stretching of water molecule adsorbed from atmosphere on the oxide surface and the band at 1530 cm⁻¹ corresponds to the presence of extending and twisting -OH bending vibration due to the physically adsorbed water molecule on the catalyst surface. This confirms the presence of Brønsted basic sites in the form of La(OH)₃ phase.⁽⁴⁵⁻⁴⁷⁾ Hence, the appearance of the above mentioned bands in the FTIR spectra confirmed the presence of La₂O₃ and the La(OH)₃ phases in accordance with XRD study.⁽⁴⁸⁾ BaO showed an intense band at 692 cm⁻¹ corresponding to Ba-O stretching frequency. Whereas, the band at 512 cm⁻¹ was assigned to the Ca-O stretching vibration. The Ce-O stretching frequency was observed at 613 cm⁻¹. In case of CaO and BaO, the absorption band due to the bending vibration of the adsorbed water molecule on the catalyst surface was observed at 1448 cm⁻¹ and intense and sharp absorption due to the -OH stretching of the adsorbed water molecule was observed at 3645 cm⁻¹ (sharp) and 3350-3655 cm⁻¹ (broad). The broad absorption band corresponds to the superposition of the hydroxyl stretching bands due to the hydroxyl groups present at the metal oxide surface and the hydrogen bond. But in Ce₂O₃, the band due to bending vibration for the adsorbed water molecule shifted

to 1626 cm^{-1} and a broad absorption band at $3200\text{--}3650\text{ cm}^{-1}$ were observed due to adsorbed water molecule at the catalytic surface. This clearly indicates the presence of hydroxyl group on the catalytic surface.

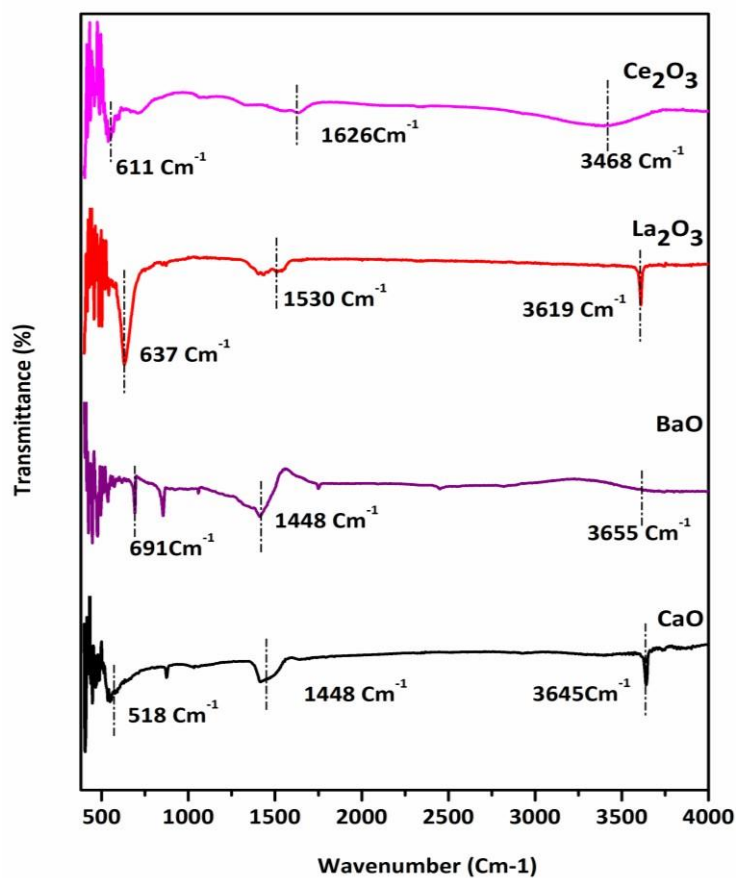


Fig. 4.4 A FT-IR spectra for all metal oxide catalyst

4.3.1.4 B MeOH Fourier Transform Infrared spectroscopy

Fig. 4.4 B represents the *in-situ* FT-IR spectra obtained by subtracting adsorbed MeOH on metal oxide and neat metal oxide spectra. The investigation of Brønsted basicity was carried out by performing *in-situ* methanol adsorption-IR spectroscopy. Earlier, Verneker et al. studied various interactions of $\text{FeO}(\text{OH})$ at the surface by MeOH adsorption IR spectroscopy.

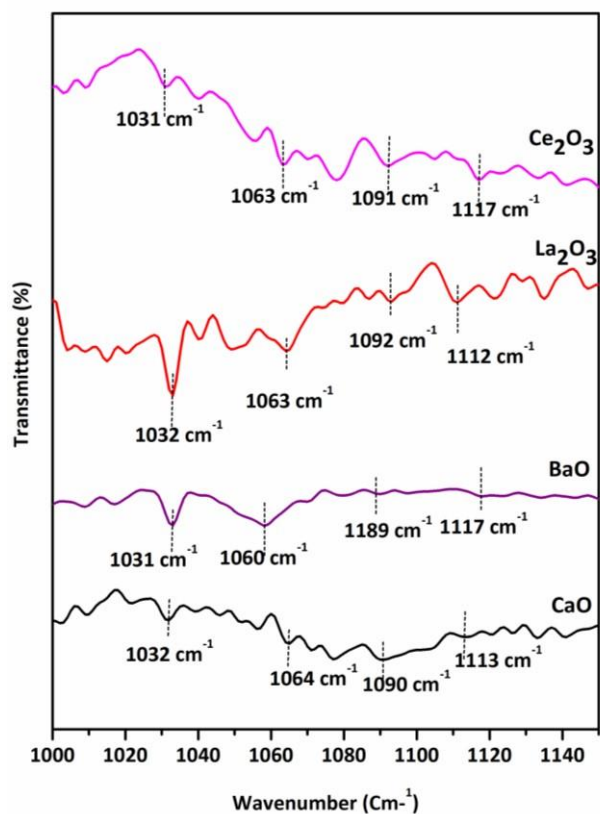


Fig. 4.4 B FT-IR spectra for MeOH adsorbed on all metal oxide catalysts

Their results showed that MeOH interacts with the basic sites on the catalytic surface to form monodentate methoxy species, bidentate methoxy species and molecularly adsorbed species with bands observed at 1115 cm^{-1} , 1092 cm^{-1} , 1064 cm^{-1} .⁽⁴⁹⁻⁵¹⁾ In **Fig. 4.4 B**, various interactions of the adsorbed MeOH with the catalytic surface can be seen. The formation of H-bonded molecularly adsorbed MeOH at the La_2O_3 surface was observed with a band at 1064 cm^{-1} . Whereas, the bands at 1115 cm^{-1} and 1092 cm^{-1} indicated the formation of monodentate and bidentate methoxy species/ metal complexed methoxy species. All these bands were observed in La_2O_3 , Ce_2O_3 , CaO and BaO catalysts. The La_2O_3 catalyst showed intense band at 1063 cm^{-1} and 1117 cm^{-1} whereas, CaO and BaO showed weak bands in this region. The presence of these intense bands in La_2O_3 catalyst clearly indicates the presence of Brønsted basic sites on the catalyst surface, which play an important role in the NAG dehydration.

4.3.1.5 Brauner Emmet and Teller (surface area) and Temperature Programmed Desorption analysis

Table 4.1 reveals the physico chemical properties of the screened catalysts. The surface areas of the catalysts determined by the Brunauer–Emmett–Teller (BET) measurement using N₂ adsorption-desorption isotherms, were found to be 98.097 m²g⁻¹ for calcium oxide, 8.073 m²g⁻¹ for barium oxide, 12.186 m²g⁻¹ for lanthanum oxide and 13.294 m²g⁻¹ for cerium oxide catalyst. **Fig. 4.26** represents the adsorption isotherm of all the catalysts. The N₂ adsorption-desorption isotherm gives detailed information of surface area, pore volume and pore size of the catalyst calculated using BJH method. The La₂O₃ catalyst exhibited adsorption isotherm which represents unrestricted multilayer formation due to strong lateral interactions between the adsorbed molecules.⁽⁵²⁾ The steepness of the isotherm was found to decrease in the order BaO>CaO>La₂O₃=Ce₂O₃. The hysteresis loop in case of CaO showed the presence of relatively uniform and narrow pores whereas, the hysteresis loop for La₂O₃ and Ce₂O₃ showed the presence of narrow pores with irregular shape and size.^(53, 54) **Table 4.1** shows the BET surface area in terms of (m²g⁻¹), it showed the total surface area of 12.186 m²/g, pore volume of 0.0413 cc/g and pore diameter of 0.1357 nm.⁽⁵⁵⁻⁵⁶⁾ whereas, Ce₂O₃ showed total surface area of 13.294 m²g⁻¹, pore volume of 0.0405 ccg⁻¹ and pore diameter of 0.1219 nm. Also, BaO and CaO exhibited total surface area of 8.073 m²/g and 98.097 m²/g, pore volume of 0.0132 cc/g and 0.1569 cc/g and pore diameter of 0.6582 nm and 0.6398 nm respectively.

Table 4.1 showed the total CO₂ desorbed in terms of mmol/gm as well as the temperature wise distribution of the basic sites at the catalytic surface for all the samples under study. It was used to determine the surface basicity of the catalytic samples. The catalytic samples exhibited three CO₂ desorption peaks corresponding to the weak, moderate and strong Brønsted basicity. The first peak in the region of 100-200 °C represents weak Brønsted basicity corresponding to the desorption of physisorbed CO₂. Whereas, the peak in the temperature range 200-400 °C represents moderate basic strength and that in the range 400-700 °C represents strong basicity.

The orders of the total basicity of the screened catalysts were found to be BaO> CaO> La₂O₃> Ce₂O₃. The total basicity of La₂O₃ was 0.3854 mmol g⁻¹, 0.0867 mmol g⁻¹ for Ce₂O₃, 0.7533 mmol g⁻¹ for CaO and highest 0.99110 mmol g⁻¹ for BaO catalyst. **Fig. 4.27** represents the TPD plots for various screened catalysts. The La₂O₃ catalyst was found to give total basicity around 0.3854 mmol g⁻¹ with peak maxima at 335 °C. Whereas, CaO was found to give basicity of 0.7533 mmol g⁻¹ with peak maxima at 420 °C, Cerium oxide showed basicity of 0.0867 mmol g⁻¹ with peak maxima at 290 °C and BaO showed

highest basicity of $0.9911 \text{ mmol g}^{-1}$. The CaO and BaO showed maximum desorption in the higher temperature range.

Whereas, La_2O_3 and Ce_2O_3 catalyst showed maximum desorption in the medium temperature range. This was due to the $-\text{OH}$ moiety at the catalytic surface and the presence of coordinated O^{2-} species as evidenced by the MeOH-FTIR (presence of Brønsted sites) and XRD analysis (presence of $\text{La}(\text{OH})_3$ phase). As, La_2O_3 catalyst showed strong desorption peak in the low temperature range than Ce_2O_3 catalyst, indicating the presence of weak but dense basic sites at the catalytic surface amongst all the catalysts. Hence, the basic properties of the metal oxide catalyst were evaluated quantitatively by CO_2 -TPD measurement.

4.3.2 Catalyst screening

One pot partial deoxygenation and dehydration of NAG to 3AF and 3A5AF was studied using various metal oxides and the results are presented in **Table 4.2**. NAG in absence of any catalyst under the same reaction conditions didn't show any formation of 3AF and 3A5AF. Interestingly, all the metal oxides showed activities according to acidic and basic nature, they possessed. Al_2O_3 catalyst gave 11 % yield of 3AF and 18 % yield towards 3A5AF (**Table 4.2, entry 1**).

For ZrO_2 as a catalyst, NAG yields 12 % of 3AF and 6 % of 3A5AF (**Table 4.2, entry 2**). BaO showed 19 % and 5 % yield for 3AF and 3A5AF, respectively (**Table 4.2, entry 3**). CaO produced 36 % yield of 3AF and 19 % yield towards 3A5AF (**Table 4.2, entry 4**). It can be seen that the basic nature of the catalyst is responsible for formation of the desired product i.e., 3AF as compared to activities shown by acidic metal oxides. The 3AF yield could be enhanced by using rare earth metal oxides which possess appreciable basic characteristics. La_2O_3 showed almost complete conversion of NAG with 50 % yield towards 3AF and 21 % yield for 3A5AF (**Table 4.2, entry 5**). Another lanthanum series metal oxide Ce_2O_3 gave 32 % 3AF yield and 11 % yield for 3A5AF (**Table 4.2, entry 6**). It can be inferred from the above results that La_2O_3 was a very promising catalyst for NAG dehydration and partial deoxygenation producing 3AF product more selectively. La_2O_3 showed better yield for 3AF as it possesses moderate basicity which are Brønsted in nature along with well distributed three-dimensional interconnected nanopores which can be clearly seen from HR-TEM micrographs.

These nanopores present on the surface of La_2O_3 play a very important role during reaction, allowing improved diffusion of reactants and products. Further using La_2O_3 as catalyst optimization of various reaction parameters was carried out for achieving the maximum yield for desired 3AF product.

Table 4.1 Physico-chemical properties of the catalysts

Sr. No.	Catalyst	S-[BET] ^a (m^2g^{-1})	Pore volume ^b (cc g^{-1})	Pore diameter ^b (nm)	Distribution of basic sites (mmol g^{-1})			Total Basicity ^c (total CO_2 desorbed, mmol g^{-1})
					Temperat ure ^c ($^\circ\text{C}$) (100-200)	Temperat ure ^c ($^\circ\text{C}$) (200-400)	Temperat ure ^c ($^\circ\text{C}$) (400-700)	
1	CaO	98.097	0.1569	0.6398	-	0.6780	0.0753	0.7533
2	BaO	8.073	0.0132	0.6582	0.00819	0.8512	0.1318	0.9911
3	La_2O_3	12.186	0.0413	0.1357	0.2739	0.0940	0.0175	0.3854
4	Ce_2O_3	13.294	0.0405	0.1219	0.0090	0.0068	0.0709	0.0867

a- BET analysis, b- BJH method, c-Determined by CO_2 TPD measurement, S-[BET] - BET surface area

Table 4.2 Catalyst screening for NAG conversion to 3AF and 3A5AF

Sr. No.	Catalyst	Yield (%)	
		3AF	3A5AF
1	Al_2O_3	11	18
2	ZrO_2	12	06
3	BaO	19	05
4	CaO	36	19
5	La_2O_3	50	21
6	Ce_2O_3	32	11

Reaction Condition: NAG (1 gm), catalyst (0.2 gm), Dioxane (25 mL), temperature, 180 $^\circ\text{C}$; reaction time, 3 h

4.3.3 Effect of substrate to catalyst ratio

Fig. 4.5 presents the effect of substrate to catalyst ratio on N-acetyl-glucosamine conversion. The catalyst loading was varied in range 5 to 25 wt. % with respect to the substrate (constant at 1 gm) to determine its effect on NAG conversion to 3AF. With increase in the catalyst loading from 5 to 20 wt. % there was an increase in the yield from 20 to 50 %, which could be imputed to the availability of nanopores as well as active basic sites at the catalytic surface for better adsorption.

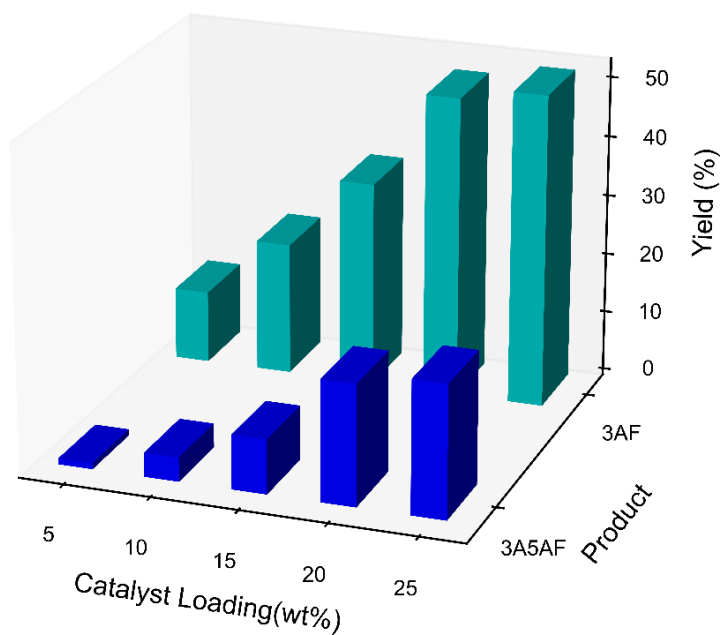


Fig. 4.5 Effect of substrate to catalyst ratios on 3AF production.

Reaction conditions: NAG (1-5 gm), Dioxane (25 mL), Time (3 h), Temp (180 °C), Catalyst (200 mg).

4.3.4 Effect of time on NAG conversion:

As the catalyst loading was further increased to 25 wt. % there was slight decrease in the yield (48 %), due to increase in the formation of humins. Thus, 20 wt. % of the catalyst was optimized for desired conversion. **Fig. 4.6** shows significant increase in 3AF and 3A5AF production with increase in time 60 to 180 min. 3AF and 3A5AF yields were found to increase linearly with

increase in time to maximum up to 50 % and 19 %, respectively. However, the yield of 3AF and 3A5AF was found to decrease after 180 min due to thermal decomposition of the products and acceleration in the rate of formation of humins as by-product was favoured by elevated temperature and prolonged time.

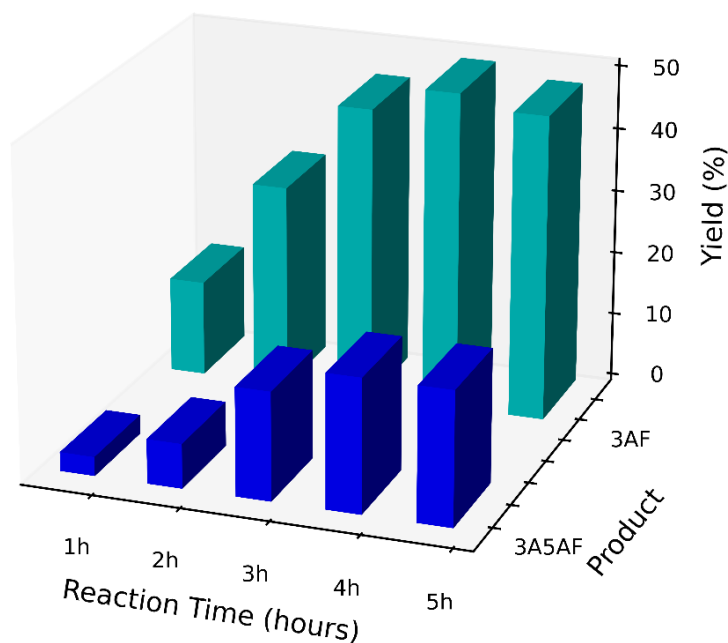


Fig. 4.6 Effect of time on 3AF production.

Reaction conditions: NAG (1 gm), Dioxane (25 mL), Time (3 h), Temp (180 °C), Catalyst (200 mg).

4.3.5 Effect of reaction temperature

Fig. 4.7 shows the effect of temperature on N-acetyl glucosamine conversion. NAG conversion to 3AF with La_2O_3 catalyst was studied by examining the reaction at various temperatures in range 120-210 °C. Fig.8 illustrates that with increase in temperature there was a linear increase in the yield of 3AF and reached to maximum at 180 °C. With further increase in the temperature to 210 °C, the product yield decreased as high temperature accelerated the humin formation. Thus, with increase in temperature above 180 °C, the selectivity to 3AF decreased due to enhancement in the formation of humins. Thus, this decreases in product yield at elevated temperature (above

180 °C) indicates that high temperature favours humin formation. The increase in temperature causes heat transfer resulting in increase in collisions between the particles thereby increasing the collision frequency. This lowers the energy of activation and enhances the reaction rates. The increasing temperature accelerated the 3AF production. Thus, maximum 50 % 3AF yield was observed within 3 h at 180 °C.

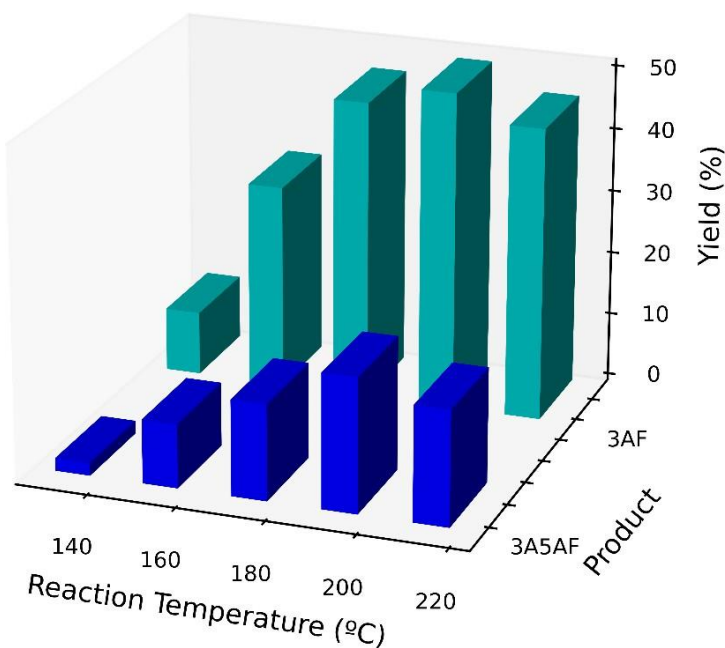


Fig. 4.7 Effect of temperature on 3AF production.

Reaction conditions: Reaction conditions: NAG (1 gm), Dioxane (25 mL), Time (3 h), Temp (180 °C), Catalyst (200 mg).

3.3.6 Solvent screening

Solvents play a vital role in various phenomena such as heat transfer, providing medium for reaction, separation and purification of the products. Fig. 4.8 exhibits the effect of solvent on N-acetyl glucosamine conversion to 3AF. In order to understand the influence of solvent system on NAG conversion to 3AF and 3A5AF, several solvents such as DMA, DMSO, DMF, MIBK and dioxane were screened. DMA, DMSO and DMF were preferred solvents as they were used for dehydration of cellulosic and chitin biomass previously.⁽⁵⁷⁾ Whereas, dioxane is an aprotic

solvent and is able to solvate various inorganic compounds in it. DMF gave highest product yield of 55 %, while DMA, DMSO, MIBK and dioxane gave 52 %, 48 %, 39 % and 50 % yields of 3AF, respectively. Among these, DMF, DMA and DMSO are toxic and have few health hazards and separation of products is quite tedious as these are high boiling solvents. Also, MIBK showed low selectivity to the product due to formation of large amount of humins. Thus, dioxane was chosen as the best solvent for this conversion.

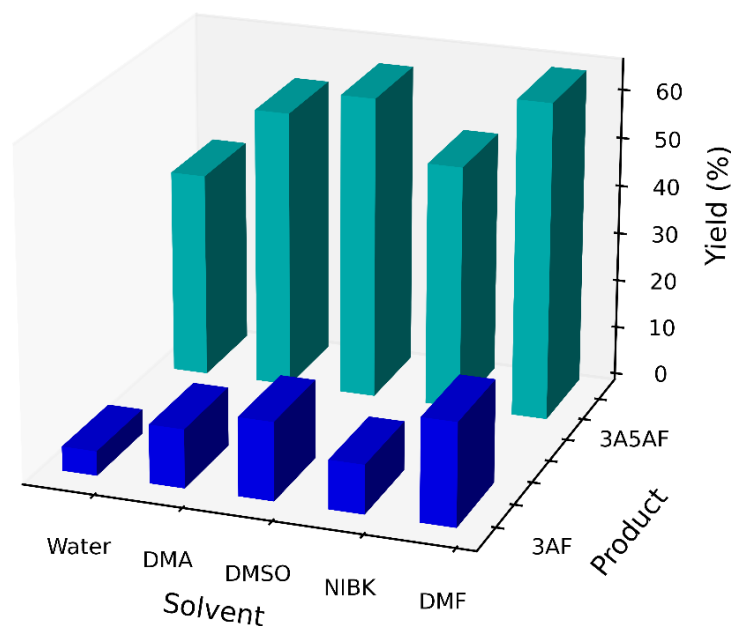


Fig. 4.8 Effect of solvent on 3AF production.

Reaction conditions: NAG (1 gm), Dioxane (25 mL), Time (3 h), Temp (180 °C), Catalyst (200 mg).

3.2.5 Effect of addition of water on reaction pathway:

As water being green solvent and chitin biomass being readily soluble in water, the mixtures of above individual solvents with water were screened for the conversion of NAG to 3 AF and 3A5AF. It was observed that the addition of water to the organic phase significantly decreased the product selectivity. Thus, the addition of water to the organic phase showed negative effect on the product yield and selectivity. This could be attributed to the fact that water caused

acceleration in the formation of humins thereby decreasing the selectivity of the product formation. The effect of addition of water on NAG conversion was studied by adding 50 % water to the solvent system chosen. **Fig. 4.9** shows the effect of addition of water to the solvents DMA, DMSO, DMF, MIBK and Dioxane on N-Acetylglucosamine conversion. Thus, water has negative effect on NAG conversion as presence of water enhances the humin formation.

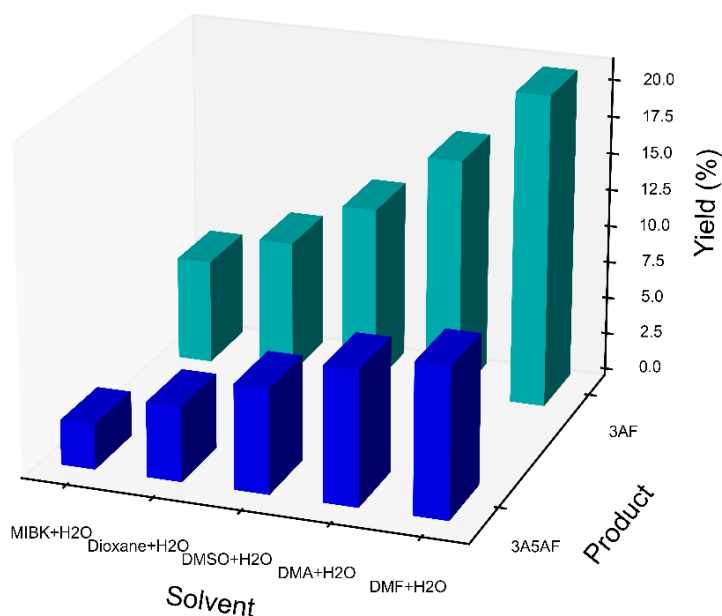


Fig. 4.9 Effect of water on 3AF production.

Reaction conditions: NAG (1 gm), Dioxane (12.5 mL), Water (12.5 mL), Time (3 h), Temp (180 °C), Catalyst (200 mg).

3.3.7 Catalyst recycle Study

The recycle study of the heterogeneous (La_2O_3) catalyst was carried out under the optimized conditions and results are as shown in **Fig. 4.10**. After the first run, catalyst was filtered and washed with deionised water till the pale-yellow coloured catalyst faded, the catalyst was dried at 110 °C in an oven and then calcined at 550 °C for further 3 runs. The procedure was followed for four successive cycles. The N-acetylglucosamine conversion decreased by marginally by 3 % (from 50 % to 47 %) due to handling losses. In order to study the changes of the catalyst surface during the reaction, the recovered catalyst was characterized by XRD, FTIR and TGA analysis. The XRD pattern of the used catalyst (**Fig. 4.11**) showed that the crystallinity of the catalyst

remained intact and there was no deposition of any carbonaceous material at the catalytic surface. The FTIR spectrum of the reused catalyst (**Fig. 4.12**) was similar with that of the fresh catalyst which confirms the stability of the catalyst. The TGA analysis **Fig. 4.28** of the catalysts confirmed that the catalyst was thermally stable. Thus, the La_2O_3 catalyst showed exquisite recyclability performance up to 5 cycles.

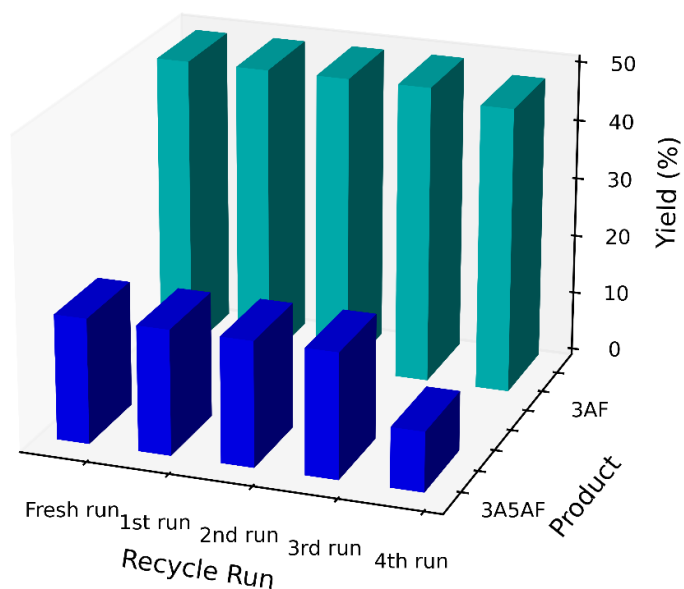


Fig. 4.10 Catalyst recycle study

Reaction conditions: NAG (1 gm), Dioxane (25 mL), Time (3 h), Temp (180 °C), Catalyst (200 mg).

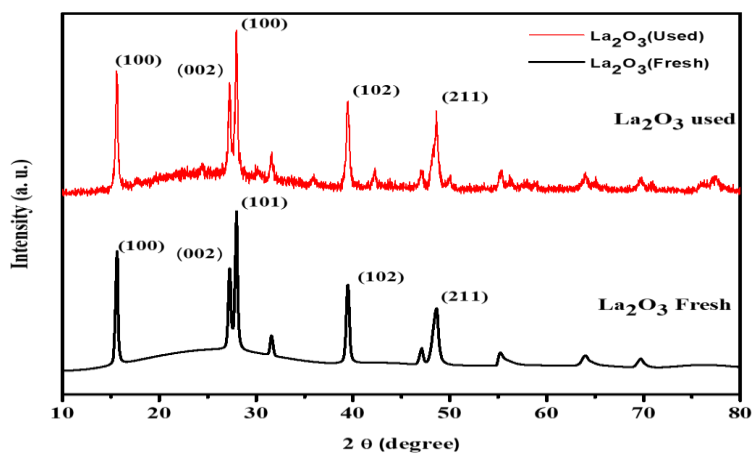


Fig. 4.11 Powder XRD pattern for fresh calcined La_2O_3 and used La_2O_3 metal oxide catalysts

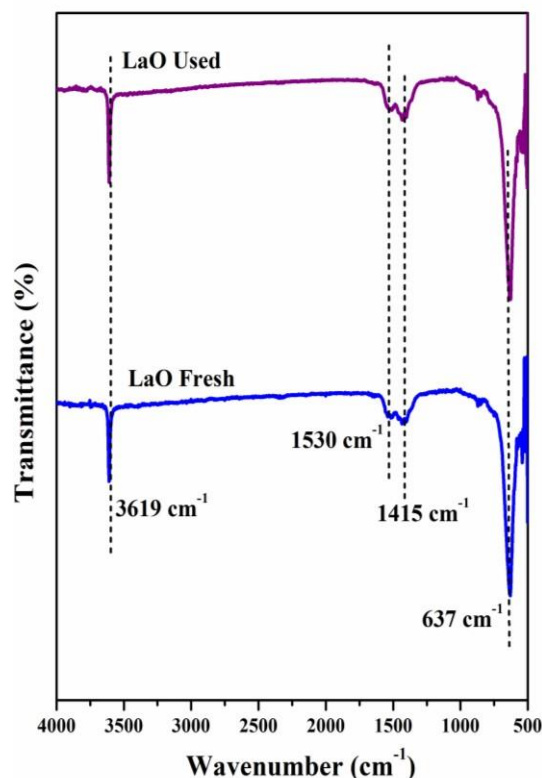
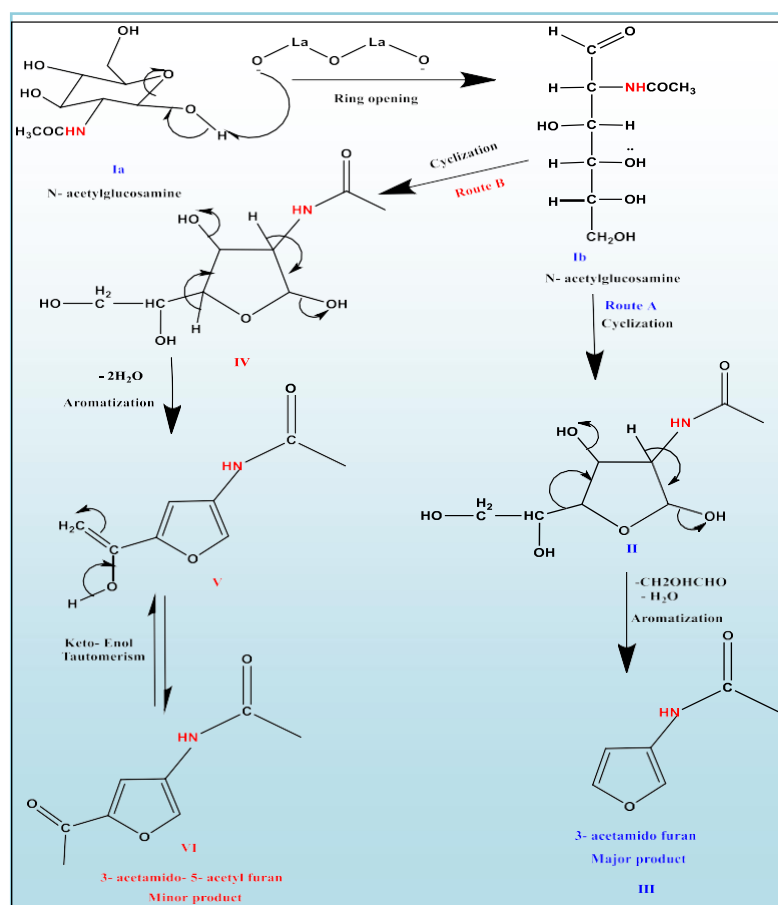


Fig. 4.12 FT-IR spectra for Fresh and used La₂O₃ catalyst

5. Plausible mechanism

The N-Acetyl glucosamine undergoes ring opening in the presence of basic sites of the catalyst to form an open chain compound as shown in **Scheme I, route A**. The presence of nano pores on the catalyst surface as confirmed by SEM and HR-TEM analysis are found to play vital role in the adsorption of the substrate molecules. The basic sites of the catalyst participate in the abstraction of C4-OH proton (I). The nucleophilic attack of C4-O on C1-carbonyl (I) results in the formation of five membered cyclic ring (II) predominantly as formation of five membered ring is favored. This (II) further undergoes dehydration followed by elimination of CH₂OHCHO moiety. The driving force for elimination and dehydration is aromatization which provides extra stability to the system thereby forming 3-acetamido furan (III) as the major product with 50 % yield. Whereas, 3A5AF (VI) is formed as a minor product with 21 % yield as shown in **Scheme I, route B**, which is formed by nucleophilic attack of C4-OH on C1-carbonyl (I) results in the formation of five-member cyclic ring (IV). This is followed by dehydration with removal of two water molecules, as it makes the system more stable due to aromatization (V) which on keto-enol

tautomerism results in the formation of 3A5AF (VI) with 21 % yield. ⁽¹⁶⁾ The insoluble polymer humins are also formed as byproduct during the course of the reaction. Both the products formed were extracted by using a mixture of ethyl acetate and water followed by its purification by column chromatography using 50 % ethyl acetate and n-hexane as the mobile phase. The products formed were confirmed by ¹H-NMR, ¹³C-NMR, HRMS and FTIR (NAG and 3AF, 3A5AF) analysis qualitatively (supporting information **Fig.s 4.13, 4.14, 4.15, 4.16, 4.17 and 4.18, 4.19, 4.20**). The NAG conversion was quantitatively determined by HPLC analysis by keeping 0.5 mL/min flow rate of the prepared mobile phase maintaining column temperature at 80 °C and total analysis time of 20 minutes. The calibration curve is given in **Fig. 4.26** which showed complete conversion of NAG.



Scheme-I Plausible mechanism for base catalyzed dehydration and partial deoxygenation of N-acetyl-D-glucosamine. (**Route A:** Formation of 3- acetamido furan, **Route B:** Formation of 3-acetamido- 5- acetyl furan)

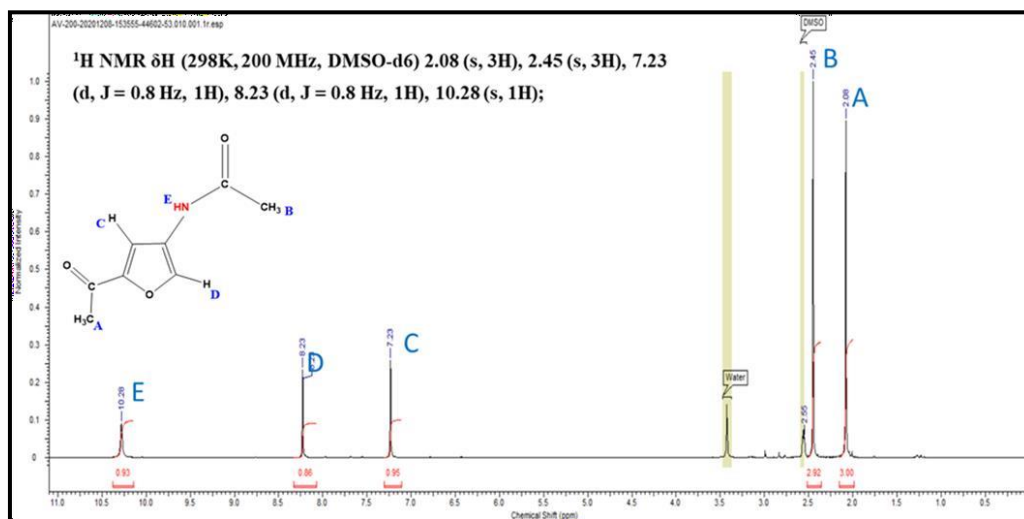


Fig. 4.13: ¹H NMR spectrum of 3A5AF produced from N-acetyl-D-glucosamine [¹H NMR δ H (298K, 200 MHz, DMSO-d₆) 2.08 (s, 3H), 2.45 (s, 3H) 7.23 (d, J = 0.8 Hz, 1H), 8.23 (d, J = 0.8 Hz, 1H), 10.28 (s, 1H)]

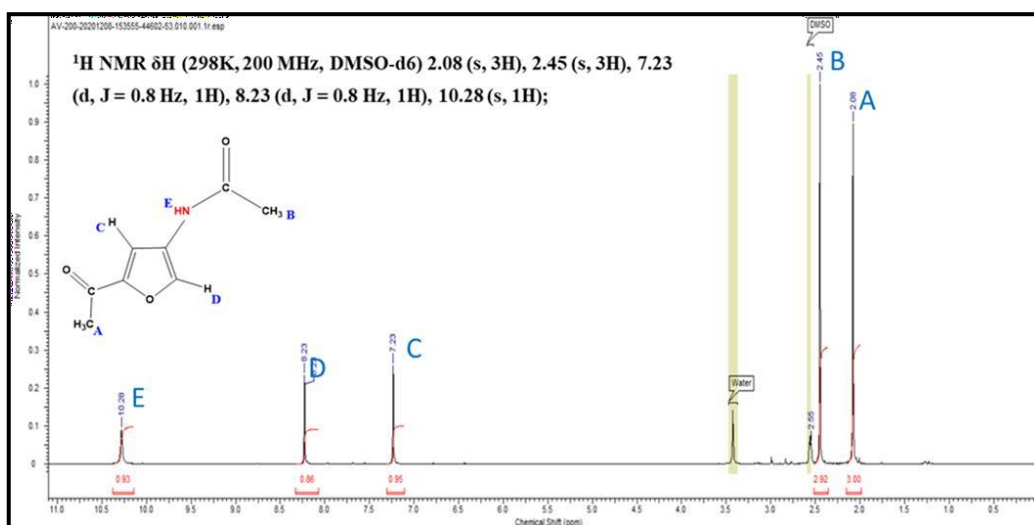


Fig. 4.14: ¹H NMR spectrum of 3AF produced from N-acetyl-D-glucosamine [¹H NMR δ H (298K, 200 MHz, DMSO-d₆) 1.99 (s, 3H), 6.38 (dd, J = 0.8 Hz, 1H), 7.51 (t, J = 0.8 Hz, 1H), 7.92 (dd, J = 0.8 Hz, 1H), 9.97 (s, 1H)]

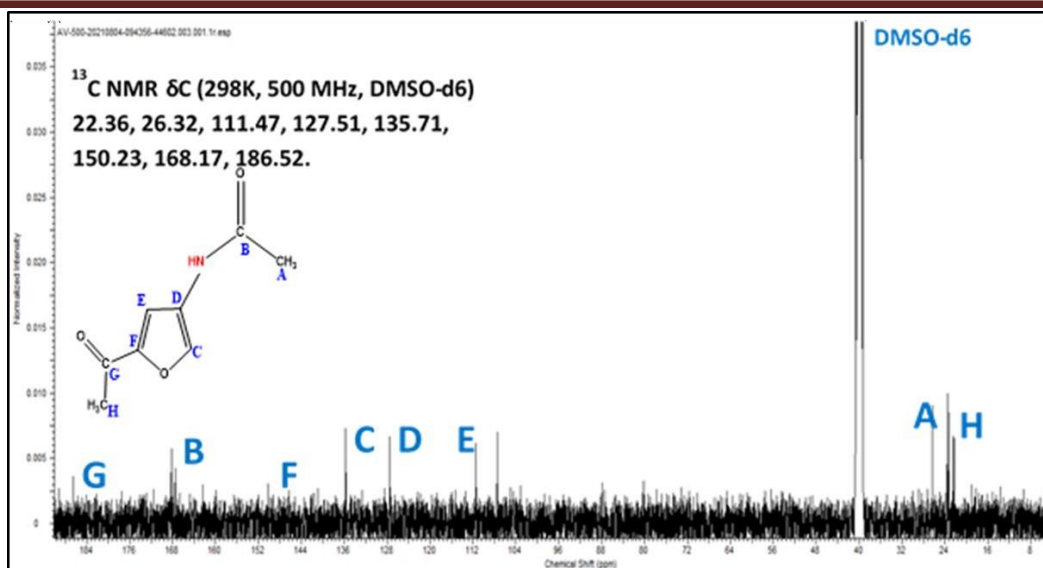


Fig. 4.15: ¹³C NMR spectrum of 3A5AF produced from N-acetyl-D-glucosamine [¹³C NMR δ C (298K, 500 MHz, DMSO-d6) 22.36, 26.32, 111.47, 127.51, 135.71, 150.23, 168.17, 186.52]

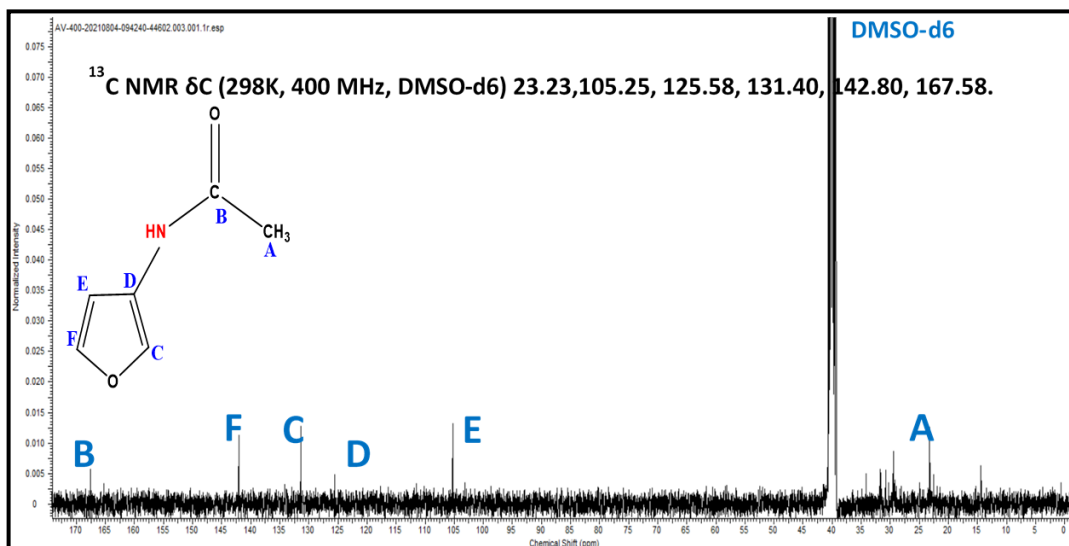


Fig. 4.16: ¹³C NMR spectrum of 3AF produced from N-acetyl-D-glucosamine [¹³C NMR δ C (298K, 400 MHz, DMSO-d6) 23.23, 105.25, 125.58, 131.40, 142.80, 167.58]

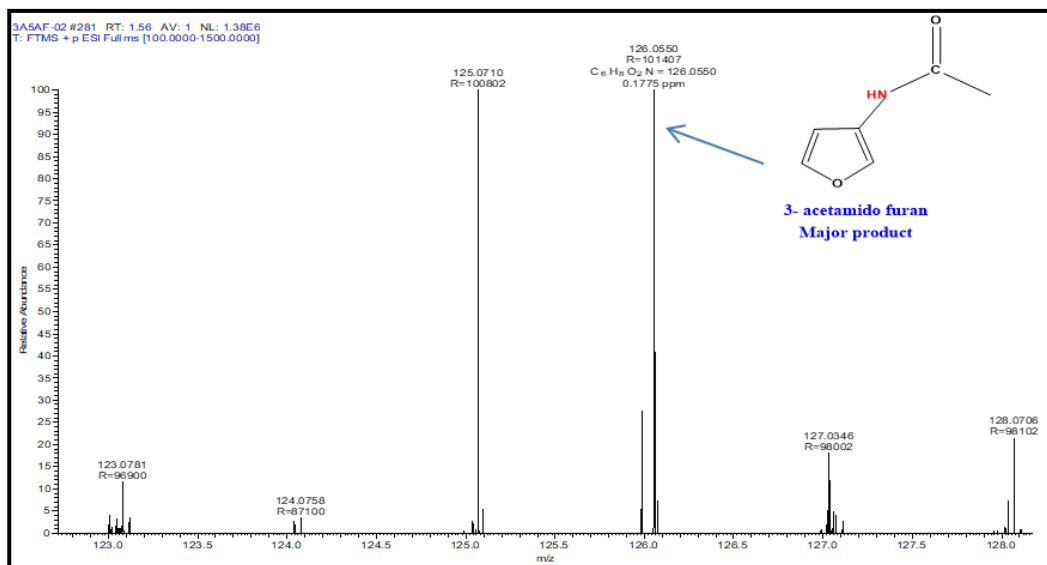


Fig. 4.17: HR-MS chromatogram of 3AF produced from N-acetyl-D-glucosamine.

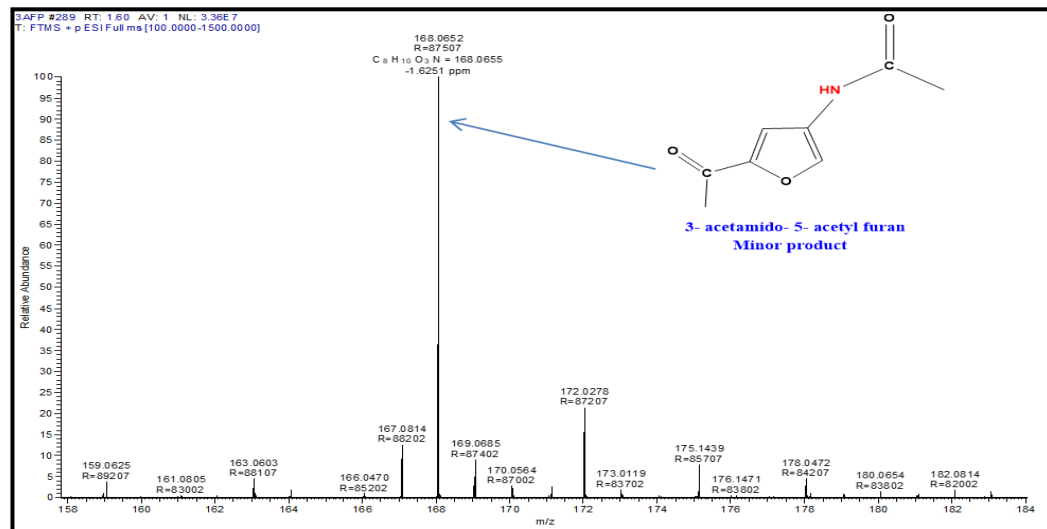


Fig. 4.18: HR-MS chromatogram of 3A5AF produced from N-acetyl-D-glucosamine.

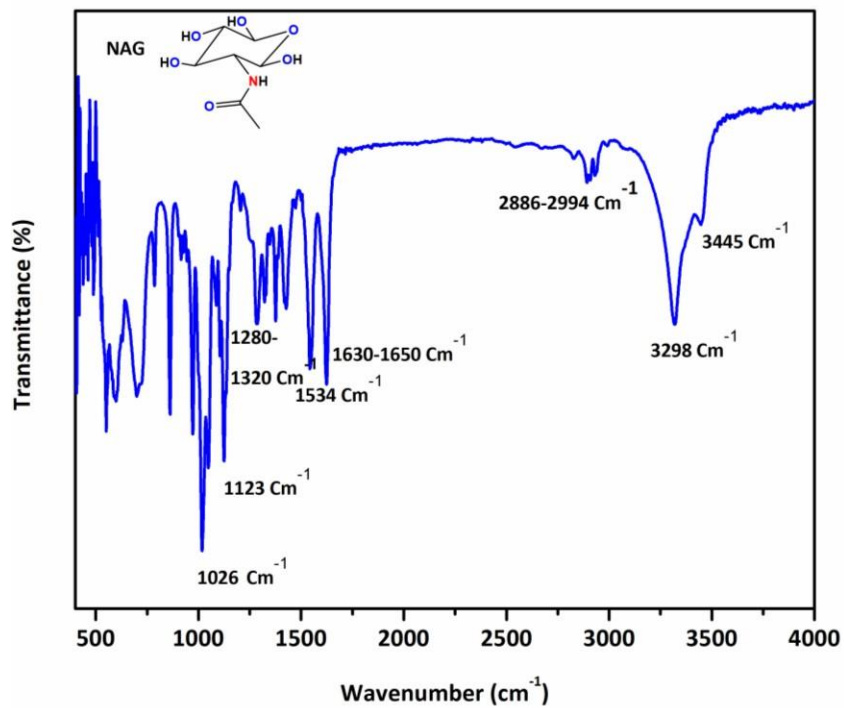


Fig. 4.19: FTIR plot for N-acetyl-D-glucosamine

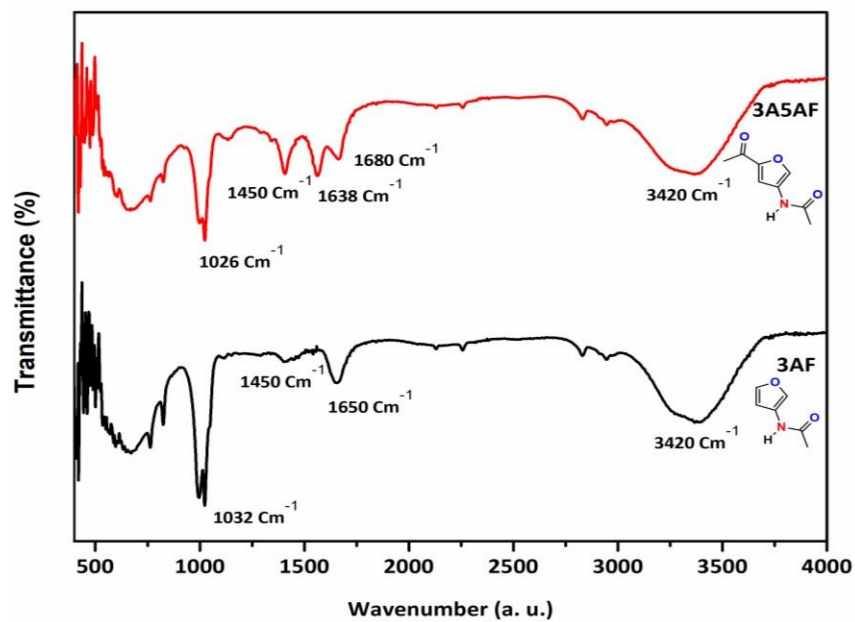


Fig. 4.20: FTIR plot for 3AF and 3A5AF.

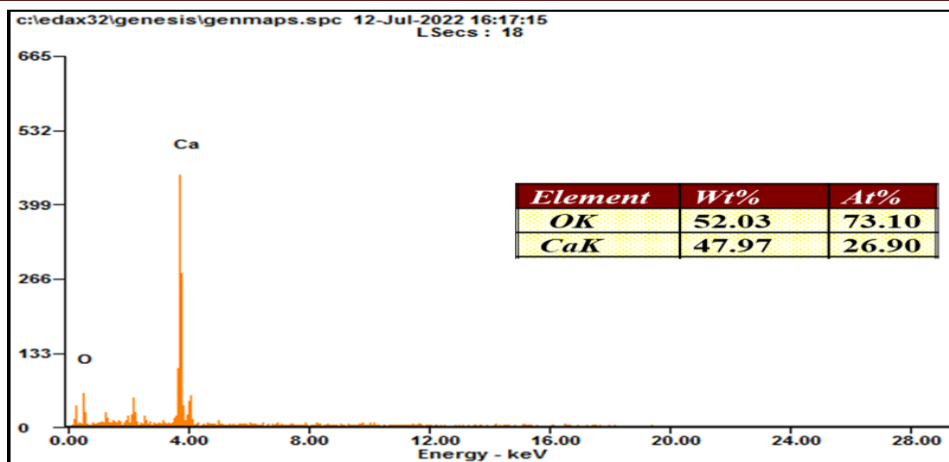


Fig. 4.21: EDS for CaO catalyst

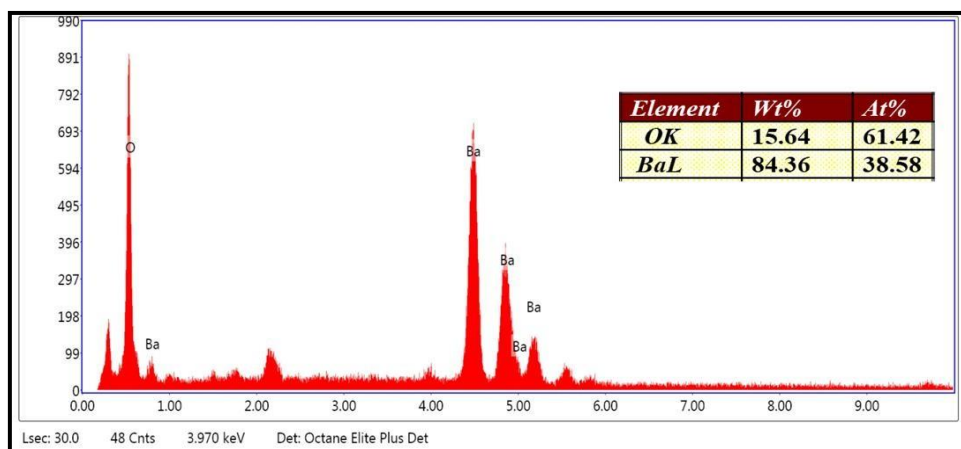


Fig. 4.22: EDS for BaO catalyst.

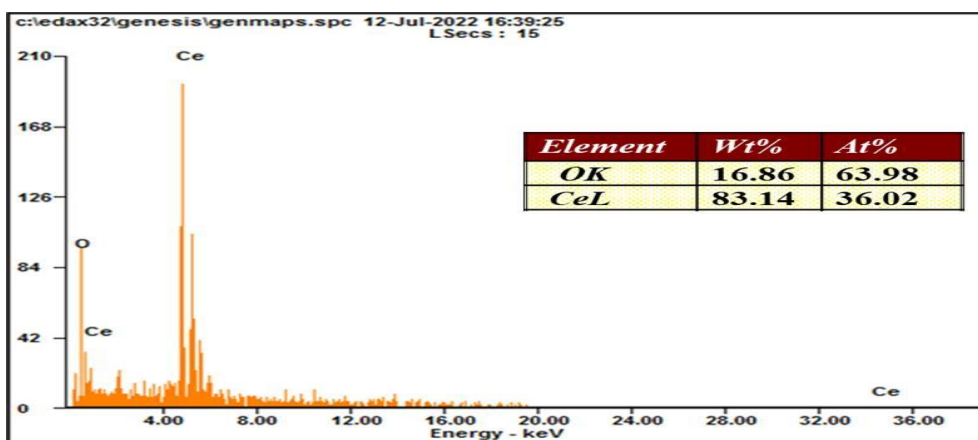


Fig. 4.23: EDS for Ce₂O₃ catalyst.

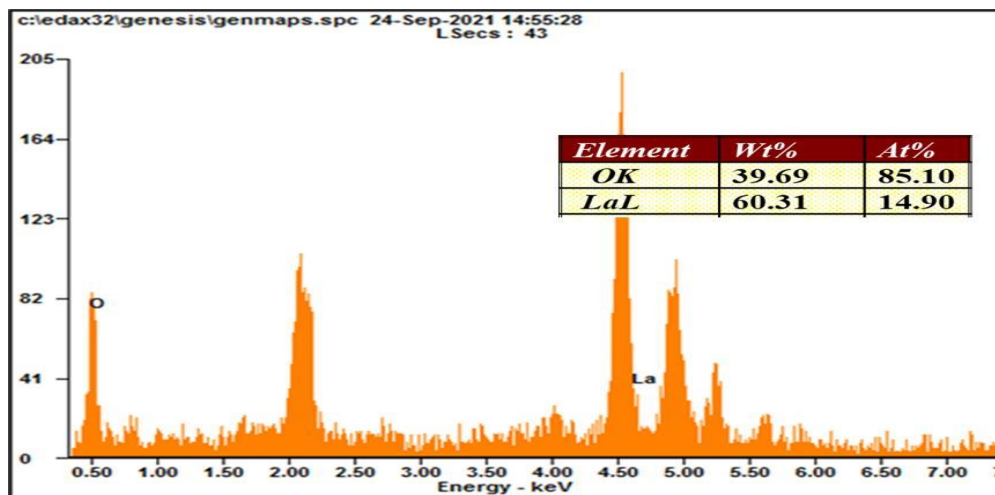


Fig. 4.24: EDS for La_2O_3 catalyst.

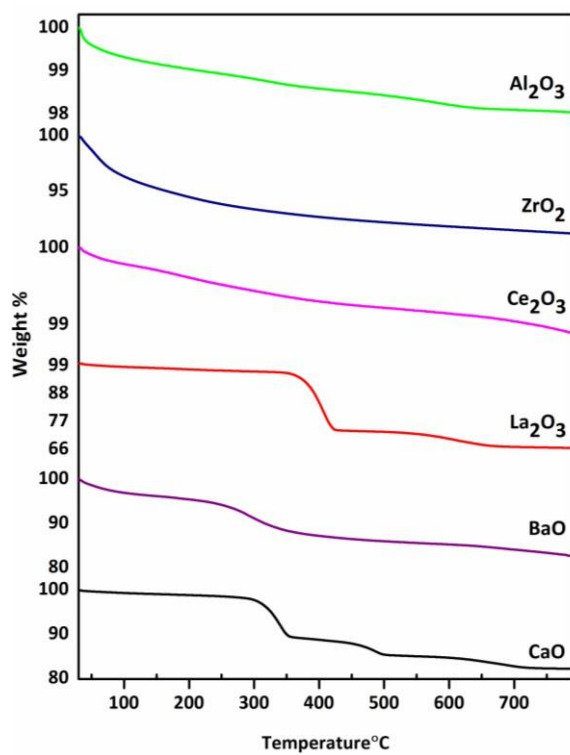


Fig. 4.25: TGA for CaO, BaO, La_2O_3 , Ce_2O_3 , ZrO_2 , Al_2O_3 catalyst.

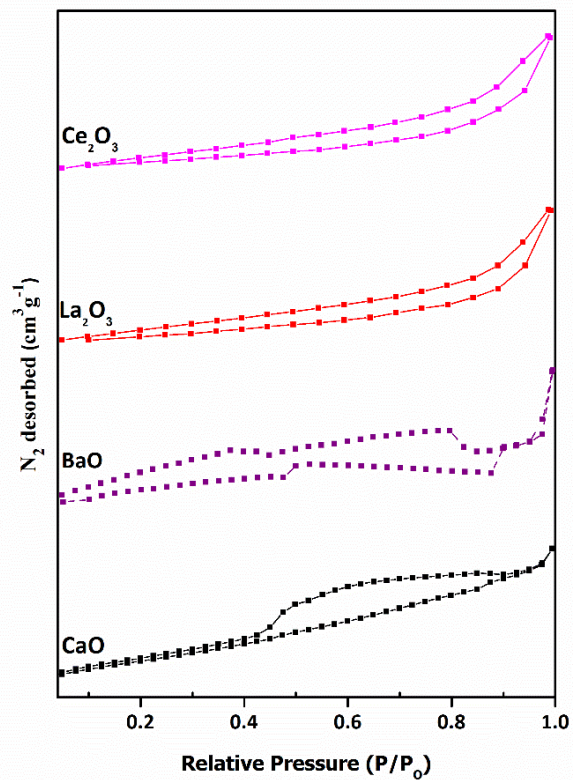


Fig. 4.26 BET Isotherm for various catalysts

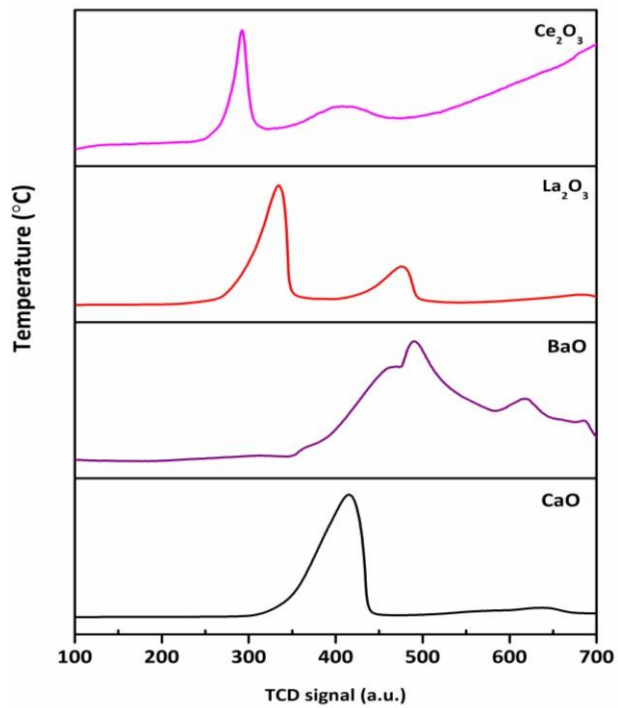


Fig. 4.27 TPD plots for various catalysts.

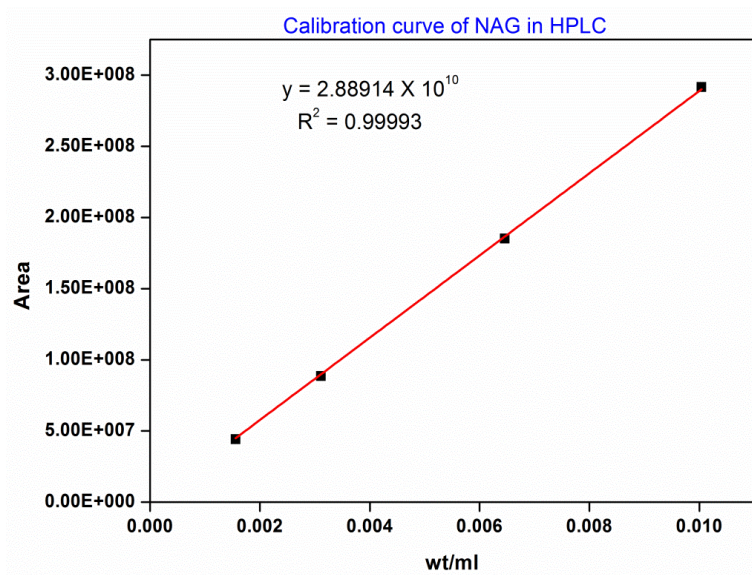


Fig 4.28: Calibration curve of N-acetyl glucosamine (NAG)

6. Conclusion

A comparative study of various metal oxide catalysts such as La_2O_3 , Ce_2O_3 , Al_2O_3 , ZrO_2 , BaO and CaO was undertaken for the dehydration of N-acetyl glucosamine to render important furanic compounds. The physico-chemical properties of the catalyst were studied by XRD, CO_2 -TPD, BET surface area measurements, SEM, HR-TEM, MeOH- FTIR analysis. The parameters such as solvent, temperature, time and substrate concentration were optimized for efficient catalytic activity. Various experiments carried out with organic solvents and their mixtures with water revealed that dioxane was the best solvent for NAG conversion whereas, water was found to inhibit the reaction thereby accelerating the formation of humins. La_2O_3 excel as catalyst for the transformation of N-Acetylglucosamine which yields 50 % 3AF and 19 % 3A5AF at 180 °C in 3h. The superior performance was attributed to the presence of moderate basicity which was Brønsted in nature as confirmed from MeOH-FTIR originating from presence of $\text{La}(\text{OH})_3$. While, FE-SEM, and HR-TEM disclosed existence of nanopores on the catalytic surface. The cooperative effect of Brønsted basicity and nanopores (90-450 nm) were found to play important role in NAG conversion to N-containing platform molecules. We reported for the first time the use of heterogeneous catalyst La_2O_3 to produce 50 % 3AF and 21 % 3A5AF yield which was 10

times more than the yield reported by the pyrolysis method. The catalyst was recyclable upto 4 cycles and easily separable.

References:

1. Nel, W. P.; and Cooper C. J. Implications of fossil fuel constraints on economic growth and global warming. *Energy Policy*. **2009**, *37*, 166—180.
2. Shafiee, S., Topal, E. When will fossil fuel reserves be diminished? *Energy policy*. 2009, *37*, 1, 181-189.
3. Arancon, R. A. D.; Lin, C. S. K.; Chan, K. M.; Kwan, T. H.; Luque, R. Advances on waste valorization: new horizons for a more sustainable society. In *Waste Management and Valorization* Apple Academic Press. **2017**, 23-66.
4. Hülsey, M. J.; Yang, H.; Yan, N. Sustainable routes for the synthesis of renewable heteroatom-containing chemicals. *ACS Sustainable Chemistry & Engineering*, **2018**, *6*, 5, 5694-5707.
5. Hussain, A.; Arif, S. M.; Aslam, M. Emerging renewable and sustainable energy technologies: State of the art. *Renewable and Sustainable Energy Reviews*. **2017**, *71*, 12-28.
6. Gooday, G. W. The ecology of chitin degradation. In *Advances in microbial ecology*. Springer, Boston, MA. **1990**, 387-430.
7. Yan, N.; Chen, X. Sustainability: Don't waste seafood waste. *Nature*. **2015**, *524*, 7564, 155–157.
8. Chen, X.; Yang, H.; Yan, N. Shell biorefinery: dream or reality? *Chemistry—A European Journal*. **2016**, *22*, 38, 13402-13421.
9. Chen, X.; Liu, Y.; Wang, J. Lignocellulosic biomass upgrading into valuable nitrogen-containing compounds by heterogeneous catalysts. *Industrial & Engineering Chemistry Research*. **2020**, *59*, 39, 17008-17025.

10. Chen, X.; Song, S.; Li, H.; Gözaydın, G.; Yan, N. Expanding the boundary of biorefinery: organonitrogen chemicals from biomass. *Accounts of Chemical Research*, **2021**, *54*, 7, 1711-1722.
11. Lucas, N.; Athawale, A. A.; Rode, C. V. Valorization of oceanic waste biomass: a catalytic perspective. *The Chemical Record*. **2019**, *19*, 9, 1995-2021.
12. Elieh-Ali-Komi, D.; Hamblin, M. R. Chitin and chitosan: production and application of versatile biomedical nanomaterials. *International journal of advanced research*. **2016**, *4*, 3, 411.
13. Khoushab, F.; Yamabhai, M. Chitin research revisited. *Marine drugs*, **2010**. *8*, 7, 1988-2012.
14. Younes, I.; Rinaudo, M. Chitin and chitosan preparation from marine sources. Structure, properties and applications. *Marine drugs*. **2015**, *13*, 3, 1133-1174.
15. Raafat, D.; Sahl, H. G. Chitosan and its antimicrobial potential—a critical literature survey. *Microb. Biotechnol.* **2009**, *2*, 2, 186-201.
16. Chen, J.; Wang, M.; Ho, C. T. Volatile compounds generated from thermal degradation of N-acetylglucosamine. *Journal of agricultural and food chemistry*. **1998**, *46*, 8, 3207-3209.
17. Omari, K. W.; Dodot, L.; Kerton, F. M. A simple one-pot dehydration process to convert N-acetyl-D-glucosamine into a nitrogen-containing compound, 3-acetamido-5-acetylfuran. *ChemSusChem*. **2012**, *5*, 9, 1767-1772.
18. Drover, M. W.; Omari, K. W.; Murphy, J. N.; Kerton, F. M. Formation of a renewable amide, 3-acetamido-5-acetylfuran, via direct conversion of N-acetyl-d-glucosamine. *Rsc Advances*. **2012**, *2*, 11, 4642-4644.
19. Chen, X; Chew, S. L.; Kerton, F. M.; Yan, N. Direct conversion of chitin into a N-containing furan derivative. *Green Chemistry*. **2014**, *16*, 4, 2204-2212.

20. Franich, R. A.; Goodin, S. J.; Wilkins, A. L. Acetamidofurans, acetamidopyrones, and acetamidoacetaldehyde from pyrolysis of chitin and n-acetylglucosamine. *Journal of analytical and applied pyrolysis*. **1984**, *7*, 1-2, 91-100.
21. Omari, K. W.; Dodot, L.; Kerton, F. M. A simple one-pot dehydration process to convert N-acetyl-D-glucosamine into a nitrogen-containing compound, 3-acetamido-5-acetylfuran. *ChemSusChem*. **2012**, *5*, 9, 1767-1772.
22. Sadiq, A. D.; Chen, X.; Yan, N.; Sperry, J. Towards the shell biorefinery: sustainable synthesis of the anticancer alkaloid proximicin A from chitin. *ChemSusChem*. **2018**, *11*, 3, 532-535.
23. Bobbink, F. D.; Zhang, J.; Pierson, Y.; Chen, X.; Yan, N. Conversion of chitin derived N-acetyl-d-glucosamine (NAG) into polyols over transition metal catalysts and hydrogen in water. *Green Chemistry*. **2015**, *17*(2), 1024-1031.
24. Dai, J.; Li, F.; Fu, X. Towards Shell Biorefinery: Advances in Chemical-Catalytic Conversion of Chitin Biomass to Organonitrogen Chemicals. *ChemSusChem*. **2020**, *13*, 24, 6498-6508.
25. Pham, T. T.; Chen, X.; Yan, N.; & Sperry, J. A novel dihydrodifuropyridine scaffold derived from ketones and the chitin-derived heterocycle 3-acetamido-5-acetylfuran. *Monatshefte für Chemie-Chemical Monthly*. **2018**, *149*, 4, 857-861.
26. T. T.; Lindsay, A. C.; Kim, S. W.; Persello, L.; Chen, X.; Yan, N.; & Sperry, J. Two-Step Preparation of Diverse 3-Amidofurans from Chitin. *ChemistrySelect*. **2019**, *4*, 34, 10097-10099.
27. Xin, Y.; Shen, X.; Liu, H.; & Han, B. Selective Utilization of N-acetyl Groups in Chitin for Transamidation of Amines. *Frontiers in Chemical Engineering*. **2021**, *2*, 634983.

28. Pham, T. T.; Chen, X.; Söhnel, T.; Yan, N.; Sperry, J. Haber-independent, diversity-oriented synthesis of nitrogen compounds from biorenewable chitin. *Green Chemistry*, **2020**, *22*, 6, 1978-1984.
29. Johdo, O.; Yoshioka, T.; Naganawa, H.; Takeuchi, T.; Yoshimoto, A. New betaclamycin and aclarubicin analogs obtained by prolonged microbial conversion with an aclarubicin-negative mutant. *The Journal of Antibiotics*. **1996**, *49*, 7, 669-675.
30. Shaaban, K. A.; Ahmed, T. A.; Leggas, M.; Rohr, J. Saquayamycins G–K, cytotoxic angucyclines from *Streptomyces* sp. including two analogues bearing the aminosugar rednose. *Journal of natural products*. **2012**, *75*, 7, 1383-1392.
31. Doyle, T. W.; Nettleton, D. E.; Grulich, R. E.; Balitz, D. M.; Johnson, D. L.; & Vulcano, A. L. Antitumor agents from the bohemic acid complex. 4. Structures of rudolphomycin, mimimycin, collinemycin, and alcindoromycin. *Journal of the American Chemical Society*. **1979**, *101*, 23, 7041-7049.
32. Hao, Y. C., Zong, M. H., Wang, Z. L., Li, N. Chemoenzymatic access to enantiopure N-containing furfuryl alcohol from chitin-derived N-acetyl-D-glucosamine. *Bioresources and Bioprocessing*. **2021**, *8*, 1, 1-9.
33. Drover, M. W.; Omari, K. W.; Murphy, J. N.; Kerton, F. M. Formation of a renewable amide, 3-acetamido-5-acetylfuran, via direct conversion of N-acetyl-d-glucosamine. *Rsc Advances*. **2012**, *2*, 11, 4642-4644.
34. Chen, X.; Chew, S. L.; Kerton, F. M.; Yan, N. Direct conversion of chitin into a N-containing furan derivative. *Green Chemistry*. **2014**, *16*, 4, 2204-2212.
35. Qi, X.; Watanabe, M.; Aida, T. M.; Smith Jr, R. L. Efficient one-pot production of 5-hydroxymethylfurfural from inulin in ionic liquids. *Green Chemistry*. **2010**, *12*, 10, 1855-1860.
- 36. Khalaf, W. M.; Al-Mashhadani, M. H. Synthesis and Characterization of Lanthanum Oxide La₂O₃ Net-like Nanoparticles by New Combustion Method. 2021**

37. Singh, A., Palakollu, V.; Pandey, A.; Kanvah, S.; Sharma, S. Green synthesis of 1, 4-benzodiazepines over La_2O_3 and $\text{La}(\text{OH})_3$ catalysts: Possibility of Langmuir–Hinshelwood adsorption. *RSC Advances*. **2016**, *6*, 105, 103455-103462.
38. Li, S. C.; Hu, S. J.; Du, N.; Fan, J. N.; Xu, L. J.; Xu, J. Low-temperature chemical solution synthesis of dendrite-like $\text{La}(\text{OH})_3$ nanostructures and their thermal conversion to La_2O_3 nanostructures. *Rare Metals*. **2015**, *34*, 6, 395-399.
39. Shaikh, S. S.; Patil, C. R.; Kondawar, S. E.; Rode, C. V. Cooperative Acid-Base Sites of Solid Ba-Zr Mixed Oxide Catalyst for Efficient Isomerization of Glucose to Fructose in Aqueous Medium. *ChemistrySelect*. **2020**, *5*, 40, 12505-12513.
40. Yazıcılar, B.; Böke, F.; Alaylı, A.; Nadaroglu, H.; Gedikli, S.; Bezirganoglu, I. In vitro effects of CaO nanoparticles on Triticale callus exposed to short and long-term salt stress. *Plant Cell Reports*. **2021**, *40*, 1, 29-42.
41. Peng, S.; Sun, X.; Sun, L.; Zhang, M.; Zheng, Y.; Su, H.; Qi, C. Selective hydrogenation of acetylene over gold nanoparticles supported on CeO_2 pretreated under different atmospheres. *Catalysis Letters*. **2019**, *149*, 2, 465-472.
42. Romero Toledo, R.; Ruíz Santoyo, V.; Moncada Sánchez, D.; Martínez Rosales, M. Effect of aluminum precursor on physicochemical properties of Al_2O_3 by hydrolysis/precipitation method. *Nova scientia*. **2018**, *10*, 20, 83-99.
43. Matsouka, V., Konsolakis, M., Lambert, R. M., Yentekakis, I. V. In situ DRIFTS study of the effect of structure ($\text{CeO}_2\text{--La}_2\text{O}_3$) and surface (Na) modifiers on the catalytic and surface behaviour of $\text{Pt}/\gamma\text{-Al}_2\text{O}_3$ catalyst under simulated exhaust conditions. *Applied Catalysis B: Environmental*, **2008**, *84*, 3-4, 715-722.
44. Tejani, J.; Shah, R., Vaghela, H.; Vajapara, S.; Pathan, A. Controlled Synthesis and Characterization of Lanthanum Nanorods. *International Journal of Thin Film Science and Technology*. **2020**, *9*, 2, 5.

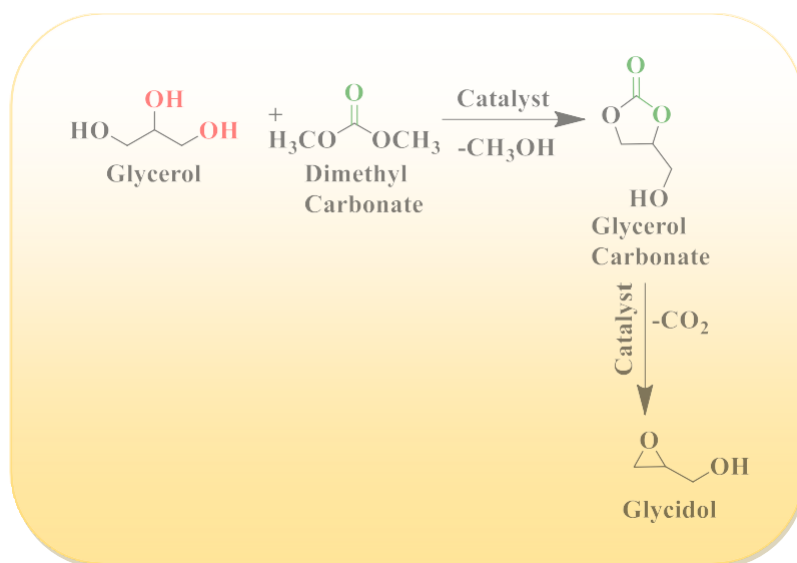
45. Verma, N. K. Study on the controlled growth of lanthanum hydroxide and manganese oxidenano composite under the presence of cationic surfactant. *Advances in Materials*. **2015**, *4*, 11-15.
46. Mu, Q.; & Wang, Y. Synthesis, characterization, shape-preserved transformation, and optical properties of La(OH)₃, La₂O₂CO₃, and La₂O₃ nanorods. *Journal of alloys and compounds*, **2011**, *509*, 2, 396-401.
47. Zhu, H.; Yang, D.; Yang, H.; Zhu, L.; Li, D.; Jin, D.; Yao, K. Reductive hydrothermal synthesis of La (OH) ₃: Tb³⁺ nanorods as a new green emitting phosphor. *Journal of Nanoparticle Research*. **2008**, *10*, 2, 307-312.
48. Fleming, P.; Farrell, R. A.; Holmes, J . D.; Morris, M. A. The rapid formation of La(OH)₃ from La₂O₃ powders on exposure to water vapor. *Journal of the American Ceramic Society*. **2010**, *93*, 4, 1187-1194.
49. Vernekar, D.; Sakate, S. S.; Rode, C. V.; Jagadeesan, D. Water-promoted surface basicity in FeO(OH) for the synthesis of pseudoionones (PS) and their analogues. *Journal of Catalysis*. **2019**, *378*, 80-89.
50. Bailly, M. L.; Chizallet, C.; Costentin, G.; Krafft, J. M.; Lauron-Pernot, H.; & Che, M. A spectroscopy and catalysis study of the nature of active sites of MgO catalysts: Thermodynamic Brønsted basicity versus reactivity of basic sites. *Journal of Catalysis*. **2005**, *235*, 2, 413-422.
51. Bensitel, M.; Saur, O.; Lavalley, J. C. Use of methanol as a probe to study the adsorption sites of different MgO samples. *Materials chemistry and physics*. **1991**, *28*, 3, 309-320.
52. Li, Y.; Lin, J.; Wang, G. La₂O₃/Fe₂O₃-CeO₂ Composite Oxide Catalyst and Its Performance. *Advances in Materials Physics and Chemistry*. **2019**, *9*, 12, 219-233.
53. AL Othman, Z. A. A review: fundamental aspects of silicate mesoporous materials. *Materials*. **2012**, *5*, 12, 2874-2902.

54. Uppal, S.; Arora, A.; Gautam, S.; Singh, S.; Choudhary, R. J.; Mehta, S. K. Magnetically retrievable Ce-doped Fe₃O₄ nanoparticles as scaffolds for the removal of azo dyes. *RSC advances*. **2019**, 9, 40, 23129-23141.
55. Adole, V. A.; Pawar, T. B.; Koli, P. B.; Jagdale, B. S. Exploration of catalytic performance of nano-La₂O₃ as an efficient catalyst for dihydropyrimidinone/thione synthesis and gas sensing. *Journal of Nanostructure in Chemistry*. **2019**, 9, 1, 61-76.
56. Ambroz, F.; Macdonald, T. J.; Martis, V.; Parkin, I. P. Evaluation of the BET Theory for the Characterization of Meso and Microporous MOFs. *Small methods*. **2018**, 2, 11, 1800173.
57. Zang, H.; Lou, J.; Jiao, S.; Li, H.; Du, Y.; Wang, J. Valorization of chitin derived N-acetyl-D-glucosamine into high valuable N-containing 3-acetamido-5-acetylfuran using pyridinium-based ionic liquids. *Journal of Molecular Liquids*. **2021**, 330, 115667.

One pot glycidol synthesis via glycerol transesterification with DMC over mixed metal oxide

Abstract:

The present article discloses use of metal oxides and mixed metal oxide of Sr:Cu:Al (2-4-4) as a heterogeneous catalysts for one pot synthesis of glycidol and process for its separation from the reaction crude. Various metals like Na, Mg, Ca, Sr, Ba, Cs, Rb were mixed with Cu-Al catalyst by co-precipitation method and their activity performance for one pot glycidol synthesis was studied. The detailed characterization of the prepared catalysts by BET, XRD, XPS, FE-SEM, HR-TEM and FTIR technique confirmed the presence of Cu^{+2} (CuO and CuAl_2O_4) as well as Cu^{+1} responsible for the efficient formation of the product GD. One-pot synthesis of GD over Sr-Cu-Al (2-4-4) mixed oxide catalyst achieved 66 % selective formation of GD with the expense of 78 % glycerol conversion as shown in the **Scheme 1** below.



Scheme 5.1. One pot synthesis of glycidol *via* glycerol transesterification of glycerol.

5.1 Introduction:

Abundant availability of glycerol through biodiesel synthesis made enforcement for the use of glycerol as a feedstock for the synthesis of various attractive chemicals like, diols, carbonates (both linear and cyclic), esters, lactic acid *etc.* One of the 12 principles of green

chemistry favours the use of bio-derived platform chemicals for the production of value-added chemicals, this has attracted the attention of the upcoming researchers towards the glycerol conversion as it has several industrial applications.

Glycerol is considered one of the top most 12 bio-derived platform molecules. The most interesting aspect of glycerol is its versatile reactivity to produce broad spectrum of compounds like acrolein, acrylic acid, lactic acid, 1,2-propanediol, 1,3-propanediol, allyl alcohol, dihydroxyacetone, hydroxyacetone, glycerol carbonate, and glycidol. Recently, glycidol (GD) has got the special attention of researchers because of its potential applications in different industries. World market price of glycidol ranges US \$ 15-18/kg which is high enough as compare to glycerol (US \$ 0.2-0.5/Kg). Hence, glycidol is a high value product with elevated demand in the commercial market. Glycidol can serve as a monomer for the synthesis of polymers like polyurethane, polycarbonate, and polyesters^[1-3] which fulfil the day-to-day life needs of modern society. Similarly, GD can serve as a raw material for the manufacture of glycidyl ethers and pharmaceuticals as well as in perfumes and cosmetics, detergents, paints, de-emulsifiers, and dye-leveling agents.^[4] It can also hand out as a plastic modifier, surfactant, and fire retardant.^[5-7] Glycidol is also having some medicinal value where it has application in analgesic and antiviral drugs actively functions against HIV (EP). Thus, the glycidol production from biomass based starting materials finds its way to replace the exhausting fossil fuel-based materials and this provides a better, cost effective and efficient pathway for the production of value-added products. A short review published by Prete et al. discusses the synthesis of various organic compound derived from glycidol having wide spread industrial applications. For eg. 1, 2 and 1, 3-propanediol, glycerol carbonate, sol-ketal, monoalkyl glyceryl ethers, and polymers.^[8]

Conventionally, glycidol is produced by the epoxidation of allyl alcohol with H_2O_2 as the oxidizing agent catalyzed by tungsten/ vanadium oxide-based catalyst. The second route involves the use of biomass derived glycerol which on treatment with Lewis or Brønsted acid catalyst produces bio-based epichlorohydrin. Epichlorohydrin has wide range of industrial applications world-wide as it is used as a monomer for the production of epoxy resins and various intermediates for the synthesis of polymers. The epichlorohydrin has huge demands and a market value of 1.8-2.5 US \$/Kg. The reaction of epichlorohydrin with bases or caustic leads to 47 % glycerol conversion with 92 % glycidol production.^[9, 10] Both the routes have major disadvantages of multistep synthesis, separation of glycidol from the reaction mixture,

decomposition of tungsten during the process eventually leading to higher product costs and generation of stoichiometric amount of inorganic wastes, thus, far from sustainability.

In the literature, one pot consecutive liquid phase GD synthesis was also studied extensively, by using urea or dimethyl carbonate as a carbonylating agent for glycerol transesterification followed by GC decarboxylation to GD and CO₂. The glycidol synthesis from glycerol carbonate was first reported by Malkemus *et al.* and Currier *et al.* by using a metal salt as homogeneous catalyst to produce 80-90 % glycidol at 175-225 °C and at low pressure in a continuous flow (1-100 mm of Hg).^[11] Gaset *et al.* reported and patented the use of Zeolite-A for the production of 72 % glycidol by using Glycerol as a substrate in 1 h, at low pressure and 185 °C temperature.^[12] Lee *et al.* employed Zn(OAc)₂ as a homogeneous catalyst for glycerol transesterification with urea in the presence of acetonitrile as a solvent yielded 67 % GD within 1.5 h.^[13]

Until recently, the one-pot synthesis of GD from GL and DMC has relied on a variety of homogeneous and heterogeneous catalysts, including tetraethylammonium amino acid ionic liquid, KF/sepiolite, tetramethylammonium hydroxide ionic liquid, and NaAlO₂. A number of one-pot GD syntheses using GL and DMC have recently been reported.^[14-17] Tetraethylammonium pipercolinate ([N2222][Pipe]) was used to produce 79 % GD with 96 % conversion of GL, by Zhou and colleagues. The results were presented using density functional theory (DFT), which revealed the carboxyl group in ([N2222][Pipe]) had outstanding performance, providing an efficient substrate activation.^[18] Parameswaram *et al.* reported that the increased basic strength of the Mg/Zr/Sr (3:1:1) MMO catalyst enhanced the decarboxylation of the glycerol carbonate to selectively yield 40 % glycidol. The catalytic activity was due to the presence of high basic character and homogeneous distribution of SrO and stability of ZrO₂ phase over MgO.^[19] In addition, Elhaj and associates reported that one of the synthesized series of functionalized quaternary ammonium salt ionic liquids produced 87 % GD with 96 % GL conversion. Elhaj *et al.* reported the catalytic transesterification of glycerol in the presence of KNO₃/Al₂O₃ nanoparticle. The solid base catalyst was prepared by wet impregnation method and the catalytic activity was attributed to the presence of K₂O to produce 64 % glycidol with 95 % glycerol conversion at 70 °C and 120 min.^[20-21] Our approach for the one pot glycidol synthesis *via* glycerol transesterification with DMC, has various merits over the conventional routes such as, simple catalyst system, short reaction

time, complete recovery of solvent with product separation and practical yield of desired product.

5.2 Experimental Section

5.2.1 Chemicals: glycerol, dimethyl carbonate, methanol, ethanol, acetonitrile, iso-propanol, dimethyl formamide, distilled water obtained by distillation followed by filtration.

5.2.2 Experimental procedure

Typical co-precipitation method was used to synthesize nano-size Sr-Cu-Al mixed metal oxide (MMO) catalyst under alkaline conditions and their detail experimental procedure is discussed in Chapter 2 (Section 2.3.9). The prepared catalysts were characterized by XRD, BET-surface area, HR-TEM, SEM-EDX, FT-IR, Py-IR, and XPS technique as mentioned in Chapter 2 (sections 2.4.1- 2.4.4, 2.4.6, and 2.4.13, respectively).

The Catalyst activity testing was done in a 50 mL parr autoclave assembly glycerol and dimethyl carbonate in 1:3 molar ratio charged along with 20 mL of methanol. Catalyst of 100 mg was also added and reaction was carried out at 140 °C for 90 min with 1000 rpm stirring. Product mixture was filtered to separate catalyst and sample from mother liquor was injected to GC for analysis. At the end of reaction, the catalyst was recovered by filtration and washed three times with 10 mL DI water, then dried at 120 °C overnight in a vacuum oven followed by calcination at 550 °C for 3 h and reused

5.3 Results and discussion

5.3.1 Catalyst Characterization

5.3.1.1 Brauner Emmet and Teller (surface area) and Temperature Programmed Desorption analysis

Table 5.1 reveals the physico-chemical properties of the screened catalysts. The N₂ adsorption- desorption isotherm gives detailed information of the total surface area, pore volume and pore width of the catalyst calculated using BJH method. The N₂ adsorption-desorption isotherms reveals the BET surface area of the catalysts which was found to be 280 m²/g for Cu-Al (5-5) and 37.89 m²/g for Sr-Cu-Al (2-4-4). The Cu-Al (5-5) exhibited pore volume of about 1.132 cc/g and pore width of 8.922 nm which was found to decrease in case of Sr-Cu-Al (2-4-4) 0.125 cc/g and 5.689 nm respectively, which indicated mesoporous

nature of both the catalysts. This decrease in the surface area may be due the incorporation of the Sr in the $\text{CuAl}_2\text{O}_4/\text{Cu-Al}$ lattice which was confirmed by XPS and XRD technique. Sr doping in the Cu-Al catalyst affected on the surface area and pore volume (considerable decrease) might be due to blocking of the pores on the surface. From **Fig. 5.1** it is clear that both the catalysts Cu-Al and Sr-Cu-Al exhibited Type-IV isotherm profiles with H-3 type of hysteresis loop located in the range 0.5 to 0.9 consistent with the cavitation induced evaporation and confirmed the mesoporous nature of the catalyst. [22-23]. As, compared with the fresh catalyst around 80 % decrease in the surface and 9-fold decrease in the pore volume was observed this may be due to sintering of Cu as a result of its exposure to high temperature. Type-IV isotherm revealed the relationship between the shape of the hysteresis loop and the textural properties such as pore size distribution, pore volume, pore geometry and pore connectivity in case of meso-porous nature of the catalysts [24-25]. Both the catalysts exhibited isotherm which represents (mixed morphology from SEM-cube, rod and sheet) like particles thereby giving rise to slit shaped pores present at the catalytic surface responsible for enhanced catalytic activity thereby resulting in selective (66 % selectivity and 78 % conversion) formation of GD.

Table 5.1. Physico-chemical properties of prepared catalyst.

Sr. No.	Catalyst	Surface Area (m^2/g)	Pore volume (cc/g)	Pore width (nm)
1	Cu-Al (5-5)	280	1.132	8.922
2	Sr-Cu-Al (2-4-4)	37.89	0.125	5.689

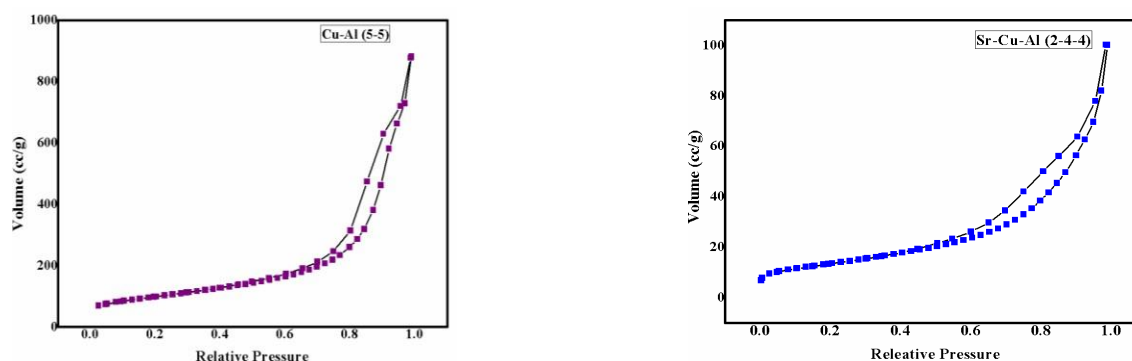


Figure 5.1. N_2 adsorption-desorption isotherm for prepared catalyst.

5.3.1.2 X-ray diffraction

Fig. 5.2 a reveals the typical wide angle XRD of bare SrO (space group Fm3m) with reflections at $2\theta=25.8^\circ$ (110), 35.0° (200), 38.5° (101), 48.2° (400), 61.3° (311), 74.15° (400). The data matches with the JCPDS Powder Diffraction File No. 75-0263. However, some low intense peaks at $2\theta = 26.2^\circ$ (110), 28.9° (101), 37.8° (111), 72.3° (131) were observed which correspond to the $\text{Sr}(\text{OH})_2$ [JCPDS Powder Diffraction File No. 71-2365]. The appearance of sharp peaks for both SrO and $\text{Sr}(\text{OH})_2$ suggests the highly crystalline nature of the compound.^[26] **Fig 5.2 b** gives the reflections at $2\theta=38.8^\circ$ (222) for Cu and Al mixed oxide phase with 1:1 ratio showing slight broadening of the peaks as compare to SrO, suggesting slight amorphous nature of the Cu-Al (1-1) composition. **Fig 5.2 c** diffractogram reveals strong reflections at $2\theta= 35.3^\circ$ (110), 38.78° (011), 48.65° (202), 58.52° (022), 61.6° (113), 66.11° (311), 68° (220) corresponds to Cu-Al mixed oxides phase. The reflections at $2\theta= 35.3^\circ$ and 38.78° (111) confirmed the presence of CuO phase [JCPDS 80-1268] and Cu_2O with $2\theta = 38.78^\circ$ (101) [JCPDS 75-2357] and Al_2O_3 ^[27]. The incorporation of Sr (in varying ratios) in to Cu-Al mixed oxide lattice showed diffractogram as shown in **Fig. 5.2 c, d, e.**^[28] The peaks at $2\theta = 38.2^\circ$ (211), 49° (312), 53° (400) revealed the presence of SrCuO_2 mixed oxide phase.^[29] There were no peaks observed for the metal carbonate phase.

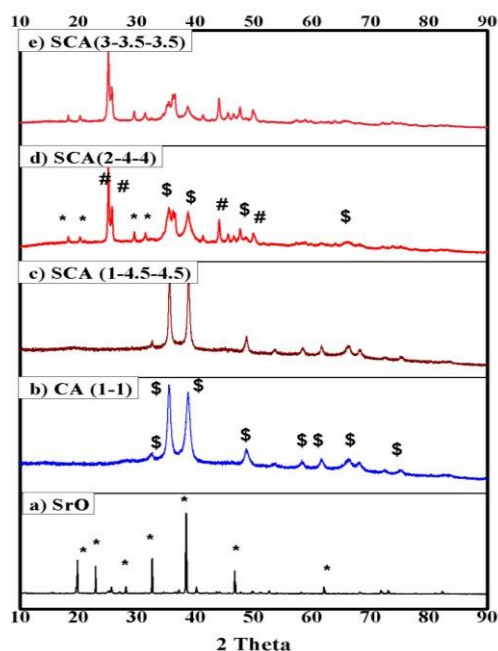


Figure 5.2. Wide angle XRD patterns of bare SrO and Mixed oxides of Cu-Al and Sr at various ratios.

5.3.1.2 Fourier Transform Infrared spectroscopy

Fig. 5.3 gives the detailed FTIR analysis in the range 400-4000 cm^{-1} . The FTIR spectrum of Sr-O showed a characteristic metal oxide peak at 616 cm^{-1} which could be ascribed to the Sr-O stretching vibration. The sharp band at 1332 cm^{-1} for OH-bending and a broad but weak band at 3457 cm^{-1} for longitudinal OH-stretching confirmed the presence of adsorbed water molecule at the catalytic surface.⁽³⁰⁾ Whereas, there was no presence of hydroxyl peak in the spectra. In case of Cu-Al catalyst the presence of broad peak at 595 cm^{-1} was assigned to Cu-O stretching vibration and the bands at 528 cm^{-1} could be assigned to Cu (II)-O ie. metal oxide stretching vibrations. The presence of a broad peak at 3435 cm^{-1} was assigned to the OH stretching and 1343 cm^{-1} for OH-bending vibration due to the adsorption of water molecule from the atmosphere at the in the interlayers.⁽³¹⁾ The peak at 455 cm^{-1} and at 848 cm^{-1} was ascribed to the presence of Cu-O and Al-O stretching vibration. Whereas, in case of Sr-Cu-Al there was presence of 600 cm^{-1} assigned to the Sr-O stretching vibration and 455 cm^{-1} and at 848 cm^{-1} ascribed to presence of Cu-O and Al-O stretching vibrations respectively which confirmed the doping of Sr on Cu-Al support.⁽³²⁾ The presence of broad band at 3600 cm^{-1} due to OH stretching vibration and 1430 cm^{-1} for OH-bending was an indication of the presence of adsorbed water molecule at the interlayers in the catalyst.

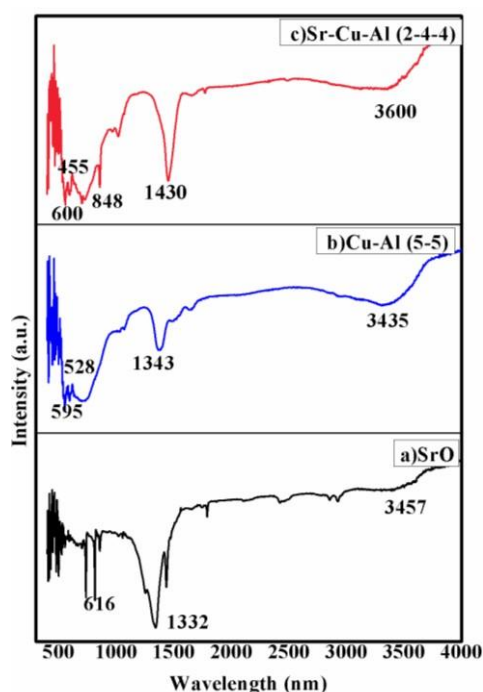


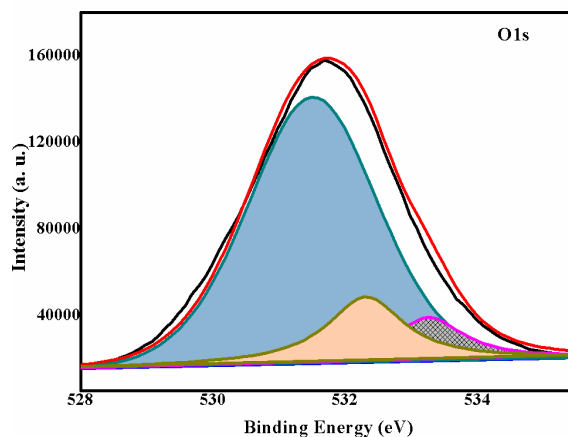
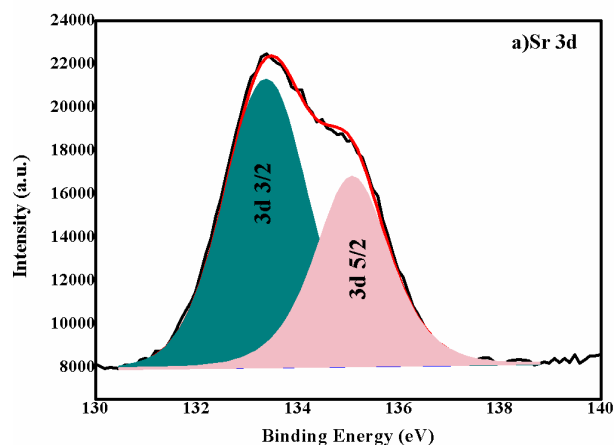
Figure 5.3. FTIR spectra for the prepared catalyst.

5.3.1.3 X-ray photoelectron spectroscopy

Fig. 5.4 represents X-ray photoelectron spectra of Sr-Cu-Al catalyst. In which **Fig. 5.4 (a)** clearly showed a doublet of Sr 3d for Sr 3d_{3/2} and Sr 3d_{5/2} spin orbital states due to two crystallographic positions observed for Sr⁺² at B.E. of 133.7 and 135.08 eV, respectively which could be attributed to the presence of bond between Sr and the perovskite matrix as shown in **Table 5.2**. This was found in good agreement with the literature reports.⁽³³⁾ XPS spectra of O 1s (**Fig. 5.4 b**), after deconvolution showed three peaks at B.E. of 533, 532.3 and 532.1 eV out of which peaks at B.E. of 533, 532.3 eV corresponded to Sr-O, Cu₂O bridging oxygen atoms in the metal oxide framework while, the peak at B.E. of 532.1 eV was assigned to non-bridging oxygen atoms as O-Cu. Cu 2p_{3/2} XPS shows a peak at 934.5 eV.⁽³⁴⁻³⁵⁾ In the Al 2p region two distinct peaks were observed at 74.3 eV and 74.8 eV for SrAl₂O₄ and Al₂O₃ respectively. The intense peak in the XPS spectra were observed due to the primary photoemission from Cu (II) O state whereas, the doublet is observed in case of Sr due to the transfer of one or two electrons from filled 2p orbitals of oxygen species into the vacant 3d orbital of Sr species. The XPS spectra of reused catalyst showed retention of all the peaks at same binding energy, which clearly suggest there was not any considerable change in oxidation state of metals after use of the catalyst.

Table 5.2 Binding energy and peak area for the two-core level excitation in Sr-Cu-Al catalyst.

Sr. No.	Core level	Binding Energy (eV)	Peak Area
1	3d _{3/2}	133.70	27500
2	3d _{5/2}	135.08	16900



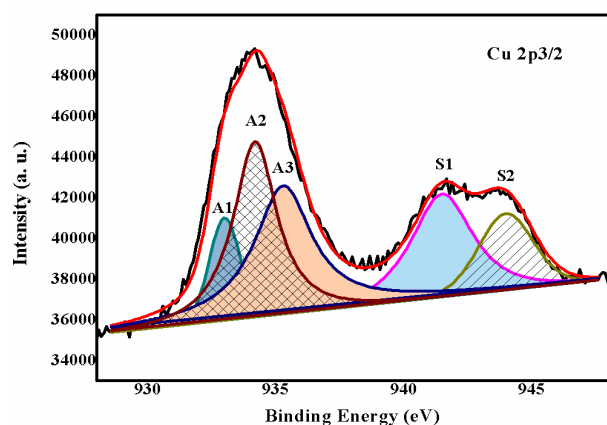


Figure 5.4. a-c High-resolution spectra (core XPS spectra) of Sr 3d, O 1s, Cu 2p, respectively.

5.3.1.4 A Field emission scanning electron microscopy (FE-SEM) and EDAX analysis

Figure 5.5 shows the morphology for bare SrO, Cu-Al (1-1), Sr-Cu-Al (2-4-4) estimated from FE-SEM imaging by epitaxial scanning (**Fig. 5.5 a, b, c**) and their elemental composition was estimated from E-DAX patterns (**Fig. 5.5 i, ii, iii**). Uneven, unordered sheet shape morphology with varying shape and size was observed in case of SrO as shown in **Fig 5.5 a**, whereas, Cu-Al catalyst exhibited defined mixed morphology of cube, rod and sphere shape particles.

The diameter of the spheres was found in the range 40-85 nm (**Fig. 5.5 b**). In **Fig. 5.5 c** after Sr doping in Cu-Al catalyst the morphology changed forming wide sheets of Cu-Al of varying size and uneven shape with cube, and spherical shaped particles well decorated all over the sheets.

E-DAX patterns matched approximately the elemental composition of corresponding oxide. In case of SrO it confirmed the presence of 72.38 Wt. % of Sr and (O) 27.62 Wt. %, Cu was 33.84 Wt. %, Al was 26.38 and (O) 39.78 Wt. % in Cu-Al (1:1) and in case of Sr-Cu-Al (2-4-4) the elemental composition was found to be Cu 22.45 Wt. %, Sr 38.32 Wt. %, Al 10.76 Wt. %, (O) 28.47 Wt. % as shown in respective Tables in the image in **Fig 5.5 (i, ii, iii)** respectively.

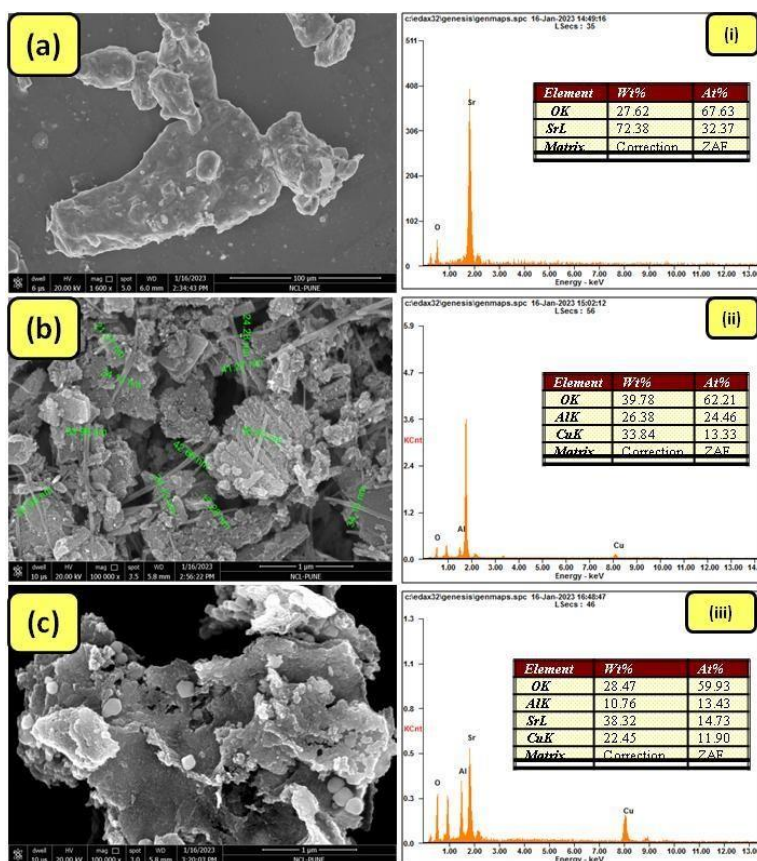


Figure 5.5. FESEM images and corresponding EDAX pattern (i, ii, iii) for a), SrO, b) Cu:Al (1:1) and c) Sr-Cu-Al (2-4-4).

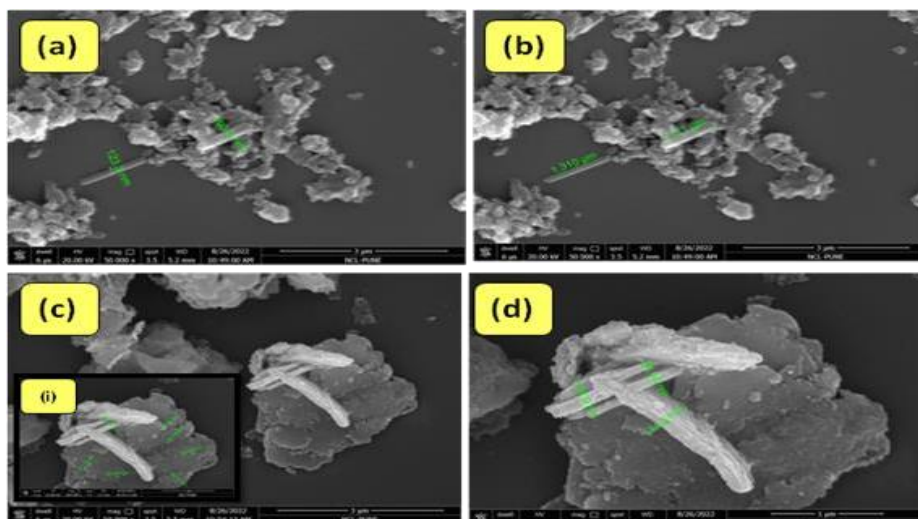


Figure 5.6. FE-SEM images of Sr-Cu-Al catalyst, a) Sr:Cu:Al (3-3.5-3.5), b) Sr:Cu:Al (3-3.5-3.5), c) Sr:Cu:Al (4-3-3), d) Sr:Cu:Al (4-3-3)

5.3.1.4 B Field emission scanning electron microscopy (FE-SEM) analysis for MMO in varying ratios

The **Fig. 5.6** illustrates the morphology of the prepared Sr-Cu-Al catalyst in varying ratios a) Sr:Cu:Al (3-3.5-3.5), b) Sr:Cu:Al (3-3.5-3.5), c) Sr:Cu:Al (4-3-3), d) Sr:Cu:Al (4-3-3) by co-precipitation method. **Fig. 5.6 (a, b)** showed the presence of mixed morphology containing spheres, cube and spherical shaped particles well distributed at the surface of the catalyst along with the presence of sheets of uneven and unordered morphology. The diameter of the spheres was found in the range 123-193 nm and the length of the spheres were found to be 1.1-1.3 μm . The **Fig. 5.6 (c, d)** represents the magnified view of the Sr:Cu:Al (4-3-3), d) Sr:Cu:Al (4-3-3) catalyst. It showed the presence of spherical shaped particles as well as large spheres deposited and well distributed over the larger uneven sheets. The size of the spherical particles was found in the range 30-45 nm and the diameter of the spheres was found to be in the range 84-135 nm. It was clearly observed that with increasing the ratio of Cu-Al in the catalyst the spherical morphology dominated over the spherical shaped particles.

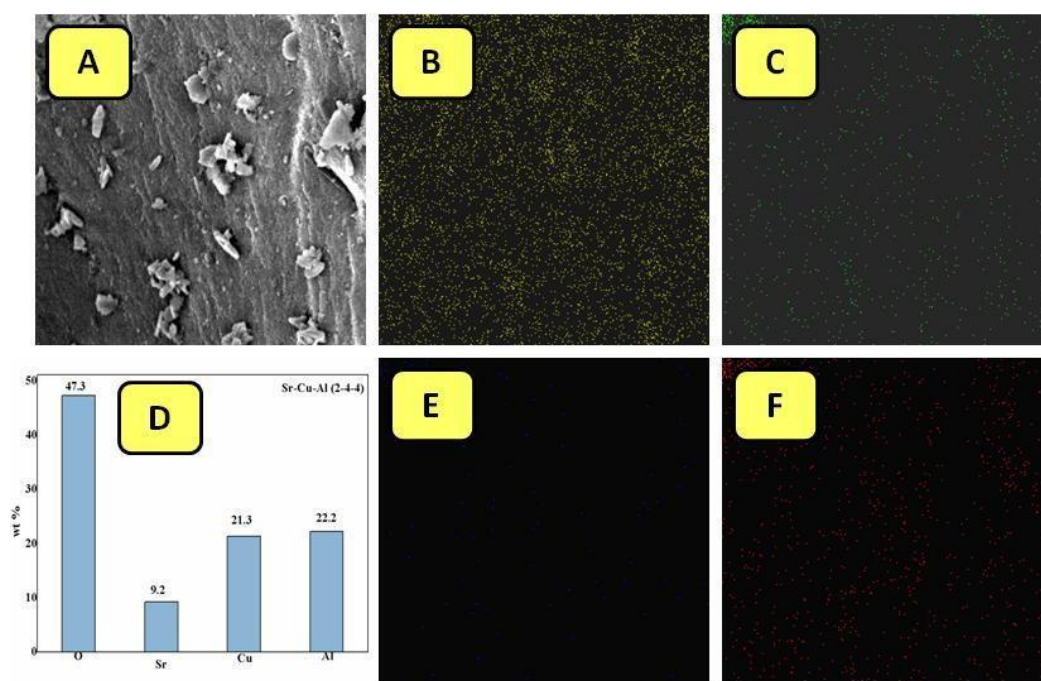


Figure 5.7. Elemental mapping images of Sr-Cu-Al catalyst, A) FESEM image, B) CuK, C) AlK, D) Sr-Cu-Al (2-4-4) elemental composition E) SrL, F) OK

5.3.1.4 C Elemental mapping

Fig. 5.7 presents the elemental mapping images of the optimized catalyst Sr-Cu-Al catalyst, A) FE-SEM image, B) CuK, C) AlK, D) Sr-Cu-Al (2-4-4) elemental composition E) SrL, F) OK. **Fig. 5.7 A)** showed the presence of well distributed spheres and spherical shaped particles on the uneven sheets with the sphere-shaped particle morphology dominating.

The dispersion pattern of Cu, Al, Sr, (O) was revealed by the elemental mapping images **Fig. 5.7. B-F** respectively. Cu was shown in yellow whereas Al was shown in green and Sr in orange. The oxygen species present in all the three metals was shown in blue colour. The EDAX pattern of the catalyst (**Fig. 5.7 D**) revealed that (O) was almost 47 % by weight, Sr was 9 % by weight, Al was 22 % by weight and Cu was found to be 21 % by weight.

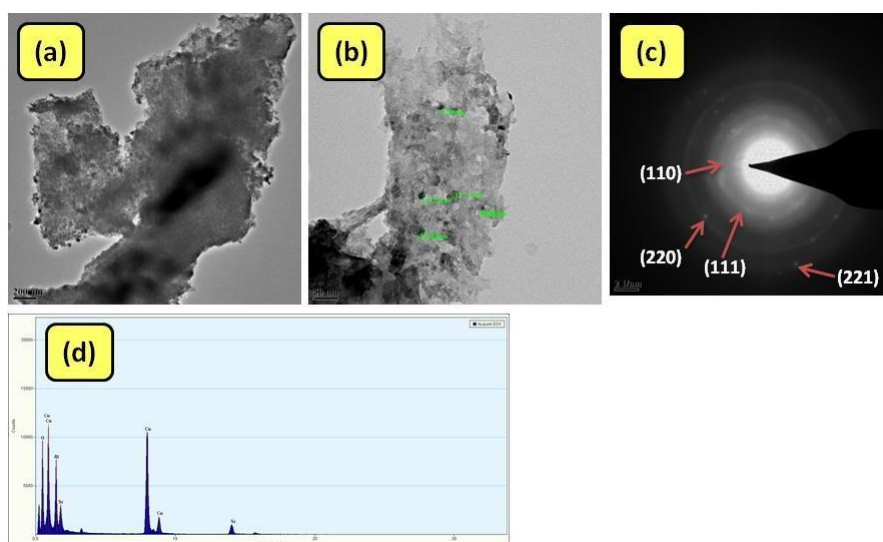


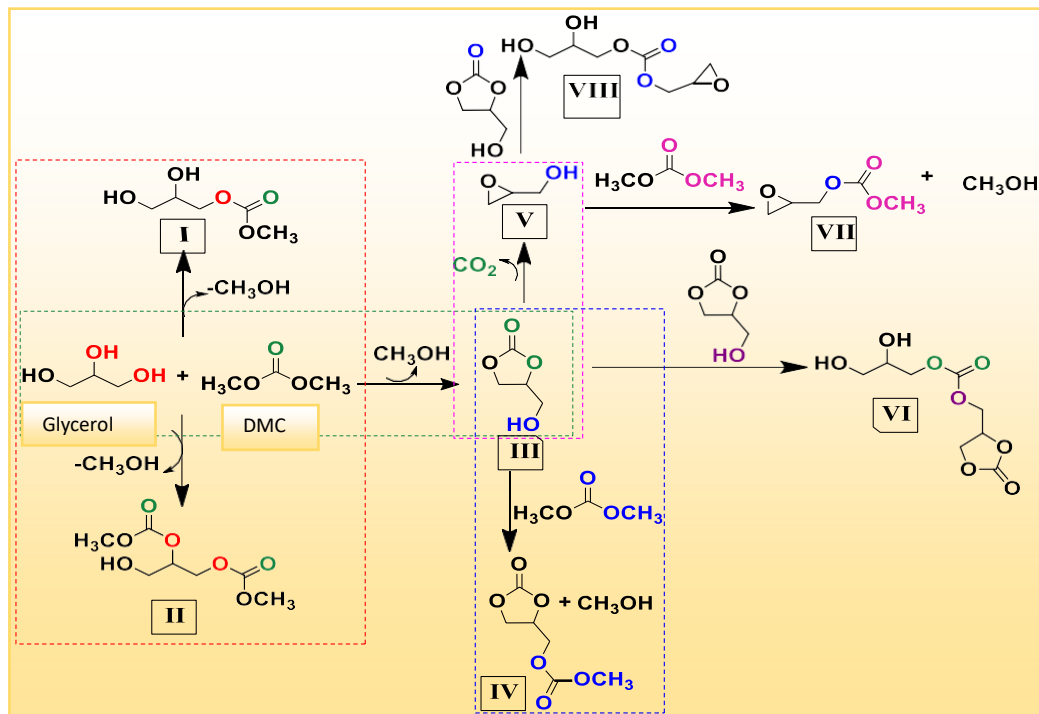
Figure 5.8. HRTEM images for Sr-Cu-Al (2-4-4) catalyst.

5.3.1.5 High Resolution-Transmission emission Microscopy analysis

Fig. 5.8. a-d HRTEM images for Sr-Cu-Al (2-4-4) catalyst. The image as shown in **Fig. 5.8 a-b** revealed the presence of various minute pores at the catalytic surface well distributed all over. The image **Fig. 5.8 c** represents the SAED pattern of the catalyst which showed the presence of characteristic planes (110), (111), (220), (221) which corresponded to the presence of SrO, Sr(OH)₂, CuO, Cu₂O and Cu-Al mixed phase as conformed by the XRD

analysis as shown in **Fig. 5.8 a** above. The image **Fig. 5.8 d** shows the elemental composition and it confirmed the presence of Sr, Cu, Al and (O) in the catalytic sample.

5.4 Activity performance



Scheme 5.2 Glycerol transesterification with DMC to produce Glycidol.

One pot synthesis of Glycidol by transesterification of glycerol over DMC:

The Lewis basic sites on the Sr-Cu-Al catalyst surface first activate the glycerol molecule, abstracting the acidic proton from the primary -OH group of the glycerol molecule, and then the Lewis acidic sites on the Cu-Al catalyst surface activate the carbonyl group of the DMC. Additionally, the attack of nucleophilic sites at the electronegative oxygen atom of the glycerol OH group on the electrophilic carbonyl carbon of the dimethyl carbonate leads to the elimination of the methanol together with the removal of the methoxy group. Following that, the attack of secondary -OH group of glycerol on the dimethyl carbonate's carbonyl carbon results in the formation of glycerol carbonate, which eliminates the second molecule of methanol. The next process is cyclization, which produces glycerol carbonate (III). Once GC is formed, the Lewis basic sites present at the catalytic surface (Sr-Cu-Al) of Sr particularly result in the abstraction of the acidic proton of the primary -OH group of glycerol carbonate followed by the cleavage of the carbon-oxygen bond (C-O) at the 1-2 and the 3-4 position of the ring due to the nucleophilic attack of the electronegative oxygen atom thereby resulting in

the formation of cyclic 3-membered glycidol ring product as the major product. The strong basic sites present at the catalytic surface (Sr) is the driving force for the decarboxylation of glycerol carbonate resulting in the formation of the product glycidol. Since both acidic and basic sites at the Sr-Cu-Al catalyst are necessary for the activation of the substrate molecule and the subsequent selective formation of glycidol (V) as the product, it follows from the above mechanism that glycerol must be trans-esterified over dimethyl carbonate to yield glycidol. According to the literature, a number of other by-products, including I, II, IV, VI, VII, and VIII, are also produced during the transition. Lewis acidic and Lewis basic sites, as well as the existence of nano-pores at the catalytic surface, might be responsible for the catalyst's enhanced activity. As a result, the Sr-Cu-Al catalyst produced GD with a nearly 66 % selectivity at the cost of a 78 % glycerol conversion.

5.4.1 Support screening

Table 5.3 Support screening for the glycidol synthesis.

Sr. No	Support	% conv.	% Sele.		
			GD	GC	Other
1	Activated charcoal	38	17	82	1
2	MCM-41	52	2	92	6
3	ZSM-5	53	35	64	1
4	Acidic graphene	40	3	97	1
5	Al ₂ O ₃	56	44	55	1
6	CuO	63	52	46	1
7	Nb ₂ O ₅	51	52	35	13
8	MMT	20	20	79	1
9	Bentonite	21	23	76	1

(Reaction Conditions: Gly; DMC; Cat; Temp;145 °C, Time; 90 min.)

Various alkali as well as alkaline earth metal mixed metal oxides with Cu-Al were prepared by co-precipitation method. Various mixed metal oxide containing most basic oxides of alkali and alkaline earth metal with Cu-Al as well as different acidic, neutral as well as basic supports were screened towards the transesterification of glycerol to glycidol production to achieve maximum conversion and selectivity towards the desired product. The effect of support on catalytic activity for glycerol transesterification followed by decarboxylation to GD was done with varied nature of support starting from acidic-neutral-basic as shown in the **Table 5.3**.

Activated charcoal showed 17 % selectivity towards GD with 82 % selective formation of GC but the glycerol conversion was only up to 38 % (Table 5.3 Entry 1). Acidic structured silica in the form of MCM-41^[36] is showing higher selectivity towards the transesterification product GC (92 %) with 2 % GD and 52 % glycerol conversion (Table 5.3 Entry 2). ZSM-5 catalyst was found to be bit active for second step of decarboxylation of GC giving 35 % GD selectivity with similar conversion range of glycerol (53 %) as that of MCM (Table 5.3 Entry 3). Further, acidic graphene (Table 5.3 Entry 4) showed selective formation of GC (97 %) with a very low glycerol conversion (40 %). Some of the bare oxides of transition metal were also screened for this one pot GD synthesis.

Interestingly, oxides of Al and Cu (Table 5.3 Entry 5 and 6) showed highest glycerol conversion among all the studied support up to 56-63 % with near about equal selectivity towards GC and GD (55-46 and 44-52, respectively). Nb₂O₅ (Table 5.3 Entry 7) was found to be active for glycerol conversion up to 51 % but the 13 % selectivity towards another byproduct was observed. Clay material like MMT and bentonite (Table 5.3 Entry 8 and 9) was found to be less active for glycerol conversion (20-21 %) with higher selectivity towards transesterification product (79 and 76 %, respectively).

Hence, support study clearly suggests oxides of transition metal and p-block elements are having balanced acid-base property which makes them most active for one pot synthesis of GD.

5.4.2 Catalyst screening and catalyst optimization:

Table 5.4 Catalyst screening for the glycidol synthesis.

Sr. No	Support	% conv.	% Sele.		
			GD	GC	Other
1	Activated charcoal	38	17	82	1
2	MCM-41	52	2	92	6
3	ZSM-5	53	35	64	1
4	Acidic graphene	40	3	97	1
5	Al ₂ O ₃	56	44	55	1
6	CuO	63	52	46	1
7	Nb ₂ O ₅	51	52	35	13
8	MMT	20	20	79	1
9	Bentonite	21	23	76	1

(Reaction Conditions: Gly; DMC; Cat; Temp;145 °C, Time; 90 min.)

The reaction did not proceed without any catalyst (blank reaction) and from above support screening it was clear that the GD synthesis required basic condition. As the basic sites were required for the abstraction of the acidic proton of the hydroxyl group of glycerol followed by its attack on the electron deficient carbonyl carbon of the DMC. Further study was done by preparing mixed oxides of Cu-Al along with most basic oxides of alkali and alkaline earth metal to achieve higher selectivity towards target compound i.e. GD as shown in **Table 5.4**. Glycerol conversion for all the metals of S-block was found to be ranging from 41-56 % with a varied selectivity towards GD and GC. Very interestingly, 10 % Sr doped Cu-Al catalyst was found to be most active with 53 % glycerol conversion without formation of any other byproducts like mono-, tri-carbonate of glycerol, glycidol carbonate, linear carbonate of pendant –OH group of GC. Whereas, in case Rb, Cs, Ca etc. the conversion was found to be

good in the range 47-56 % with GD selectivity in the range 11-44 % but these MMO showed formation of more amount of byproducts (10-15 %) which was not feasible for the given transformation.

Task specific Sr-Cu-Al catalyst was further studied in detail as discussed in the consecutive sections. Thus, Sr-Cu-Al was chosen to be the optimum catalyst for the glycerol transesterification to glycidol with lowest formation of byproduct (1 %) which can be evidenced from the **Fig. 5.9**.

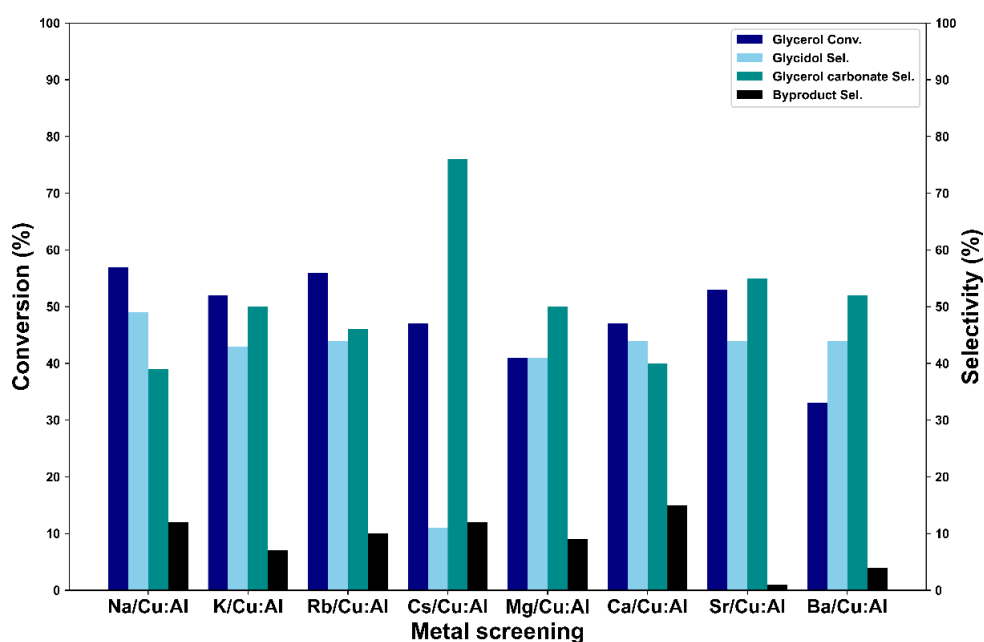


Figure 5.9. Activity performance of various alkali and alkaline earth metal for the one pot synthesis of glycidol.

5.4.3 Parameter optimization

The effect of various parameters such as the time, temperature, catalyst loading, metal loading and the catalyst recycle study was performed. These results have been discussed in detail as given below.

5.4.3.1 Temperature Effect

The effect of temperature on activity of the catalyst was studied in the temperature range 120-180 °C. It was observed that there is a linear rise in the glycerol conversion from 35-86 %, but the selectivity pattern has varied tremendously. At 120 °C temperature, glycerol

transesterification with DMC giving selective formation of GC and no further decarboxylation of GC accomplished. However, further 20 °C rise, triggers the decarboxylation of GC to GD (66 % sel.) along with cyclization of by-product like mono carbonate of glycerol. Further 20 °C rise in temperature give rise to excess carbonylation products by reaction of DMC with pendent hydroxyl group of GC and GD.

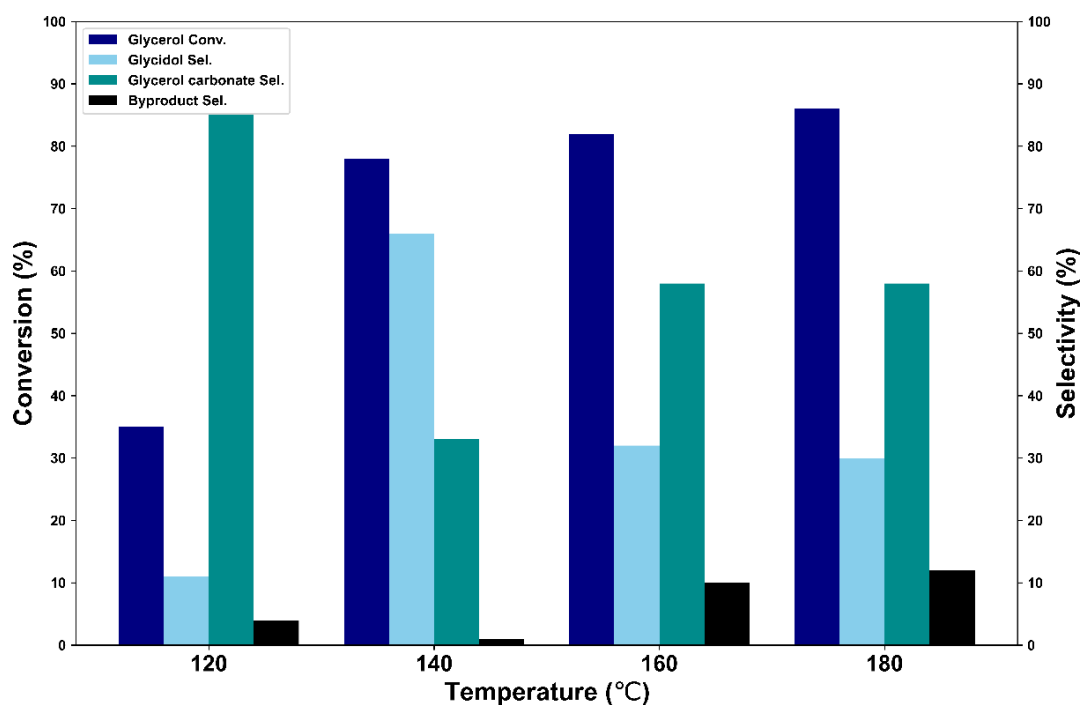


Figure 5.10. Effect of temperature

5.4.3.2 Time on stream

The reaction progress with time was studied by withdrawing sample from the reactor with every 30 min of time interval. Initially, reaction rate was faster achieving almost half of the glycerol conversion with higher selectivity towards transesterification product GC. After 1h of reaction time conversion was increased just by 10 % but the selectivity towards decarboxylation product GD (51 %) was enhanced with the expense of GC (48 %). Later on, as the time passes conversion was reached up to 80 % within 2 h of reaction time but no any considerable change was observed in selectivity pattern of GC (30 %) and GD (66 %). Therefore, 90 min reaction time was optimized for the one pot synthesis of GD via glycerol transesterification.

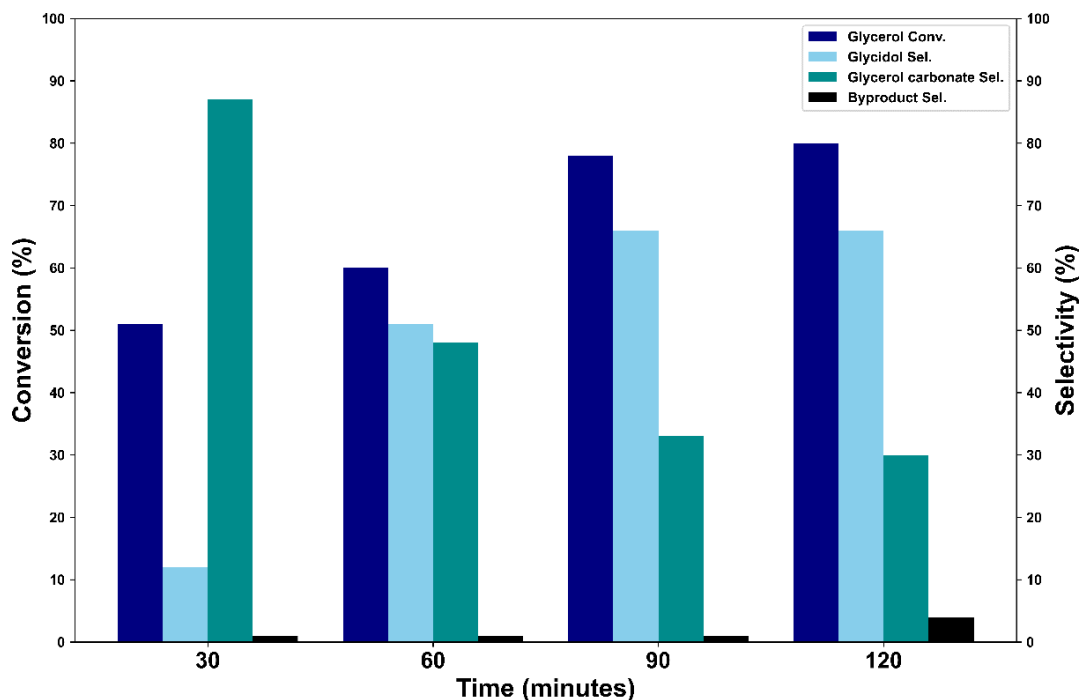


Figure 5.11. Time on stream

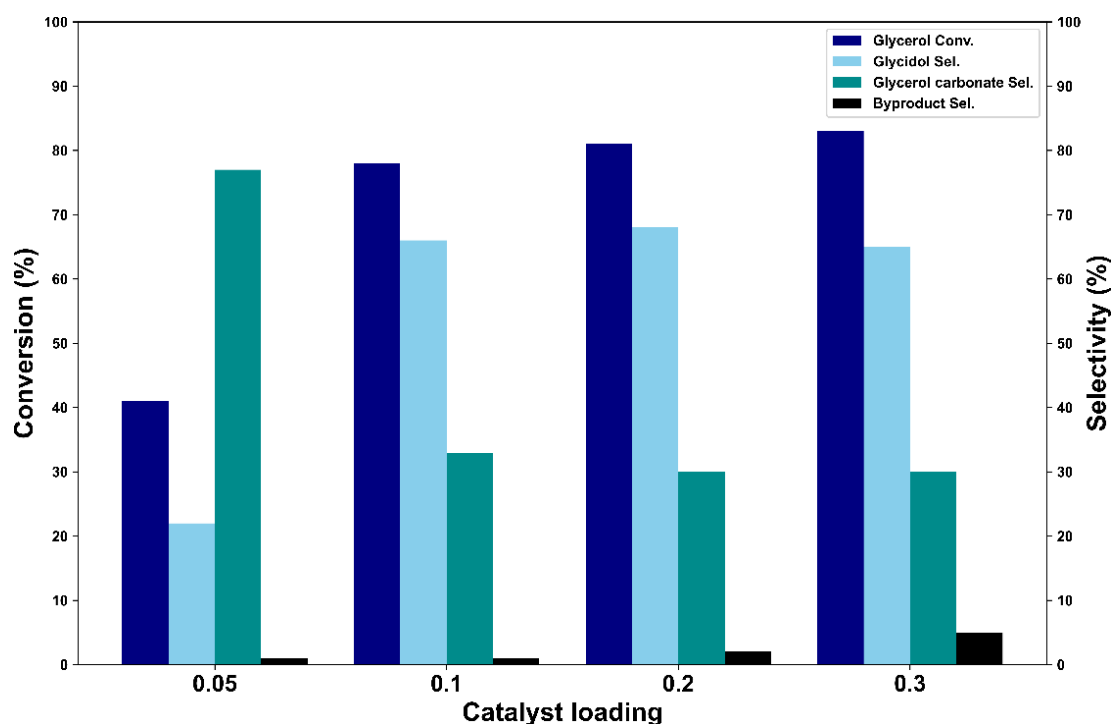
5.4.3.3 Catalyst Loading

The impact of catalyst concentration on glycerol transesterification and GC decomposition is shown in the below table. The glycerol conversion increased successively from 42 % to 83 % with an increase in catalyst dosage from 0.05 g to 0.3 g. Whereas, with increase in the amount of catalyst there was increase in the GD selectivity for 0.05g (22 %), 0.1 g (66 %), 0.2 g (68 %) but for 0.3 g it was found to decrease slightly to 65 %. In case of GC selectivity there was consecutive decrease in the selectivity from 77 % for 0.05 g to 30 % for 0.3 g respectively.

Also, the GD yield for 0.05g (9 %), 0.1 g (51 %), 0.2 g (53 %) but for 0.3 g it was found to increase slightly to 55 %. In case of GC yield there was consecutive decrease in the yield from 32 % for 0.05 g to 24 % for 0.3 g respectively. Thus, with increase in the catalyst loading the GD yield was found to increase whereas, the GC yield decreased and 0.05g loading reported the least conversion (42 %) and 0.3g with highest conversion (83 %).

Table 5.5 Effect of catalyst loading on Glycerol transesterification

Sr. No.	Catalyst wt.(g)	% conversion	% Selectivity			% yield	
			GD	GC	Other	GD	GC
1	0.05	42	22	77	1	9.24	32.34
2	0.1	78	66	33	1	51.48	25.74
3	0.2	81	68	30	2	55.08	24.3
4	0.3	83	65	30	5	53.95	24.9

**Figure 5.12.** Effect of catalyst loading

5.4.3.4 Metal loading effect

Studying the impact of different Sr-Cu-Al molar ratios on glycerol transesterification with DMC and presenting the findings in **Table 5.6** allows us to better understand the function of the base and acid sites on the catalytic surface that are responsible for conversion.

Table 5.6 Effect of Sr-loading on Glycerol transesterification

Sr. No.	Support	% conv.	% Sele			% yield	
			GD	GC	Other	GD	GC
1	Sr-Cu:Al (1:4:4)	53	44	55	1	24.2	29.15
2	Sr-Cu:Al (2:4:4)	78	66	33	1	51.48	25.74
3	Sr-Cu:Al (2.5:4:4)	75	63	30	7	47.25	22.5
4	Sr-Cu:Al (3:4:4)	73	60	30	10	43.8	21.9

With a ratio of (1:4:4) loading of Sr/Cu-Al, the catalyst produced 53 % glycerol conversion with 44 % glycidol selectivity and 55 % glycerol carbonate. Higher glycerol conversion of 78 %, 66 % glycidol selectivity, and 33 % glycerol carbonate were seen in Sr-Cu-Al ((2:4:4) loading). With a slightly lower 63 % glycidol selectivity and 30 % selectivity towards glycerol carbonate with a 75 % glycerol conversion, Sr-Cu-Al ((2.5:4:4) loading) produced results. Further increasing the molar ratio of Sr/Cu-Al ((3:4:4) loading) revealed further lowering of the glycerol conversion (73 %) and maximum GD yield of (51 %).

While GD selectivity continued to decline, reaching 60 % and 30 % for GC, respectively. In light of this, it was found that Sr-Cu-Al ((2:4:4) loading) generated results with the maximum GL conversion and the highest selectivity towards GD and GC as shown in **Table 5.6.** and **Fig. 5.13.** While both GL conversion and selectivity towards GD and GC decreased with further increase in catalyst loading, respectively.

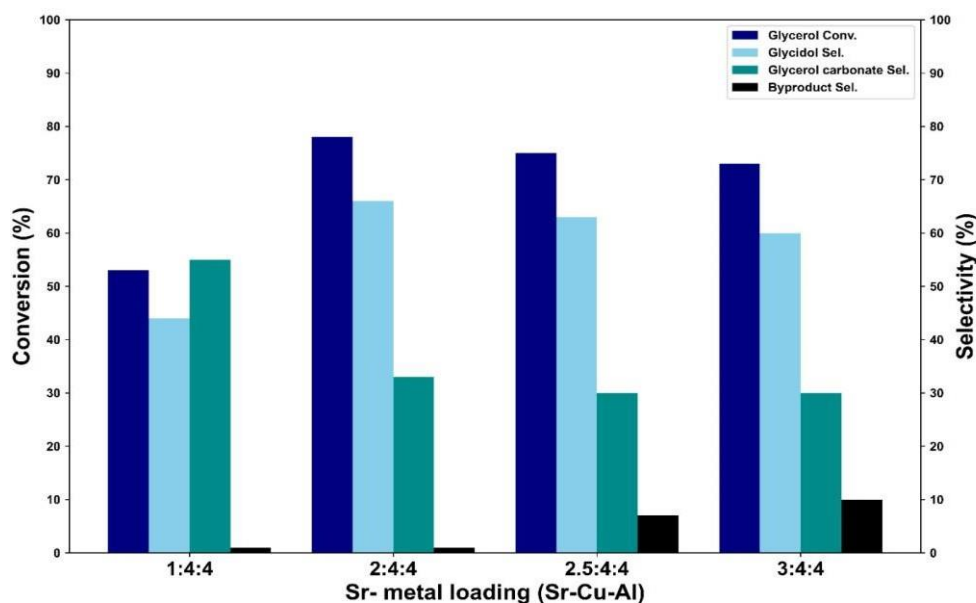


Figure 5.13. Effect of Sr loading.

5.5 Analysis of the products:

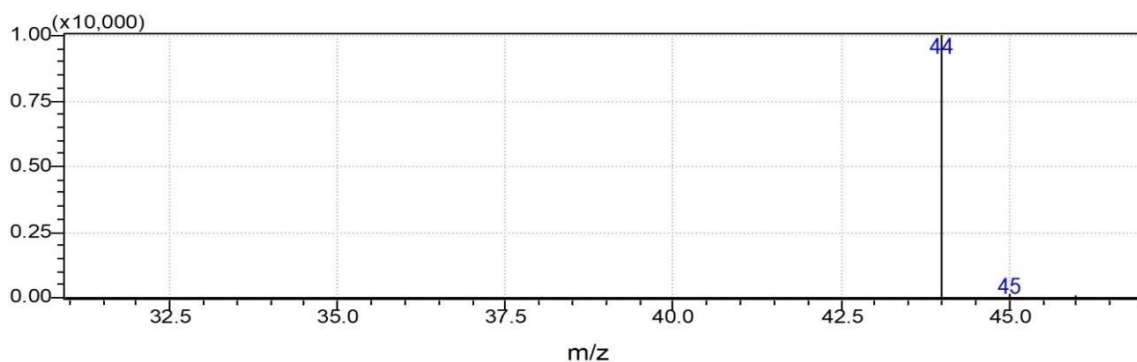
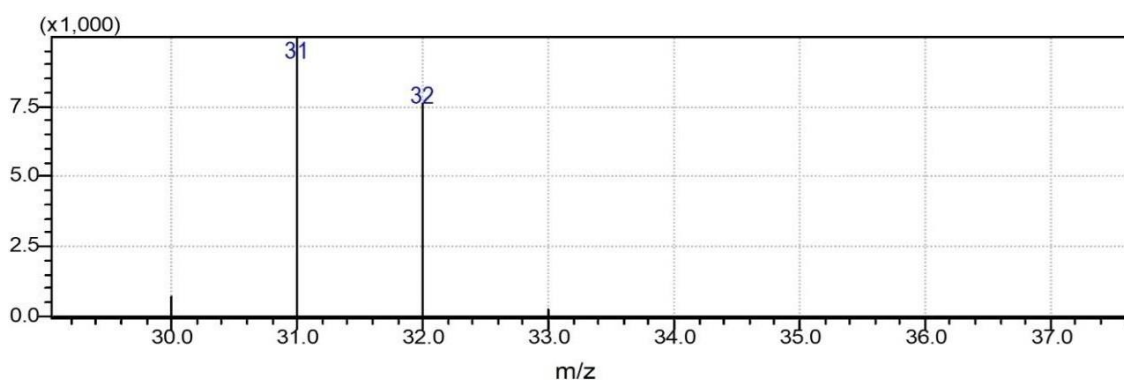
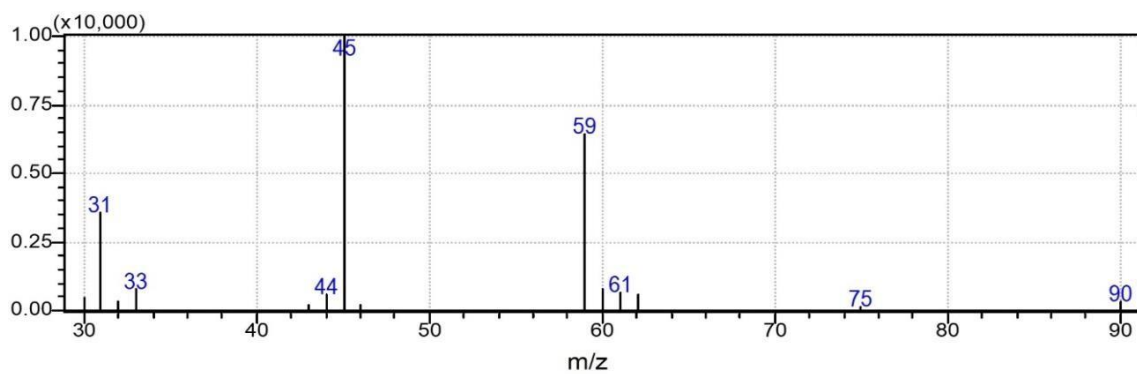
The complete reaction was studied and the reactants, products as well as various by-products were examined and detected by using the Gas Chromatography as shown in the **Fig. 5.14-5.21**. The GC conditions were as follows:

GC Conditions:

- GC: shimadzu 2025
- Column: Capillary HP-FFAP (Free fatty acid phase column)
- Column details: 30 m length x 0.53 mm ID x 1 μ m film thickness.
- Column stationary phase: Polyethylene glycol (highly polar)
- Carrier gas: He
- Detector: FID
- Injector temp.: 300 $^{\circ}$ C
- Detector temp.: 300 $^{\circ}$ C
- Total run time: 37.00 min.
- Injection volume: 1 μ L.
- Oven temperature program as given in Table 2.1.

Table 5.7. GC oven temperature program.

Sr. No.	Ramp (°C/min)	Temperature (°C)	Hold time (min)
1	-	80	1
2	20	200	30

**Figure 5.14.** GC chromatogram for CO₂ (44 g/mol).**Figure 5.15.** GC chromatogram for MeOH (32 g/mol)**Figure 5.16.** GC chromatogram for DMC

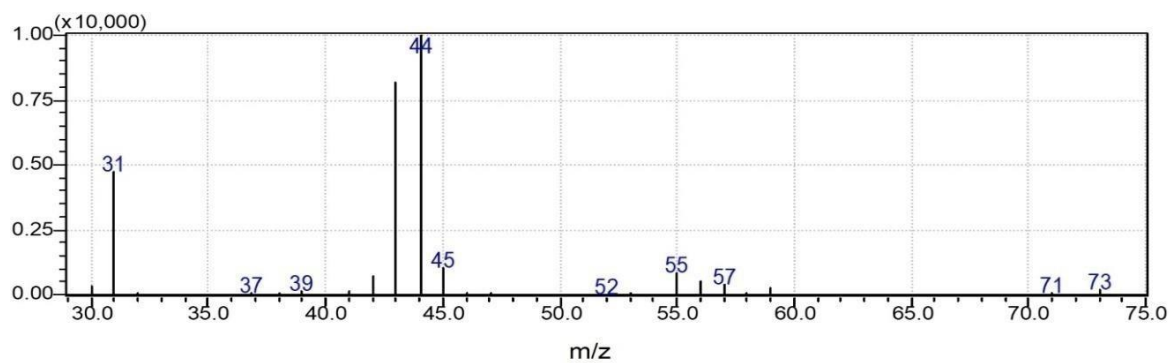


Figure 5.17. GC chromatogram for Glycidol

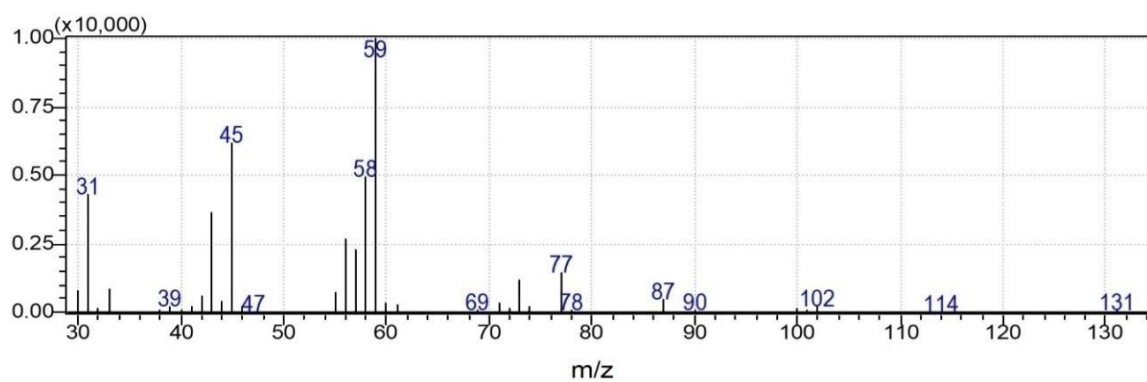


Figure 5.18. GC chromatogram for Glycidol carbonate

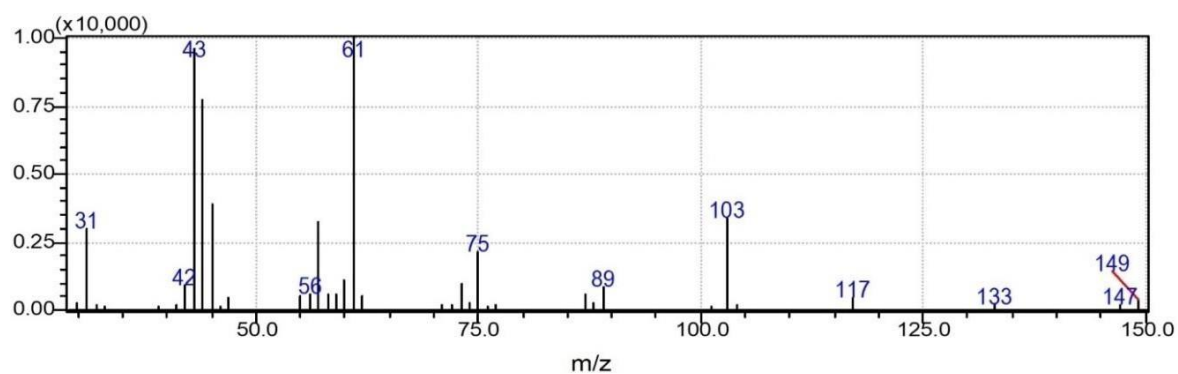


Figure 5.19. GC chromatogram for Glycerol mono-carbonate

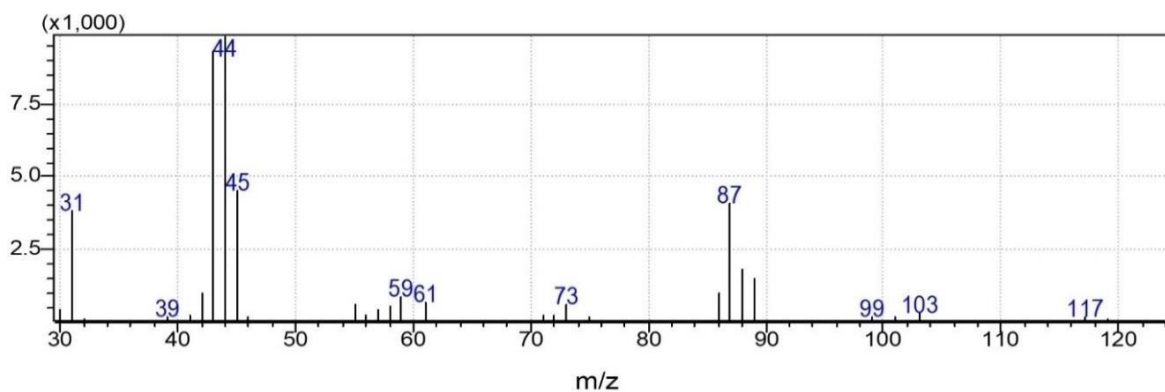


Figure 5.20. GC chromatogram for Glycerol carbonate

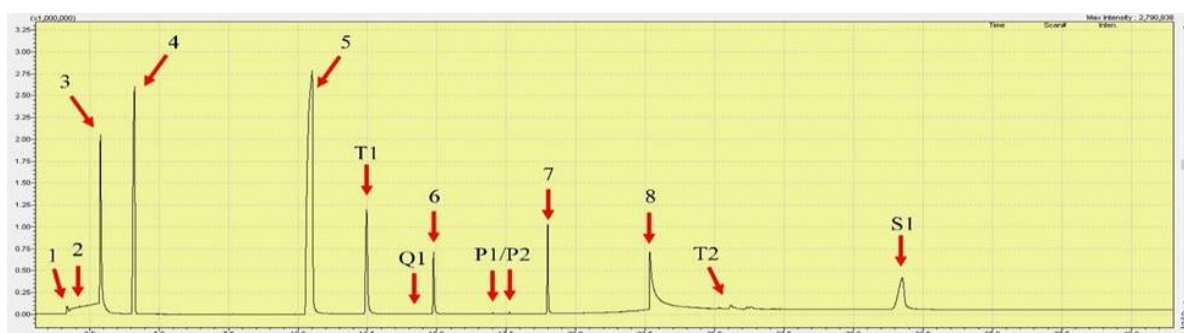


Figure 5.21. GC chromatogram for total analysis of reactants and products formed

Figure 5.21. represents the total analysis of the glycerol transesterification products. Where, 1: CO₂; 3: methanol; 4: dimethyl carbonate; (T1): glycidol; (Q1): glycidol carbonate; 6: P1/P2: glycerol monocarbonates; glycerol; T2: glyceroltricarbonate and (S1): glycerol carbonate. The peak 3 is from the solvent, dimethylformamide and the peaks 2: trimethylamine; 5: 1-Hexadecene; and 7: Hexadecyldimethylamine are from partial CTA⁺ decomposition.

5.6. Product separation by vacuum distillation.

The glycerol transesterification reaction was carried out in a parr reactor at 140 °C temperature. Once the reaction was over after 1.5 h, then it was allowed to cool at room temperature and then filtered to remove the catalyst from the reaction mixture. The vacuum distillation technique was used to separate various products (GC, GD) from the reaction mixture, the basis of separation was the difference in the boiling point. The obtained product was dried and its NMR was recorded as shown in the **Fig. 5.22** which confirmed the purity of the product.

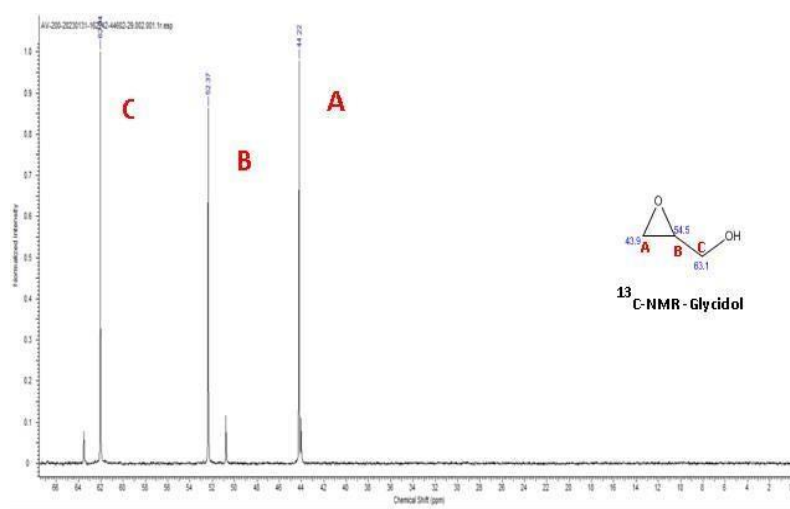


Figure 5.22. ^{13}C -NMR of glycidol

6. Conclusions

The work reported in this study, transesterification of Glycerol with DMC was accomplished in one pot using a Sr-Cu-Al mixed metal oxide catalyst. The simultaneous co-precipitation and digestion approach, which involves including Sr in Cu-Al lattice structure, was used to prepare the catalyst. Because both basic and acidic sites were evenly distributed across the catalytic surface, the catalytic activity of Sr-Cu-Al was observed towards glycerol transesterification reaction to selectively yield glycidol.

It was discovered that the solvent was crucial to the one-pot synthesis of GD. The integration of Sr in varying ratios in the Cu-Al mixed oxide lattice was amply demonstrated by the XRD data. The existence of SrCuO_2 mixed oxide phase was shown by the peaks at $2\theta = 38.2^\circ$ (211), 49° (312), and 53° (400). The XPS analysis revealed the presence of a doublet of Sr 3d for Sr $3d_{3/2}$ and Sr $3d_{5/2}$ orbitals due to two crystallographic positions observed for Sr^{+2} at B.E. of 133.7 and 135.08 eV, respectively which could be attributed to the presence of bond between Sr and the perovskite matrix, this confirmed the incorporation of Sr in the Cu-Al matrix. The SEM and EDAX analysis confirmed the presence of mixed morphology at the catalytic surface containing spheres and spherical shaped particles distributed on uneven and unordered sheets with varying sizes containing several nano-pores at the catalytic surface.

The effect of various parameters such as the catalyst loading, time, temperature and solvent were studied in-order to achieve efficient glycerol conversion and for selective formation of

glycidol with minimum formation of the by-products. Thus, Sr-Cu-Al (2-4-4) mixed oxide catalyst achieved 66 % selective formation of GD with the expense of 78 % glycerol conversion at 140 °C temperature. The reused catalyst, which is significant, showed good recyclability, easy separation and the catalyst was found to be recyclable up to 3 cycles.

7. References

1. Ubaghs, L.; Fricke, N.; Keul, H.; Höcker, H. *Macromol. Rapid Commun.* **2004**, *25*, 517–521.
2. Rokicki, G.; Rakoczy, P.; Parzuchowski, P.; Sobiecki, M. *Green Chem.* **2005**, *7*, 529–539.
3. Mei, H.; Zhong, Z.; Long, F.; Zhuo, R. *Macromol. Rapid Commun.* **2006**, *27*, 1894–1899.
4. Algoufi, Y. T.; Akpan, U. G.; Asif, M.; Hameed, B. H. *Appl. Catal., A* **2014**, *487*, 181–188.
5. Choi, J. S.; Simanjuntaka, F. S. H.; Oh, J. Y.; Lee, K. I.; Lee, S. D.; Cheong, M.; Kim, H. S.; Lee, H. J. *Catal.* **2013**, *297*, 248–255.
6. Pagliaro, M.; Rossi, M. *RSC Green Chemistry Book Series*; RSC Publishing: Cambridge, **2010**; p 108.
7. Gomez-Jimenez-Aberasturi, O.; Ochoa-Gomez, J. R.; Pesquera-Rodriguez, A.; Ramirez-Lopez, C.; Alonso-Vicario, A.; Torrecilla-Soria, J. J. *Chem. Technol. Biotechnol.* **2010**, *85*, 1663–1670.
8. Prisco Prete, Daniele Cespi, Fabrizio Passarini, Carmine Capacchione, Antonio Protoi and Raffaele Cucciniello, *Current Opinion in Green and Sustainable Chemistry* 2022, *35*:100624.
9. N. Mizuno, S. Hikichi, K. Yamaguchi, S. Uchida, Y. Nakagawa, K. Uehara, K. Kamata, *Catal. Today*, **2006**, *117*, 32.
10. W. F. Richey, Chlorohydrins, in: J.I. Kroschwitz, M. Howe-Grant (Eds.), *Kirk-Othmer Encyclopedia of Chemical Technology*, 4th ed., vol. 6, John Wiley, New York, **1993**, p. 140.
11. Endah, Y.K.; Kim, M.S.; Choi, J.; Jae, J.; Lee, S.D.; Lee, H. Consecutive Carbonylation and Decarboxylation of Glycerol with Urea for the Synthesis of Glycidol via Glycerol Carbonate. *Catal. Today* **2017**, *293–294*, 136–141
12. **EP 3 733 654 A1**
13. Choi, J.S.; Simanjuntaka, F.S.H.; Oh, J.H.; Lee, K.I.; Lee, S.D.; Cheong, M.; Kim, H.S.; Lee, H. Ionic-liquid-catalyzed decarboxylation of glycerol carbonate to glycidol. *J. Catal.* **2013**, *297*, 248–255.]

14. Ha, J.H.; Kim, J.S.; Kim, M.H.; Lee, K.Y.; Lee, M.S. Synthesis of Glycidol by Decarboxylation of Glycerol Carbonate Over Zn–La Catalysts with Different Molar Ratio. *J. Nanosci. Nanotechnol.* **2016**, *16*, 10898–10902.].
15. Parameswaram, G.; Srinivas, M.; Hari Babu, B.; Sai Prasad, P. S.; Lingaiah, N. Transesterification of glycerol with dimethyl carbonate for the synthesis of glycerol carbonate over Mg/Zr/Sr mixed oxide base catalysts *Catal. Sci. Technol.* **2013**, *3*, 3242– 3249 DOI: 10.1039/c3cy00532a]
16. Bolívar-Díaz, C.L.; Calvino-Casilda, V.; Rubio-Marcos, F.; Fernández, J.F.; Beñares, M.A. New Concepts for Process Intensification in the Conversion of Glycerol Carbonate to Glycidol. *Appl. Catal. B Environ.* **2013**, *129*, 575–579.]
17. A. Kostyniuk, D. Bajec, P. Djinović, B. Likozar, One-step synthesis of glycidol from glycerol in a gas-phase packed-bed continuous flow reactor over HZSM-5 zeolite catalysts modified by CsNO₃, *Chemical Engineering Journal* (2020), doi: <https://doi.org/10.1016/j.cej.2020.124945>.
18. Zhou Y, Ouyang F, Song ZB, Yang Z, Tao DJ. Facile one-pot synthesis of glycidol from glycerol and dimethyl carbonate catalyzed by tetraethylammonium amino acid ionic liquids. *Catalysis Communications*. 2015 Jun 5;66:25-9.
19. Parameswaram G, Srinivas M, Babu BH, Prasad PS, Lingaiah N. Transesterification of glycerol with dimethyl carbonate for the synthesis of glycerol carbonate over Mg/Zr/Sr mixed oxide base catalysts. *Catalysis science & technology*. 2013;3(12):3242-9.
20. Elrasheed Elhaj, Huajun Wang, Mohd Imran, Salah Eldeen F Hegazi, Mohamed Hassan, Mubarak A Eldoma, Jabir Hakami, Waseem A. Wani, and Anis Ahmad Chaudhary Nano-catalyst-Assisted Facile One-Pot Synthesis of Glycidol from Glycerol and Dimethyl Carbonate, *ACS Omega* 2022, *7*, 31778–31788.
21. Elhaj E, Wang H, Imran M, Hegazi SE, Hassan M, Eldoma MA, Hakami J, Wani WA, Chaudhary AA. Nanocatalyst-Assisted Facile One-Pot Synthesis of Glycidol from Glycerol and Dimethyl Carbonate. *ACS omega*. 2022 Aug 29;7(36):31778-88.
22. Sing, Kenneth SW, and Ruth T. Williams. "Physisorption hysteresis loops and the characterization of nano-porous materials." *Adsorption Science & Technology* 22.10 (2004): 773-782,

23. Chen, Junjie, et al. "Performant Au hydrogenation catalyst cooperated with Cu-doped Al_2O_3 for selective conversion of furfural to furfuryl alcohol at ambient pressure." *Green Energy & Environment* 6.4 (2021): 546-556
24. AL Othman, Zeid A. "A review: fundamental aspects of silicate mesoporous materials." *Materials* 5.12 (2012): 2874-2902,
25. Thommes, Matthias, et al. "Physisorption of gases, with special reference to the evaluation of surface area and pore size distribution (IUPAC Technical Report)." *Pure and applied chemistry* 87.9-10 (2015): 1051-1069
26. JOURNAL OF CRITICAL REVIEWSISSN- 2394-5125 VOL 7, ISSUE 06, 2020, Energy Fuels 2017, 31, 6228–6239, RSC Adv., 2016, 6, 65338–65348
27. R. Soc. Open Sci. 7: 200290, Catalysis Today 198 (2012) 321– 329
28. Int. J. Electrochem. Sci., Vol. 14, 2019, which clearly revealed the appearance of additional peaks at 25.5° and 25.8° corresponds to SrAl_4O_7 [Journal of Catalysis 281 (2011) 241–253
29. Thin Solid Films 444 (2003) 70–74
30. Tabah, Betina, et al. "Solar-heated sustainable biodiesel production from waste cooking oil using a sonochemically deposited SrO catalyst on microporous activated carbon." *Energy & Fuels* 31.6 (2017): 6228-6239.)
31. Radhakrishnan, A. Asha, and B. Baskaran Beena. "Structural and optical absorption analysis of CuO nanoparticles." *Indian J. Adv. Chem. Sci* 2.2 (2014): 158-161.
32. Palapa, Neza Rahayu, RisfidianMohadi, and Addy Rachmat. "Adsorption study of malachite green removal from aqueous solution using Cu/M^{3+} ($\text{M}^{3+} = \text{Al}, \text{Cr}$) layered double hydroxide." *Mediterranean Journal of Chemistry* 10.1 (2020): 33-45.
33. Vasquez RP. X-ray photoelectron spectroscopy study of Sr and Ba compounds. *J Electron Spectrosc Relat Phenom* 1991; 56:217–40.
34. van der Heide PAW. Systematic X-ray photoelectron spectroscopic study of $\text{La}_{1-x}\text{Sr}_x$ -based perovskite-type oxides. *Surf Interface Anal* 2002; 33:414–25.
35. Crumlin EJ, Mutoro E, Liu Z, et al. Surface strontium enrichment on highly active perovskites for oxygen electrocatalysis in solid oxide fuel cells. *Energy Environ Sci* 2012; 5:6081.]
36. Gustavo Medeiros de Paula, Janaina Guedes Eid, Dilson Cardoso1, Converting glycerol into glycerol carbonate by transesterification with different esters: reaction

steps and coproducts, Reaction Kinetics, Mechanisms and Catalysis
<https://doi.org/10.1007/s11144-023-02349-4>.

Conclusion, and future scope

6.1 Conclusive remarks:

This thesis work presents a detail account of the strategies employed in designing, and developing various shape and size controlled bifunctional i.e., containing both Lewis and Brønsted acidic as well as basic sites at the catalyst surface for the transformation of both lignocellulosic as well as marine biomass into value added products. The lignocellulosic biomass being the major renewable and cheap feedstock for the production of C-5 and C-6 sugars and their derivatives. Chemo-catalytic pathways were employed for the production of fructose which not only acts as a sweetener for the production of HFCS but also as a platform chemical for the synthesis of several value-added chemicals with wide range of applications in the commercial market.

The marine biomass as compared to the lignocellulosic biomass has remained unexplored for decades but upon transformation chitin and chitosan can be used for the synthesis of several value-added compounds containing not only C, H, O, but also 7 Wt. % of renewable N atom in its skeleton that can be otherwise produced by the energy consuming ammonia synthesis. Thus, taking into account the importance of the availability of cost-effective feedstock from biomass waste and its transformation into value added products, several multifunctional heterogeneous catalytic systems were synthesized and screened for the valorization of glucose, glycerol and chitin biomass.

The catalytic isomerization of glucose led to the formation of fructose which acts as a potential platform chemical that can be further used for the synthesis of several value-added products such as 5-HMF, Levulinic acid, 2, 5-FDCA etc. Keeping this in account several inexpensive, robust, easily recyclable, mixed metal oxides were designed and developed by tuning the acidic and basic character at the surface and its potential was explored for the efficient conversion of glucose to selectively yield fructose which has tremendous demands in the commercial market. For the very first time solid basic metal oxide catalyst was employed for the synthesis of 3AF and 3A5AF which acts as a drug precursor for the synthesis of anti-tumour drug proximicin A, B and C from marine biomass n-acetyl-D-glucosamine, a monomer unit of chitin.

The detailed characterization studies were done along with the parameter optimization for every reaction scheme that aided in the determination of the plausible reaction mechanism and the structure-activity co-relation in our investigations. The salient features and the dominant conclusions of the thesis work have been summarized below:

- ❖ Bifunctional Ba-Zr mixed metal oxide catalyst was prepared in varying ratios (0.5:1, 1:1, 2:1, 3:1) by Co-precipitation method and were screened for the isomerization of glucose to fructose. The incorporation of Ba in the Zr lattice was confirmed by the XRD, XPS and EDS analysis.

Ba-Zr (2:1) catalyst with a metal loading of 20 Wt. % was found to be optimum for the selective formation of fructose. Various experiments with organic solvents and their mixtures with water revealed that water acts as best solvent system for this transformation. Thus, the bifunctional Ba-Zr (2:1) MMO was found to play an important role by providing base/acid active sites on the catalytic surface for selective (89 %) isomerization of glucose to fructose by participating in the reaction pathway in presence of water at 100 °C, within 6 h with 57 % conversion.

- ❖ The heterogeneous catalysts were developed for the transformation of marine biomass i.e., N-acetyl glucosamine (NAG) to N-substituted furan derivatives 3AF and 3A5AF which act as a precursor for the synthesis of antitumor drug proximicin for the very first time using a solid basic catalyst.

The physicochemical properties of the metal oxide catalyst were investigated by various techniques which revealed the presence of oxide and hydroxide phase with the presence of nanopores and weak Brønsted basic sites at the catalytic surface as confirmed by XRD, FTIR, MeOH-FTIR, TPD, SEM, N₂ sorption studies and HR-TEM analysis for structure-activity relationship responsible for improved dehydration of the chitin biomass. Efficacious exploitation of marine biomass to value-added platform chemicals using heterogeneous catalysts through simple routes and easy separation of N-substituted furan derivatives as an alternate renewable source for amines was the most innovative aspect of my study.

- ❖ Sr/Cu-Al catalyst was prepared in various ratios by co-precipitation method.

The existence of SrCuO₂ mixed oxide phase was confirmed by the peaks at $2\theta = 38.2$ (211), 49 (312), and 53 (400). The SEM and EDAX analysis confirmed the presence

of mixed morphology at the catalytic surface containing spheres and spherical shaped particles distributed on uneven and unordered sheets with varying sizes containing several nano-pores at the catalytic surface. The effect of various parameters such as the catalyst loading, time, temperature and solvent were studied in-order to achieve efficient glycerol conversion and for selective formation of glycidol with minimum formation of the by-products.

The bifunctional Sr/Cu-Al catalyst was found to play a vital role by providing base/acid active sites for selective (66 %) trans-esterification of glycerol to glycidol in presence of EtOH at 140 °C, within 1.5 h with 78 % conversion. The catalyst showed good recyclability, easy separation, stability and the catalyst were found to be reused up to 3 cycles without any change in conversion and selectivity.

6.2 Future Scope:

The Isomerization of glucose to fructose has recently gained tremendous applications worldwide because of the potential use of fructose as a sweetener in the form of HFCS as well as its use as a platform chemical for synthesis of several value-added products with wide range of commercial applications in the global market. As mentioned in **Chapter 3**, the glucose conversion achieved was around 57 % with high selectivity towards fructose about 89 %. Thus, there is still scope to enhance the efficiency of the glucose conversion and yield of fructose. Also, the tuning of the catalyst structural properties, acidity and basicity ratio and further optimization of parameters with scale up study would provide a broad spectrum and a way for the commercialisation of the process.

The dehydration of NAG into 3AF and 3A5AF represents a novel and unique route for its transformation into a nitrogen containing furan derivative from abundantly available marine waste as mentioned in **Chapter 4**. As compared with the lignocellulosic biomass the marine biomass has advantage of generating value added compounds containing the renewable N atom in the skeleton which makes it a promising molecule for exploring. Literature survey reports the use of pyrolysis that employs very high temperature at about 1000 °C, microwave irradiation that increases the formation of humins as the by-products and certain homogeneous systems that face difficulties in product separation and purification. According to the literature the transformation of NAG into 3A5AF has been reported in the presence of

several additives and boron containing compounds and mostly homogeneous catalysts, thus current approach as mentioned in the thesis can be further used and modified for similar kind of transformations as in our approach, we have achieved the formation of the products in an additive free and mild operating conditions. I strongly recommend the development and designing of a highly efficient and tuneable catalytic system for this transformation that would aid achieving the 3AF or 3A5AF yield to about 80-90 %. Further scale up and parameter optimization would provide an efficient route for the industrialization of this process.

For better understanding of the reaction routes for NAG dehydration isotope labelling experiments can be carried out. Computational studies can be employed for designing a better route in order to achieve more efficient and selective formation of the product. As 3A5AF and 3AF has not been studied and explored much the lack of information may cause challenges in further research. Although, I have obtained ample amount of data about the NAG transformation and this would and further mechanistic investigations can be carried out for the detail study of the product as these molecules act as potential precursors for the antitumour drug molecule proximicin A, B and C.

Chapter 5 provides a detailed study of the transesterification of glycerol which acts as one of the most abundantly produced platform chemicals during biodiesel synthesis. Thus, glycerol can be further valorized in the presence of heterogeneous catalytic systems into value added compounds glycerol carbonate and glycidol that has wide range of applications in the commercial market. Sr-Cu-Al (2-4-4) mixed oxide catalyst screened in varying ratios that gave about 66 % selective formation of GD with the expense of 78 % glycerol conversion at 140 °C temperature. This transformation has a wide scope to achieve higher yields of the products. Further studies can be extended in order to develop a cost effective, environmentally benign and more efficient route to achieve about 80-90 % of product yield and product separation. The reused catalyst, which is significant, showed good recyclability, easy separation and the catalyst was found to be recyclable up to 3 cycles.

ABSTRACT

Name of the Student: Samrin Salim Shaikh
Faculty of Study: Chemical science
AcSIR academic centre/CSIR Lab: NCL, Pune.

Registration No.:10CC21J26034
Year of Submission:2023
Name of the Supervisor(s):
Dr. V. V. Bokade
Dr. C. V. Rode

Title of the thesis: Development of multifunctional catalysts for the valorization of lignocellulosic and marine biomass into value added products

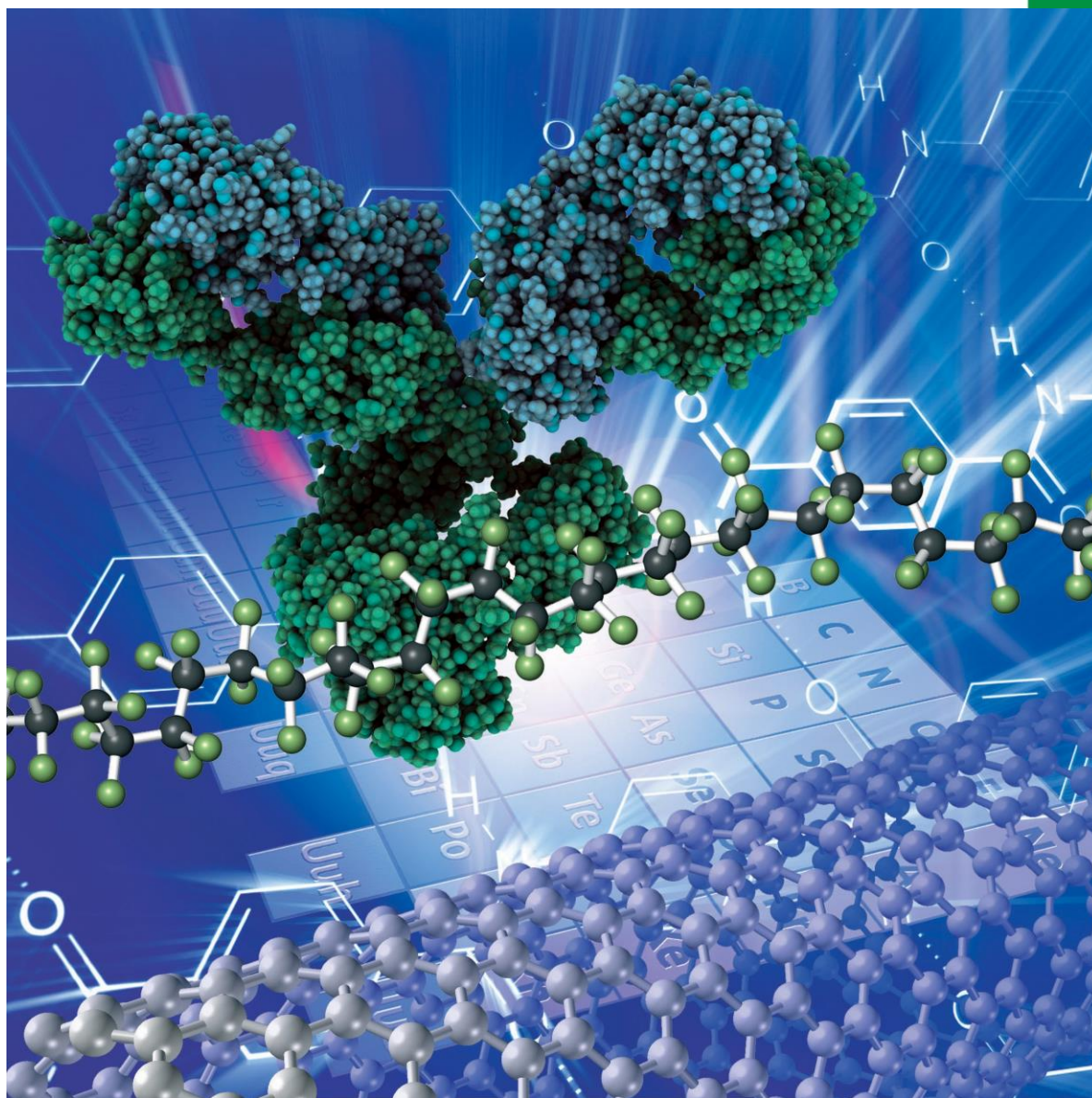
My dissertation entitled “**Development of multifunctional catalysts for the valorization of lignocellulosic and marine biomass into value added products**” comprises of 6 chapters. This is a brief summary of the observations and results obtained by carrying out several experiments in the presence of synthesized, shape and size controlled, inexpensive and easily recyclable heterogeneous catalytic systems on lignocellulosic as well as chitin biomass. **Chapter 1** presents an overview of the need for biomass valorization and the importance of the concept of bio-refinery towards the eco-friendly production of value-added products from renewable biomass feedstock. It also highlights the concept of catalysis and its vital role in biomass transformations. It gives a brief introductory remark on the efficient production of fructose, 3A5AF, 3AF and glycidol from lignocellulosic and marine biomass by employing catalytic pathways. **Chapter 2** gives us detail information about the experimental procedures, characterization techniques and the methodology employed during the process optimization. **Chapter 3** explores the use of inexpensive Ba-Zr mixed metal oxide catalyst for the efficient and highly selective isomerization of glucose to fructose. Under the optimized reaction conditions Ba-Zr (2:1) catalyst exhibited excellent results in terms of 57% of glucose conversion with 89% selective formation of glucose. **Chapter 4**, We reported for the first time the transformation of marine biomass i.e., NAG into drug precursor 3AF and 3A5AF in the presence of solid basic catalyst without making use of any additive and boron containing compound. We achieved 10 times more yield of the products as reported by the pyrolysis method. **Chapter 5**, a trimetallic catalyst Sr-Cu-Al was designed and developed for the one pot synthesis of glycidol by the transesterification of glycerol over DMC. The bifunctional Sr/Cu-Al catalyst plays an important role by providing base/acid active sites for selective (66 %) trans-esterification of glycerol to glycidol. **Chapter 6** summarizes and concludes the entire dissertation work briefly and describes in detail the future scope of the work that has been carried during my PhD tenure.

- List of publication(s) in SCI Journal(s) (published & accepted) emanating from the thesis work, with complete bibliographic details.
 1. **Shaikh SS**, Patil CR, Kondawar SE, Rode CV. Cooperative Acid-Base Sites of Solid Ba-Zr Mixed Oxide Catalyst for Efficient Isomerization of Glucose to Fructose in Aqueous Medium. *ChemistrySelect*. 2020 Oct 29;5(40):12505-13.
 2. **Shaikh SS**, Patil CR, Lucas N, Bokade VV, Rode CV. Direct Conversion of N-acetyl-d-glucosamine to N-containing Heterocyclic Compounds 3-Acetamidofuran and 3-Acetamido-5-acetyl Furan. *Waste and Biomass Valorization*. 2023 Apr 11:1-4.
- List of Papers with abstract presented (oral/poster) at national/international conferences/seminars with complete details.
- **Details of National and international Conferences:**
 1. Selected as the best top five performer for 3 Minutes PhD thesis communication presentation-2023 held at CSIR-National Chemical Laboratory, Pune, India.
 2. Received best poster award on the occasion of Science Day-2023 held at CSIR-National Chemical Laboratory, Pune, India
 3. Attended the workshop held in the Institute of electrochemistry and energy systems, BAS Sofia, Bulgaria, 2022.
 4. Participated in 16th International Conference on Science and technology of polymers and advanced materials through innovation, entrepreneurship and industry 2022, organized by NCL research foundation and CSIR-NCL, Pune, IISER- Pune and Pune University, India.
 5. Participated in one day programme on Patent Search-2022, organized CIPAM and DPIIT, Government of India.
 6. Participated in Annual student's conference 2022, organized by NCL research foundation and CSIR-NCL, Pune.
 7. Participated in one day National Seminar on 'Recent Advances in Chemical Sciences organized by Department of chemistry and IQAC, KMR college-2021
 8. Participated in Annual student's conference 2021, organized by NCL research foundation and CSIR-NCL, Pune.

Chemistry **SELECT** ✓

www.chemistryselect.org

A journal of



REPRINT

WILEY-VCH

z Catalysis

Cooperative Acid-Base Sites of Solid Ba-Zr Mixed Oxide Catalyst for Efficient Isomerization of Glucose to Fructose in Aqueous Medium

Samrin S. Shaikh,^[a, b] Chetana R. Patil,^[a] Sharda E. Kondawar,^[a] and Chandrashekhar V. Rode^{*[a, b]}*Samrin. S. S dedicates this paper to her family and lab mates.*

Efficient and highly selective isomerization of glucose to fructose was achieved by using the inexpensive Ba-Zr mixed metal oxide catalyst. Catalyst was prepared by varying Ba-Zr ratios using co-precipitation method. Various phases formed, planes exposed, morphology, elemental composition and particle size, basic site density and strength, oxidation state of elements were well studied by using various characterization techniques. The XRD analysis clearly indicates the presence of Ba⁺² and Zr⁺⁴ in the form of BaO, ZrO₂ and BaZrO₃ phases. The SEM and HR-TEM images indicate that, Ba-Zr (2:1) catalyst

prepared showed uniform morphology with spherical and rod-shaped particles ranging from 300 to 600 nm. Under the optimized reaction conditions Ba-Zr (2:1) catalyst exhibited excellent results in terms of 57% of glucose conversion with 89 % selective formation of fructose. The presence of both acidic as well as basic sites play vital roles in activating the substrate molecules to selectively yield fructose. Ba-Zr (2:1) catalyst showed excellent recyclability performance up to four recycles.

Introduction


Around 87 % of energy globally comes from non-renewable fossil fuels, whose rapid depletion urges a need for development of an alternative renewable and green energy resource. This can be achieved by developing cost effective and environmentally benign pathways for valorization of biomass into fuels and commodity chemicals. This would aid the human society to mitigate various alarming situations such as global warming, energy and food crises.^[1]

In recent years, glucose to fructose isomerization has gained tremendous importance in food and beverage industry, as fructose is sweeter than glucose. Fructose is not only used for the production of High Fructose Corn Syrup (HFCS), where it is used as a sweetener but also in the production of various platform molecules, fuel additives and value-added chemicals like 5-hydroxymethylfurfural, 2,5-furandicarboxylic acid,^[2-5] levulinic acid and its esters, lactic acid, alkoxy fructoside, 5-alkoxymethylfructoside.^[6-12] Lobry-de-Bryun-Van-Ekenstein, first reported aldose to ketose isomerization in both acidic as well

as basic medium, where formation of ene-diol as an intermediate i. e. proton transfer mechanism yields a mixture of glucose, fructose and mannose, which is a well accepted mechanism.^[13] This pioneering discovery enhanced the large scale glucose to fructose isomerization. The glucose isomerization is carried out commercially by bio-catalytic pathway, which employs glucose isomerase/xylose isomerase enzyme (GI).^[9] But thermal and chemical deactivation of the enzyme, narrow pH range, low operating temperature and presence of Ca⁺² hinders the activity of GI thus making the process less economical.^[14] Industrial chemical isomerization of glucose involves the homogenous process using mineral acid or alkali, which suffers from several drawbacks such as low fructose yield, low rate of reaction, formation of large amount of byproducts due to side reactions such as aldolization/ retro aldolization, β -elimination and benzilic rearrangement reactions that take place simultaneously with isomerization and post synthesis neutralization step.^[15,16] Various bases such as sodium hydroxide, sodium carbonate, calcium hydroxide, magnesium hydroxide, trisodium phosphate, and sodium sulphite, basic ion-exchange resins and derivatives of ammonia have been reported for the conversion of glucose to fructose but with low fructose yields (20-30 %), due to side reactions that lead to the formation of colored substances, organic acids, saccharinic acid and other undesired products.^[17,18] Liuet *al.* reported glucose to fructose isomerization by using organic amines such as triethyl amine in water at 100 °C, to give 57 % glucose conversion with 54 % and 31 % fructose selectivity and yield, respectively. The mixture of glucose, fructose and triethyl amine was further separated by

[a] S. S. Shaikh, C. R. Patil, S. E. Kondawar, C. V. Rode
Chemical Engineering and Process Development Division
CSIR-National Chemical Laboratory
Dr Homi Bhabha Road, Pashan, Pune-411008
E-mail: cv.rode@ncl.res.in

[b] S. S. Shaikh, C. V. Rode
Academy of Scientific and Innovative Research (AcSIR), Ghaziabad-
201002, India

 Supporting information for this article is available on the WWW under <https://doi.org/10.1002/slct.202003071>

chromatography.^[19] Rendleman *et al.* reported maximum yield of fructose (72 %) by using aluminate resin containing hydroxide group^[20] with 68 % glucose conversion and 72 % fructose selectivity.^[21] Among solid catalysts, magnesium-aluminum hydrotalcites have been also reported to catalyze the glucose isomerization to fructose with 30 % fructose yield, whereas Yabushita *et al.* reported 56% fructose yield with 80% fructose selectivity in ethanol as a solvent. The gradual decrease in the catalytic activity could be restored by calcination and rehydration of the hydrotalcites.^[22,23] The use of MgO as a catalyst has been reported by Marianou *et al.* to afford 44 % fructose yield with 75 % fructose selectivity, which has been attributed to the basicity of the catalyst.^[24] Glucose to fructose isomerization has been also carried out in the presence of Lewis acids such as AlCl₃, FeCl₃ but the major drawback is the deactivation of the catalyst in aqueous media, which requires maintenance of anhydrous conditions.^[25] Lewis acids such as CrCl₃ has been also reported for glucose isomerization in which [Cr(H₂O)₅OH]⁺² complex acts as active species for catalyzing the isomerization *via* de-protonation, hydride shift and proton donation to sugar.^[26] The heterogeneous catalyst Sn- β zeolite, in which tin metal acts as Lewis acid has been reported to show 31 % fructose yield.^[27,28] Thus, isomerization of glucose to fructose has been reported to be carried out in the presence of either acidic or basic catalytic system. In the present work for the first time, we report mixed metal oxides of Ba and Zr as an acid-base heterogeneous catalyst for selective glucose isomerization to fructose. There are various methods reported for the synthesis of nano structured BaZrO₃ which involve sol-gel,^[29,30] co-precipitation,^[31] thermal decomposition^[32] and hydrothermal techniques.^[33] Urea-induced precipitation followed by a low-temperature thermal treatment was also reported for the synthesis of nano scale BaZrO₃.^[34] The present research is focused on co-precipitation method for the size and shape controlled synthesis of BaZrO₃ particles which catalysed the glucose isomerisation. Our Ba@Zr catalyst exhibited both Lewis acidic as well as basic sites which play an important role in glucose to fructose isomerization to give the highest selectivity of 89 % towards fructose. Detail studies on the catalyst characterization by XRD, TEM, SEM, NH₃ and CO₂-TPD and FT-IR, along with effect of reaction parameters on glucose conversion and selectivity for fructose have been also carried out.

Results and Discussion

Catalyst characterization

Figure 1 shows the powder XRD patterns for both single components (Ba and Zr) and mixed metal oxides prepared by varying Ba@Zr ratio. The wide angle XRD patterns for ZrO₂ samples showed the reflections at $2\theta = 23.7^\circ, 29.1^\circ$ and 55.8° ascribed to ZrO₂ phase [JCPDS#86-1451] whereas, reflections at $2\theta = 19.6^\circ, 23.7^\circ, 45.1^\circ$ confirmed the presence of BaO phase [JCPDS#47-1488].

However in case of MMO samples, intensities of ZrO₂ peaks were found to be weak with the doping of Ba in the zirconium

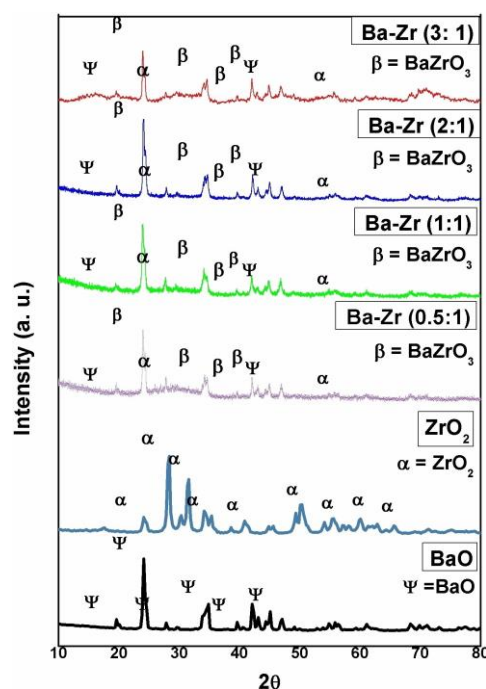


Figure 1. Powdered XRD pattern for calcined BaO, ZrO₂ and Ba@Zr mixed metal oxide.

lattice, which clearly suggests that there might be deformation of the crystal structure of ZrO₂. This was further supported by appearance of new reflections other than BaO and ZrO₂ phases at $2\theta = 23.7^\circ, 27.7^\circ, 34.1^\circ, 39.5^\circ, 41.9^\circ$ corresponding to (211), (220), (222), (330) and (400) planes, respectively, which indicated the presence of perovskite type cubic phase of BaZrO₃ [JCPDS#01-0890].^[35]

It is well reported that during calcination process, the barium present at the surface reacted with zirconia to form BaZrO₃ phase. All the peaks can be indexed to the cubic phase of BaZrO₃ (Figure 1). The crystallite size of BaZrO₃ phase calculated for Ba@Zr (2:1) catalyst by Scherrer equation was found to be 29.35 nm. Moreover in case Ba@Zr (2:1) catalyst, it was observed that all the phases including BaO (49.5 nm), ZrO₂ (44.2 nm) and BaZrO₃ was found to have lowest crystallite size as compared to all the other catalysts studied in this work. This might be the reason for its better performance (Table S1). The XRD pattern for Ba@Zr (2:1) used catalyst remains same with no change in the phases observed (Figure S1.). The morphologies of various Ba@Zr MMO samples were studied by SEM analysis.

Figure 2 displays the SEM images for BaO and Ba@Zr MMO catalysts. In case of bare BaO, mixed morphology of rod and sphere was observed with predominant presence of rod shaped particles as encircled in Figure 2a. The introduction of Zr in MMO clearly showed that there was a growth of small particles on the surface which might be due to the formation of BaZrO₃ perovskite type cubic phase or ZrO₂ phase, presence of which has already been revealed by XRD. The Ba@Zr MMO samples showed the presence of mixed morphology with spherical deposits on rod shape particles (Figure S 2 b-f).

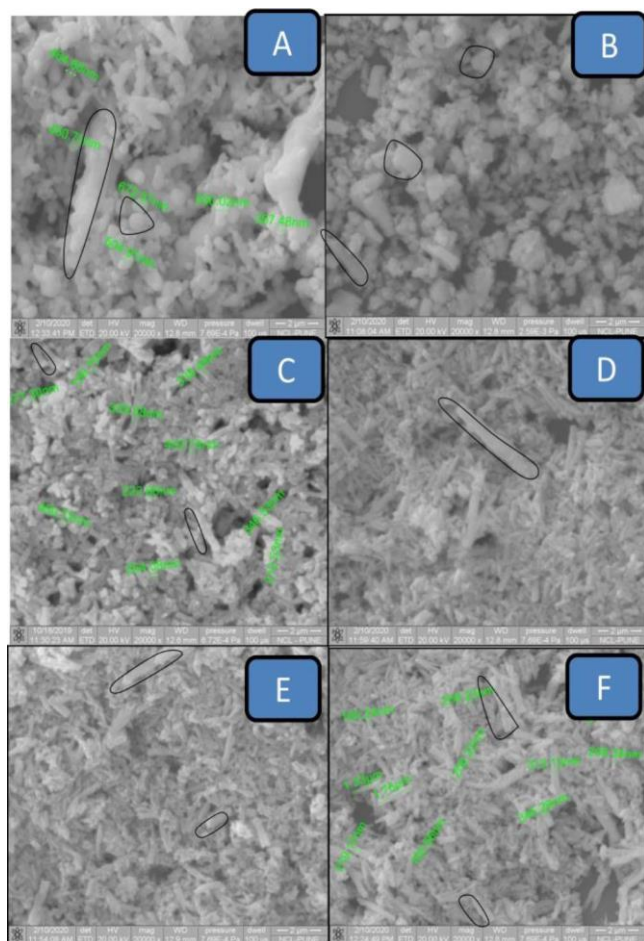


Figure 2. Scanning Electron Micrographs for a) BaO, b) Ba@Zr (0.5 :1), c) Ba@Zr (1 :1), d) Ba@Zr (2:1) fresh e) Ba@Zr (2:1) used f) Ba@Zr (3:1) catalysts.

Interestingly, as Ba concentration was increased in Ba@Zr MMO (for ratios of 0.5 :1 and 1 : 1), rod shape morphology started appearing. The size of the rod shape particles was found to be in the range 250-300 nm for Ba@Zr (1 : 1) (Figure 2 B), which increased to about 250-550 nm in case of Ba@Zr (2 : 1) (Figure 2d), which was the best catalyst. The size of the spherical particles was found to be in the range 220-450 nm while, the length of the rod was found to be in the range 1-2.8 μm . The EDX measurement of the optimized Ba@Zr (2:1) catalyst confirmed the presence of Ba, Zr and O having the composition as 54%, 24%, and 21% by weight; respectively.

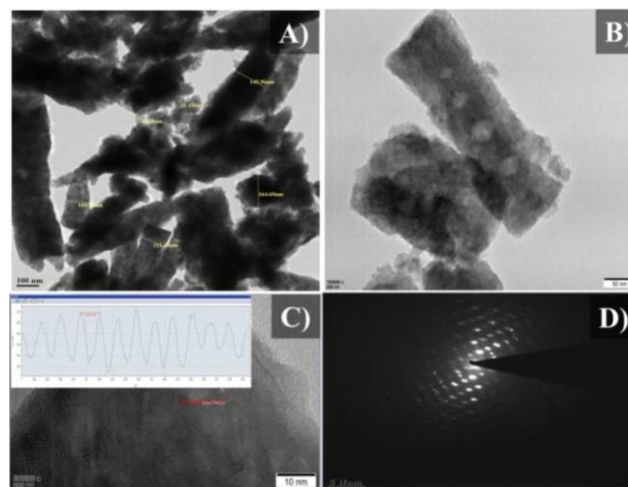


Figure 3. (A-C) shows TEM images of Ba@Zr (2 : 1) catalyst which clearly exhibited cubic morphology of a typical individual particle. The d-spacing of the observed lattice fringes was 0.27 nm, which can be associated with the [110] plane of the cubic phase of BaZrO₃.

Figure 3 (A-C) shows TEM images of Ba-Zr (2:1) catalyst which clearly exhibited cubic morphology of a typical individual particle. The d-spacing of the observed lattice fringes was 0.27 nm, which can be associated with the [110] plane of the cubic phase of BaZrO₃. The spacings of the observed lattice fringes are 0.27 and 0.36 nm, and have been correspondingly indexed to the [110] and [100] planes of the cubic phase of BaZrO₃. The SAED pattern for Ba@Zr (2 : 1) catalyst in Figure 3 (D) with spacing of lattice fringes of 0.30 nm shows the cubic phase of BaZrO₃ which could be indexed to the [110] planes, and was in good agreement with the XRD result.^[36]

Table 1 reveals the physico-chemical properties of the prepared catalysts. The specific surface areas of Ba@Zr catalysts were found in the range of 11-24 $\text{m}^2 \text{g}^{-1}$. Ba@Zr (2 : 1) catalyst showed 11.50 $\text{m}^2 \text{g}^{-1}$ surface area which was the lowest among all the studied catalysts.

The basic property of the Ba@Zr mixed metal oxide catalysts was evaluated by CO₂-TPD measurement since it is known that the catalysts with the strong basic sites promote the glucose isomerization. Table 1 shows the total and temperature range wise CO₂ desorbed in terms of mmol g^{-1} for all the samples under study. The first peak in the region of 100-200 °C was due to the weak basicity corresponding to desorption of phys-

Table 1. Physico-chemical properties of the prepared catalysts.

Sr. No.	Catalyst	BET SA ^[a] m^2/g	Total Basicity ^[b] total CO ₂ desorbed mmol g^{-1}	Total Acidity ^[c] total NH ₃ desorbed mmol g^{-1}	Basicity/ Acidity ratio
1	Ba@Zr (0.5:1)	13	0.19	0.88	0.21
2	Ba@Zr (1:1)	14.	0.31	0.48	0.64
3	Ba@Zr (2:1)	12	0.54	0.27	2.00
4	Ba@Zr (3:1)	24	0.76	0.20	3.78

^[a] Determined by N₂ physisorption measurement., ^[b] Determined by CO₂ TPD, ^[c] Determined by NH₃ TPD.

isorbed CO₂. Catalyst showed a broad peak in the region of 200–400 °C revealing the presence of medium strength basic sites.

A broad peak in the region of 450–650 °C indicated the presence of strong basic sites. The trend of basicity was found to be Ba-Zr (0.5:1) < Ba-Zr (1:1) < Ba-Zr (2:1) < Ba-Zr (3:1). The acidic strength and acidic site density were estimated in terms of total NH₃ desorbed (mmol g⁻¹) by NH₃-TPD analysis. From Table 1, NH₃-TPD trend was opposite to that of CO₂-TPD as Ba-Zr (3:1) < Ba-Zr (2:1) < Ba-Zr (1:1) < Ba-Zr (0.5:1). The activity results of all the prepared Ba-Zr MMO and bare oxides of Ba and Zr catalysts were correlated with their total basic site density calculated from CO₂ TPD and discussed later. Furthermore, ratio of basic site density/ acidic site density was also calculated and it was observed that BaO possessed the highest basicity and as Ba concentration was increased in zirconium lattice, the ratio also increased, the later was the lowest for single component of Zr (Table 1). Out of all the catalyst studied, Ba-Zr (2:1) catalyst exhibited basicity/ acidity ratio of 2.0 which was the most balanced ratio required for the selective glucose isomerization to fructose observed in this work.

Figure 4 shows the Raman spectra of all Ba-Zr samples which consist of a band at two photon lines around 87 and 135 cm⁻¹ which could be ascribed to TO1, TO2 first-order modes. The second order modes were ascribed to the band at 223 cm⁻¹. The band at 153 cm⁻¹ indicates that the crystal structure of zirconium oxide remaining intact after increasing the Ba concentration. Incorporation of barium in zirconium matrix did not completely distort the octahedral structure of zirconium but it induced oxygen vacancies in the zirconium oxide material.^[37,38] In other words, it supports the doping of Ba in zirconium lattice, which form perovskite phase and provides strong basic sites required for glucose isomerization.

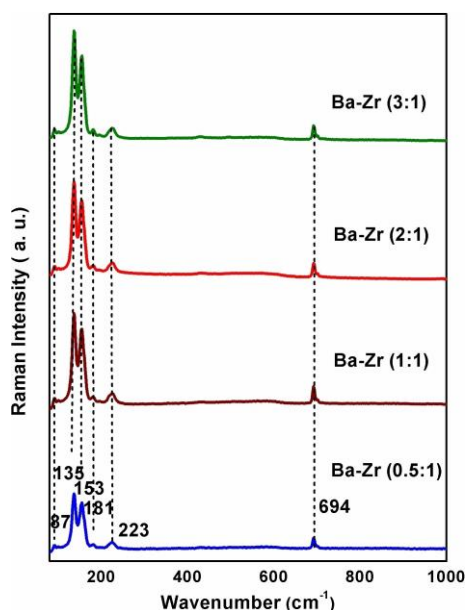


Figure 4. Raman Spectra for Ba@Zr (0.5–3:1) catalysts.

Figure 5 represents FT-IR spectra of calcined BaO, ZrO₂, and Ba-Zr mixed metal oxide catalysts. The FTIR spectrum of Ba-Zr samples with various ratios of Ba-Zr showed a prominent band at 3400–3500 cm⁻¹ which was assigned to the @OH stretching vibration due to the adsorbed water molecule on the catalytic surface. The absorption peaks in the range 400–780 cm⁻¹, 780–1145 cm⁻¹, 1145–1500 cm⁻¹, 450–560 cm⁻¹ were also observed. The absorption peak at 450–560 cm⁻¹ corresponds to Zr-O stretching mode of vibration in BaZrO₃, which clearly indicates the presence of ZrO₂ phase^[38] which is in accordance with XRD [JCPDS#86-1451] studies as discussed above. The peak at 1416 cm⁻¹ is due to the oxalate vibrational frequency in BaZrO₃. The peak at 560 cm⁻¹ corresponds to the Zr present in the octahedral site in the perovskite structure.^[39] Hence, FTIR study also confirms the presence of three phases viz. BaO, ZrO₂ and BaZrO₃ which was already characterized by other techniques.

Figure 6 represents X-ray photoelectron spectra of Ba@Zr (1:1) catalyst. Figure 6 (a) clearly showed a doublet of Zr 3d for Zr 3d_{3/2} and Zr 3d_{5/2} at B.E. of 183.2 and 185.5 eV, respectively.^[40] XPS spectra of O 1s (Figure 6c), after deconvolution showed three peaks at B.E. of 533, 532.3 and 530.8 eV out of which peaks at B.E. of 533, 532.3 eV corresponded to Si-O-Si, Si-O-Zr bridging oxygen atoms in the silica framework while, the peak at B.E. of 530.8 eV was assigned to non-bridging oxygen atoms as O₂. Ba 3d_{5/2} XPS shows a peak at 780.5 eV.^[41] XPS spectra of reused catalyst showed retention of all the peaks at same binding energy for Ba 3d_{5/2}, which clearly suggest that there was any considerable change in oxidation state of metals after use of the catalyst (Figure 6a, d). It was inferred that BaO phase mostly possessed rod shape morphology covered with some spherical particles of zirconium oxide and cubic shape particles of BaZrO₃.

Activity studies

The base catalyzed glucose isomerization is reported to proceed through the ene-diol mechanism.^[13] Since, Fructose is obtained as a major product, it is proposed that C-2 proton on

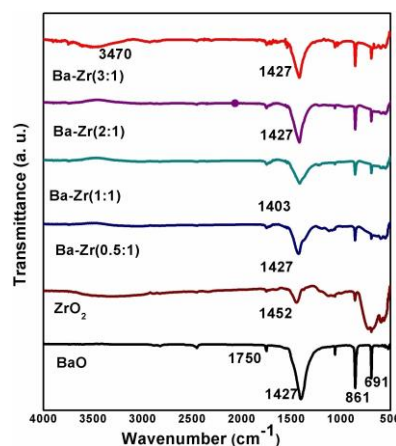


Figure 5. FT-IR spectra for calcined BaO, ZrO₂, and Ba@Zr mixed metal oxide catalyst.

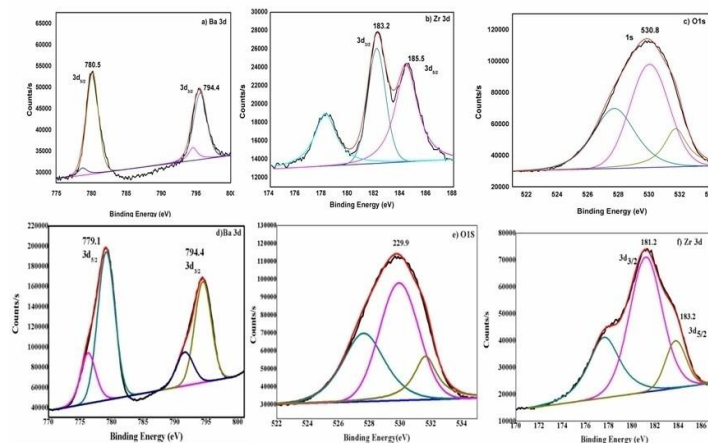
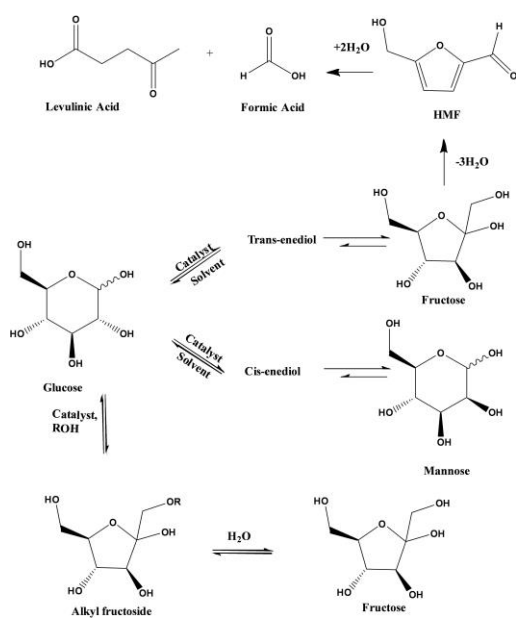


Figure 6. XPS analysis of different phases in the screened catalyst.

acyclic form of glucose is abstracted by the basic catalyst resulting in the formation of an ene-diol intermediate and followed by hydrogen transfer from O-2 to O-1 and protonation of C-1. This results in the formation of fructose as the major product and mannose as byproduct. The ene-diol mechanism involves the formation of trans-ene-diol to give D-fructose whereas; cis-enediol produces D-mannose as shown in Scheme 1.^[42,43] Another byproduct HMF formation is possible at higher temperature and/or enhanced acidity of the catalyst. Whereas the Lewis acid catalysed glucose to fructose isomerization involves opening of the glucose ring to open chain form followed by H-shift from C₂ to C₁ position and ring closure to form fructose. The acidic sites on catalytic surface play an important role in H-shift during isomerization



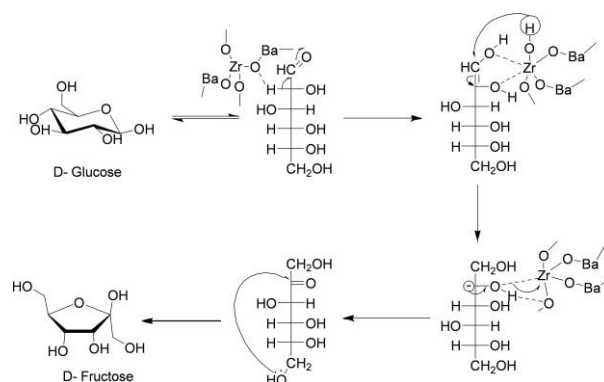
Scheme 1. Glucose isomerization to fructose, mannose and other by-products.

reaction.^[44] The mixed metal oxide catalyst prepared in this work, from alkaline earth metal Ba being basic and early transition metal Zr more acidic renders the Ba@Zr (2 : 1) catalyst to exhibit tunable base/acid bifunctional character efficiently catalyzed the glucose isomerization as shown in Scheme 2. Initially glucose molecule gets adsorbed on the catalyst surface where the basic sites actively participate in deprotonation at C₂ to form the ene-diol intermediate. The acidic sites are responsible for the stabilization of ene-diol intermediate formed and drive the deprotonation of the O-2 proton.

The final step involves cyclization to give fructofuranose as the major product. Our study revealed that the Ba@Zr (2 : 1) MMO provides the accessibility to both the base and acid sites present on the catalytic surface that play an important role in the selective (89 %) isomerization of glucose to fructose in presence of water at 100 °C, 1 atm pressure within 6 h with 57% conversion.

Catalyst screening and catalyst optimization

Keeping in view that isomerization of glucose to fructose is catalyzed either by Lewis acid sites or basic sites, we have



Scheme 2. Base catalysed isomerization of glucose to fructose.

screened various metal oxide and mixed metal oxide catalysts for this reaction and the results are as shown in Table 2. Zirconia (ZrO_2) has been used extensively as a catalyst and also as a support as it possesses both acidic as well as basic properties and high thermal stability. Whereas, the basic sites generated from hydration of SnO_2 promote glucose isomerization. The experimental results showed that bare SnO_2 and ZrO_2 showed 12 % and 27 % conversion for glucose, respectively (Table 2, entries 1 and 2, respectively). Al_2O_3 gave very low conversion (04%) (Table 2, entry 3). The basic metal oxides BaO and CaO also catalysed isomerization of glucose and gave conversions of 20 and 34 %, respectively (Table 2, entries 4 and 5). As metal oxides gave lower conversion, these were supported on SBA-15 as it provides high thermal stability, variable framework composition and high surface to volume ratio to promote the catalytic activity. Glucose isomerization did not proceed in absence of the catalyst as well as in presence of bare SBA-15 (Table 2, entry 6). Interestingly, SBA-15 supported metal oxides as Sn-SBA-15 and Zr-SBA-15 increased conversion of glucose to 36 and 32 %, respectively (Table 2, entries 7 and 8). To explore the role of acidity on the catalytic activity and glucose isomerization, 20 % PWA-SBA-15 catalyst was used, which showed only 12 % conversion of glucose (Table 2, entry 9). Although acidic catalyst like 20 % PWA-SBA-15 showed poor performance, the mixed metal oxides of barium with acidic zirconium in Ba@Zr (1 : 1) showed excellent results with 50 % glucose conversion and 82 % fructose selectivity (Table 2, entry 10). Our study revealed that the Ba@Zr (1 : 1) MMO provides high surface to volume ratio and accessibility, to both the base/ acid sites present on the catalytic surface that plays an important role in the selective isomerization of glucose to fructose. The base/ acid sites present on the catalytic surface are found to accelerate the isomerization rate by participating in the reaction pathway. In order to study the effect of increased acidity, 20 % PWA was introduced to Ba@Zr (1 : 1) catalyst which showed no any improvement with 53% glucose conversion and 65 % fructose selectivity (Table 2, entry 11). As Ba@Zr (1 : 1) MMO catalysed glucose isomerization effectively, further glucose isomerization studies were carried out using Ba@Zr mixed metal oxides prepared in various ratios. The

objective being to tailor the basic character of the bifunctional catalyst by increasing the Ba concentration in varying ratios to enhance the glucose isomerization. The effects of varying Ba@Zr ratios on glucose conversion and fructose selectivity are discussed below. CO_2 -TPD and NH_3 -TPD study revealed that although bare BaO exhibits highest basicity but it showed very low conversion of glucose (20 %). On the other hand, ZrO_2 had negligible basicity in other words has highest acidity and showed slightly higher conversion (27 %). Whereas, all the MMO exhibited increasing order of basic site density with increasing Ba concentration, which effectively showed a linear rise in activity.

Effect of various molar ratios of Ba-Zr

Effect of various molar ratios of Ba@Zr on glucose isomerization was studied and the results are presented in Figure 7 which helps to explore role of base/ acid sites on the catalytic surface responsible for conversion. Ba@Zr (0.5 : 1) catalyst gave 44 % conversion of glucose with 80% selectivity to fructose. Ba@Zr (1 : 1) showed higher conversion of 50 % glucose conversion and 82 % fructose selectivity towards fructose. Ba@Zr (2 : 1) gave the highest selectivity of 89 % to fructose with 57 % conversion of glucose. Further increase in barium molar ratio that is Ba@Zr (3 : 1), did not show much improvement in the glucose conversion (57-59 %). While, all Ba@Zr MMOs show very less selectivity towards mannose between 11-20 %. From previous reports, glucose isomerization mainly depends on base/ acid mole ratio of metal oxides as base/ acid ratio greater than 1.0 would increase the fructose selectivity.^[45] Since Ba@Zr (2 : 1) catalyst possessed the balanced ratio of basicity/ acidity it was found to be the most efficient catalyst for glucose isomerization and further studied for optimization of reaction parameters.

Effect of substrate to catalyst ratio

Figure 8 presents the effect of substrate to catalyst ratios on glucose isomerisation. A range of substrate loading with respect to catalyst (constant at 100 mg) was studied to

Sr. No.	Catalyst	Conv. (%)	Sel. (%) Fructose
1	SnO_2	12	37
2	ZrO_2	27	78
3	Al_2O_3	04	52
4	BaO	20	64
5	CaO	39	60
6	SBA-15	-	-
7	Sn-SBA-15	36	72
8	Zr-SBA-15	32	69
9	20%PWA-SBA-15	12	42
10	Ba@Zr(1:1)	50	82
11	20 %PWA-Ba@Zr(1:1)	53	65

Reaction Conditions: Glucose (180 mg, 1 mmol), Water (6 mL), Time (6 h), Temp (100 °C), Catalyst (100 mg).

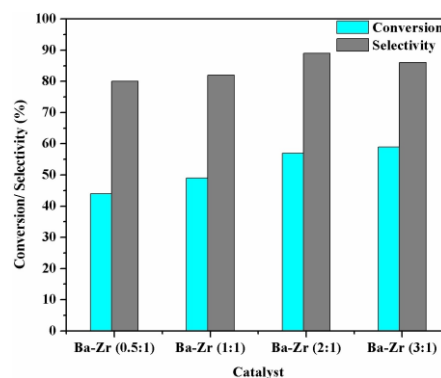


Figure 7. Effect of various molar ratios of Ba@Zr. Reaction conditions: Glucose (180 mg, 1 mmol), Water (6 mL), Time (6 h), Temp (100 °C), Catalyst (100 mg).

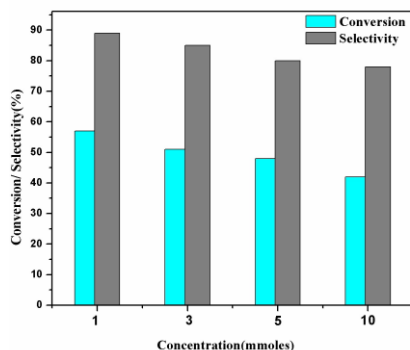


Figure 8. Effect of substrate to catalyst ratios on glucose isomerization. Reaction conditions: Glucose (1-10 mmol), Water (6 mL), Time (6 h), Temp (100 °C), Catalyst (100 mg).

determine the optimal condition for glucose isomerization. The glucose to the Ba@Zr (2:1) catalyst ratio was varied from 1.8 to 18. The increase in substrate loading (moles of glucose) resulted in a decrease in the glucose conversion from 57 to 42 %, which could be attributed to low availability of active sites. As expected, fructose selectivity was found to be highest at glucose to catalyst ratio of 1.8 due to availability of increased number of active sites on catalytic surface. Thus, the catalyst is highly selective towards glucose isomerisation to fructose.

Figure 9 shows the effect of temperature on glucose isomerization. The study of the influence of temperature on glucose isomerisation was conducted in the temperature range of 80-110 °C to accelerate the isomerization reaction. As glucose to fructose isomerization requires high activation energy, it is carried out at higher temperature ($T > 100$ °C). However higher temperature leads to low fructose selectivity as glucose and fructose being unstable, decompose at higher temperatures. Figure 9 illustrates that with increase in temperature there was a linear increase in the glucose conversion from 36-59 % and fructose selectivity to 89% with fructose yield of about 29%.

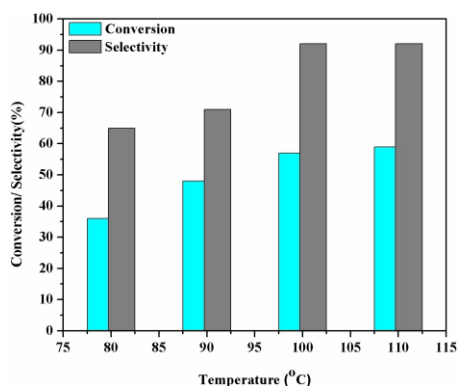


Figure 9. Effect of temperature on glucose isomerisation. Reaction conditions: Glucose (180 mg, 1 mmol), Water (6 mL), Time (6 h), Temp (80-110 °C), Catalyst (100 mg).

The increase in temperature increased the reaction rates by increasing the number of collisions and lowering the energy of activation thereby resulting in glucose isomerization. The increasing temperature accelerated the isomerization and shortened the equilibration time for isomerization reaction. Thus maximum fructose yield was observed at 100 °C in 6 h.

Solvent screening

Figure 10 reveals the effect of solvent on glucose isomerisation. In order to understand the influence of solvent system on glucose isomerization various mixtures of solvents such as (MeOH+H₂O), (DMSO+H₂O), (DMF+H₂O) and H₂O were screened. From Figure 10, it is clear that the addition of organic phase to aqueous phase causes significant decrease in glucose conversion as well as fructose selectivity. Glucose being highly soluble in polar protic solvent i. e. water seems to have strong positive effect on glucose conversion. But the mixtures of polar aprotic i. e. organic solvents with water showed decrease in reaction rate, low glucose conversion with drastic decrease in the fructose selectivity. This could be attributed to the formation of by-products such as mannose, organic acids, methyl glucoside *etc.* in presence of organic solvents as shown in Scheme 1. Thus, water was used as a solvent for optimising the other reaction parameters as it favours the proton exchange required for glucose to fructose isomerisation. Water as a solvent gave 57% glucose conversion and 89% fructose selectivity. Whereas, other mixture of solvents gave low conversion, (DMSO+H₂O) gave 46 %, (MeO+H₂O) gave 44 % and (DMF+H₂O) gave 10% glucose conversion.

Catalyst Recycle Study

One of the most important advantages of heterogeneous catalyst over homogeneous catalyst is its easy separation and reuse. In order to study the stability of the heterogeneous mixed metal oxide catalyst, the recycle study was carried out and results are shown in Figure 11. Hence, the optimised Ba@Zr (2:1) catalyst after the first run was filtered and washed with

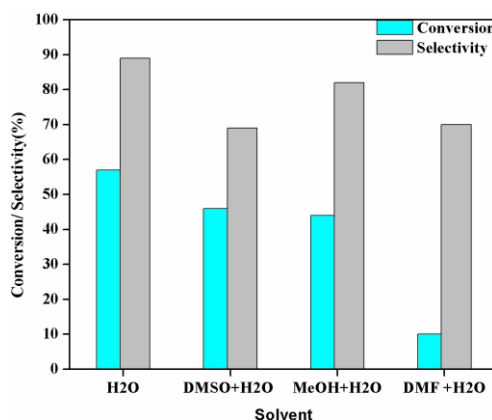


Figure 10. Effect of solvent on glucose isomerisation. Reaction conditions: Glucose (180 mg, 1 mmol), Time (6 h), Temp (100 °C), Catalyst (100 mg).

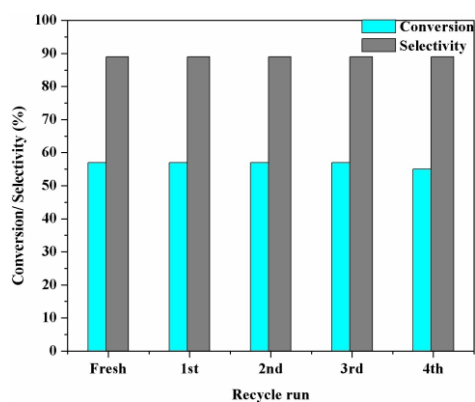


Figure 11. Recycle study.

deionised water till the pale yellow coloured catalyst became white; the catalyst was dried at 110 °C and then calcined at 550 °C for 3 neat reuse. The procedure was followed for four subsequent runs. The glucose conversion was found to decrease marginally from 57 % to 55% due to handling losses, whereas the selectivity was found to be constant at 89 % to fructose and 11 % to mannose. Thus, the catalyst prepared by Co-precipitation method showed excellent recyclability performance up to 4 cycles.

Conclusion

Ba@Zr (2 : 1) MMO was found to be highly selective towards glucose to fructose isomerization (89 %) and this could be attributed to the structural and physico-chemical properties of the catalyst confirmed by XRD, SEM, CO₂ TPD and XPS analysis. XRD pattern for mixed metal oxides of Ba@Zr (2 : 1) clearly indicated the presence of BaO, ZrO₂ phases along with perovskite type cubic phase of BaZrO₃ with reflections corresponding to (211), (220), (222), (330) and (400) planes. Various molar ratios of Ba@Zr were screened out of which Ba@Zr (2 : 1) was found to be efficient catalyst whereas on further increasing the concentration of Ba, there was not much increase in glucose conversion. This could be attributed to the base/acid mole ratio of metal oxide. Various parameters such as solvent, temperature and substrate to catalyst ratio were studied in order to determine appropriate condition for efficient catalytic activity. Various experiments carried out with organic solvents and their mixtures with water revealed that neat water acts as the best solvent for glucose isomerization thereby enhancing the glucose conversion. Thus, the bifunctional Ba@Zr (2 : 1) MMO plays an important role by providing base/ acid active sites on the catalytic surface for selective (89%) isomerization of glucose to fructose by participating in the reaction pathway in presence of water at 100 °C, 1 atm pressure within 6 h with 57 % conversion. The reaction pathway involved adsorption of glucose molecule at the catalytic surface where the basic sites actively participate in deprotonation at C₂ to form the ene-diol intermediate which is stabilized by the acidic sites present on the catalytic surface. The deprotonation of the O-2 proton

followed by cyclization gives fructofuranose as the major product. Finally, the experimental results proved that the catalyst was easily separable and reused up to 4 cycles without any loss in activity.

Supporting information summary

The supporting information contains **Experimental section**, Table S1 Crystallite sizes of all the three phases formed in all Ba: Zr MMO catalyst, Figure S1 Powdered XRD pattern for **A)** Ba@Zr (2 : 1) fresh and **B)** Ba@Zr (2 : 1) used mixed metal oxide catalysts.

Acknowledgements

Samrin S. Shaikh is thankful to AcSIR for providing the research facilities to carry out this research work. Chetna R. Patil acknowledges for the award of CSIR-RA fellowship. Sharda E. Kondawar gratefully acknowledges Council of Scientific and Industrial Research, New Delhi for awarding her CSIR-Nehru Science Postdoctoral Fellowship.

Conflict of Interest

The authors declare no conflict of interest.

Keywords: Co-precipitation • Fructose • Glucose • Isomerization • Mixed metal oxide.

- [1] J. O. Metzger, A. Huttermann, *Naturwissenschaften* **2009**, *96*, 279-288.
- [2] X. Han, L. Geng, Y. Guo, R. Jia, X. Liu, Y. Zhang, Y. Wang, *GreenChem.* **2016**, *18*, 1597-1604.
- [3] Z. Zhang, K. Deng, *ACSCatal.* **2015**, *5*, 6529-6544.
- [4] E. Nikolla, Y. R. Leshkov, M. Moliner, M. E. Davis, *ACSCatal.* **2011**, *1*, 408-410.
- [5] C. R. Patil, C. V. Rode, *Fuel* **2018**, *217*, 38-44.
- [6] R. J. V. Putten, J. C. van der Waal, E. Jong, C. B. Rasrendra, H. J. Heeres, J. G. de Vries, *Chem. Rev.* **2013**, *113*, 1499-1597.
- [7] S. P. Teong, G. Yi, Y. Zhang, *GreenChem.* **2014**, *16*, 2015-2026.
- [8] B. Saha, M. A. O. Mahdi, *GreenChem.* **2014**, *16*, 24-38.
- [9] H. Li, S. Yang, S. Saravanamurugan, A. Riisager, *ACSCatal.* **2017**, *7*, 3010-3029.
- [10] A. Corma, S. Iborra, A. Velty, *Chem. Rev.* **2007**, *107*, 2411-2502.
- [11] A. A. Rosatella, S. P. Simeonov, R. F. M. Fradea, C. A. M. Afonso, *Green Chem.* **2011**, *13*, 754-793.
- [12] P. M. Arvela, I. L. Simakova, T. Salmi, D. Y. Murzin, *Chem. Rev.* **2014**, *114*, 3, 1909-1971.
- [13] C. A. Lobry de Bruyn, W. A. van Ekenstein, *Recl. Trav. Chim. Pays-Bas* **1895**, *14*, 203-216.
- [14] A. Illanes, C. Altamirano, M. E. Zuniga, *Biotechnol. Bioeng.* **1996**, *50*, 609-616.
- [15] S. Saravanamurugan, M. Paniagua, J. A. Melero, A. Riisager, *J. Am. Chem.* **2013**, *135*, 5246-5249.
- [16] C. Kooyman, K. Vellenga, H. G. J. De Wilt, *Carbohydr. Res.* **1977**, *54*, 33-44.
- [17] J. B. Gottfried, D. G. Benjamin, *Ind. Eng. Chem.* **1952**, *44*, 141-145.
- [18] S. Suzuki, N. Tsumura, *JARQ* **1972**, *6*, 245-248.
- [19] C. Liu, J. M. Carraher, J. L. Swedberg, C. R. Herndon, C. N. Fleitman, J.-P. Tessonnier, *ACSCatal.* **2014**, *4*, 4295-4298.
- [20] J. A. Rendleman Jr., J. E. Hodge, *Carbohydr. Res.* **1979**, *75*, 83-99.
- [21] S. Despax, B. Estrine, N. Hoffmann, J. L. Bras, S. Marinkovic, J. Muzart, *Catal. Commun.* **2013**, *39*, 35-38.
- [22] I. Delidovich, R. Palkovits, *Catal. Sci. Technol.* **2014**, *4*, 4322-4329.

- [23] S. Kumar, S. Sharma, S. K. Kansal, S. Elumalai, *ACSCatal.* **2019**, *9*, 2101-2109.
- [24] A. A. Marianou, C. M. Michailof, D. K. Ipsakis, S. A. Karakoulia, K. G. Kalogiannis, H. Yiannoulakis, K. S. Triantafyllidis, A. A. Lappas, *SSustainableChem. Eng.* **2018**, *6*, 16459-16470.
- [25] J. Tang, X. Guo, L. Zhu, C. Hu, *ACSCatal.* **2015**, *5*, 5097-5103.
- [26] S. H. Mushrif, J. J. Varghesea, D. G. Vlachos, *Phys.Chem. Chem. Phys.* **2014**, *16*, 19564-19572.
- [27] M. Moliner, Y. Román-Leshkov, M. E. Davis, *PNAS* **2010**, *107*, 6164-6168.
- [28] H. Ling, A. Li, D. Wu, Y. Tang, Z. Liu, N. Ming, *Mater. Chem. Phys.* **2002**, *75*, 170-173.
- [29] A. Sin, B. E. Montaser, P. Odier, F. J. Weiss, *Am. Ceram. Soc.* **2002**, *85*, 1928-1932.
- [30] J. Brzezinska-Miecznik, K. Haberko, M. M. Bucko, *Mater. Lett.* **2002**, *56*, 273-278.
- [31] N. M. Kirby, A. Van Riessen, C. E. Buckley, V. W. Wittorff, *J. Mater. Sci.* **2005**, *40*, 97-106.
- [32] N. Millot, B. Xin, C. Pighini, D. J. Aymes, *Eur. Ceram. Soc.* **2005**, *25*, 2013-2016.
- [33] F. Boschini, B. Robertz, A. Rulmont, R. J. Cloots, *Eur. Ceram. Soc.* **2003**, *23*, 3035-3042.
- [34] H. Kleineberg, M. Eisenacher, H. Lange, H. Strutz, R. Palkovits, *Catal. Sci. Technol.* **2016**, *6*, 6057-6065.
- [35] H. Zhou, Y. Mao, S. S. Wong, *Chem. Mater.* **2007**, *19*, 5238-5249.
- [36] E. C. Aguiar, A. Z. Simoes, C. A. Paskocimas, M. Cilense, E. Longo, J. A. Varela, *J. Mater. Sci. Mater. Electron.* **2015**, *26*, 1993-2001.
- [37] Z. G. Lu, Y. G. Tang, L. M. Chen, Y. D. Li, *J. Cryst. Growth* **2004**, *266*, 4, 539-544.
- [38] A. B. Lavand, Y. S. Malghe, *J. Therm. Anal. Calorim.* **2014**, *118*, 1613-1618.
- [39] C. R. Patil, C. V. Rode, *ChemistrySelect* **2018**, *3*, 12504-12511.
- [40] P. Nachimuthu, Y. J. Kim, S. V. N. T. Kuchibhatla, Z. Q. Yu, W. Jiang, M. H. Engelhard, V. Shutthanandan, Ja'nosSzanyi, S. Thevuthasan, *J. Phys. Chem. C* **2009**, *113*, 14324-14328.
- [41] H. Kitajima, Y. Higashino, S. Matsuda, H. Zhong, M. Watanabe, T. M. Aida, R. L. Smith, Jr. *CatalysisToday* **2016**, *274*, 67-72.
- [42] J. M. Carraher, C. N. Fleitman, J.-P. Tessonnier, *ACSCatal.* **2015**, *5*, 3162-3173.
- [43] V. Choudhary, A. B. Pinar, R. F. Lobo, D. G. Vlachos, S. I. Sandler, *ChemSusChem* **2013**, *6*, 2369-2376.
- [44] G. Li, E. A. Pidko, E. J. M. Hensen, *ACSCatal.* **2016**, *6*, 4162-4169.
- [45] Q. Guo, L. Ren, S. M. Alhassan, M. Tsapatsis, *Chem. Commun.* **2019**, *55*, 14942-14945.

Submitted: August 4, 2020

Accepted: October 9, 2020



Direct Conversion of *N*-acetyl-D-glucosamine to *N*-containing Heterocyclic Compounds 3-Acetamidofuran and 3-Acetamido-5-acetyl Furan

Samrin S. Shaikh^{1,2} · Chetana R. Patil¹ · Nishita Lucas¹ · Vijay V. Bokade^{2,3} · Chandrashekhar V. Rode^{1,2}

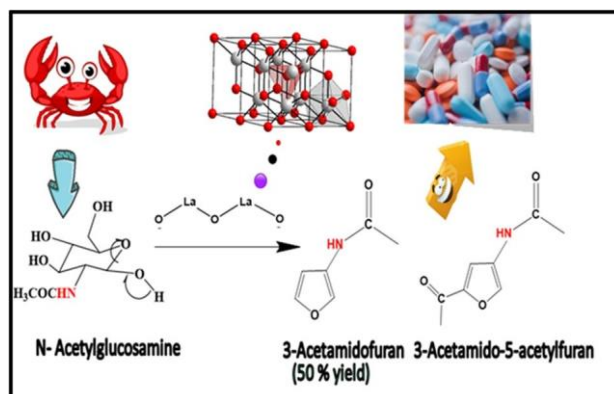
Received: 9 November 2022 / Accepted: 25 March 2023
© The Author(s), under exclusive licence to Springer Nature B.V. 2023

Abstract

Purpose Effectual waste utilization from plant as well as marine biomass has gained tremendous importance with reference to sustainability. The valorization of marine biomass produces value added compounds containing not only C, H, O but also renewable N atom in the skeleton which widens the scope for its exploration which may prove to be economically beneficial to the society. Heterogeneous catalytic transformation of marine biomass i.e. *N*-acetyl glucosamine (NAG) to *N*-substituted aromatic heterocyclic furan derivatives is reported for the very first time. Cost effective and stable metal oxide catalysts were deployed for the transformation. Catalyst screening study showed that La_2O_3 was found to be an excellent catalyst for *N*-acetyl glucosamine (NAG) dehydration which mainly produced 3-acetamidofuran (3AF). **Methods** The physicochemical properties of the metal oxide catalyst were investigated by various techniques such as XRD, FTIR, MeOH-FTIR, TPD, SEM, N_2 sorption studies and HR-TEM analysis for structure activity relationship. **Results** The effect of various reaction parameters such as catalyst concentration, reaction temperature, reaction time and solvent effect on dehydration of *N*-acetyl glucosamine has been studied in detail for higher yields. The results revealed that the presence of weak basic sites which are Brønsted in nature and nano pores present on the surface were responsible for improved dehydration of the chitin biomass to selectively yield 3-acetamidofuran (3AF). La_2O_3 catalyst showed optimum 50% 3AF yield from *N*-acetyl glucosamine at 180 °C in 3 h. **Conclusion** Efficacious exploitation of marine biomass to value added chemicals using heterogeneous catalysts can be extensively exploited. Separation of *N*-substituted heterocyclic aromatics is the most innovative aspect of the current study. Thus, utilization of heterogeneous catalyst and renewable biomass as a raw material indicates a transition towards more sustainable and greener approach.

Graphical Abstract

With reference to valorization of biomass waste towards sustainability. We report for the first time heterogeneous catalytic transformation of marine biomass i.e. *N*-acetyl glucosamine (NAG) over La_2O_3 catalyst to yield 50% 3-acetamido furan (3AF) and 20% 3-acetamido-5-acetylfuran with 100% NAG conversion. The superior performance of La_2O_3 catalyst was attributed to the presence of Brønsted basicity and nanopores present at catalysts surface.



Extended author information available on the last page of the article

Keywords Lanthanum oxide · N-acetyl-D-glucosamine · Heterogeneous catalysis · Dehydration · Renewable feedstock · 3-acetamidofuran · 3-acetamido-5-acetylfuran

Abbreviations

DMSO	Dimethyl sulfoxide
NAG	N-Acetyl-D-glucosamine
GlcNH ₂	Glucosamine
HMF	5-Hydroxymethylfurfural
IL	Ionic liquid
LA	Levulinic acid
NAG	N-Acetyl-D-glucosamine
EtOAc	Ethylacetate
DMA	Dimethylacetamide
DMF	Dimethylformamide
MIBK	Methylisobutylketone
3AF	3-Acetamido furan
3A5AF	3-Acetamido-5-acetyl furan
3A5HEF	3-Acetamido-5-(1-hydroxyethyl)furan

Statement of Novelty

We report for the first time, dehydration of NAG to *N*-containing renewable platform molecules by heterogeneous catalyst without use of any additives, ionic liquids or boron compounds. The catalyst showed high stability, easy separation and excellent recyclability upto 5 cycles. The cooperative effects of Brønsted basicity and nanopores on the catalyst activity play vital role in NAG conversion (100%) to yield 50% 3AF and 20% 3A5AF yield. The physicochemical properties of the metal oxide catalyst were investigated by XRD, FTIR, MeOH-FTIR, TPD, SEM, N₂ sorption studies and HR-TEM analysis for structure activity relationship. As far as sustainability is concerned this study represents a direct one pot conversion of NAG to *N*-substituted renewable compounds by valorization of marine biomass.

Introduction

Efficient waste valorization has been in limelight as it could aid the society to mitigate the alarming environmental issues arising due to the depletion of fossil fuels such as energy crises, green house effects etc. [1, 2]. Among the biomass variants, marine biomass is readily available as oceans occupy around 71% of earth's surface. But for decades, the advancement and valorization of marine biomass has remained unexplored, which could emerge as a strong feedstock to bring sustainability and economic benefit to the society. After cellulosic biomass, chitin stands second most abundant biomass on earth with 100 billion tons produced annually [4]. Chitin biomass is obtained from shells

of several marine animals like crabs, lobsters, shrimps, crayfish, arthropods as well as from cell wall of fungi and yeast [5–7]. Cellulosic biomass on valorization produces value added compounds containing mainly C, H, and O. Whereas, the marine biomass on valorization widens the scope for production of *N*-containing platform chemicals having various applications as adsorbents, for waste water treatment, agricultural chemicals, polymers, in food industries, biomedical applications, formation of films, fibers, composites and cosmetics [8–10]. Chitin biomass comprises of *N*-acetyl glucosamine units linked through β -1, 4 glycosidic linkages to form polymeric chains in three different allomorphic forms viz. α , β , γ . Therefore, the chitin biomass exhibits distinct physicochemical properties due to the presence of *N*-functionality in its skeleton and serves as most important natural source of nitrogen [11–13]. Cellulosic biomass and chitin biomass have structural similarities with the exception that cellulosic biomass on valorization produces value added compounds and platform chemicals containing C, H and O whereas, chitin biomass produces chemicals containing C, H, O and N. Owing to the presence of 7 wt. % renewable N atom in chitin it has put the marine biomass on fame and has attracted the attention of researchers as it has tremendous scope for its valorization with wide range of applications [14, 15]. The chitin hydrolysis is carried out by biological, physical and chemical pretreatment methods which produces NAG, which requires number of steps and harsh conditions like use of mineral acids, high temperature and, thus suffers from major drawbacks making the process non feasible. Also, the biological methods fail to eliminate the minerals and proteins from the crustacean shells and high cost of enzymes makes the process less cost effective [16, 17]. Prior to chitin hydrolysis, microwave irradiation and sonication were used to increase the chitin solubility in HCl thereby enhancing the chitin hydrolysis to produce NAG [18, 19]. Franich et al. reported for the first time that the pyrolysis of tar produced several degradation products with 5% 3-acetamidofuran (3AF), 2% 3-acetamido-5-acetyl furan (3A5AF) and 3% 3-acetamidoacetaldehyde yield [20]. Chen et al. studied the NAG pyrolysis at 200 °C for 30 min to produce 3A5AF as the major product with 3AF and several furanic and pyrazine derivatives as minor products. The pyrolysis pathway results in the formation of number of products thus making the process less economical due to lower selectivity towards desired product formation [16]. The platform chemical 3A5AF, is a precursor for the synthesis of an anticancer drug proximycin A [21, 22]. Both the products 3AF and 3A5AF have *N*-containing amide functionality in the form of furanic aromatic platform chemicals which can further be explored for their transformations to value added products. But the challenge is retention of amide group as it easily gets fragmented from the main chain [23]. 3AF and 3A5AF may find a role as synthetic precursors for

the synthesis of naturally occurring antibiotic and antitumor drug proximycin A, B and C and amino sugars, amino acids and dihydrodifuro pyridine derivatives, aminated bicyclic ethers, pyridine derivatives, bicyclic pyrrolidines via various multi step organic transformations due to its structural similarity and presence of N atom in its skeleton [1, 2, 24–28]. 3A5AF on asymmetric reduction, produced (3-acetamido-5-(1-hydroxyethyl)furan, a precursor for the synthesis of amino sugar, L-rednose which is a precursor forming the structural unit of biologically active natural products such as anthracycline [29], saquamyacin [30] and rudolphomycin [31]. Ha et al. reported chemoenzymatic dehydration of NAG and its further enantioselective asymmetric reduction to 3-Acetamido-5-(1-hydroxyethyl)furan (3A5HEF) with good yield [32]. Omari et al. reported the conversion of NAG to 3A5AF in the presence of $B(OH)_3$ and NaCl under high temperature microwave irradiation (220 °C for 15 min) to give 58% 3A5AF yield. His group highlighted the importance of the presence of chloride and boron atoms in the hydrolysis of chitin and dehydration of NAG to 3A5AF, respectively [21]. Drover et al. studied the transformation of NAG into 3A5AF with 60% yield under microwave heating with ionic liquid, [BMIM]Cl in which imidazolium ring was found to play an important role in the conversion of NAG to 3A5AF [18]. Chen et al. introduced the acidic proton at C-2 position and reported the importance of Cl anion in the solubility and dissolution of chitin thereby accelerating its hydrolysis to yield value added products. They reported the direct conversion of chitin to 3A5AF with 7% yield in ionic liquid using boric acid and HCl as an additive [19]. Wang et al. reported conversion of chitin to yield 43% 3A5AF in glycine chloride ionic liquid [33]. Hence, ionic liquids can be used as ideal solvents as they can bear high temperature range, non-volatile and are non-inflammable. But certain disadvantages like toxicity, handling difficulty and higher cost make ionic liquids less economical for use [34]. Surprisingly, the synthesis of furanic compounds remains unexplored using heterogeneous catalysts which excel others in cost, recyclability, ease of separation, catalyst tunability and process improvisation. Visualizing the importance of the marine waste valorization and advantages of the heterogeneously catalyzed conversion, the current study gives first hand report on dehydration and partial deoxygenation of NAG to N-containing renewable platform molecules using various metal oxide catalysts. Choice of catalyst originated from some striking features like stability, cost effectiveness and ease of preparation. A comparative study of acid and basic catalysts has been attempted to furnish insights into type of sites required for selective formation of furans. The best catalyst was characterized by XRD, FTIR, MeOH-FTIR and SEM along with effect of reaction parameters on NAG dehydration to produce 3AF has been carried out.

Experimental

Materials

N-acetyl glucosamine, lanthanum oxide (La_2O_3), calcium oxide (CaO), cerium oxide (Ce_2O_3), zirconium oxide (ZrO_2), aluminium oxide (Al_2O_3) and barium hydroxide ($Ba(OH)_2$) were purchased from Thomas Baker Chemicals, India. The chemicals were used as received without further purification. The solvents such as MeOH, DMF, DMSO, ACN, n-Hexane, EtOAc, DMA, MIBK, dioxane and other chemicals were also purchased from HIMEDIA chemicals, India. DMSO-d₆ was purchased from Sigma Aldrich, India and was used as NMR solvent.

Catalyst Preparation

Barium hydroxide was calcined at 550 °C for 6 h to produce barium oxide.

Catalyst Characterization

The catalyst was characterized by using various techniques. The X-ray diffraction (XRD) analysis was carried out on a P Analytical PXRD system (Model X-Pert PRO-1712), using Ni filtered Cu K α radiation ($\lambda=0.154$ nm) as an X-ray source (current intensity, 30 mA; voltage, 40 kV) and an X-accelerator detector. XRD measurements were carried out in a 2θ range of 5°–85° with a scanning rate of 5°/min. The SEM-EDAX analysis was carried out in order to study the morphology and elemental composition of the catalysts on a LEO – LEICA STEREOSCAN 440 instrument. Prior to the analysis the powdered samples were dispersed in iso-propanol and sonicated for 15 min. Then drops of the suspension were deposited on a carbon-coated copper grid and dried, at room temperature. The samples were gold coated before analysis. HR-TEM analysis was carried out on JEOL 1200 EX model which provided information about the morphology, particle size, d-spacing and fringe width. Prior to the analysis the powdered samples were dispersed in iso-propanol and sonicated for 15 min. Then drops of the suspension were deposited on a carbon-coated copper grid dried, at room temperature before analysis. FTIR spectra of the catalysts were done on a Perkin Elmer 2000 FTIR spectrometer in the range of 4000–400 cm^{-1} . The surface areas of all the catalysts using BET equation were measured on Quantachrome v 2.0 instrument. The basic sites present on the catalyst surface were quantitatively analyzed by CO_2 -TPD carried out on Micromeritics-2720 (ChemisoftTPx) volumetric instrument. The samples were pre-treated from room temperature to 200 °C under a helium flow rate of 25 $mL\ min^{-1}$ followed by CO_2 adsorption at

40 °C and finally CO₂ desorption with heating rate of 10 °C min⁻¹ starting from adsorption temperature to 700 °C. The TGA analysis of the catalyst was carried out on Simultaneous Thermal Analyzer SDT-650 apparatus. The analysis was carried out in air (40 mLmin⁻¹) at a heating rate of 10 °C min⁻¹ from room temperature to 800 °C.

Catalyst Activity Measurement

In a 50 mL Parr reactor, N-acetyl-glucosamine (1 gm), dioxane (25 mL) and catalyst (200 mg) were heated at 180 °C under constant stirring for 4 h. After the reaction was complete, the reaction mixture was filtered and the filtrate was concentrated on Buchi Rotavap at 140 mbar and 60 °C. Yellowish-red viscous liquid was obtained from which product was separated by solvent extraction using ethyl acetate and water. The humins were separated in water layer whereas the product was extracted in the ethyl acetate layer. The crude product thus obtained was then purified by silica gel column chromatography. The detailed procedure for isolation of 3AF and 3A5AF are given in supplementary material. Fig. S1a, Fig.S1b, Fig.S2a and Fig.S2b show ¹H NMR and ¹³C NMR spectra of the isolated 3A5AF and 3AF, respectively. Fig.S3 and Fig.S4 represent the HR-MS chromatograms of 3AF and 3A5AF and Fig.S5 and Fig.S6 shows FTIR (NAG and 3AF, 3A5AF) analysis qualitatively. The NAG conversion was analyzed by HPLC (Agilent 1260) equipped with Hiplax-Pb column (300 mm length) equipped with refractive index detector. Deionized water (DI) was used as a mobile phase, which was filtered and used. The NAG conversion was quantitatively determined by HPLC analysis by keeping 0.5 mL/min flow rate of the prepared mobile phase maintaining column temperature at 80 °C and total analysis time of 20 min. The products formed were identified, separated by solvent extraction and purified by column chromatography, confirmed by HRMS, ¹H and ¹³C NMR and isolated mass yield was reported. The calibration curve is given in supplementary material Fig.S7.

Recycling of Catalyst

At the end of reaction, the catalyst was recovered by filtration and washed four times with 10 mL DI water until pale yellow-colored impurities faded, then dried at 110 °C overnight in a vacuum oven followed by calcination at 550 °C for 3 h and reused. In order to determine the reusability and stability of the catalyst, the recovered catalyst was characterized by XRD, FTIR and TGA.

Results and Discussion

Catalyst Characterization

Figure 1b shows the powder XRD patterns of various metal oxide catalysts. The wide angle XRD patterns of the sample of La₂O₃ showed reflections at 2θ = 15.70°, 27.18°, 28.09°, 39.41°, 48.2° ascribed to La₂O₃ phase [JCPDS # 05-0602] corresponding to (100), (002), (101), (102), (211) planes, respectively, with lattice constants as a = 3.397 nm and b = 6.129 nm which indicated the presence of hexagonal

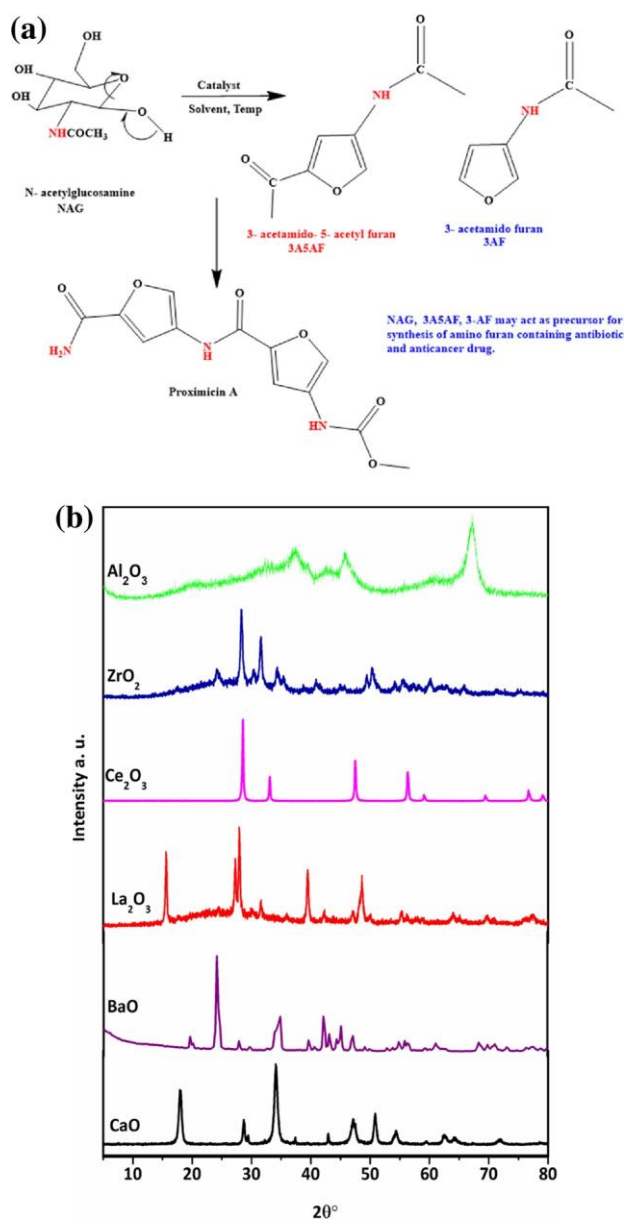


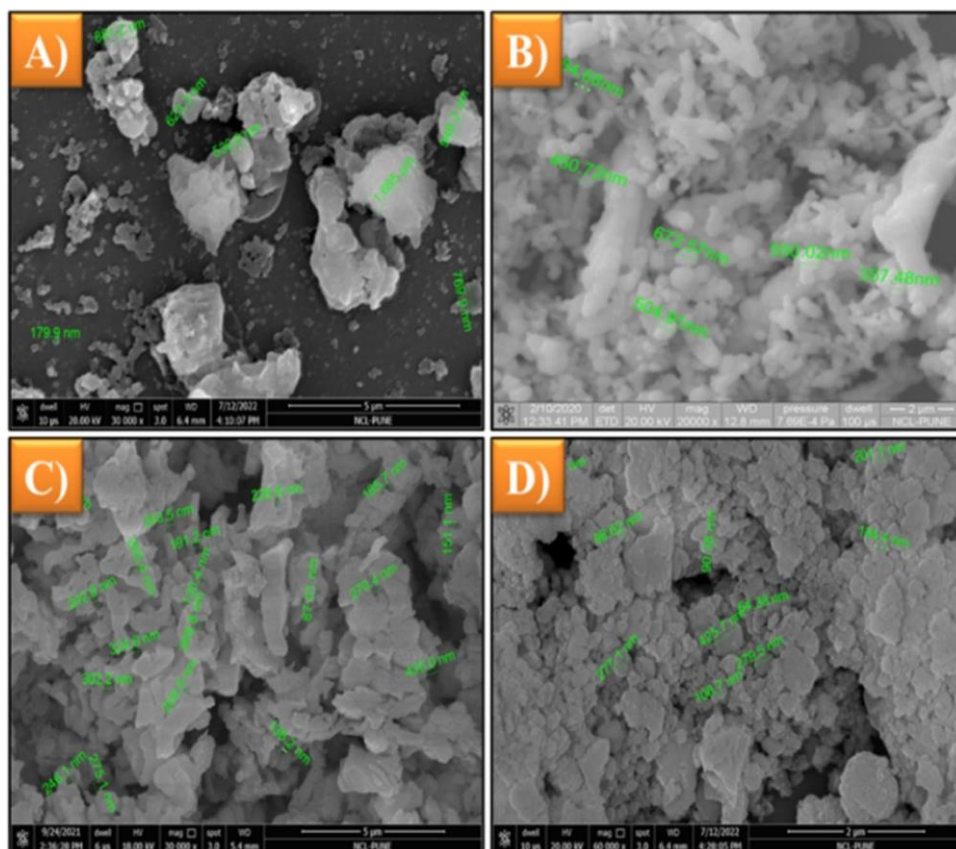
Fig. 1 a Chemical structure of NAG, 3A5AF, 3AF and proximicin A. b PXRD plots of CaO, BaO, La₂O₃, Ce₂O₃, ZrO₂, Al₂O₃ catalysts

phase of La_2O_3 [JCPDS # 05-0602] [35]. The diffraction peaks at $2\theta = 15.70^\circ$ and 48.80° can be indexed to the hexagonal phase of $\text{La}(\text{OH})_3$ corresponding to (100) and (211) planes with lattice constants as $a = 0.652 \text{ nm}$ and $b = 0.858 \text{ nm}$ [36]. The appearance of sharp peaks for the hexagonal phases of La_2O_3 and $\text{La}(\text{OH})_3$ denote high crystallinity of La_2O_3 . La_2O_3 didn't show typical peak for carbonated form of lanthanum which can be observed at $2\theta = 10.2^\circ$, it confirmed the presence of La_2O_3 phase and small amount of $\text{La}(\text{OH})_3$ phase in the examined sample [37]. All the other catalysts used for comparison also showed well defined phase. The wide angle XRD pattern for tetragonal phase of BaO showed the reflections at $2\theta = 19.6^\circ, 23.7^\circ, 45.1^\circ$, [JCPDS#47-1488]. Whereas, reflections at $2\theta = 23.7^\circ, 29.1^\circ$ and 55.8° were ascribed to monoclinic ZrO_2 phase [JCPDS#86-1451] [38]. The XRD pattern for CaO showed peaks at $18.14^\circ, 28.73^\circ, 34.16^\circ, 47.11^\circ, 50.86^\circ, 54.36^\circ, 62.76^\circ, 64.41^\circ, 72.05^\circ, \text{ and } 84.87^\circ$ which confirmed the presence of CaO phase [39]. The cubic phase of CeO_2 as confirmed by the presence of the characteristic peaks observed at $2\theta = 28.83^\circ, 33.2^\circ, 47.9^\circ, 56.7^\circ$ and 59.4° corresponding to (111), (200), (220), (311) and (222) planes, respectively [40]. The XRD pattern for Al_2O_3 showed weak diffraction peaks, observed at $2\theta = 19.2^\circ, 31.0^\circ, 36.6^\circ, 39.3^\circ, 46^\circ, 61.5^\circ$, and 67° , which can be indexed to the reflections at (111),

(220), (311), (222), (400), (511), and (440) corresponding to the presence of γ -alumina phase according to JCPDS card: 100425 [41]. The detailed morphology, surface topography of the catalysts was studied by FE- SEM.

Figure 2 displays the SEM images of various catalysts, with different magnifications viz. (a) CaO , (b) BaO , (c) La_2O_3 , (d) Ce_2O_3 . In case of calcined La_2O_3 , irregular and uneven shaped particles were predominantly present as shown in Fig. 2c. The SEM images clearly indicated the presence of pores of varied sizes in the range 90–450 nm on the surface. The presence of these nano pores aid in providing high surface area for adsorption. The SEM analysis of cerium oxide is shown in Fig. 2d. The morphological investigation revealed the presence of pores with spherical shaped particles distributed on the surface with size 90–420 nm. BaO showed the presence of mixed morphology with spherical and rod shaped particles. Rod shaped particles were present predominantly with length in the range of 1–2.8 μm and the size of the spherical particles in the range 220–450 nm as shown in Fig. 2b [38]. In case of CaO as shown in Fig. 2a, the morphology revealed to contain clusters of flakey particles with particle size, viz. 150–750 nm. The percentage elemental composition was acquired by EDS analysis for all four metal oxide catalysts screened (Supporting information Fig.S-10, S-11, S-12, S-13). It confirmed the presence of

Fig. 2 Scanning Electron Micrographs of **A** CaO **B** BaO **C** La_2O_3 and **D** Ce_2O_3



La_2O_3 phase having composition in mass percentage of the elements as 39.69% O and 60.31% La by weight. The peak indexing of the elements for lanthanum was 4.63 keV and for oxygen was 0.51 keV.

High Resolution-Transmission Electron Microscopy (HR-TEM) was utilized for detailed study of the size, shape, morphology and surface distribution of the particles as shown in Fig. 3 Irregular, unordered distributions of the particles were observed at the surface. The agglomeration of the nano particles due to aggregation of the particles by weak forces was observed with average pore size in the range 90–500 nm [42]. Thus, from the HR-TEM characterization we conclude that the agglomerated catalyst possess good porosity due to the presence of pores in the nano range [43].

Figure 4A presents FT-IR spectra of calcined (La_2O_3) in the range 400–4000 cm^{-1} which showed detailed information about the metal and oxygen bonds present in the metal oxide catalysts. The FTIR spectrum of La_2O_3 sample showed a prominent band at 637 cm^{-1} which was assigned to the stretching vibration of La–O. The intense and sharp absorption band at 3619 cm^{-1} was ascribed to the –OH stretching of water molecule adsorbed from atmosphere on the oxide surface and the band at 1530 cm^{-1} corresponds to the presence of extending and twisting –OH bending vibration due to the physically adsorbed water molecule on the catalyst surface. This confirms the presence of Brønsted basic sites in the form of $\text{La}(\text{OH})_3$ phase [1, , 44–46]. Hence, the appearance of the above mentioned bands in

the FTIR spectra confirmed the presence of La_2O_3 and the $\text{La}(\text{OH})_3$ phases in accordance with XRD study [47]. BaO showed an intense band at 692 cm^{-1} corresponding to Ba–O stretching frequency. Whereas, the band at 512 cm^{-1} was assigned to the Ca–O stretching vibration. The Ce–O stretching frequency was observed at 613 cm^{-1} . In case of CaO and BaO, the absorption band due to the bending vibration of the adsorbed water molecule on the catalyst surface was observed at 1448 cm^{-1} and intense and sharp absorption due to the –OH stretching of the adsorbed water molecule was observed at 3645 cm^{-1} (sharp) and 3350–3655 cm^{-1} (broad). The broad absorption band corresponds to the superposition of the hydroxyl stretching bands due to the hydroxyl groups present at the metal oxide surface and the hydrogen bond. But in Ce_2O_3 , the band due to bending vibration for the adsorbed water molecule shifted to 1626 cm^{-1} and a broad absorption band at 3200–3650 cm^{-1} was observed due to adsorbed water molecule at the catalytic surface. This clearly indicates the presence of hydroxyl group on the catalytic surface.

Figure 4B represents the in-situ FT-IR spectra obtained by subtracting adsorbed MeOH on metal oxide and neat metal oxide spectra. The investigation of Brønsted basicity was carried out by performing in-situ methanol adsorption-IR spectroscopy. Earlier, Verneker et al. studied various interactions of $\text{FeO}(\text{OH})$ at the surface by MeOH adsorption IR spectroscopy. Their results showed that MeOH interacts with the basic sites on the catalytic surface to form monodentate

Fig. 3 A, B Transmission Electron Micrographs La_2O_3 catalyst and C d-spacing for La_2O_3 catalyst

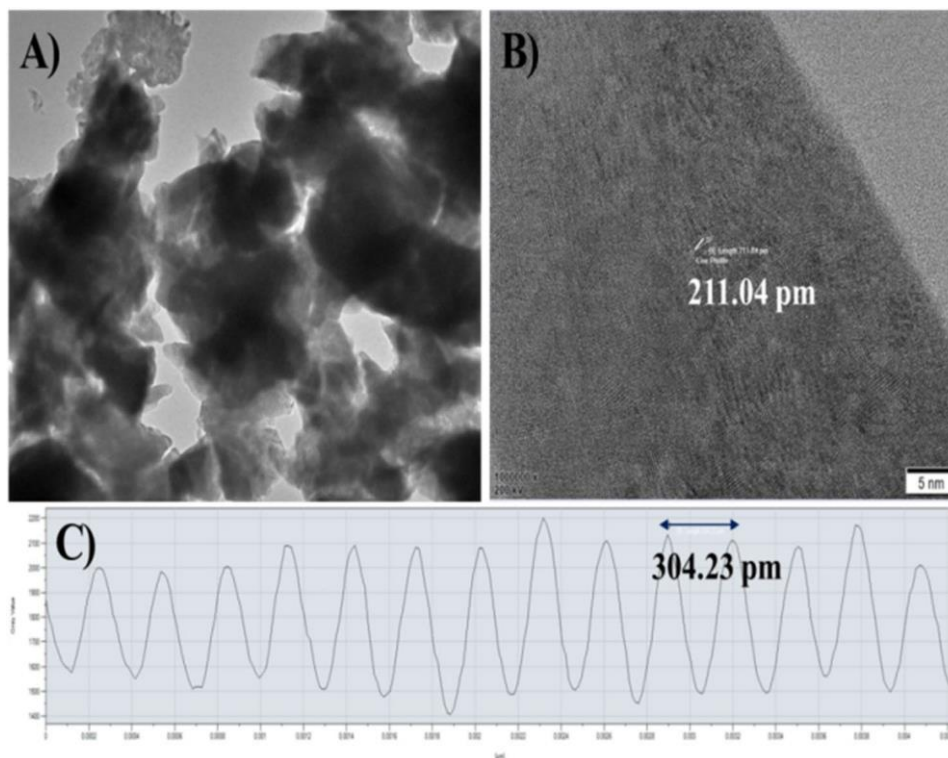
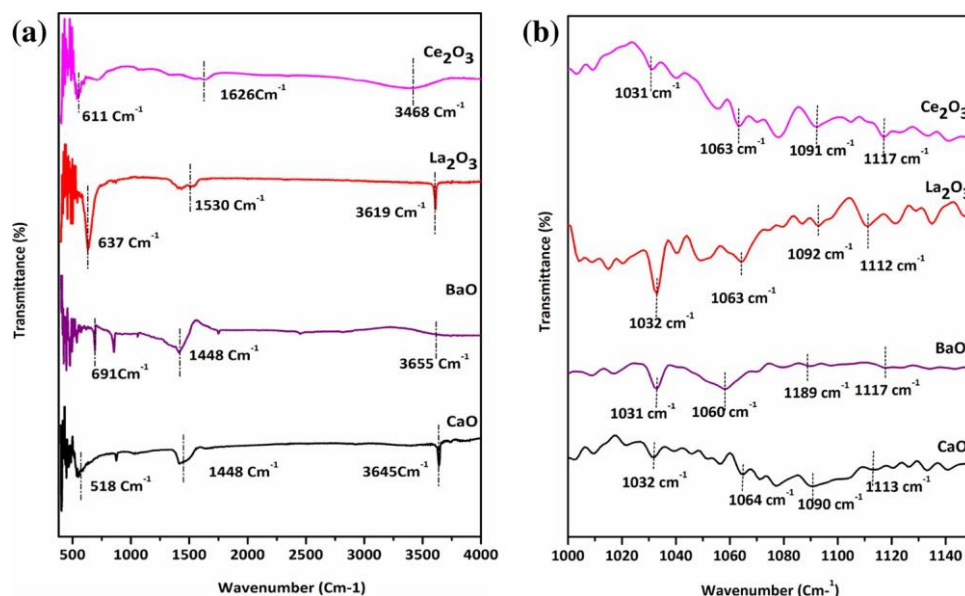


Fig. 4 **A** FT-IR spectra for all metal oxide catalyst. **B** FT-IR spectra for MeOH adsorbed on all metal oxide catalysts



methoxy species, bidentate methoxy species and molecularly adsorbed species with bands observed at 1115 cm⁻¹, 1092 cm⁻¹, 1064 cm⁻¹ [48–50]. In Fig. 4B, various interactions of the adsorbed MeOH with the catalytic surface can be seen. The formation of H-bonded molecularly adsorbed MeOH at the La₂O₃ surface was observed with a band at 1064 cm⁻¹. Whereas, the bands at 1115 cm⁻¹ and 1092 cm⁻¹ indicated the formation of monodentate and bidentate methoxy species/metal complexed methoxy species. All these bands were observed in La₂O₃, Ce₂O₃, CaO and BaO catalysts. The La₂O₃ catalyst showed intense band at 1063 cm⁻¹ and 1117 cm⁻¹ whereas, CaO and BaO showed weak bands in this region. The presence of these intense bands in La₂O₃ catalyst clearly indicates the presence of Brønsted basic sites on the catalyst surface, which play an important role in the NAG dehydration.

Table 1 reveals the physico-chemical properties of the screened catalysts. The surface areas of the catalysts determined by the Brunauer–Emmett–Teller (BET) measurement using N₂ adsorption-desorption isotherms, were found to be

98.097 m²g⁻¹ for calcium oxide, 8.073 m²g⁻¹ for barium oxide, 12.186 m²g⁻¹ for lanthanum oxide and 13.294 m²g⁻¹ for cerium oxide catalysts. Fig.S8 (supporting info.) represents the adsorption isotherm of all the catalysts. The N₂ adsorption-desorption isotherm gives detailed information of surface area, pore volume and pore size of the catalyst calculated using BJH method. The La₂O₃ catalyst exhibited adsorption isotherm which represents unrestricted multi-layer formation due to strong lateral interactions between the adsorbed molecules [51]. The steepness of the isotherm was found to decrease in the order BaO > CaO > La₂O₃ = Ce₂O₃. The hysteresis loop in case of CaO showed the presence of relatively uniform and narrow pores whereas, the hysteresis loop for La₂O₃ and Ce₂O₃ showed the presence of narrow pores with irregular shape and size [52, 53]. Table 1 shows the BET surface area in terms of (m²g⁻¹), it showed the total surface area of 12.186 m²/g, pore volume of 0.0413 cc/g and pore diameter of 0.1357 nm [54, 55]. whereas, Ce₂O₃ showed total surface area of 13.294 m²g⁻¹, pore volume of 0.0405 ccg⁻¹ and pore diameter of 0.1219 nm. Also, BaO

Table 1 Physico-chemical properties of the catalysts

Sr. No	Catalyst	S-[BET] ^a (m ² g ⁻¹)	Pore volume ^b (cc g ⁻¹)	Pore diameter ^b (nm)	Distribution of basic sites (mmol g ⁻¹)			Total Basicity ^c (total CO ₂ desorbed, mmol g ⁻¹)
					Temperature ^c (°C) (100–200)	Temperature ^c (°C) (200–400)	Temperature ^c (°C) (400–700)	
1	CaO	98.097	0.1569	0.6398	–	0.6780	0.0753	0.7533
2	BaO	8.073	0.0132	0.6582	0.0081	0.8512	0.1318	0.9911
3	La ₂ O ₃	12.186	0.0413	0.1357	0.2739	0.0940	0.0175	0.3854
4	Ce ₂ O ₃	13.294	0.0405	0.1219	0.0090	0.0068	0.0709	0.0867

S-[BET] BET surface area

^aBET analysis, ^bBJH method, ^cDetermined by CO₂ TPD measurement

and CaO exhibited total surface area of 8.073 m²/g and 98.097 m²/g, pore volume of 0.0132 cc/g and 0.1569 cc/g and pore diameter of 0.6582 nm and 0.6398 nm, respectively.

Table 1 showed the total CO₂ desorbed in terms of mmol/gm as well as the temperature wise distribution of the basic sites at the catalytic surface for all the samples under study. It was used to determine the surface basicity of the catalyst samples. The catalyst samples exhibited three CO₂ desorption peaks corresponding to the weak, moderate and strong Brønsted basicity. The first peak in the region of 100–200 °C represents weak Brønsted basicity corresponding to the desorption of physisorbed CO₂. Whereas, the peak in the temperature range 200–400 °C represents moderate basic strength and that in the range 400–700 °C represents strong basicity. The orders of the total basicity of the screened catalysts were found to be BaO > CaO > La₂O₃ > Ce₂O₃. The total basicity of La₂O₃ was 0.3854 mmol g⁻¹,

0.0867 mmol g⁻¹ for Ce₂O₃, 0.7533 mmol g⁻¹ for CaO and highest 0.99110 mmol g⁻¹ for BaO catalyst. Fig.S9 (supporting info.) represents the TPD plots for various screened catalysts. The La₂O₃ catalyst was found to give total basicity around 0.3854 mmol g⁻¹ with peak maxima at 335 °C. Whereas, CaO was found to give basicity of 0.7533 mmol g⁻¹ with peak maxima at 420 °C, Cerium oxide showed basicity of 0.0867 mmol g⁻¹ with peak maxima at 290 °C and BaO showed highest basicity of 0.9911 mmol g⁻¹. The CaO and BaO showed maximum desorption in the higher temperature range. Whereas, La₂O₃ and Ce₂O₃ catalyst showed maximum desorption in the medium temperature range. This was due to the –OH moiety at the catalytic surface and the presence of coordinated O²⁻ species as evidenced by the MeOH-FTIR (presence of Brønsted sites) and XRD analysis (presence of La(OH)₃ phase). As, La₂O₃ catalyst showed strong desorption peak in the low temperature range than Ce₂O₃ catalyst, indicating the presence of weak but dense basic sites at the catalytic surface amongst all the catalysts. Hence, the basic properties of the metal oxide catalyst were evaluated quantitatively by CO₂-TPD measurement.

Catalyst Screening

One pot partial deoxygenation and dehydration of NAG to 3AF and 3A5AF was studied using various metal oxides and the results are presented in Table 2. NAG in absence of any catalyst under the same reaction conditions didn't show any formation of 3AF and 3A5AF. Interestingly, all the metal oxides showed activities according to acidic and basic nature, they possessed. Al₂O₃ catalyst gave 11% yield of 3AF and 18% yield towards 3A5AF (Table 2, entry 1). For ZrO₂ as a catalyst, NAG yields 12% of 3AF and 6% of 3A5AF (Table 2, entry 2). BaO showed 19% and 5% yield for 3AF and 3A5AF, respectively (Table 2, entry 3). CaO

Table 2 Catalyst screening for NAG conversion to 3AF and 3A5AF

Sr. No	Catalyst	Yield (%)	
		3AF	3A5AF
1	Al ₂ O ₃	11	18
2	ZrO ₂	12	06
3	BaO	19	05
4	CaO	36	19
5	La ₂ O ₃	50	21
6	Ce ₂ O ₃	32	11

Reaction Condition: NAG (1 g), catalyst (0.2 g), Dioxane (25 mL), temperature, 180 °C; reaction time, 3 h

produced 36% yield of 3AF and 19% yield towards 3A5AF (Table 2, entry 4). It can be seen that the basic nature of the catalyst is responsible for formation of the desired product i.e. 3AF as compared to activities shown by acidic metal oxides. The 3AF yield could be enhanced by using rare earth metal oxides which possess appreciable basic characteristics. La₂O₃ showed almost complete conversion of NAG with 50% yield towards 3AF and 21% yield for 3A5AF (Table 2, entry 5). Another lanthanum series metal oxide, Ce₂O₃ gave 32% 3AF yield and 11% yield for 3A5AF (Table 2, entry 6). It can be inferred from the above results that La₂O₃ was a very promising catalyst for NAG dehydration and partial deoxygenation producing 3AF product more selectively. La₂O₃ showed better yield for 3AF as it possesses moderate basicity which are Brønsted in nature along with well distributed three-dimensional interconnected nanopores which can be clearly seen from HR-TEM micrographs. These nanopores present on the surface of La₂O₃ play a very important role during reaction, allowing improved diffusion of reactants and products. Further studies on optimization of various reaction parameters was carried out using La₂O₃ as catalyst for achieving the maximum yield for desired 3AF product.

Effect of Substrate to Catalyst Ratio

Figure 5 presents the effect of substrate to catalyst ratio on N-acetyl-glucosamine conversion. The catalyst loading was varied in range 5 to 25 wt.% with respect to the substrate (constant at 1 gm) to determine its effect on NAG conversion to 3AF. With increase in the catalyst loading from 5 to 20 wt. % there was an increase in the yield from 20 to 50%, which could be imputed to the availability of nanopores as well as active basic sites at the catalytic surface for better adsorption. As the catalyst loading was further increased to 25 wt. % there was slight decrease in the yield (48%), due to increase in the formation of humins. Thus, 20 wt. % of the catalyst was optimized for desired conversion.

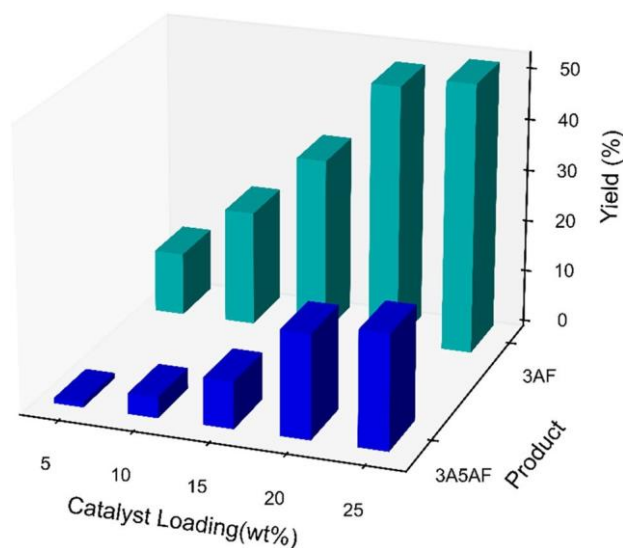


Fig. 5 Effect of substrate to catalyst ratios on 3AF production. Reaction conditions: NAG (1–5 g), Dioxane (25 mL), Time (3 h), Temp (180 °C), Catalyst (200 mg)

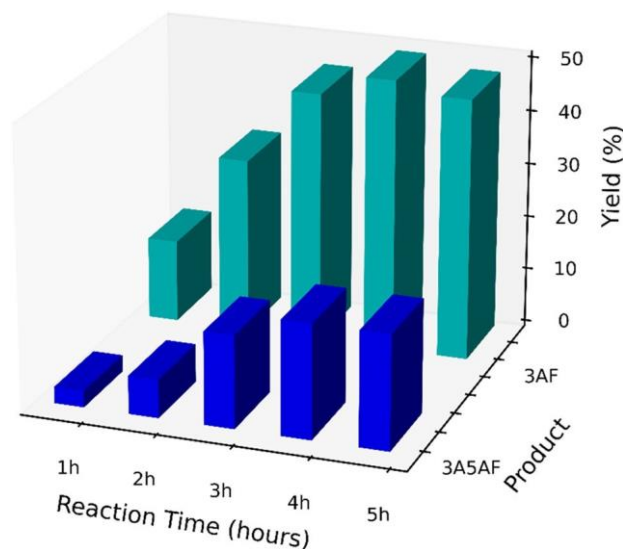


Fig. 6 Effect of time on 3AF production. Reaction conditions: NAG (1 g), Dioxane (25 mL), Time (3 h), Temp (180 °C), Catalyst (200 mg)

Effect of Time

Figure 6 shows significant increase in 3AF and 3A5AF production with increase in reaction time from 60 to 180 min. 3AF and 3A5AF yields were found to increase linearly with increase in time to maximum up to 50% and 20%, respectively. However, the yield of 3AF and 3A5AF was found to decrease after 180 min due to thermal decomposition of the products and acceleration in the rate of formation of

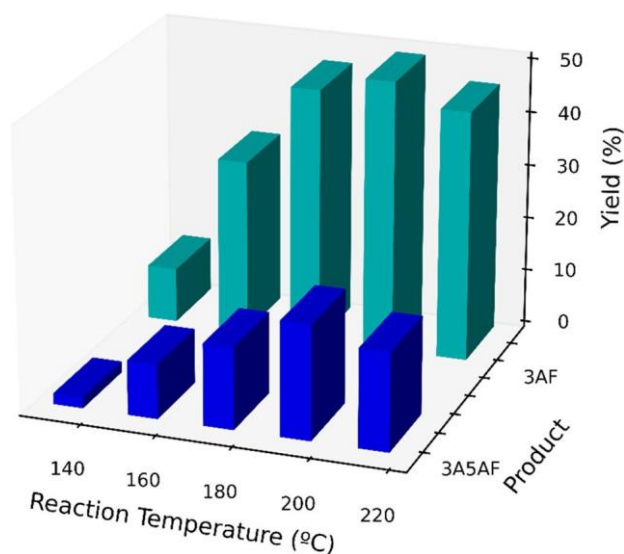


Fig. 7 Effect of temperature on 3AF production. Reaction conditions: NAG (1 g), Dioxane (25 mL), Time (3 h), Temp (180 °C), Catalyst (200 mg)

humins as by-product was favoured by elevated temperature and prolonged time.

Effect of Reaction Temperature

Figure 7 shows the effect of temperature on N-acetyl glucosamine conversion. NAG conversion to 3AF with La_2O_3 catalyst was studied by examining the reaction at various temperatures in range 120–210 °C. Figure 8 illustrates that with increase in temperature there was a linear increase in the yield of 3AF and reached to maximum at 180 °C. With further increase in the temperature to 210 °C, the product yield decreased as high temperature accelerated the humin formation. Thus, with increase in temperature above 180 °C, the selectivity to 3AF decreased due to enhancement in the formation of humins. Thus, this decrease in product yield at elevated temperature (above 180 °C) indicates that high temperature favours humin formation. The increase in temperature causes heat transfer resulting in increase in collisions between the particles thereby increasing the collision frequency. This lowers the energy of activation and enhances the reaction rates. The increasing temperature accelerated the 3AF production. Thus, maximum 50% 3AF yield was observed within 3 h at 180 °C.

Solvent Screening

Solvents play a vital role in various phenomena such as heat transfer, providing medium for reaction, separation and purification of the products. Figure 8 exhibits the effect of solvent on N-acetyl glucosamine conversion to 3AF. In order

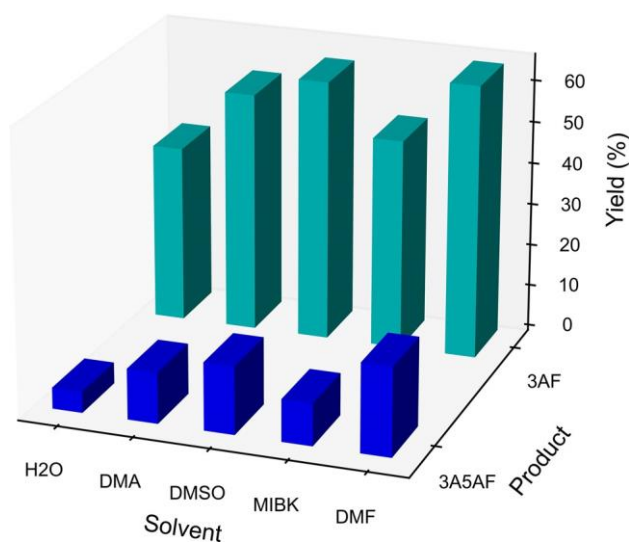


Fig. 8 Effect of solvent on 3AF production. Reaction conditions: NAG (1 g), Dioxane (25 mL), Time (3 h), Temp (180 °C), Catalyst (200 mg)

to understand the influence of solvent system on NAG conversion to 3AF and 3A5AF, several solvents such as DMA, DMSO, DMF, MIBK and dioxane were screened. DMA, DMSO and DMF were preferred solvents as they were used for dehydration of cellulosic and chitin biomass previously [56]. Whereas, dioxane is an aprotic solvent and is able to solvate various inorganic compounds in it. DMF gave highest product yield of 55%, while DMA, DMSO, MIBK and dioxane gave 52%, 48%, 39% and 50% yields of 3AF, respectively. Among these, DMF, DMA and DMSO are toxic and have few health hazards and separation of products is quite tedious as these are high boiling solvents. Also, MIBK showed low selectivity to the product due to formation of large amount of humins. Thus, dioxane was chosen as the best solvent for this conversion.

Effect of Addition of Water on Reaction Pathway

As water being green solvent and chitin biomass being readily soluble in water, the mixtures of above individual solvents with water were screened for the conversion of NAG to 3AF and 3A5AF. It was observed that the addition of water to the organic phase significantly decreased the product selectivity. Thus, the addition of water to the organic phase showed negative effect on the product yield and selectivity. This could be attributed to the fact that water caused acceleration in the formation of humins thereby decreasing the selectivity of the product formation. The effect of addition of water on NAG conversion was studied by adding 50% water to the solvent system chosen. Figure 9 shows the effect of addition of water to the solvents DMA, DMSO, DMF, MIBK and dioxane on N-Acetylglucosamine conversion.

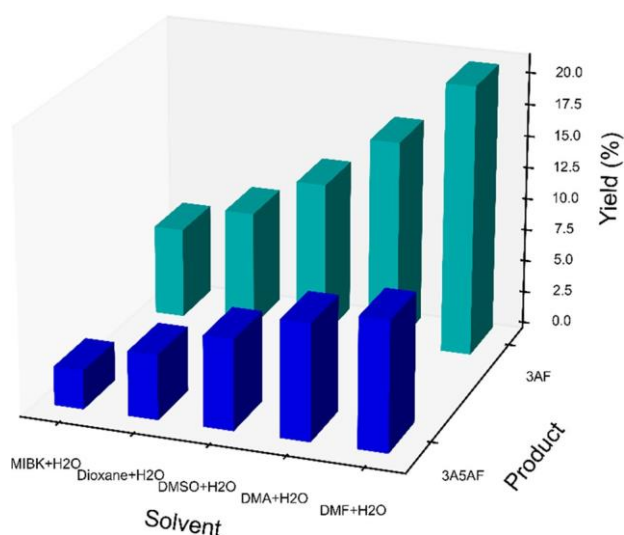


Fig. 9 Effect of water on 3AF production. Reaction conditions: NAG (1 g), Dioxane (12.5 mL), Water (12.5 mL), Time (3 h), Temp (180 °C), Catalyst (200 mg)

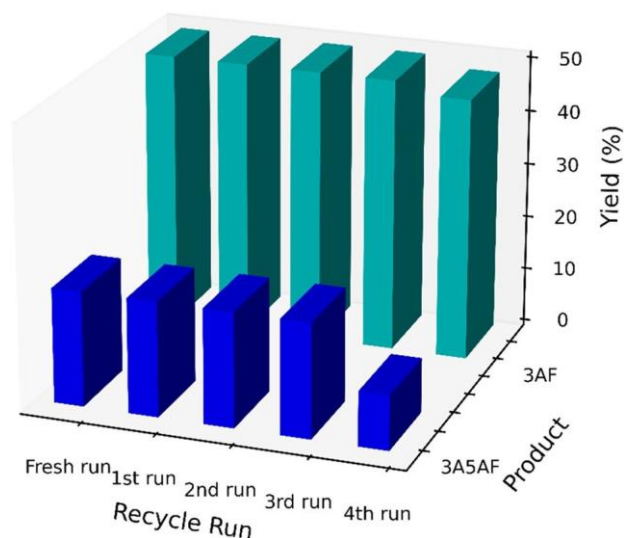


Fig. 10 Catalyst recycle study. Reaction conditions: NAG (1 g), Dioxane (25 mL), Time (3 h), Temp (180 °C), Catalyst (200 mg)

Thus, water has negative effect on NAG conversion as presence of water enhances the humin formation.

Catalyst Recycle Study

The recycle study of the heterogeneous (La_2O_3) catalyst was carried out under the optimized conditions and results are as shown in Fig. 10. After the first run, catalyst was filtered and washed with deionised water till the pale-yellow coloured catalyst faded, the catalyst was dried at 110 °C in an oven and then calcined at 550 °C for further 3 runs. The procedure

was followed for four successive cycles. The N-acetylglucosamine conversion decreased marginally by 3% (from 50 to 47%) due to handling losses. In order to study the changes of the catalyst surface during the reaction, the recovered catalyst was characterised by XRD, FTIR and TGA analysis. The XRD pattern of the used catalyst (Fig. 11) showed that the crystallinity of the catalyst remained intact and there was no deposition of any carbonaceous material at the catalytic surface. The FTIR spectrum of the reused catalyst (Fig. 12) was similar with that of the fresh catalyst which confirms the stability of the catalyst. The TGA analysis (Fig.S14, supporting info.) of the catalysts confirmed that the catalyst was thermally stable. Thus, the La_2O_3 catalyst showed exquisite recyclability performance up to 4 cycles.

Plausible Mechanism

In the proposed mechanism, N-acetyl glucosamine undergoes ring opening in the presence of basic sites of the catalyst to form an open chain compound as shown in Scheme 1, route A. The presence of nano pores on the catalyst surface as confirmed by SEM and HR-TEM analysis are found to play vital role in the adsorption of the substrate molecules. The basic sites of the catalyst participate in the abstraction of C4-OH proton (I). The nucleophilic attack of C4-O on C1-carbonyl (I) results in the formation of five membered cyclic ring (II) predominantly as formation of five membered ring is favored. This (II) further undergoes dehydration followed by elimination of CH_2OHCHO moiety. The driving force for elimination and dehydration is aromatization which provides extra stability to the system thereby forming 3-acetamido furan

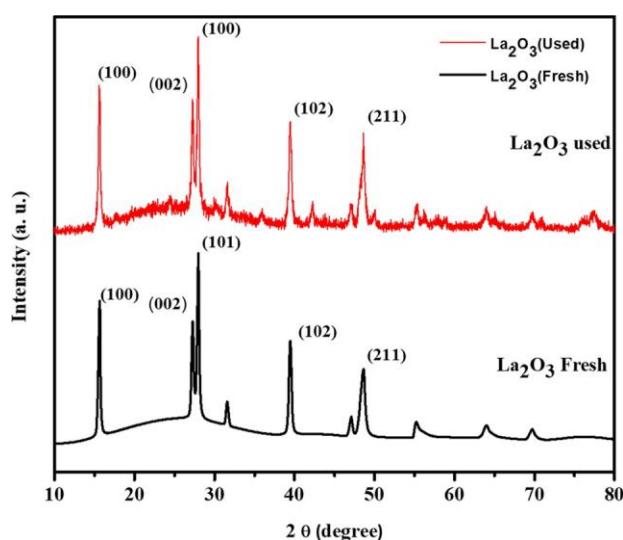


Fig. 11 Powder XRD pattern for fresh calcined La_2O_3 and used La_2O_3 metal oxide catalysts

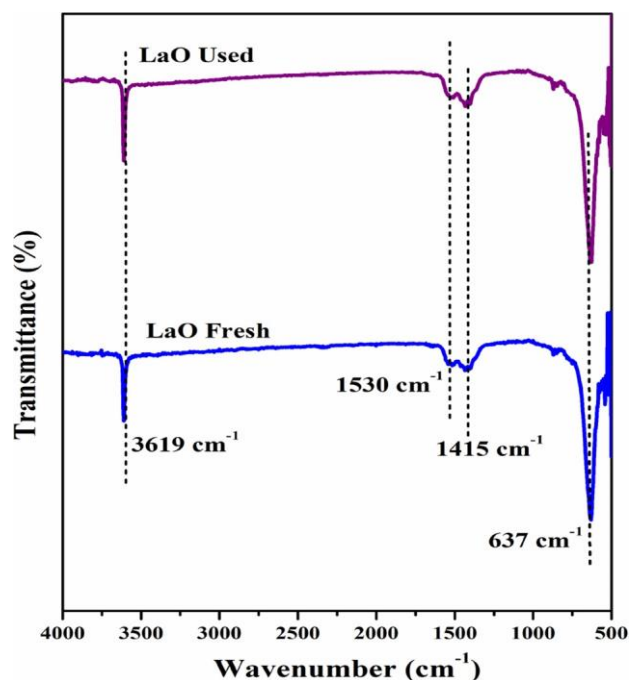
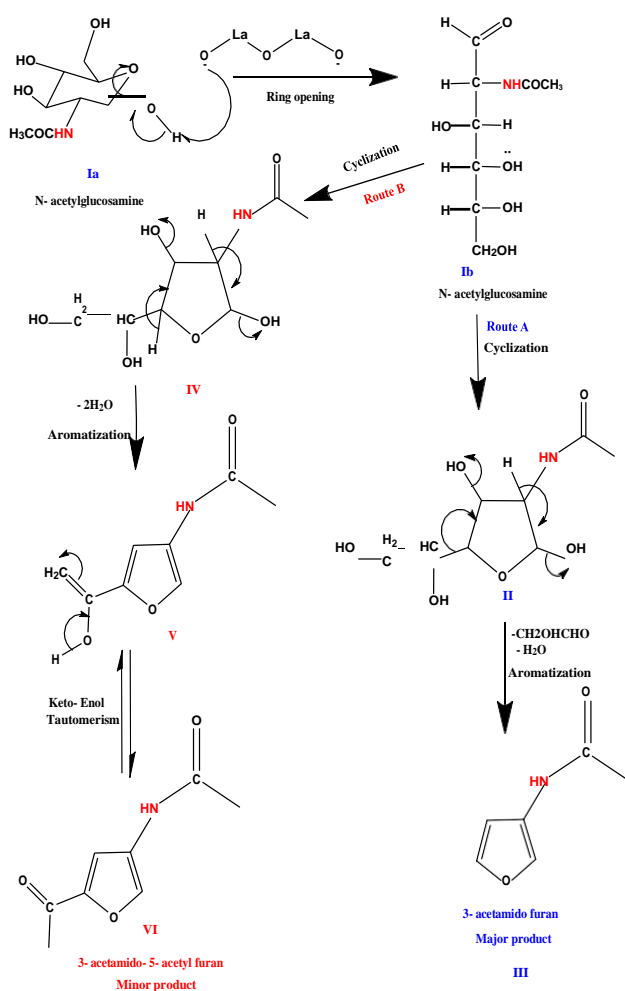


Fig. 12 FT-IR spectra for Fresh and used La_2O_3 catalyst

(III) as the major product with 50% yield. Whereas, 3A5AF (VI) is formed as a minor product with 21% yield as shown in Scheme 1, route B, which is formed by nucleophilic attack of C4-OH on C1-carbonyl (I) results in the formation of five member cyclic ring (IV). This is followed by dehydration with removal of two water molecules, as it makes the system more stable due to aromatization (V) which on keto-enol tautomerism results in the formation of 3A5AF (VI) with 21% yield [16]. The insoluble polymer humins are also formed as byproduct during the course of the reaction. Both the products formed were extracted by using a mixture of ethyl acetate and water followed by its purification by column chromatography using 50% ethyl acetate and n-hexane as the mobile phase. The products formed were confirmed by $^1\text{H-NMR}$, $^{13}\text{C-NMR}$, HRMS and FTIR (NAG and 3AF, 3A5AF) analysis qualitatively (supporting information Figs.S-1a, S-1b, S-2a, S-2b, S-3 and S-4, S-5, S-6). The NAG conversion was quantitatively determined by HPLC analysis by keeping 0.5 mL/min flow rate of the prepared mobile phase maintaining column temperature at 80 °C and total analysis time of 20 min. The calibration curve is given in supplementary material. Fig. S7 which showed complete conversion of NAG (supporting information).



Scheme 1 Plausible mechanism for base catalyzed dehydration and partial deoxygenation of N-Acetyl-D-glucosamine. (Route A: Formation of 3-acetamido furan, Route B: Formation of 3-acetamido-5-acetyl furan)

Conclusion

A comparative study of various metal oxide catalysts such as La_2O_3 , Ce_2O_3 , Al_2O_3 , ZrO_2 , BaO and CaO was undertaken for the dehydration of N-acetyl glucosamine to render important furan compounds. The physico-chemical properties of the catalyst were studied by XRD, CO_2 -TPD, BET surface area measurements, SEM, HR-TEM, MeOH-FTIR analysis. The parameters such as solvent, temperature, time and substrate concentration were optimized for efficient catalytic activity. Various experiments carried out with organic solvents and their mixtures with water revealed that dioxane was the best solvent for NAG conversion whereas, water was found to inhibit the reaction due to accelerating the formation of humins. La_2O_3 excelled as a catalyst for the transformation of N-acetylglucosamine which yields 50% 3AF and 20% 3A5AF at 180 °C in 3 h. The superior performance

was attributed to the presence of moderate basicity which was Brønsted in nature as confirmed from PXRD analysis and MeOH-FTIR originating from presence of $\text{La}(\text{OH})_3$ phase. While, FE-SEM, and HR-TEM disclosed existence of nanopores on the catalytic surface. The cooperative effect of Brønsted basicity and nanopores (90–450 nm) were found to play an important role in NAG conversion to N-containing

platform molecules. We reported for the first time the use of heterogeneous catalyst La_2O_3 to produce 50% 3AF and 21% 3A5AF yield which was 10 times more than the yield reported by the pyrolysis method. The catalyst was recyclable upto 4 cycles and easily separable. As far as sustainability is concerned this study represents a direct one pot conversion of NAG to N-substituted renewable compounds by valorization of marine biomass.

Supplementary Information The online version contains supplementary material available at <https://doi.org/10.1007/s12649-023-02127-2>.

Acknowledgements Samrin S. Shaikh acknowledges Council of Scientific & Industrial Research (CSIR) for providing financial support, reference no. 21(1054)/18/EMR-II and AcSIR for providing various facilities to carry out the research work successfully. One of the authors, Chetana R. Patil acknowledge Council of Scientific & Industrial Research (CSIR), for the award of Research Associateship vide reference no. 31/011(1141)/2020-EMR-I for the financial assistance to carry out this work.

Author Contributions The first draft of the manuscript was written by SSS and CVR commented on previous versions of the manuscript. All authors read and approved the final manuscript. CVR and SSS, Conceptualization, Data analysis, Investigation, Methodology, Writing, CRP, Writing, VVB, supervision, NL, writing and Dr. CVR, Supervision and Writing revisions.

Funding This study was supported by National Chemical Laboratory, [Grant Numbers 21/(1054)/18/EMR-II, 31/011(1141)/2020-EMR-I].

Data Availability Enquiries about data availability should be directed to the authors.

Declarations

Conflict of interest The authors declare that they have no conflict of interest.

References

- Nel, W.P., Cooper, C.J.: Implications of fossil fuel constraints on economic growth and global warming. *Energy Policy* **37**, 166–180 (2009)
- Shafiee, S., Topal, E.: When will fossil fuel reserves be diminished? *Energy Policy* **37**(1), 181–189 (2009)
- Arancon, R.A.D., Lin, C.S.K., Chan, K.M., Kwan, T.H., Luque, R.: *Advances on Waste Valorization: New Horizons for a More Sustainable Society*. In: Rada, E.C. (ed.) Waste Management and Valorization. Apple Academic Press, New Jersey (2017)
- Hülsey, M.J., Yang, H., Yan, N.: Sustainable routes for the synthesis of renewable heteroatom-containing chemicals. *ACS Sustain. Chem. Eng.* **6**(5), 5694–5707 (2018)

- Hussain, A., Arif, S.M., Aslam, M.: Emerging renewable and sustainable energy technologies: state of the art. *Renew. Sustain. Energy Rev.* **71**, 12–28 (2017)
- Gooday, G.W.: The ecology of chitin degradation. In: *Advances in Microbial Ecology*, pp. 387–430. Springer, Boston, MA (1990)
- Yan, N., Chen, X.: Sustainability: don't waste seafood waste. *Nature* **524**(7564), 155–157 (2015)
- Chen, X., Yang, H., Yan, N.: Shell biorefinery: dream or reality? *Chem. Eur. J.* **22**(38), 13402–13421 (2016)
- Chen, X., Liu, Y., Wang, J.: Lignocellulosic biomass upgrading into valuable nitrogen-containing compounds by heterogeneous catalysts. *Ind. Eng. Chem. Res.* **59**(39), 17008–17025 (2020)
- Chen, X., Song, S., Li, H., Gözaydın, G., Yan, N.: Expanding the boundary of biorefinery: organonitrogen chemicals from biomass. *Acc. Chem. Res.* **54**(7), 1711–1722 (2021)
- Lucas, N., Athawale, A.A., Rode, C.V.: Valorization of oceanic waste biomass: a catalytic perspective. *Chem Rec.* **19**(9), 1995–2021 (2019)
- Elieh-Ali-Komi, D., Hamblin, M.R.: Chitin and chitosan: production and application of versatile biomedical nanomaterials. *Int. J. Adv. Res. Publ.* **4**(3), 411 (2016)
- Khoushab, F., Yamabhai, M.: Chitin research revisited. *Mar. Drugs*. **8**(7), 1988–2012 (2010)
- Younes, I., Rinaudo, M.: Chitin and chitosan preparation from marine sources Structure, properties and applications. *Mar. Drugs*. **13**(3), 1133–1174 (2015)
- Raafat, D., Sahl, H.G.: Chitosan and its antimicrobial potential—a critical literature survey. *Microb. Biotechnol.* **2**(2), 186–201 (2009)
- Chen, J., Wang, M., Ho, C.T.: Volatile compounds generated from thermal degradation of N-acetylglucosamine. *J. Agric. Food Chem.* **46**(8), 3207–3209 (1998)
- Omari, K.W., Dodot, L., Kerton, F.M.: A simple one pot dehydration process to convert N-acetyl-D-glucosamine into a nitrogen containing compound, 3-acetamido-5-acetyl-furan. *Chemsuschem* **5**(9), 1767–1772 (2012)
- Drover, M.W., Omari, K.W., Murphy, J.N., Kerton, F.M.: Formation of a renewable amide, 3-acetamido-5-acetyl-furan, via direct conversion of N-acetyl-d-glucosamine. *RSC Adv.* **2**(11), 4642–4644 (2012)
- Chen, X., Chew, S.L., Kerton, F.M., Yan, N.: Direct conversion of chitin into a N-containing furan derivative. *Green Chem.* **16**(4), 2204–2212 (2014)
- Franich, R.A., Goodin, S.J., Wilkins, A.L.: Acetamidofurans, acetamidopyrones, and acetamidoacetaldehyde from pyrolysis of chitin and n-acetylglucosamine. *J. Anal. Appl. Pyrolysis.* **7**(1–2), 91–100 (1984)
- Omari, K.W., Dodot, L., Kerton, F.M.: A simple one pot dehydration process to convert N-acetyl D glucosamine into a nitrogen containing compound, 3-acetamido 5 acetyl-furan. *Chemsuschem* **5**(9), 1767–1772 (2012)
- Sadiq, A.D., Chen, X., Yan, N., Sperry, J.: Towards the shell biorefinery: sustainable synthesis of the anticancer alkaloid proximicin A from chitin. *Chemsuschem* **11**(3), 532–535 (2018)
- Bobbink, F.D., Zhang, J., Pierson, Y., Chen, X., Yan, N.: Conversion of chitin derived N-acetyl-d-glucosamine (NAG) into polyols over transition metal catalysts and hydrogen in water. *Green Chem.* **17**(2), 1024–1031 (2015)
- Dai, J., Li, F., Fu, X.: Towards shell biorefinery. *Advances in chemical catalytic conversion of chitin biomass to organonitrogen chemicals.* *Chemsuschem* **13**(24), 6498–6508 (2020)
- Pham, T.T., Chen, X., Yan, N., Sperry, J.: A novel dihydrodi-furopyridine scaffold derived from ketones and the chitin-derived heterocycle 3-acetamido-5-acetyl-furan. *Monatsh. Chem.* **149**(4), 857–861 (2018)
- Pham, T.T., Lindsay, A.C., Kim, S.W., Persello, L., Chen, X., Yan, N., Sperry, J.: Two step preparation of diverse 3-amidofurans from chitin. *ChemistrySelect* **4**(34), 10097–10099 (2019)
- Xin, Y., Shen, X., Liu, H., Han, B.: Selective utilization of n-acetyl groups in chitin for transamidation of amines. *Front Chem Sci Eng.* **2**, 634983 (2021)
- Pham, T.T., Chen, X., Söhnle, T., Yan, N., Sperry, J.: Haber-independent, diversity-oriented synthesis of nitrogen compounds from biorenewable chitin. *Green Chem.* **22**(6), 1978–1984 (2020)
- Johdo, O., Yoshioka, T., Naganawa, H., Takeuchi, T., Yoshimoto, A.: New betaclamycin and aclarubicin analogs obtained by prolonged microbial conversion with an aclarubicin-negative mutant. *J. Antibiot.* **49**(7), 669–675 (1996)
- Shaaban, K.A., Ahmed, T.A., Leggas, M., Rohr, J.: Saquayamycins G-K, cytotoxic angucyclines from streptomyces sp. including two analogues bearing the aminosugar rednose. *J. Nat. Prod.* **75**(7), 1383–1392 (2012)
- Doyle, T.W., Nettleton, D.E., Grulich, R.E., Balitz, D.M., Johnson, D.L., Vulcano, A.L.: Antitumor agents from the bohemic acid complex. 4. Structures of rudolphomycin, mimimycin, collinemycin, and alcindoromycin. *J. Am. Chem. Soc.* **101**(23), 7041–7049 (1979)
- Hao, Y.C., Zong, M.H., Wang, Z.L., Li, N.: Chemoenzymatic access to enantiopure N-containing furfuryl alcohol from chitin-derived N-acetyl-D-glucosamine. *Bioresour. Bioprocess* **8**(1), 1–9 (2021)
- Wang, J., Zang, H., Jiao, S., Wang, K., Shang, Z., Li, H., Lou, J.: Efficient conversion of N-acetyl-d-glucosamine into nitrogen-containing compound 3-acetamido-5-acetyl-furan using amino acid ionic liquid as the recyclable catalyst. *Sci. Total Environ.* **710**, 136293 (2020)
- Qi, X., Watanabe, M., Aida, T.M., Smith, R.L., Jr.: Efficient one-pot production of 5-hydroxymethylfurfural from inulin in ionic liquids. *Green Chem.* **12**(10), 1855–1860 (2010)
- Khalaf, W.M., Al-Mashhadani, M.H.: Synthesis and characterization of lanthanum oxide La₂O₃ net-like nanoparticles by new combustion method. *Biointerface Res. Appl. Chem.* **12**, 3066–3075 (2022)
- Singh, A., Palakollu, V., Pandey, A., Kanvah, S., Sharma, S.: Green synthesis of 1, 4-benzodiazepines over La₂O₃ and La(OH)₃ catalysts: possibility of Langmuir-Hinshelwood adsorption. *RSC Adv.* **6**(105), 103455–103462 (2016)
- Li, S.C., Hu, S.J., Du, N., Fan, J.N., Xu, L.J., Xu, J.: Low-temperature chemical solution synthesis of dendrite-like La(OH)₃ nanostructures and their thermal conversion to La₂O₃ nanostructures. *Rare Met.* **34**(6), 395–399 (2015)
- Shaikh, S.S., Patil, C.R., Kondawar, S.E., Rode, C.V.: Cooperative acid base sites of solid BaZr mixed oxide catalyst for efficient isomerization of glucose to fructose in aqueous medium. *ChemistrySelect* **5**(40), 12505–12513 (2020)
- Yazıcılar, B., Böke, F., Alaylı, A., Nadaroglu, H., Gedikli, S., Bezirganoglu, I.: In vitro effects of CaO nanoparticles on triticale callus exposed to short and long-term salt stress. *Plant Cell Rep.* **40**(1), 29–42 (2021)
- Peng, S., Sun, X., Sun, L., Zhang, M., Zheng, Y., Su, H., Qi, C.: Selective hydrogenation of acetylene over gold nanoparticles supported on CeO₂ pretreated under different atmospheres. *Catal Lett.* **149**(2), 465–472 (2019)
- Romero Toledo, R., Ruíz Santoyo, V., Moncada Sánchez, D., Martínez Rosales, M.: Effect of aluminum precursor on physicochemical properties of Al₂O₃ by hydrolysis/precipitation method. *Nova scientia.* **10**(20), 83–99 (2018)
- Matsouka, V., Konsolakis, M., Lambert, R.M., Yentekakis, I.V.: In situ DRIFTS study of the effect of structure (CeO₂-La₂O₃) and surface (Na) modifiers on the catalytic and surface behaviour

- of Pt/ γ -Al₂O₃ catalyst under simulated exhaust conditions. *Appl. Catal. B: Environ* **84**(3–4), 715–722 (2008)
43. Tejani, J., Shah, R., Vaghela, H., Vajapara, S., Pathan, A.: Controlled synthesis and characterization of lanthanum nanorods. *Int. J. Thin Film Sci. Technol.* **9**(2), 5 (2020)
 44. Verma, N.K.: Study on the controlled growth of lanthanum hydroxide and manganese oxidenano composite under the presence of cationic surfactant. *Adv. Mater.* **4**, 11–15 (2015)
 45. Mu, Q., Wang, Y.: Synthesis, characterization, shape-preserved transformation, and optical properties of La (OH)₃, La₂O₂CO₃, and La₂O₃ nanorods. *J. Alloys Compd.* **509**(2), 396–401 (2011)
 46. Zhu, H., Yang, D., Yang, H., Zhu, L., Li, D., Jin, D., Yao, K.: Reductive hydrothermal synthesis of La(OH)₃: Tb³⁺ nanorods as a new green emitting phosphor. *J. Nanoparticle Res.* **10**(2), 307–312 (2008)
 47. Fleming, P., Farrell, R.A., Holmes, J.D., Morris, M.A.: The rapid formation of La (OH)₃ from La₂O₃ powders on exposure to water vapor. *J. Am. Ceram. Soc.* **93**(4), 1187–1194 (2010)
 48. Vernekar, D., Sakate, S.S., Rode, C.V., Jagadeesan, D.: Water-promoted surface basicity in FeO (OH) for the synthesis of pseudoionones (PS) and their analogues. *J. Catal.* **378**, 80–89 (2019)
 49. Bailly, M.L., Chizallet, C., Costentin, G., Krafft, J.M., Lauron-Pernot, H., Che, M.: A spectroscopy and catalysis study of the nature of active sites of MgO catalysts: thermodynamic brønsted basicity versus reactivity of basic sites. *J. Catal.* **235**(2), 413–422 (2005)
 50. Bensitel, M., Saur, O., Lavalley, J.C.: Use of methanol as a probe to study the adsorption sites of different MgO samples. *Mater. Chem. Phys.* **28**(3), 309–320 (1991)
 51. Li, Y., Lin, J., Wang, G.: La₂O₃/Fe₂O₃-CeO₂ composite oxide catalyst and its performance. *Adv. Mater. Phys. Chem.* **9**(12), 219–233 (2019)
 52. Othman, Z.A.L.: A review: fundamental aspects of silicate mesoporous materials. *Materials.* **5**(12), 2874–2902 (2012)
 53. Uppal, S., Arora, A., Gautam, S., Singh, S., Choudhary, R.J., Mehta, S.K.: Magnetically retrievable Ce-doped Fe₃O₄ nanoparticles as scaffolds for the removal of azo dyes. *RSC adv.* **9**(40), 23129–23141 (2019)
 54. Adole, V.A., Pawar, T.B., Koli, P.B., Jagdale, B.S.: Exploration of catalytic performance of nano-La₂O₃ as an efficient catalyst for dihydropyrimidinone/thione synthesis and gas sensing. *J. Nanostruct. Chem.* **9**(1), 61–76 (2019)
 55. Ambroz, F., Macdonald, T.J., Martis, V., Parkin, I.P.: Evaluation of the BET theory for the characterization of Meso and microporous MOFs. *Small methods.* **2**(11), 1800173 (2018)
 56. Zang, H., Lou, J., Jiao, S., Li, H., Du, Y., Wang, J.: Valorization of chitin derived N-acetyl-D-glucosamine into high valuable N-containing 3-acetamido-5-acetyl furan using pyridinium-based ionic liquids. *J. Mol. Liq.* **330**, 115667 (2021)

Publisher's Note Springer Nature remains neutral with regard to jurisdictional claims in published maps and institutional affiliations.

Springer Nature or its licensor (e.g. a society or other partner) holds exclusive rights to this article under a publishing agreement with the author(s) or other rightsholder(s); author self-archiving of the accepted manuscript version of this article is solely governed by the terms of such publishing agreement and applicable law.

Authors and Affiliations

Samrin S. Shaikh^{1,2} · Chetana R. Patil¹ · Nishita Lucas¹ · Vijay V. Bokade^{2,3} · Chandrashekhar V. Rode^{1,2} 

✉ Chandrashekhar V. Rode
cv.rode@ncl.res.in; cvrode8@gmail.com

¹ Chemical Engineering and Process Development Division, Pune, India

² Academy of Scientific and Innovative Research (AcSIR), Ghaziabad 201002, India

³ Catalysis Division, CSIR-National Chemical Laboratory, Dr. HomiBhaba Road, Pune 411008, India